Doctoral Thesis

Particle Acceleration at Shocks in Galaxy Clusters

Ji-Hoon Ha

Department of Physics

Ulsan National Institute of Science and Technology

2022

Particle Acceleration at Shocks in Galaxy Clusters

Ji-Hoon Ha

Department of Physics

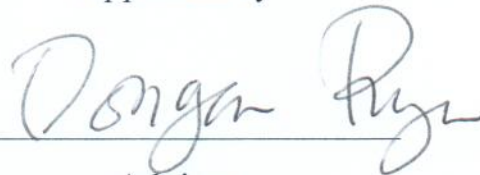Ulsan National Institute of Science and Technology

Particle Acceleration at Shocks in Galaxy Clusters

A thesis/dissertation submitted to

Ulsan National Institute of Science and Technology

in partial fulfillment of the

requirements for the degree of

Doctor of Philosophy

Ji-Hoon Ha

06/16/2022 of submission

Approved by

_____

Advisor

Dongsu Ryu

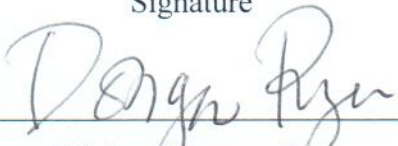# Particle Acceleration at Shocks in Galaxy Clusters

Ji-Hoon Ha

This certifies that the thesis/dissertation of Ji-Hoon Ha is approved.

06.16.2022 of submission

Signature

Advisor: Dongsu Ryu

Signature

Kyujin Kwak: Thesis Committee member #1

Signature

Min Sup Hur: Thesis Committee member #2

Signature

Jungyeon Cho: Thesis Committee member #3

Signature

Hyesung Kang: Thesis Committee member #4

Abstract

Major mergers between two sub-clusters drive shocks with Mach number, $M_s \sim 2˘4$ inside the hot "intracluster medium"(ICM) with temperature, $T \sim 10^7 - 10^8$ K and plasma beta, $\beta \sim 50 - 100$. Those merger-driven shocks, like most astrophysical shocks, are collisionless shocks and Cosmic-ray (CR) are expected to be accelerated at such shocks through Diffusive Shock Acceleration (DSA; a.k.a 1st-order Fermi acceleration). Mpc-scale diffuse radio synchrotron emissions from the outskirts of galaxy clusters (i.e., the so-called radio relics) indicate electron acceleration at ICM shocks and future observation of π^0-decay gamma-ray emission could provide an evidence for the production of CR protons as well. To investigate the kinetic plasma processes that govern the particle preacceleration for DSA at ICM shocks, we performed Particle-in-Cell (PIC) simulations with relevant parameters for ICM plasmas. In particular, both electron and proton are energized effectively through the preacceleration mechanism mediated by the multi-scale plasma waves in the shocks with $M_s \gtrsim 2.3$, and so the origin of observed radio relics could be explained through such preacceleration process. In addition, considering the results obtained from our PIC simulations, we proposed a DSA model for CR proton acceleration and examined the feasibility of detecting gamma-ray from galaxy clusters. We have confirmed that the predicted gamma-ray emission is below the Fermi-LAT upper limits for observed clusters. Our findings will help to understand high-energy astrophysical processes in galaxy clusters.

Contents

List of Figures

I Introduction

According to the current observations, the matters distributed in the universe are not homogenous but they form the cosmic web which is the so-called the large-scale structure (LSS) of the universe. Based on the current ΛCDM cosmology, the LSS of the universe has been evolved through hierarchical cluster and it consists of clusters and filaments of galaxies and void regions. In particular, cluster of galaxies is the largest gravitationally bounded object which contains the thousands of galaxies and the range of mass is $\sim 10^{14} - 10^{15} M_\odot$. Along with tons of galaxies and dark matters, the hot ($T \sim 10^7 - 10^8$ K) and weakly magnetized ($B \sim 10^{-6} G$) plasma permeates a galaxy cluster which is called the intracluster medium (ICM).

In the astrophysical environments, shock waves are ubiquitous due to the supersonic motions such as solar winds, supernova remnants and relativistic jets from active galactic nuclei. Because of the hierarchical structure formation, the complex supersonic flow motions exist inside the galaxy clusters as well, and thus shock waves are naturally induced in the ICM. Those ICM shocks, like most astrophysical shocks, are collisionless shocks and their kinetic energy fluxes are dissipated into gas thermalization and particle acceleration. Using cosmological hydrodynamic simulations for the large-scale structure (LSS) formation of the universe, the properties and roles of shocks in the ICM as well as around clusters have been extensively studied [1–9].

According to such numerical studies, the cosmological shocks can be classified into two types, which are summarized as follows: external accretion shocks form around galaxy clusters due to the gas accretion from void regions with $T \sim 10^4$ K. With the accretion velocity of $\sim 10^2 - 10^3$ km s^{-1} and the sound speed of $c_s \sim 10$ km s^{-1}, their Mach number is in the range of $M_s \sim 10 - 100$. Although the external shocks are strong shocks, the kinetic energy flux dissipated through those shocks, $f_\phi = (1/2)\rho_1 v_s^3$ (where ρ_1 is the preshock gas density and v_s is the shock speed) is very small because they propagate in the very low density regions. Inside clusters, internal shocks are induced by supersonic flow motions such as the major mergers between two sumclumps, gas infall from filaments of galaxies and turbulent flow motions [2]. Because they propagate in the hot ICM, they have lower Mach numbers ($M_s \sim 2 - 4$). But the gas density of ICM is higher than that of the medium around galaxy clusters, kinetic energy dissipation through such internal shocks is much more substantial for heating ICMs and producing CRs, compared to external shocks.

Depending on the type of supersonic flow motions, internal shocks can be further categorized into three types. *turbulent shocks*, induced by turbulent flow motions, are mostly weak with at most $M_s \lesssim 2$ [10], since ICM flow motions are subsonic with turbulent Mach number $M_t \sim 0.5$ [11–15]. *Infall shocks* are formed by continuous infall of the WHIM of $T \sim 10^5 - 10^7$ K, often with streams of minor mergers, into the hot ICM of $T \sim 10^7 - 10^8$ K [16–18]. They can have higher Mach numbers of up to $M_s \sim 10$ [8]. With relatively high Mach numbers, infall shocks could be sites for efficient CR acceleration. But they form mostly in the cluster outskirts, since the gas accretion from filaments normally halts around the virial radius and does not penetrate into the core. Moreover, they have small cross sections. *merger shocks* are induced by "major mergers" between two small galaxy clusters. A merger of $M \sim 10^{14} M_{\text{sun}}$

clumps with speed $\sim 10^3$ km s^{-1} involves the kinetic energy of $E_{\mathrm{merg}} \sim 10^{63}$ ergs, and a substantial fraction of it could be dissipated at merger shocks in the time-scale of $\sim 1 - 2$ Gyr [19]. Because a substantial fraction of the merger kinetic energy during $\sim 1 - 2$ Gyr, $E_{\mathrm{merg}} \sim 10^{63}$ erg is dissipated through merger shocks, merger shocks should be energetic enough to result in observable phenomena. For this reason, most shocks observed in X-ray and/or radio, usually in the outskirts of merging clusters, have been interpreted as merger shocks (see Section II for further details such as properties of merger shocks).

Typical collisionless shocks in the astrophysical enviroments accelerate cosmic rays (CRs) via the first-order Fermi acceleration (in other words, diffusive shock acceleration (DSA)) [20–22]. In order to understand kinetic plasma processes for CR acceleration at collisionless shocks, particle-in-cell (PIC) and hybrid plasma simulations have been extensively performed (e.g., [23–29]). In particular, majority of such studies have focused on the strong shocks in front of supernova remnants (SNRs) with $M_s \sim 10 - 100$, $\beta \sim 1$ and $T \sim 10^4$ K (e.g., [26–28]), where the plasma beta, β is the ratio between thermal energy and magnetic energy (i.e., lower β indicates that plasma is strongly magnetized). In the higher β-range, on the other hand, not many PIC simulations have been performed. This is partly because simulating high-β plasma is computationally very expansive compared to the low-β system. Moreover, compared to the SNR, the evidence of CR proton acceleration by ICM shocks has failed to be detected.

It is important that the micro physics at the collisionless shocks for particle acceleration is sensitively affected by the shock Mach number and the plasma beta (e.g., [29, 30]). Compared to the SNR shocks, the ICM shocks are very weak ($M_s \sim 2 - 4$) and propagate in the weakly magnetized medium ($\beta \sim 50 - 100 \gg 1$) and thus more detailed numertical studies with the relevant parameters for the ICM plasma shoud be required to understand particle acceleration at the ICM shocks. In this regards, we have performed sets of PIC simulations to investigate kinetic plasma processes for particle acceleration at the ICM shocks.

By studying particle acceleration process through numerical simulations, in this thesis, we address two outstanding problems regarding particle acceleration in the galaxy clusters, which are summarized as follows:

1. Non-detection of diffuse γ-ray emission from galaxy clusters: It is expected that CR protons could be accelerated at the ICM shocks via DSA and the diffuse γ-ray emission from galaxy clusters is also expected to be detected due to the inelastic collision between CR protons and thermal ICM protons. However, currently available γ-ray telescopes such as Fermi-LAT and Veritas have yet to detect the cluster-wide γ-ray emission from galaxy clusters. To resolve this problem, it is necessary to understand the detailed proton acceleration process at the ICM shocks and estimate the expected γ-ray flux from galaxy clusters more precisely, compared to the previous works (e.g., [31]). In particular, in this thesis, we present the early DSA process at the ICM shocks by following micro plasma instabilities in the first principle through a set of PIC simulations.

2. The origin of observed radio relics in the outskirts of galaxy clusters: The shocks in the outskirts of galaxy clusters have been detected through radio observations and such radio emission has been interpreted as synchrotron radiation emitted by CR electrons produced at the ICM shocks via DSA. While

the DSA theory states that particles can be accelerated by the crossing the shock and interacting plasma waves near the shock surface many times, thermal electrons are hard to be directly accelerated through DSA because the width of shock transition layer is an order of the gyroradius of thermal electrons. In this context, in order to be injected into DSA, thermal electrons should be preaccelerated to become suprathermal electrons with suprathermal momentum, $p_e \gtrsim$ a few $\times p_{\mathrm{th,p}}$ (i.e., the so-called electron injection problem; e.g., [32]). Here, $p_{\mathrm{th,p}} = (2m_p k_B T_2)^{1/2}$ is the proton thermal momentum in the post-shock gas of temperature T_2, m_p is the proton mass, and k_B is the Boltzmann constant. In this thesis, we present the recent PIC simulation results to examine the microinstabilites and electron preacceleration mechanisms mediated by plasma waves induced by such microinstabilities.

The thesis is organized as follows. Note that all results shown in this thesis are originally from the papers cited below.

In Section II, to understand dynamical evolution of merging galaxy clusters and merger-driven shocks in there, we study properties of such shocks based on a set of cosmological hydrodynamic simulations (Ha, J.-H., Ryu, D., & Kang, H. 2018, The Astrophysical Journal, 857, 26; [33]).

In Sections III and IV, the detailed proton acceleration process at the ICM shocks and the detectability of high energy γ-ray and neutrino emission from galaxy clusters are covered (Ha, J.-H., Ryu, D., Kang, H., & van Marle, A. J. 2018, The Astrophysical Journal, 864, 105; Ha, J.-H., Ryu, D., & Kang, H. 2020, The Astrophysical Journal, 892, 86; [83, 105]).

In Sections V, VI, VII & VIII, the recent PIC simulation results regarding electron acceleration at the ICM shocks are provided. Especially, microinstabilities in the shock upstream and downstream are examined in Sections V and VI and the electron acceleration mechanisms mediated by such microinstabilities are given in Sections VII and VIII as follows (Kim, S., Ha, J.-H., Ryu, D., & Kang, H. 2020, The Astrophysical Journal, 892, 85; Kim, S., Ha, J.-H., Ryu, D., & Kang, H. 2021, The Astrophysical Journal, 913, 35; Ha, J.-H., Kim, S., Ryu, D., & Kang, H. 2021, The Astrophysical Journal, 915, 18 ;Ha, J.-H., Ryu, D., Kang, H., & Kim, S. 2022, The Astrophysical Journal, 925, 88; [143, 163, 164, 194]).

II   Properties of Merger Shocks in Galaxy Clusters

As mentioned in the Introduction, shocks driven by major merger between two subclumps play an important role in energy dissipation inside the galaxy clusters and so they have been detected through X-ray and/or radio observations. In this Section, we study merger shocks in merging galaxy clusters that produced with a set of cosmological hydrodynamic simulations. Note that all results shown here are originally presented in the paper (Ha, J.-H., Ryu, D., & Kang, H. 2018, The Astrophysical Journal, 857, 26; [33]).

Because the ICM gas is heated by shock propagating to the outskirts of galaxy clusters, thermal bremsstrahlung is emitted by the heated gas in the X-ray range. As consequence of that, merger-driven shocks have been observed through X-ray telescopes such as *Chandra*, *XMM-Newton*, and *Suzaku* [34–37]. For example, the well-known Bullet Cluster (1E 0657-56) contains the shock driven by major merger [38]. They are very weak with $M_s \sim 1.5 - 3$ and typically located at the outskirts of galaxy clusters (i.e., ~ 1 Mpc from the cluster center).

Along with the X-ray observations, merger-driven shocks have been detected through radio observation in the outskirts of galaxy clusters as well. Their radio emission has been interpreted as synchrotron radiation from CR electrons accelerated at shocks. Including well studied radio relics such as the so-called Sausage relic in the cluster CIZA J2242.8+5301 [39,40], double relics in ZwCl 0008.8+5215 [41] and PLCK G287.0+32.9 [42,43], and the so-called Toothbrush relic in RX J0603.3+4214 [44,45], tons of observed radio relics [14,46–48] indicate that CRs are efficiently produced through the shocks in the galaxy clusters. They are also located at the outskirts of galaxy clusters, but it is interesting that the shock Mach number inferred from X-ray and radio observations for the same object does not always agree with each other. In the case of the Sausage relic, for instance, the estimated mach number based on the radio spectral index near the edge is $M_{\mathrm{radio}} \approx 4.6$ [39], while the Mach number calculated by the temperature jump obtain from the X-ray observations is in the range of $M_{\mathrm{X}} \approx 2.5 - 3.1$ [35,49]. In the case of the Toothbrush relic, the Mach number estimated with the radio spectral index, $M_{\mathrm{radio}} \approx 2.8$ [45] is also larger than that obtained from X-ray observations, $M_{\mathrm{X}} \lesssim 2$ [36,45].

Understanding the discrepancy between M_{X} and M_{radio} explained above still remains as an outstanding problem. The so-called reacceleration model has been recognized as a possible scenario to resolve this problem. This model states that a shock with $\sim M_{\mathrm{X}}$ sweeps through and reaccelerates pre-existing "fossil CR electrons" of a flat energy spectrum consistent with the observed radio spectrum [50] (see also Section VIII for further details). In contrast, [51] proposed that generating and/or maintaining such flat spectrum fossil CR electrons may not be feasible considering the short cooling time scales of GeV electrons, so a shock with $\sim M_{\mathrm{radio}}$ is needed to reproduce the aforementioned radio observations. Alternatively, from mock X-ray and radio observations of relic shocks in clusters from simulations of the LSS formation, [52] reported that the surfaces of ICM shocks are highly inhomogeneous with different M_s values at various locations. In the nonuniform shock surfaces, radio emissions come from parts with higher M_s and thus higher electron acceleration, while X-ray observations pick up the parts with higher shock energy flux but lower M_s. Therefore, M_s inferred from X-ray discontinuities is generally lower

than that derived from radio spectral indices, explaining the discrepancy between the M_s derived from X-ray and radio observations. Indeed, according to the recent numerical studies for electron preacceleration at ICM shocks including the detailed kinetic plasma processes (see sections V to VIII for more details), acceleration efficiency increases as M_s increases, in agreement with the interpretation about the nonuniform nature of shocks.

The mass distributions of observed clusters can be reconstructed through weak lensing observations. Especially, merging galaxy clusters contain at least two Dark matter (DM) peaks because of the collisionless feature of DM and thus multiple peaks have been detected through weak lensing techniques. The weak lensing analysis have provided the results to confine the interpretation and modeling of reported shocks in numerous merging clusters. Several findings are summarized as follows. DM clumps behind shocks were discovered in a weak lensing investigation of the Bullet Cluster, for example, whose peaks are offset from the X-ray peaks [53]. [54] discovered two DM clumps of almost identical masses, whose distributions are offset from the galaxy distribution as well as the X-ray emission, in a weak lensing mass reconstruction of CIZA J2242.8+5301. On the other hand, [55] suggested that the clump behind the Sausage relic is less massive, while the one on the other side of the cluster and close to the X-ray emission peak is around twice more massive. Furthermore, mass reconstructions identified, for instance, two DM clumps of mass ratio ~ 5 in ZwCl 0008.8+5215 [56], two dominant DM clumps of mass ratio ~ 3 and a few smaller clumps in RX J0603.3+4214 [57], and one dominant DM clump and several smaller clumps in PLCK G287.0+32.9 [58]. In these clusters, heavy clumps are seen behind the major relics in these clusters.

In merging clusters, "cold fronts" have been observed along with merger shocks [19, 38, 59, 60]. In fluid dynamics, cold fronts indicate the structures with opposite density and temperature gradients (a.k.a. contact discontinuities). They are frequently modeled as the edges of cool clumps [61], alternatively clump sloshing motions possibly form the cold front [62]. Some of them show up behind merger shocks in merging clusters, usually half way between the cluster core and the shocks [38, 63] and we have confirmed that the cold front found inside the simulated clusters through cosmological simulation is also located behind merger shocks. Weak lensing observations show that their locations are close to the DM distribution's peak [64, 65].

All of the observations mentioned above suggest that the nature of merger shocks, as well as other observables like X-ray and DM distributions, should be understood and described in the context of the LSS formation. However, formation of merger-driven shocks inside merging galaxy clusters have been mainly investigated through a controlled-box simulation, modelling modeling specific objects, i.e., merger shocks in 1E 0657-56, CIZA J2242.8+5301, or ZwCl 0008.8+5215 [66–69]. Here, a controlled-box indicates that only two massive clumps are distributed in the box and there is no further mass and energy injection from outside of box, therefore, the effects of LSS are omitted in the simulation employing a controlled-box. Properties of shocks have been examined through cosmological simulations, on the other hand, previous works have not focused on the properties of merger-driven shocks. For instance, some previous studies performed cosmological simulations examined on the overall statistics of cosmological shocks, however, did not particularly highlight merger-driven shocks (e.g., [2]). Moreover,

Table 1: Merging Cluster Sample

	$M_{\text{heavy}}/M_{\text{light}}$ [a]	$T_{X,\text{heavy}}$ (keV) [b]	$T_{X,\text{light}}$ (keV) [b]	T_X (keV) [c]	z_i [d]
Cluster 1	1.84	4.26	2.99	5.12	0.36
Cluster 2	1.97	3.88	2.20	4.65	0.35
Cluster 3	1.96	4.08	2.33	4.92	0.23
Cluster 4	2.00	3.79	2.15	4.55	0.30
Cluster 5	1.99	3.83	2.18	4.60	0.25

a: Mass ratio between two merging clusters, estimated by including both baryon gas and DM at 0.174 Gyr before the axial shock launching time.

b: X-ray weighted temperatures of two merging clumps, estimated at 0.174 Gyr before the axial shock launching time.

c: X-ray weighted temperature of merged clusters, estimated at 1 Gyr after the axial shock launching time.

d: Redshift of axial shock launching time (see Section Properties of Merger Shocks).

paul2011 and [70] studied merging clusters in the context of the LSS formation, but the properties of merger shocks are not examined in detail.

In this Section, we study properties of merger shocks and their time evolution by performing a set of comsmological hydrodynamic simulations. In particular, the main improvement compared to previous studies listed above is that we fully follow LSS evolution and analyze major merger events during LSS formation. While observed merger events have a wide parameter space of subclump number, mass and impact parameter (e.g., [53, 55–57]), we focus on a particular case for CIZA J2242.8+5301 [55] that contains bright and giant Mpc-scale radio relic. According to the previous weak lensing analysis [55] and numerical modeling [68], the impact parameter of that event is very small (i.e., very close to head-on collision) and clump mass ratio is around 2. We leave the study of mergers with different parameter space of mass ratios and impact parameters as future works. In the Results Section, We first provide the spatial distributions of gas, temperature, X-ray emission, and DM to understand the dynamical evolution of major merger including shock propagation. Especially, using cosmological hydrodynamic simulations, merger-driven shocks quantified here are propagating in the realistic turbulent ICM and gas accretion from filament is considered as well. In addition, the quantities, such as the means and variations of v_s and M_s at shock surfaces and their time evolution, should provide informations for detailed modeling of synchrotron emissions [50, 51] and also constrain M_X and M_{radio} obtained from X-ray and radio observations of radio relics [52].
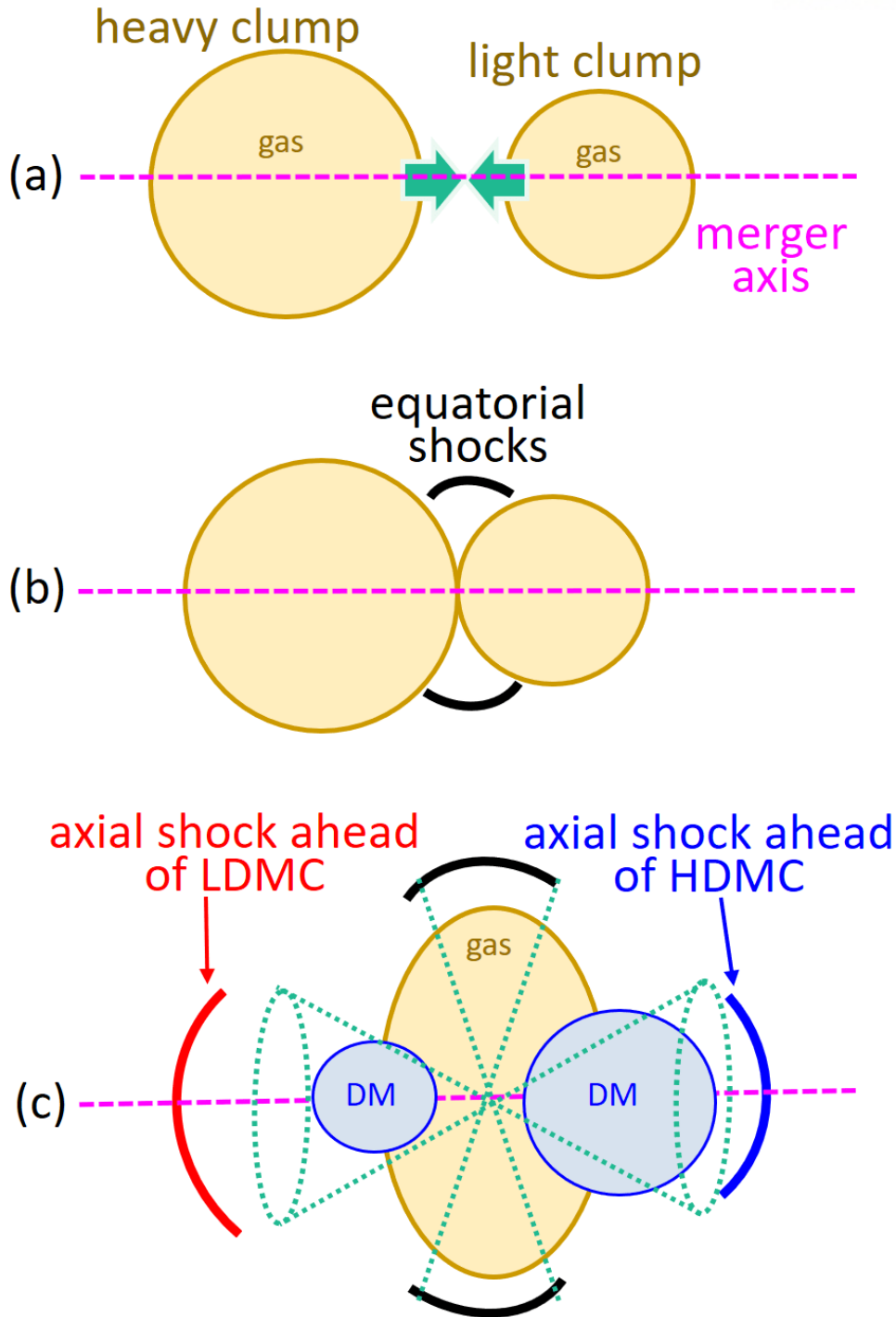
Figure 1: Schematic diagram of merging galaxy clusters undergoing a head-on collision (a) two sub-clumps undergo a head-on approach. (b) Due to the gas compression along the merger axis (i.e., magenta dashed line), "equatorial shocks" are first induced and propagating perpendicular to the merger axis. (c) two "axial shocks" are generated and propagating along the merger axis as follows. While Light DM clump (LDMC) and heavy DM clump (HDMC) are undergoing core passage because of the collisionless feature of DM, two gas subclumps become a single gas clump. Green lines in (c) express the cone and disk over which the average quantities such as Mach number and energy flux of axial and equatorial shocks are estimated (see Section "Properties of Merger Shocks").

7

2.1 Numerics

Simulations and Cluster Sample

Merging cluster samples used in this Section are produced by performing a set of numerical simulations of the LSS formation of the universe for a ΛCDM cosmology model with baryon density $\Omega_{\mathrm{BM}} = 0.044$, DM density $\Omega_{\mathrm{DM}} = 0.236$, cosmological constant $\Omega_\Lambda = 0.72$, rms density fluctuation $\sigma_8 = 1.05$, Hubble parameter $h \equiv H_0/(100 \text{ km s}^{-1}\mathrm{Mpc}^{-1}) = 0.7$, and primordial spectral index $n = 0.96$. Except σ_8, the parameters are consistent with the WMAP7 data [71]. While $\sigma_8 \approx 0.82$ is the most reasonable value based on the WMAP7 data, for the sake of producing more massive clusters in the simulation boxes, we here adopted a slightly larger σ_8. Some previous works argued that the properties of clusters produced in the simulation box and shocks inside those samples weakly depend on σ_8 [7,72] and we have also confirmed the cluster properties such as luminosity-temperature and mass-temperature relations are almost independent of σ_8, although the detailed results are not provided here.

We employ a PM/Eularian hydrodynamic cosmology code [73] to generate cosmological structure. A cubic box of comoving size of $50h^{-1}$ Mpc with periodic boundaries was employed. A grid of 1024^3 uniform zones was used, so the spatial resolution is $\Delta l = 48.8h^{-1}$ kpc. Nongravitational effects such as radiative and feedback processes were not included because most of energetic shocks are located outskirts of galaxy clusters and thus nongravitational effects are expected to be negligible (see e.g., [4]).

10 simulation boxes with different realizations of the initial condition were performed to obtain sample clusters. As mentioned above, we here focus on mergers with clump mass ratio ~ 2, going through almost head-on collisions (i.e., accroding to the modeling for CIZA J2242.8+5301 the impact parameter is roughly ~ 140 kpc, which is corresponding to ~ 2 grid zones). In addition, we constrained the epoch of the launching of axial shocks to the redshift range of $0.23 \lesssim z_i \lesssim 0.36$, ensuing the shocks have the best chance to be observed in X-ray and radio at $0.14 \lesssim z \lesssim 0.25$ (~ 1 Gyr after the shock launching). The latter z's match the redshift range of most of giant radio relics; for instance, CIZA J2242.8+5301 and RX J0603.3+4214 have $z = 0.188$ and 0.225, respectively (see the references in the Introduction). Finally, for the uniformity of the sample, we chose clusters with the X-ray weighted temperature $T_{\mathrm{X}} \sim 5$ keV after merger. CIZA J2242.8+5301 and RX J0603.3+4214, on the other hand, are observed to have $T_{\mathrm{X}} \sim 7 - 10$ keV [49,74], higher than those of sample clusters. Because the temperature and mass of clusters depend on the box size of simulation, the box size, $50h^{-1}$ Mpc is not enough to produce such massive clusters, even with extremely large $\sigma_8 = 1.05$. Characteristic parameters of 5 selected clusters are listed in Table 1. The virial masses of merging clumps (baryons plus DM) are in the range of $\langle M_{\mathrm{heavy}} \rangle \sim [2-3] \times 10^{14} M_\odot$ and $\langle M_{\mathrm{light}} \rangle \sim [1-1.5] \times 10^{14} M_\odot$, respectively, and the total mass of clusters after merger is in the range of $\sim [3-5] \times 10^{14} M_\odot$.

Compared to different numerical techniques such as smoothed particle hydrodynamic (SPH) or adaptive mesh refinement (AMR) methods, the resolution of our simulation is not enough to capture shocks with small surface areas that located in the cluster core. However, we are mostly concerned about shocks in the outskirts of galaxy clusters, which have been observed as X-ray shocks and radio relics. Because such outskirts shocks have large enough shock surfaces, the statistics of those shocks weakly depend on

the resolution of simulation box [8, 75].

Shock Identification and Energy Flux Calculation

In sample clusters, shocks (actually grid zones containing shocks) were identified with the algorithm described in [2] and [8] (See [75] for comparisons of different shock identification algorithms). Shocked grid zones were tagged if they satisfy the following three conditions: (1) $\nabla \cdot v < 0$, i.e., converging local flow, (2) $\Delta T \times \Delta \rho > 0$, i.e., same temperature and density gradient signs, and (3) $|\Delta \log T| > 0.11$, i.e., the Mach number greater than 1.3. In numerical simulations, shocks are represented by jumps typically spread over 2 - 3 zones, and "shock zones" were defined as the minima of $\nabla \cdot v$. The sonic Mach number can be estimated from the temperature jump across the shock jump, $T_2/T_1 = (5M_s^2 - 1)(M_s^2 + 3)/(16M_s^2)$. Here, the subscripts 1 and 2 denote the preshock and postshock quantities, respectively. The Mach number of shock zones was defined as $M_s = \max(M_{s,x}, M_{s,y}, M_{s,z})$. Very weak shocks are not energetically important, yet are easily confused with sonic waves, so only shocks with $M_s \geq 1.5$ were considered. Note that a shock surface consists of a number of shock zones.

At shock zones, the shock kinetic energy flux was calculated as

$$f_\phi = (1/2)\rho_1 v_s^3, \tag{1}$$

where $v_s = M_s(\gamma P_{th,1}/\rho_1)^{1/2}$. A part of the shock kinetic energy is dissipated to accelerate CRs via DSA as well as to heat the gas, since ICM shocks are collisionless, as noted in the Introduction. The energy flux of CRs emerging from shock zones was estimated as

$$f_{CR} = \eta(M_s) \times f_\phi \tag{2}$$

[2]. Here, $\eta(M_s)$ is the CR acceleration efficiency as a function of Mach number, and we employed the model presented in [76]. While our model η converges to ~ 0.23 for strong shocks with $M_s \gg 1$, it is much smaller with $7 \times 10^{-3} \lesssim \eta \lesssim 4 \times 10^{-2}$ for $3 \lesssim M_s \lesssim 4$, and almost negligible for $M_s \leq 2$ (see Figure 2 of [8]). Such behavior of η is consistent with the recent hybrid plasma simulations by [26], although the magnitudes of two model η's differ by up to a factor of two in the shock parameter range where a comparison can be made. This difference is not important here, since we concern mainly the relative importance of shocks with different Mach numbers, rather than the absolute amount of CR generation at these shocks.

The integrated kinetic and CR energies through shock surfaces were also calculated as

$$F_{\phi \text{ or CR}} = \sum_{\text{shocks}} f_{\phi \text{ or CR}} \Delta S, \tag{3}$$

where ΔS is the surface area of shock zone.

In the following section, we will present the quantitative properties of merger shocks averaged over the entire population in the our sample clusters of relatively uniform characteristics.
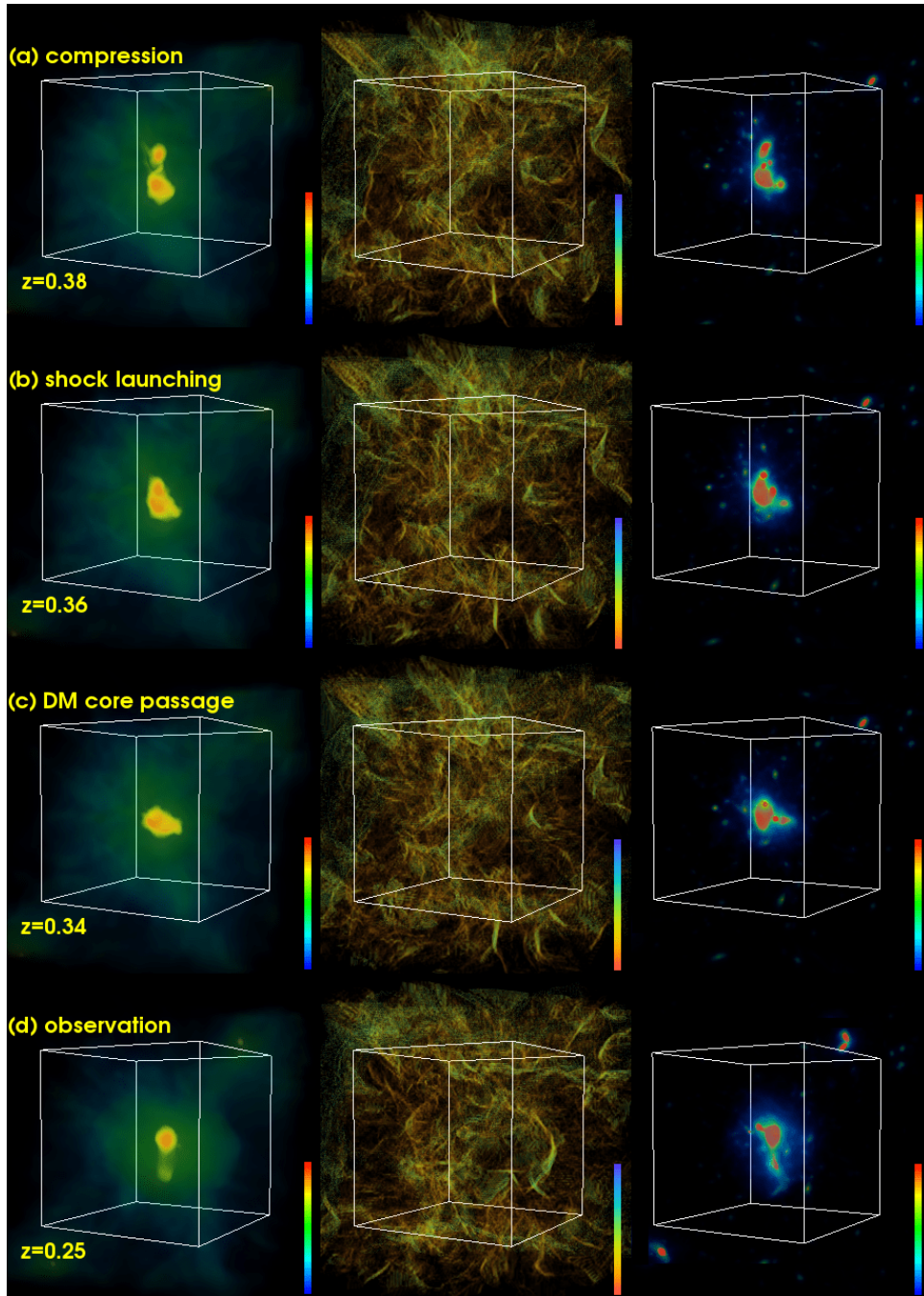
Figure 2: Three dimensional distributions of X-ray (left panels; colorbar $L_x = 10^{48}$ ergs/s (red) to 10^{39} ergs/s (blue)), shock Mach number (middle panels; colorbar $M_s = 7$ (blue) to 1.5 (red)) and DM (right panels; colorbar $\rho_{DM}/\langle \rho_{DM} \rangle = 2 \times 10^3$ (red) to 1 (blue)) for Cluster 1 of Table 1 in a comoving box of 5.7 Mpc size (white box) are displayed at four different epochs: (a) compression, (b) shock launching, (c) DM core passage and single gas core formation, and (d) the time of radio relic observation.
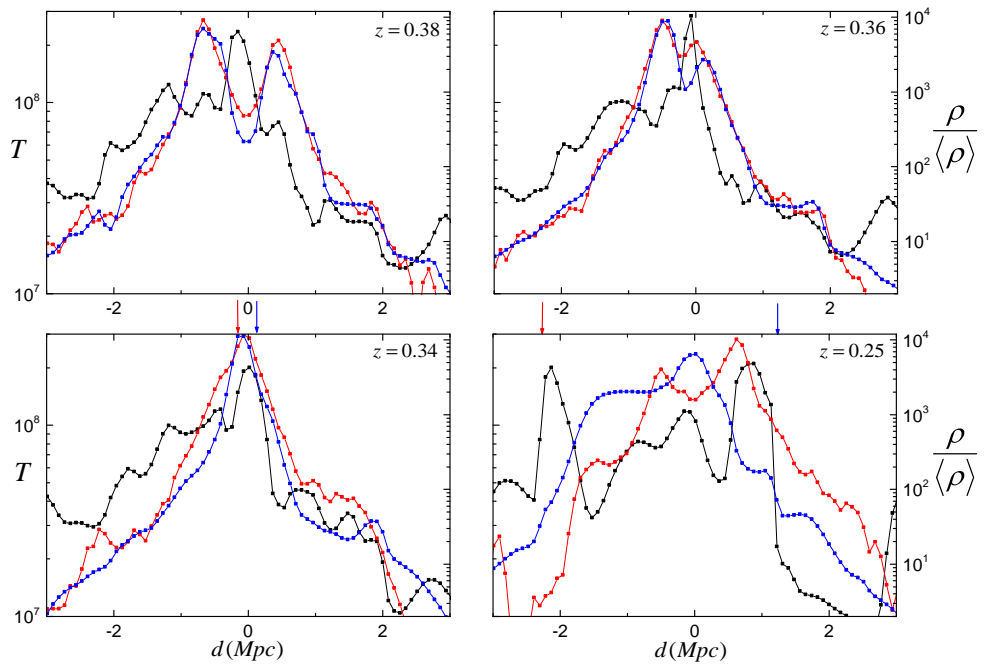
Figure 3: 1D line plot along the merger axis in Cluster 1 of Table 1 at four different timesteps, same as those in Figure 2. The gas temperature (in units of K, black), the gas density ($\rho_{\text{gas}}/\langle\rho_{\text{gas}}\rangle$, blue), and the DM density ($\rho_{\text{DM}}/\langle\rho_{\text{DM}}\rangle$, red) are shown. Red and blue arrows In the panels of $z = 0.34$ and 0.25 stand for the axial shock ahead of LDMC and the axial shock ahead of HDMC, respectively.
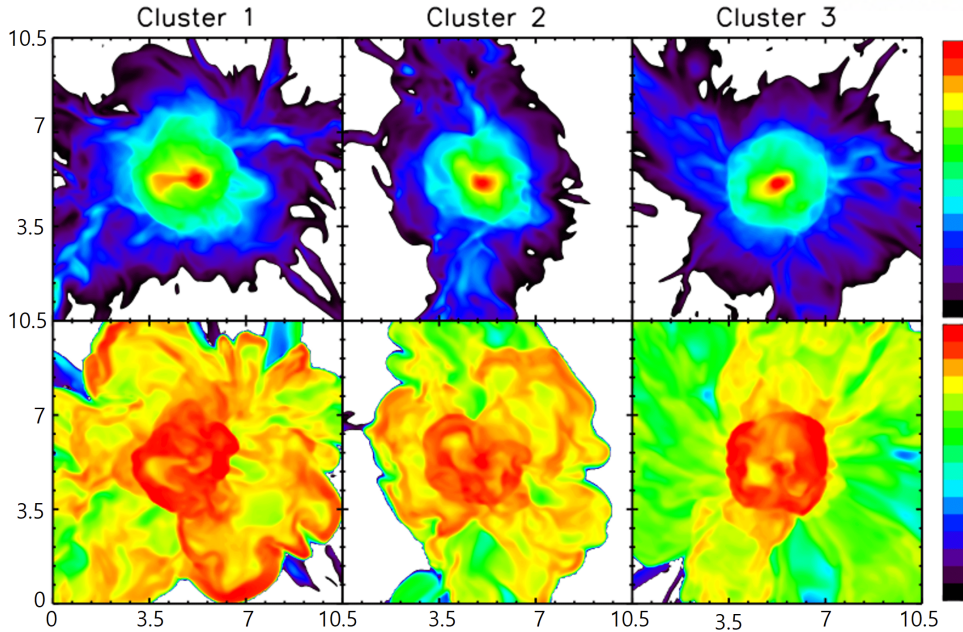
Figure 4: Two-dimensional density (upper panels; colorbar $\rho_{\mathrm{gas}}/\langle\rho_{\mathrm{gas}}\rangle = 10^4$ (red) to 1 (blue)) and temperature (bottom panels; colorbar $T = 10^8$ K (red) to 10^4 K (blue)) are plotted in a comoving size of 10.5 Mpc for three clusters listed in Table 1 at $z = 0.25$, 0.24, and 0.14 (i.e., the time epochs of shock observation). Here, the X-ray peak is employed to define the cluster center of each image.

2.2 Results

Overview of Merging Process

To set the scenario for presenting the merging process, Figure 1 depicts a general overview of an idealized binary merger [67, 68]. As two clumps are approaching and being compressed, shocks form and first propagate outwards in the equatorial plane, perpendicular to the merger axis. We name these shocks *equatorial shocks*. Later, two *axial shocks* launch into the opposite directions along the merger axis. Following the shock launch, the *core passage* of DM clumps and the formation of a single gas core occur.

Major mergers are, of course, far more complicated in our structure formation simulations. They drive turbulent flow motions and are frequently accompanied by multiple minor mergers and secondary infall along connected filaments. As a result, the generation of merger shocks is more complicated than the generation shown in the idealized binary mergers.

Figure 2 shows the merging process in a representative cluster, Cluster 1 (see Table 1). Two clumps, composed of baryons and DM, are approaching in an almost head-on collision, and for the sake of convenience, we refer to the four epochs in Figure 2 as the following terms: (a) compression phase ($z = 0.38$) during which the two clumps are approaching, (2) shock launching phase ($z = 0.36$) when the first axial shocks launch, (3) DM core passage phase ($z = 0.34$) when the two DM cores pass each other and two gas clumps merge to form a single core, (4) the time of radio relic observation ($z = 0.25$) at ~ 1 Gyr after the first axial shocks launch (see Section "Properties of Merger Shocks").

12

The middle column of Figure 2 shows the presence of complex shock surface networks in the ICM, even before the two clumps come into contact and compress. With filamentary structures of high Mach number areas, shock surfaces generated during the merger are patchy and very intermittent.

Figure 3 shows the one-dimensional (1D) distributions of gas temperature (black), gas density (blue), and DM density (red) along Cluster 1's merger axis at the same four epochs as Figure 2. Except at earlier epochs ($z = 0.38$ and 0.36), we define the zero point of distance, d, along the merger axis as the position of maximum X-ray peak at a given time. At $z = 0.36$, $d = 0$ corresponds to the X-ray peak that appeared during compression, and at $z = 0.38$, the same zero point as at $z = 0.36$ is used. The heavy (light) gas and DM clumps are arriving from the left-hand side (right-hand side), as described in the panel for $z = 0.38$. A temperature peak forms between the gas clumps when they are being compressed. Axial shocks begin to occur at $d = 0$ in the panel for $z = 0.36$, but the density peaks of gas clumps are still moving near to one other. A single DM peak near the zero point is visible in the panel for $z = 0.34$, indicating that it is close to the DM core passage epoch. The gas density and temperature distributions both show a single peak at $d = 0$ at that moment, indicating the formation of a merged core. Two axial shocks in the both sides of the peak are apparent.

The last epoch at $z = 0.25$ represents the time, around when the axial shocks have the "best chance" to be observed as a radio relic or double radio relics (see Section "Properties of Merger Shocks"). This corresponds to ~ 1 Gyr after the axial shock launching. The axial shocks are identified at $d_s \sim 1 - 2$ Mpc from the X-ray peak. The Mach number of the axial shock traveling ahead of the light DM clump (LDMC, hereafter) is $M_s \approx 3.5$ (the red arrow), while that of the shock traveling ahead of the heavy DM clump (HDMC, hereafter) is $M_s \approx 4$ (the blue arrow). Earlier studies for idealized binary mergers also found that the shock ahead of HDMC is stronger than that ahead of LDMC [67, 68].

Figure 4 shows the two-dimensional (2D) slices of the gas density (top panels) and temperature (bottom panels), passing through X-ray peaks in the first three clusters of Table 1 at the times of radio relic observation. The heavy clumps approached from the left in all three sample clusters, while the light clumps approached from the right. The clumps merged into cores, and the X-ray peaks are visible in the images' center. The merging axes are roughly represented by the elongation axis of density cores. Merger shocks (both axial and equatorial shocks) are characterized by abrupt changes in temperature and density distributions.

In addition, all three merging galaxy clusters contain other structures induced by other dynamical activities and/or complex turbulent flow motions. Especially, we identify two cold fronts behind the axial shocks from the merger galaxy clusters produced by the cosmological simulation, as noticed in the observations (e.g., [19, 38, 61, 63]). We interpret that cold fronts formed in the merging clusters shown in Figures 3 & 4 represents the bolder of cluster core, as modeled through observational results [61], however, more detailed study in a wide range of merging parameters such as mass ratio between two subclumps and impact parameter should be required to understand the formation of cold front. In this study, we focus on the properties of shock and so we leave the detailed fluid dynamics regarding the cold front as future works.
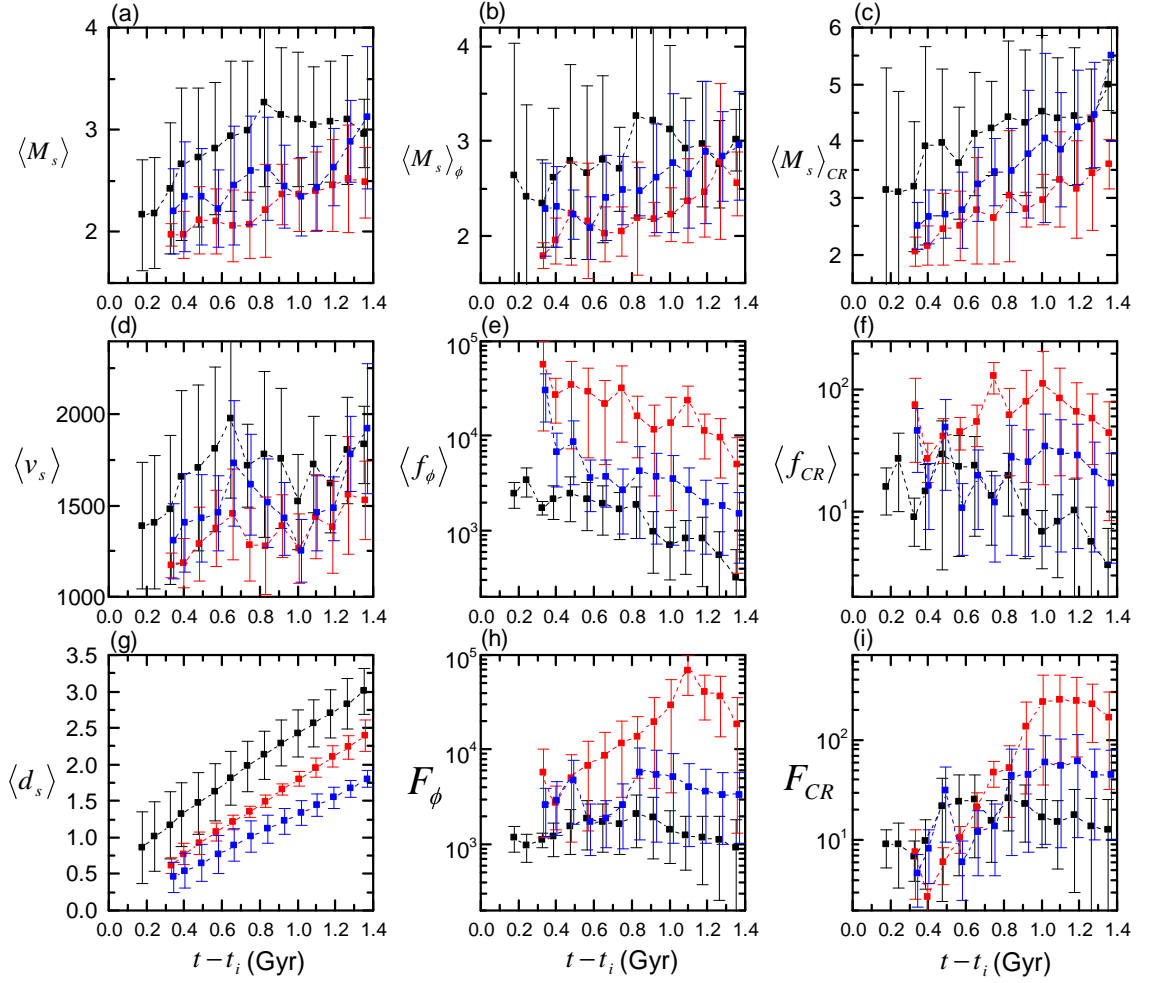
Figure 5: Time evolution of physical quantities for merger-driven shocks during ~ 1.4 Gyr after the axial shock launching, t_i. Red, blue and balck are for axial shocks ahead of LDMCs, axial shocks ahead of HDMCs, and equatorial shocks, respectively. (a) Mach number $\langle M_s \rangle$, (b) kinetic energy flux-weighted Mach number $\langle M_s \rangle_\phi$, (c) CR energy flux-weighted Mach number $\langle M_s \rangle_{\mathrm{CR}}$, (d) shock speed $\langle v_s \rangle$, (e) kinetic energy flux through shock surfaces $\langle f_\phi \rangle$, (f) CR energy flux through shock surfaces $\langle f_{\mathrm{CR}} \rangle$, (g) proper distance from the center of cluster $\langle d_s \rangle$, (h) integrated kinetic energy through shock surfaces F_ϕ, and (i) integrated CR energy through shock surfaces F_{CR} are shown. Here, v_s is in units of km s^{-1}, d_s in units of Mpc, f's in units of 10^{40} ergs s^{-1} Mpc^{-2}, and F's in units of 10^{40} ergs s^{-1}. Squares denote averaged values and error bars (standard deviations) are displayed along with squares. Except F_ϕ and F_{CR}, the vales for all shock tagged zones in 5 clusters listed in Table 1 were considered to calculate the averages and standard deviations the averages and standard deviations. For F_ϕ and F_{CR}, the averages and standard deviations are for 5 cluster samples.

14
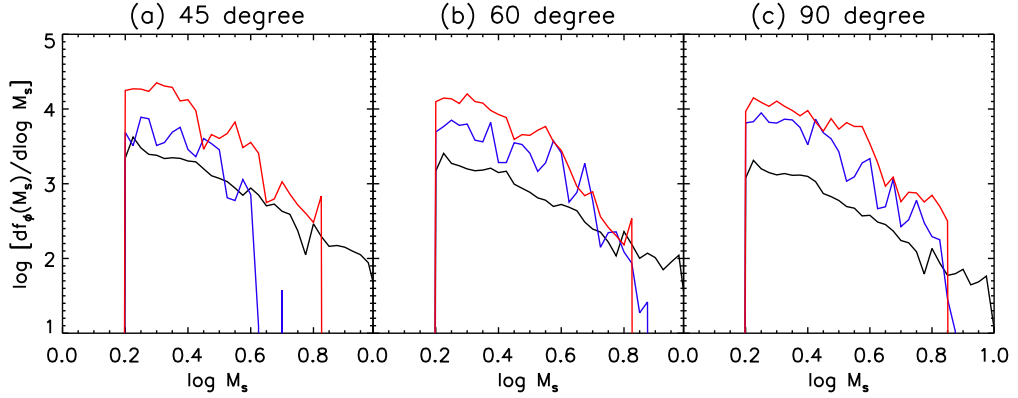
Figure 6: The shock statistics, $df_\phi/d\log M_s$ as a function of Mach number for different cone opening angles, $\Delta\theta$'s, for Cluster 1 at $z = 0.25$ (the time epoch of shock observation). Here, f_ϕ is in units of 10^{40} ergs s^{-1} Mpc^{-2} and the logarithmic Mach number bin, $\log M_s$ to $\log M_s + d\log M_s$ is considered. Red, blue and black are for axial shocks ahead of LDMC, axial shocks ahead of HDMC, equatorial shocks, same as those in Figure 5.

Properties of Merger Shocks

In the merging cluster samples listed in Table 1 from cosmological hydrodynamic simulations, numerous shocks are induced due to the supersonic flow motions from turbulence and gas accretion from filaments of galaxies. As a result, it is hard to characterize merger shocks and distinguish them from other types of shocks (i.e., turbulence and infall shocks). For this reason, bearing the merging process described above in mind, we simply attempted to pick up merger shocks "visually" by using three-dimensional (3D) images like those in Figure 2, as well as 1D and 2D distributions like those in Figures 4 and 3.

Merger shocks were divided into three different categories, axial shocks ahead of LDMC, axial shocks ahead of HDMC, and equatorial shocks. As illustrated in Figure 1, for the axial shocks we counted those within the two polar cones with opening angles of $\Delta\theta = 45°$, confined by either the polar angle of $\theta \leq 22.5°$ or $\theta \geq 157.5°$ around the merger axis. For the equatorial shocks, we considered those located within a disk-like zone confined by $-22.5° \leq (\theta - 90°) \leq 22.5°$ around the equatorial plane. Here, the cluster center is the peak of X-ray emission at each epoch. The mean distance, $\langle d_s \rangle$, of the three shock categories were estimated by taking the average value of d_s of the shocks that belong to each category. Then, the shock selection process was repeated and refined with shocks within $\langle d_s \rangle \pm 0.3$ Mpc for axial shocks, and with shocks within $\langle d_s \rangle \pm 0.5$ Mpc for equatorial shocks. A larger distance span was considered for equatorial shocks, because they form over $360°$ of the azimuthal angle, thus showing a larger fluctuation in the position. Figure 5(g) shows the time evolution of the converged value of $\langle d_s \rangle$. In this iteration procedure, some of merger shocks could be missed, and some shocks of other types, particularly turbulent shocks, could be counted in erroneously. However, we interpret that such limitations would not change the main results shown in this Section, because the major source for shock generation is the major merger event. Indeed, according to the shock statistics shown in Figure 6, the

15

statistical properties of merger shocks are overall insensitive to the choice of the opening angle, nor to the distance spanning.

As a reference point of time, we define the *axial shock launching time*, t_i, which was calculated as follows. Once the axial shock launching was identified, the average distance between two axial shocks as a function of time, $D(t)$, was estimated. At the initial stage of mergers, shocks are hard to be identified reliably, since they have very low Mach number with $M_s \sim 1-2$ and small shock surfaces and form in the turbulent core regions. Reliable identification of axial shocks becomes feasible typically after the core passage epoch. So t_i was estimated by extrapolating the shock distance backward in time, that is, as the time when $D(t_i) = 0$. The redshift of t_i is given in the last column of Table 1.

To follow the detailed time evolution of merger shocks, physical quantities and their statistics obtained at 15 different time epochs after t_i with separation $\Delta z \sim 0.01$ (corresponding $\Delta t \sim 0.09$ Gyr) were considered for the five sample clusters in Table 1. The means and dispersions of shock properties were calculated for each shock category over all the shocks detected in five sample clusters. The number of counted shocks (shock zones) in each category increases from $N_s \lesssim 100$ at the axial shock launching time to $\sim 1500 - 2000$ (corresponding to the shock surface area of $\sim 2-3$ (Mpc)^2) during the time period of 1.4 Gyr in each sample cluster.

Figure 5 shows the time evolution of physical quantities averaged over the shock surfaces corresponding to axial shocks ahead of LDMC (red), axial shocks ahead of HDMC (blue), and equatorial shocks (black). Because of the complex nature inside merging galaxy clusters due to the turbulence and other dynamical activities induced by consequence of hierarchical clustering, the statistical fluctuations (error bars in the figure) are very large. In spite of that, all quantities shows clear trends in terms of time evolution.

As shown in Figure 5(g), the mean distance of equatorial shocks is the largest among three shock categories, since they launch earlier. And $\langle d_s \rangle$ for axial shocks ahead of LDMC is larger than that for axial shocks ahead of HDMC, indicating that the X-ray peaks are close to HDMCs in our merging clusters. The mean distances of all three shock categories increase in time, and axial shocks, for instance, reach $\langle d_s \rangle \sim 1-2$ Mpc by the time $t - t_i \simeq 1$ Gyr.

The top panels of Figure 5 show the mean values of shock Mach numbers, $\langle M_s \rangle$, $\langle M_s \rangle_\phi$ weighted with shock kinetic energy flux (f_ϕ), and $\langle M_s \rangle_{CR}$ weighted with CR energy flux (f_{CR}). Firstly, the Mach numbers overall increase in time, while the mean shock speed, $\langle v_s \rangle$, in Figure 5(d) increases in the early phase during ~ 0.6 Gyr, but then fluctuates afterward. The overall increase of shock Mach numbers in the late stage reflects the fact that the gas temperature tends to decrease in the cluster outskirts ($\gtrsim 1$ Mpc), as can be seen in Figures 3 and 4. Secondly, both $\langle v_s \rangle$ and $\langle M_s \rangle$ of equatorial shocks have the largest values, since they propagate mostly to low density regions surrounding merging clumps. Moreover, $\langle v_s \rangle$ and $\langle M_s \rangle$ of axial shocks ahead of HDMC are larger than those of axial shocks ahead of LDMC. Yet, $\langle d_s \rangle$ for axial shocks ahead of HDMC is smaller, owing to the fact that $\langle d_s \rangle$ includes not only the propagation of shocks but also the displacement of X-ray peaks. Thirdly, while $\langle M_s \rangle$ and $\langle M_s \rangle_\phi$ are comparable, $\langle M_s \rangle_{CR}$ is larger by about unity or so, especially in the late stage. This is due to the dependence of the CR acceleration efficiency, $\eta(M_s)$, on the shock Mach number; our model $\eta(M_s)$ is larger for stronger

16

shocks (see Section "Shock Identification and Energy Flux Calculation").

The average kinetic energy flux through shock surfaces, $\langle f_\phi \rangle$, in Figure 5(e) tends to decrease in time as shocks move outwards, since the gas density decreases in the cluster outskirts. The average CR energy flux produced at shocks, $\langle f_{CR} \rangle$, in Figure 5(f), on the other hand, shows complicated time evolution, reflecting the Mach number dependence of the CR acceleration efficiency. Both $\langle f_\phi \rangle$ and $\langle f_{CR} \rangle$ for axial shocks ahead of LDMC are the largest, because these shocks propagate into the gas with higher density that is originally associated with heavier gas clumps.

Figures 5(h) and 5(i) show the shock kinetic and CR energy fluxes integrated over shock surfaces, $\langle F_\phi \rangle$ and $\langle F_{CR} \rangle$, averaged for five sample clusters. Again, $\langle F_\phi \rangle$ and $\langle F_{CR} \rangle$ of axial shocks ahead of LDMC are the largest, while those of equatorial shocks are the smallest. Although axial shocks ahead of LDMC are the weakest with smallest $\langle M_s \rangle$ among shocks of three categories, they are energetically the most important; that is, they process the largest amount of kinetic energy and also generate the largest amount of CRs, especially at late times of $t - t_i \simeq 0.8 - 1.4$ Gyr.

In particular, in Figure 5(h), F_ϕ for axial shocks ahead of LDMC peaks at $\sim 10^{44} - 10^{45}$ ergs s^{-1} during $t - t_i \simeq 0.8 - 1.4$ Gyr. The total energy processed during the period is $\sim$ several $\times 10^{60}$ ergs, which is a substantial fraction of the merger energy $\sim 10^{62}$ ergs (see the Introduction). F_ϕ for axial shocks ahead of HDMC is about an order of magnitude smaller, and F_ϕ for equatorial shocks is even smaller by a factor of several. So axial shocks ahead of LDMC should have the best chance to be observed as X-ray shocks, especially at ~ 1 Gyr after the launching of the shocks. During the peak period, for these axial shocks, the f_ϕ-weighed Mach number ranges $\langle M_s \rangle_\phi \sim 2 - 3$ and their distance from the cluster center ranges $\langle d_s \rangle \simeq 1 - 2$ Mpc. These are in reasonable agreement with the observed characteristics of X-ray shocks, as noted in the Introduction.

In Figure 5(i), again, F_{CR} for axial shocks ahead of LDMC is several to tens times larger than F_{CR} for other category shocks during $t - t_i \simeq 0.8 - 1.4$ Gyr. So they should have the best chance to light up as radio relics and thus be observed in radio. The f_{CR}-weighed Mach number for the shocks during the peak period is, on the other hand, in the range of $\langle M_s \rangle_{CR} \sim 3 - 4$, higher than $\langle M_s \rangle_\phi$, as noted above. This range of $\langle M_s \rangle_{CR}$ is consistent with the range of the shock Mach numbers estimated from the radio spectral indices of observed radio relics (see the references in the Introduction). The potential manifestation of larger M_s in radio relic observations than in X-ray shock observations was pointed out in [52]. Our results confirm such tendency, indicating that the difference between M_X and M_{radio} might be due to the representations of different parts of shock surfaces, that is, higher M_s parts for radio observations while lower M_s parts for X-ray observations, as noted in the Introduction. The range of $\langle d_s \rangle \simeq 1 - 2$ Mpc for axial shocks ahead of LDMC during the peak of CR production is also comparable to the positions of observed radio relics.

We note that the Sunyaev-Zel'dovich (SZ) decrements found CIZA J2242.8+5301 could be interpreted as high pressure regions generated by equatorial shocks propagating in the direction perpendicular to the merger axis [77]. An X-ray temperature break found in the merger system between Abell 399 and Abell 401 could also indicate a signature of equatorial shocks [78]. Although the nature of these observed features should be further investigated, their positions are consistent with the equatorial shocks

defined in this study. These indicate that although energetically sub-dominant, equatorial shocks could have possibly observable imprints.

From Figure 5(d), one can see that $\langle v_s \rangle$ increases during the peak period of F_ϕ and F_{CR}. The adiabatic blast wave solution for a point explosion requires the density gradient steeper than ρ^{-3} for accelerating shock fronts [79]. Apparently, the blast wave assumption does not hold for merger-driven shocks, since the kinetic and gravitational energies of merging clumps are continuously dissipated through shocks and additional energies are supplied by secondary infall and multiple minor mergers. In addition, $\langle v_s \rangle$ includes the contributions not only from the shock propagation, but also from turbulent flow motions ahead of shocks. As a matter of fact, large fluctuations in $\langle v_s \rangle$ as well as in $\langle M_s \rangle$ reflect complicated flow dynamics of clusters.

2.3 Summary and Discussion

In this work, we examined the properties of merger shocks in galaxy clusters from cosmological hydro-dynamic simulations for the LSS formation of the universe. We first compiled a sample of five merging clusters in ten simulations with different initialization; all undergo through almost head-on collisions of mass ratio ~ 2 at $z < 0.5$, which result in merged systems with $T_X \sim 5$ keV. We then isolated shocks produced by merger activities, and quantified their properties such as the shock speed, Mach number, and shock energy flux. Due to the turbulent nature of the ICM, the properties of the shocks can be described only statistically with means and standard deviations for a population of identified shocks associated with merger events. We also calculated the time evolution of those shock properties.

Our findings are summarized as follows.

(1) The surfaces of merger shocks are not smooth. The Mach number distribution on the surfaces is highly intermittent and the high Mach number parts form filamentary structures.

(2) As the merger shocks propagate out from the cores to the outskirts, the shock Mach number, M_s, on average increases in time, while the shock speed does not necessarily.

(3) The kinetic energy flux through shock surfaces, f_ϕ, decreases in time, since the gas density is lower in the outskirts. But the CR energy flux produced at shocks, f_{CR}, shows complicated time evolution.

(4) Axial shocks propagating ahead of LDMC are most energetic. They process large amounts of the kinetic energy, F_ϕ, and the CR energy, F_{CR}, and thus have the best chance to be observed as X-ray shocks and radio relics.

(5) F_ϕ and F_{CR} of axial shocks ahead of LDMC peak at $t - t_i \sim 1$ Gyr after the shocks launched, or when the shocks are located at $d_s \sim 1 - 2$ Mpc from the cluster center. At the time, the shocks have $\langle M_s \rangle_\phi \simeq 2 - 3$ (weighted with f_ϕ), while $\langle M_s \rangle_{CR} \simeq 3 - 4$ (weighted with f_{CR}). This is because the CR acceleration is more efficient at the parts of shock surfaces with higher Mach numbers.

(6) Both DM clumps survive through merger, and their peaks persist. In our sample clusters, after the DM core passage, the LDMC is located behind the most energetic axial shocks, while the HDMC lies in the other side but closer to the peak of X-ray emission which coincides with the gas core.

Recently, the evidence of "equatorial shocks" has been suggested through X-ray observations [80,

81]. For instance, [80] identified the temperature jump corresponding to $M_s \sim 3$ in the pre-merger stage (A1758N & A1758S). In addition, [81] also found the proof of equatorial shocks on the equatorial plane of an pre-merger cluster pair. Such results are in agreement with the prediction of equatorial shocks discussed in this Section.

Finally, we note that the properties of merger shocks, as well as their positions relative to X-ray peak and DM clumps, should depend on a number of merger parameters. For example, according to simple calculation in the system satisfying energy conservation, Mach number of merger-driven shocks sensitively depends on the clump mass ratio [82] . More comprehensive investigation of such dependence requires a very large sample of simulated merging clusters, and we will leave it as future works.

III   Proton Acceleration at Weak Quasi-parallel Shocks in Intracluster Medium

In the observed merging galaxy clusters, the radio synchrotron emission indicates that the ICM shocks accelerate CRs via DSA, like most astrophysical shocks. While the previous studies using hydrodynamic simulations have been focused on the properties and dynamical evolution of ICM shocks as shown in the Section II, it is necessary to understand particle acceleration process in such shocks. In this Section, we examine the detailed proton acceleration mechanism at the weak ICM shocks including the kinetic plasma processes. Note that all results shown here are originally presented in the paper (Ha, J.-H., Ryu, D., Kang, H., & van Marle, A. J. 2018, The Astrophysical Journal, 864, 105; [83]).

Just like Earth's bow shocks and supernova remnant shocks, ICM shocks are thought to accelerate cosmic ray (CR) protons and electrons via diffusive shock acceleration (DSA, *a.k.a.* Fermi I acceleration) [20–22]. Although the acceleration of relativistic electrons by putative shocks has been observed as the so-called giant radio relics such as the Sausage relic in the merging cluster CIZA J2242.8+5301 [39], the presence of CR protons produced by ICM shocks has yet to be confirmed [84–86]. Inelastic collisions of CR protons with thermal protons followed by the decay of neutral pions can produce diffuse $\gamma-$ray emission, which has not been detected so far by the Fermi-LAT $\gamma-$ray telescope [87]. According to theoretical estimations using cosmological hydrodynamics simulations that adopt prescriptions for the *CR proton acceleration efficiency* at shocks, $\eta(M_{\rm s})$, non-detection of $\gamma-$ray emission from galaxy clusters constrains $\eta(M)$ to be less than 10^{-3} for $2 \leq M_{\rm s} \leq 5$ [31].

The key element in estimating the DSA efficiency is the so-called 'injection process', which energizes thermal protons to the suprathermal energies sufficient to diffuse across the shock. In order to understand CR injection and early acceleration at collisionless shocks, kinetic plasma processes have been studied through particle-in-cell (PIC) and hybrid plasma simulations [23–29]. In PIC simulations, both ions and electrons are treated kinetically, therefore wave-excitation and wave-particle interactions can be followed from first principles. In hybrid simulations, on the other hand, only ions are treated kinetically, while electrons are treated as charge-neutralizing fluid with zero-mass. They are suitable for studying ion acceleration well into full Fermi-I acceleration regime on many ion gyration periods, since they are computationally much less expensive than PIC simulations. However, collisioness shock formation and particle acceleration involve kinetic processes due to both electrons and protons, so PIC simulations should be more appropriate in the investigation of the ion injection problem.

Comprehensive studies by Caprioli and collaborators using hybrid simulations showed that CR ions are accelerated efficiently with $\eta \sim 0.05 - 0.15$ at strong quasi-parallel shocks with $M_{\rm s} \gtrsim 5$ and $\theta_{\rm Bn} \lesssim 45°$, where $\theta_{\rm Bn}$ is the obliquity angle between the shock normal and the background magnetic field direction [26–28]. The magnetic field obliquity angle $\theta_{\rm Bn}$ is one of the key parameters that govern the characteristics of shocks: quasi-parallel shocks with $\theta_{\rm Bn} \lesssim 45°$ versus quasi-perpendicular shocks with $\theta_{\rm Bn} \gtrsim 45°$. In particular, [28] showed that at quasi-parallel shocks a substantial fraction of ions impinging on the shock potential barrier can be specularly reflected, when the quasi-periodically reforming

shock potential is in a high state (i.e., $e\Delta\phi > \frac{1}{2}m_i v_x^2$). The reflected ions escaping upstream along the parallel magnetic field generate low-frequency waves and amplify the transverse magnetic fields via CR ion-driven instabilities, transforming upstream quasi-parallel fields to locally quasi-perpendicular fields in the shock transition layer. Then ions arriving subsequently at the shock are reflected at locally perpendicular portions of turbulent magnetic fields [88]. Due to perpendicular components of the magnetic field the reflected ions gain sufficient energies via multiple cycles of shock drift acceleration (SDA), and then start participating to the Fermi I cycle of shock acceleration. Thus reflection of ions at the overshoot of the shock potential, self-excitation of turbulent waves, and SDA are integral parts of ion injection at quasi-parallel shocks.

On the other hand, at quasi-perpendicular shocks the reflected ions are advected downstream along with the background magnetic fields typically after one gyromotion, so they may undergo only a few cycles of SDA and do not reach energies sufficient to be injected to Fermi I acceleration [26]. Since the gyrostream of the reflected ions penetrates upstream less than one ion gyroradius from the shock ramp, turbulent waves are not excited efficiently in the precursor of quasi-perpendicular shocks [27]. Consequently, Fermi-I acceleration of protons is efficient only at quasi-parallel shocks, which will be the main focus of this study.

We further comment about particle reflection at the shocks. Firstly, ion reflection is governed by both the shock potential and the magnetic mirror at the shock, however, the fraction of ion reflection satisfying the reflection condition in terms of shock potential dominates over that satisfying the condition for magnetic mirror conditions (i.e., the particles are not in the loss cone). Secondly, while upstream ions are mainly reflected by the shock potential, the reflection of upstream electrons are suppressed by the shock potential because electrons have opposite charge. And thus, electron reflection is mainly governed by the magnetic mirror at the shock surface. In Section VII, we provide the detailed physics regarding electron reflection at the shock surface.

Unlike collisional shocks, physics of collisionless shocks include complex kinetic plasma processes such as particle reflection, self-excitation of waves, and wave-particle interaction, well beyond MHD Rankine-Hugoniot jump conditions [29]. From studies of collisionless shocks such as Earth's bow shocks and interplanetary shocks, the concept 'shock criticality' has been adopted. 'Subcritical shock' denotes that the shock kinetic energy can be fully dissipated through resistivity so the shock structure is smooth without complex plasma waves. 'Supercritical' shock, on the other hand, the shock kinetic energy cannot be fully dissipated through resistivity alone, so a substantial fraction of incoming ions must be reflected upstream to satisfy the Rankine-Hunoniot jump conditions [89]. Such shock criticality can be described through the certain critical Mach number. For instance, the fast mode Mach number of shock satisfies the condition, $M_f > M_f^*$ where M_f^* stands for the *fast first critical Mach number*, then such shock is 'supercritical' shock. We also provide different critical Mach numbers regarding different criteria in Section VII.

In typical astrophysical environment, the plasma beta $\beta = P_{gas}/P_B \sim 1$, so the Alfvén Mach number M_A is often used to characterize a shock and the critical Alfvén Mach number $M_A^* \approx 2.76$ is commonly quoted for quasi-perpendicular shocks [29]. As for the papers by Caprioli and collaborators cited above,

CR acceleration at supercritical shocks has been explored through plasma simulations mainly for $\beta \lesssim 1$ cases (i.e., $M_A \sim M_s$). In the typical hot ICM plasma, however, $\beta \sim 100$, so shocks have relatively high Alfvén Mach number, $M_A \approx 10 M_s \approx 20 - 30$, but low sonic Mach number, $M_s \approx 2 - 3$. Note that for these ICM shocks, $M_f \approx M_s$. To our knowledge, the supercriticality of weak ($M_s \approx 2 - 4$) quasi-parallel shocks in such high β environment has not yet been studied by PIC or hybrid simulations.

PIC simulations of $M_s = 3$ shocks in high β ICM plasmas were considered by [23, 24], focusing mainly on electron acceleration at quasi-perpendicular shocks. They showed that for the shock model with $\beta = 20$, $\theta_{Bn} = 63°$, and $M_s = 3$, about 20 % of incoming ions are reflected at the shock and gain a small amount of energy via a few cycles of SDA. Those energized ions overcome the potential barrier and advect downstream along with the magnetic fields. Note that their simulations were not intended to study ion acceleration in the DSA regime in sufficiently long ion gyro-time scales.

Excitation of magnetic turbulence by protons streaming upstream of quasi-parallel shocks is an integral part of injection and acceleration of CR particles. There are two dominant modes: (1) resonant streaming instability which excites left-handed circularly polarized waves [20], and (2) nonresonant current-driven instability which excites right-handed circularly polarized wave [90]. Using hybrid simulations of quasi-parallel shocks in $\beta \sim 1$ plasma, [27] showed that the resonant streaming instability is dominant in the precursor of shocks with $M_A \lesssim 30$, while the nonresonant current-driven instability operates faster at stronger shocks with $M_A \gtrsim 30$. The magnetic field amplification factor increases with increasing Alfvén Mach number as $\langle B/B_0 \rangle^2 \propto M_A$. Both instabilities amplify primarily transverse components of the magnetic field, so they generate locally perpendicular fields in the shock foreshock and downstream region, which in turn facilitate SDA of the reflected ions and reflect subsequently arriving ions. Eventually, excited turbulent waves act as scattering centers both upstream and downstream of the shock, which are required for the Fermi I acceleration.

In this Section, we examine the physics of 'shock criticality' in weak ICM shocks by using PIC simulations. To identify ion injection and early stage acceleration, we study shock structures and ion energy spectra. In order to understand the nature of CR ion-driven instabilities and turbulent magnetic field amplification, we perform Fourier analysis of upstream self-excited magnetic field components. We then discuss dependence of ion injection and CR ion-driven instabilities on the pre-shock conditions such as M_s, β, and θ_{Bn}.

3.1 Numerics

We use the parallel electromagnetic PIC code TRISTAN - MP to study non-relativistic collisionless shocks in 2D planar geometry, while the particle velocity and the electromagnetic fields are solved in 3D [91, 92]. Here the same simulation setup as that of [23, 24] is adopted: an ion-electron magnetized plasma with the Maxwell distribution moves with the bulk velocity $\mathbf{v_0} = -v_0 \hat{\mathbf{x}}$ toward a reflecting wall at the leftmost boundary ($x = 0$). Due to the interactions between the incoming and reflected flows, a shock propagates along $+\hat{\mathbf{x}}$ direction. So in effect the simulations are performed in the rest frame of the shock downstream flow.

Table 2: Model Parameters for the Simulations

	$M_s \approx M_f$	M_A	v_0/c	θ_{Bn}	β	$T_e = T_i[K(keV)]$	$\frac{m_i}{m_e}$	$L_x[c/w_{pe}]$	$L_y[c/w_{pe}]$	$t_{end}[\Omega_{ci}^{-1}]^b$
M3.2^c	3.2	29.2	0.052	13°	100	$10^8(8.6)$	100	2×10^4	2	90.2
M2.0	2.0	18.2	0.027	13°	100	$10^8(8.6)$	100	2×10^4	2	90.2
M2.15	2.15	19.6	0.0297	13°	100	$10^8(8.6)$	100	2×10^4	2	90.2
M2.25	2.25	20.5	0.0315	13°	100	$10^8(8.6)$	100	2×10^4	2	90.2
M2.5	2.5	22.9	0.035	13°	100	$10^8(8.6)$	100	2×10^4	2	90.2
M2.85	2.85	26.0	0.0395	13°	100	$10^8(8.6)$	100	2×10^4	2	90.2
M3.5	3.5	31.9	0.057	13°	100	$10^8(8.6)$	100	2×10^4	2	90.2
M4	4.0	36.5	0.066	13°	100	$10^8(8.6)$	100	2×10^4	2	90.2
M3.2-θ23	3.2	29.2	0.052	23°	100	$10^8(8.6)$	100	2×10^4	2	90.2
M3.2-θ33	3.2	29.2	0.052	33°	100	$10^8(8.6)$	100	2×10^4	2	90.2
M3.2-θ63	3.2	29.2	0.052	63°	100	$10^8(8.6)$	100	2×10^4	2	90.2
M2.0-β30	2.0	10.0	0.027	13°	30	$10^8(8.6)$	100	2×10^4	2	165
M2.0-β50	2.0	12.9	0.027	13°	50	$10^8(8.6)$	100	2×10^4	2	128
M3.2-β30	3.2	16.0	0.052	13°	30	$10^8(8.6)$	100	2×10^4	2	165
M3.2-β50	3.2	20.6	0.052	13°	50	$10^8(8.6)$	100	2×10^4	2	128
M2.0-m400	2.0	18.2	0.013	13°	100	$10^8(8.6)$	400	2×10^4	2	22.6
M2.0-m800	2.0	18.2	0.009	13°	100	$10^8(8.6)$	800	2×10^4	2	22.3
M3.2-m400	3.2	29.2	0.026	13°	100	$10^8(8.6)$	400	2×10^4	2	22.6
M3.2-m800	3.2	29.2	0.018	13°	100	$10^8(8.6)$	800	2×10^4	2	22.3
M2.0-r2	2.0	18.2	0.027	13°	100	$10^8(8.6)$	100	2×10^4	2	22.3
M2.0-r0.5	2.0	18.2	0.027	13°	100	$10^8(8.6)$	100	2×10^4	2	22.3
M3.2-r2	3.2	29.2	0.052	13°	100	$10^8(8.6)$	100	2×10^4	2	22.3
M3.2-r0.5	3.2	29.2	0.052	13°	100	$10^8(8.6)$	100	2×10^4	2	22.3
M2.0-2D	2.0	18.2	0.027	13°	100	$10^8(8.6)$	100	2×10^4	60	34.6
M3.2-2D	3.2	29.2	0.052	13°	100	$10^8(8.6)$	100	2×10^4	60	34.6

a: See the Section "Numerics" for model-naming convention

b: $\Omega_{ci}^{-1} = m_i c/(eB_0)$ is the ion gyration period.

c: The fiducial model.
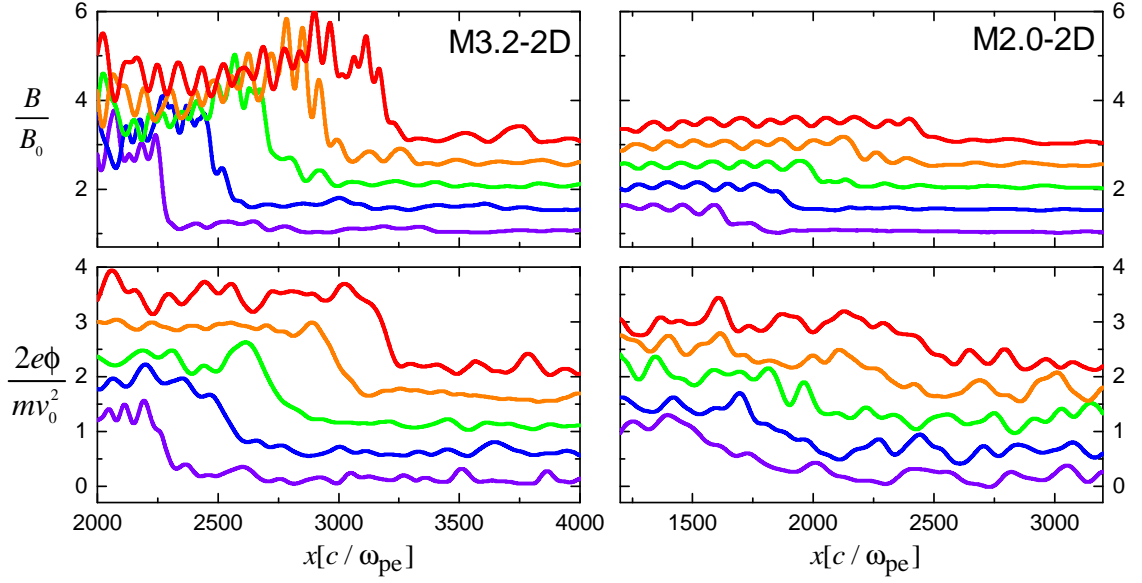
Figure 7: Stack plots of total magnetic field strength, $B(x)$, and electric potential for $e\phi(x)$, averaged over the transverse direction in M3.2-2D (left) and M2.0-2D (right) models for five different time epochs (from $w_{pe}t = 0.8 \times 10^5$ (purple) to 1.2×10^5 (red)).

In typical PIC simulations, due to severe requirements for computational resources, 'ions' with a reduced mass ratio $m_i/m_e \ll 1836$ are adopted to represent the real proton population. Thus, hereafter we will refer 'ions' as positively charges particles with a reduced mass ratio $m_i/m_e = 100 - 800$.

The flow Mach number M_0 of the upstream bulk flow is specified as

$$M_0 \equiv \frac{v_0}{c_s} = \frac{v_0}{\sqrt{2\Gamma k_B T_i/m_i}}, \tag{4}$$

where c_s is the sound speed in the upstream medium, $\Gamma = 5/3$ is the adiabatic index, and k_B is the Boltzmann constant. Here, thermal equilibrium is assumed for the incoming flow, so the ion temperature T_i is the same as the electron temperature T_e. In the weakly magnetized limit, the sonic Mach number, M_s, of the induced shock is related with M_0 as follows:

$$M_s \equiv \frac{v_{sh}}{c_s} \approx M_0 \frac{r}{r-1}. \tag{5}$$

Here $v_{sh} = v_0 \cdot r/(r-1)$ is the upstream flow speed in the shock rest frame and

$$r = \frac{\Gamma+1}{\Gamma-1+2/M_s^2} \tag{6}$$

is the Rankine–Hugoniot compression ratio across the shock.

The strength of the uniform background magnetic field $\mathbf{B_0}$ in the x-y plane is parameterized by plasma beta β as follow:

$$\beta = \frac{8\pi n k_B(T_i+T_e)}{B_0^2} = \frac{2}{\Gamma}\frac{M_A^2}{M_s^2}. \tag{7}$$

24
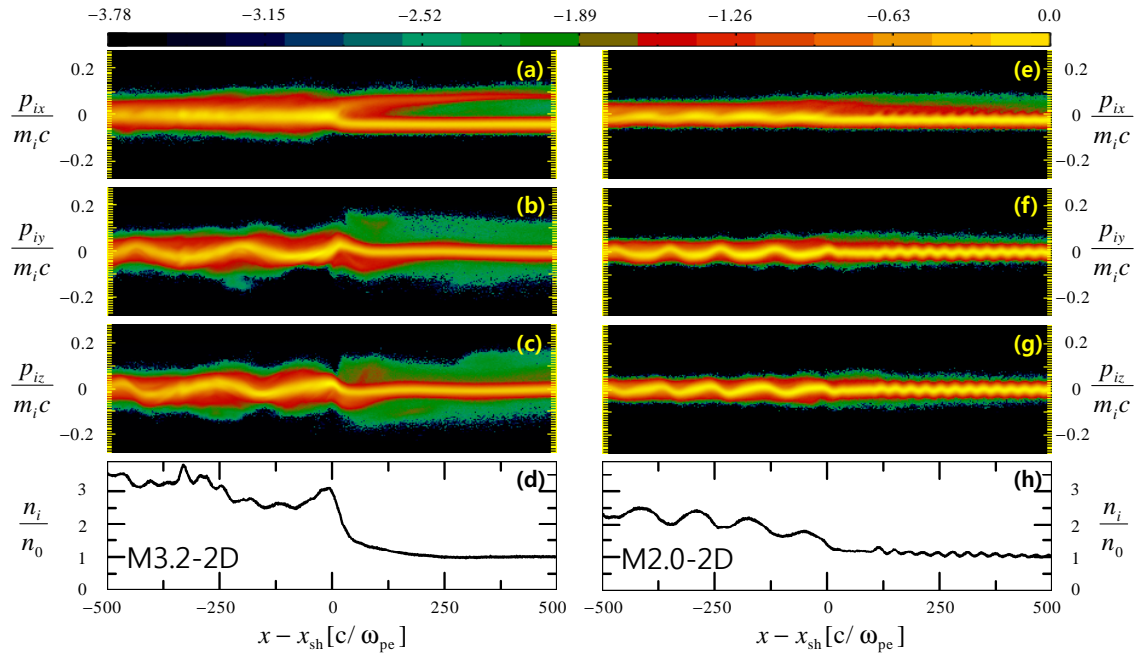
Figure 8: Shock structure of the M3.2-2D (left panels) and M2-2D (right panels) at $w_{pe}t \approx 4.5 \times 10^4$ ($\Omega_{ci}t \approx 12$). Here, x_{sh} denotes the shock position and the length scale is expressed in the unit of c/ω_{pe}. From top to bottom, the ion momentum phase space plots $x - p_{ix}$, $x - p_{iy}$ & $x - p_{iz}$ (normalized by $m_i c$ and colorbar indicates $\log f(p_{i,\alpha})$), and the one-dimensional profile of ion density (normalized by number density of incoming plasma) are shown.

Then the Alfvén Mach number of the shock, M_A, is defined as:

$$M_A \equiv \frac{v_{sh}}{v_A} = \frac{v_0}{B_0/\sqrt{4\pi n m_i}} \frac{r}{r-1} = M_{A,0} \frac{r}{r-1}, \tag{8}$$

where $n = n_i = n_e$ is the number density of the incoming plasma, $v_A = B_0/\sqrt{4\pi n m_i}$ is the Alfvén speed along the background magnetic field, and $M_{A,0} = v_0/v_A$ is the flow Alfvén Mach number. The fast mode Mach number is defined as

$$M_f \equiv \frac{v_{sh}}{v_f} = \frac{v_{sh}}{\sqrt{c_s^2 + v_A^2}}, \tag{9}$$

where v_f is the fast mode speed for the wave propagating perpendicular to the magnetic fields (i.e. magnetosonic speed). For $\beta \gg 1$, $M_f \approx M_s$, since $v_A \ll c_s$.

The orientation of magnetic field is given by the obliquity angle θ_{Bn}, which is the angle between the shock normal direction ($\hat{\mathbf{n}} = \hat{\mathbf{x}}$) and $\mathbf{B_0}$. Thus the background magnetic field is given by

$$\mathbf{B_0} = B_0(\cos\theta_{Bn}\hat{\mathbf{x}} + \sin\theta_{Bn}\hat{\mathbf{y}}). \tag{10}$$

Initial electric field is zero, but the incoming magnetized plasma carries a uniform magnetic field B_0 and the motional electric field, $\mathbf{E_0} = -\mathbf{v_0}/c \times \mathbf{B_0}$, is induced, where c is the speed of light. Since ion injection and acceleration depends only weakly on the obliquity angle as shown by [26], we choose $\theta_{Bn} = 13°$ for our fiducial model.

PIC simulations follow kinetic plasma processes on different length scales for different species: the electron skin depth, c/w_{pe}, and the ion skin depth, c/w_{pi}, where $w_{pe} = \sqrt{4\pi e^2 n/m_e}$ and $w_{pi} = \sqrt{4\pi e^2 n/m_i}$ are the electron plasma frequency and the ion plasma frequency, respectively. Here the simulation results are presented in term of $x/[c/w_{pe}]$ and $t/[w_{pe}^{-1}]$. On the other hand, the shock structure varies and evolves at length scales of the Larmor radius for ions with the particle speed v_0,

$$r_{L,i} \equiv \frac{m_i v_0 c}{e B_0} = M_{A,0}\sqrt{\frac{m_i}{m_e}} \frac{c}{w_{pe}}, \tag{11}$$

and in timescales of the ion gyration period $\Omega_{ci}^{-1} = m_i c/(e B_0) = r_{L,i}/v_0$.

The simulations are performed in two-dimensional computational domains. The longitudinal dimension, L_x, corresponds to $2 \times 10^4 c/w_{pe}$, which is represented by $N_x = 2 \times 10^5$ cells with a grid resolution of $\Delta x = 0.1 c/w_{pe}$. The transverse dimension, L_y, comes in two different modes: $N_y = 20$ cells for "almost 1D" simulations and $N_y = 600$ cells for 2D simulations ($\Delta y = \Delta x$). We place 32 particles per cell (16 per species). The time step is $w_{pe}\Delta t = 0.045$.

Based on the previous studies on one-dimensional PIC simulations for strong shocks [25], we assume "almost 1D" simulations would be good enough to investigate ion injection at weak ICM shocks (see Section "shock structures and ion injection" for the dependence of the simulation results on transverse box size). We also find that simulations with different spatial resolutions give essentially the same results.

The model parameters of our simulations are summarized in Table 2. We consider $\beta = 30 - 100$ and $k_B T = k_B T_e = k_B T_i = 0.0168 m_e c^2 = 8.6$ keV, relevant for typical ICM plasmas [10, 11]. For given
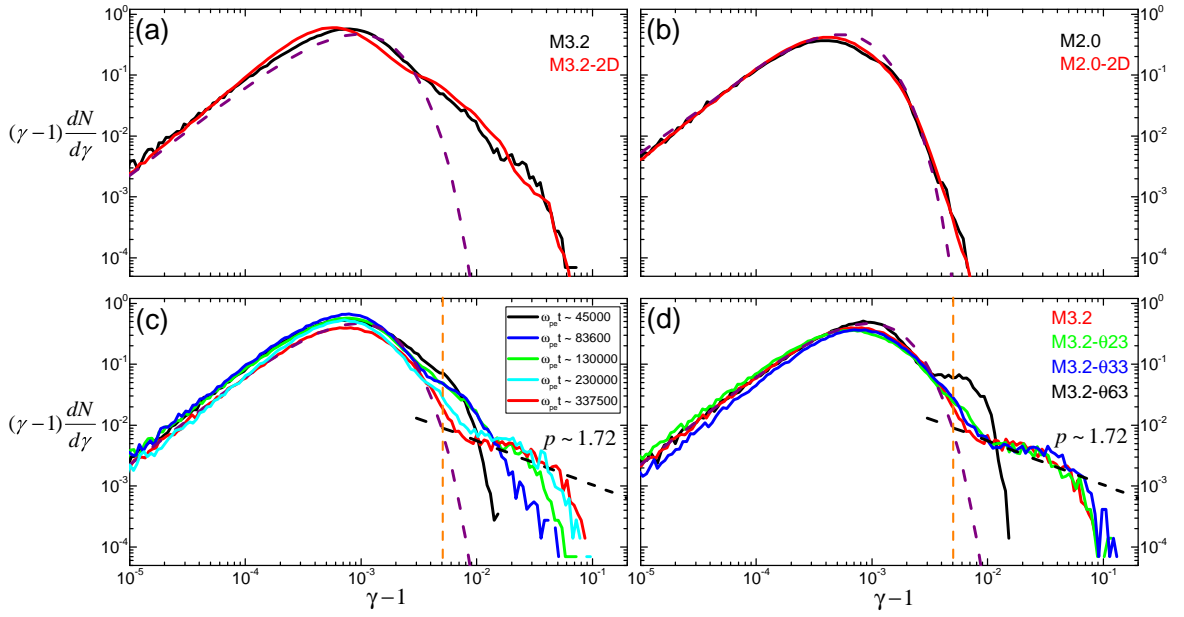
Figure 9: Panels (a) & (b) show downstream ion energy spectrum at $w_{\mathrm{pe}}t \approx 1.3 \times 10^5$ ($\Omega_{ci}t \approx 35$) in M3.2 and M2.0 models. Downstream ion spectra of 1D M3.2 model for 5 different time epochs from $w_{\mathrm{pe}}t \approx 4.5 \times 10^4$ ($\Omega_{ci}t \approx 12$) to 3.4×10^5 ($\Omega_{ci}t \approx 90$) are displayed in panel (c). Downstream ion spectra at $w_{\mathrm{pe}}t \approx 3.4 \times 10^5$ of $M_{\mathrm{s}} \approx 3.2$ shocks for 4 different obliquity angles are plotted in panel (d). The energy spectra shown in all panels are taken from the downstream region $[1.5 - 2.5]r_{L,i}$ behind the shock position. The black and purple dashed lines indicate the test-particle power-law spectrum and the thermal Maxwellian distribution in the postshock region, respectively. In (c) and (d), the injection energy, $E_{\mathrm{inj}} \approx 5 \times 10^{-3}m_ic^2$ for the M3.2 model is marked as the orange dashed line.
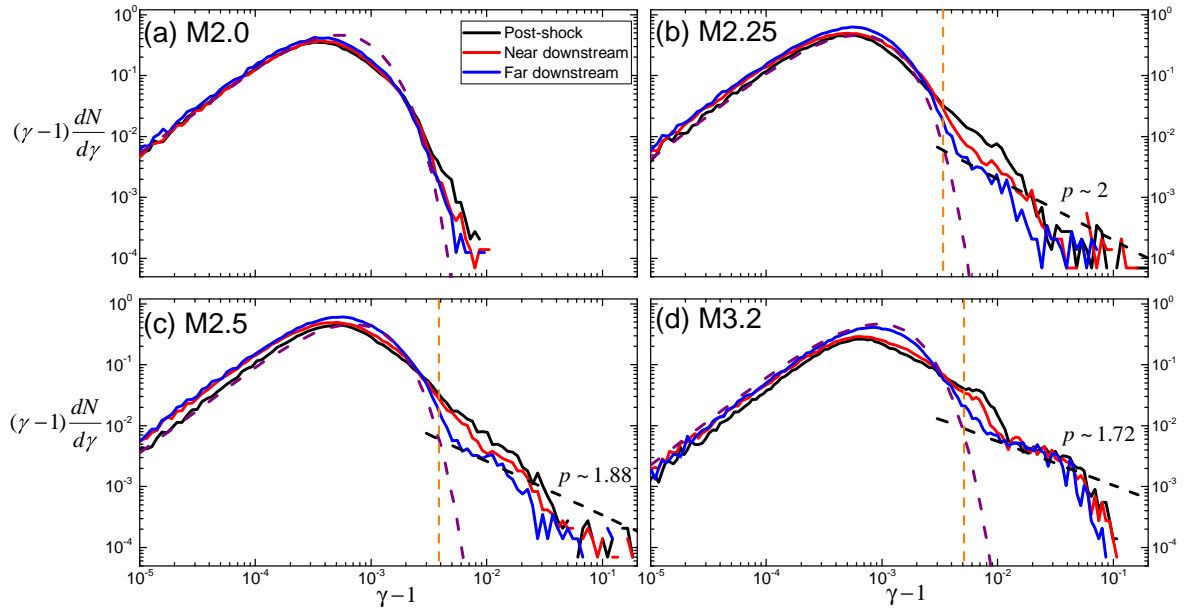
Figure 10: Ion energy spectra measured in the shock downstream at $w_{\mathrm{pe}}t \approx 3.4 \times 10^{5}$ ($\Omega_{ci}t \approx 90$) for M2.0, M2.25, M2.5, and M3.2 models. Here, energy spectra are taken from three different positions: Post-shock (black; $(0-1)r_{L,i}$ behind the shock), near downstream (red; $(1-2)r_{L,i}$ behind the shock), far downstream (blue; $(5-6)r_{L,i}$ behind the shock). The black and purple dashed lines show the test-particle spectrum expected for a shock with given M_{s} and thermal Maxwellian distribution in the postshock region, respectively. In (b), (c) and (d), the injection energy, E_{inj} for each model is marked as the orange dashed line.

β and c_s, the incident flow velocity, v_0, is specified to induce the shock with the sonic Mach number, $M_s \sim 2 - 4$, which is characteristic for cluster merger shocks [33]. The model M3.2 in the first row of Table 2 represents the *fiducial* model in 1D with the following parameters: $M_s = 3.2$, $\theta_{Bn} = 13°$, $\beta = 100$, and $m_i/m_e = 100$. Models with different M_s are named with the combination of the letter 'M' and the sonic Mach numbers (for example, M2.25 model has $M_s = 2.25$). Models with parameters different from the fiducial model have names that are appended by a character for the specific parameter and its value. For example, M3.2-θ33 model has $\theta_{Bn} = 33°$, while M3.2-m400 model has $m_i/m_e = 400$. We refer M3.2-2D and M2-2D models as 2D runs with the larger transverse dimension. M3.2-r2 and M3.2-r0.5 models are considered to explore the effects of different spatial resolution.

The last two columns of Table 2 show the end of simulation time for each model in units w_{pe}^{-1} and Ω_{ci}^{-1}. For the fiducial model M3.2, $t_{end}w_{pe} \approx 3.4 \times 10^5$, which corresponds to $t_{end}\Omega_{ci} \approx 90$. The ratio of the ion gyration period to the electron oscillation period scales as $w_{pe}/\Omega_{ci} \propto (m_i/m_e)\sqrt{\beta}$. So with a smaller mass ratio m_i/m_e a shorter simulation time is required to see ion acceleration at early stage of Fermi I acceleration. On the other hand, with $\beta = 100$, it would take 10 times longer simulation time to reach the similar stage of ion acceleration, compared to simulations with $\beta = 1$.

3.2 Results

shock structures and ion injection

Supercritical quasi-parallel shocks with $M_f > M_f^*$ (the fast first critical Mach number) are nonstationary and subject to quasi-periodic reformation due to the accumulation of self-generated magnetic waves in the foreshock region, resulting in the time-varying overshoots in electric shock potential and magnetic field structure [29]. At such shocks the specular reflection of inflowing ions is thought to provide additional dissipation to steepen the shock structure and seed particles to Fermi I acceleration. [89] calculated $M_f^*(\beta, \theta_{Bn})$ for $0 \leq \beta \leq 4$ and $0° \leq \theta_{Bn} \leq 90°$ from the condition that the downstream flow speed normal to the shock equals the downstream sound speed ($v_{n2} = c_{s2}$) by solving the Rankine-Hugoniot jump condition. Based on their Figure 4, we may deduce that for $\beta \gg 1$, $M_f^* \approx 1.0 - 1.1$ for quasi-parallel shocks, implying that all ICM shocks could be supercritical and accelerate CR protons efficiently. However, wave excitation and wave-particle interactions can provide *anomalous dissipation* inside the shock transition, which may suppress ion reflection. In fact, the ion reflection process is expected to depend on the reforming shock potential, time-varying magnetic shock ramp structure, and turbulent wave spectrum in the shock [29]. In addition, thermal motions in high β plasma can smooth out the overshoot in the shock potential. So anomalous dissipation and thermal effects could suppress ion reflection at weak shocks at the high β ICM plasma, resulting in a higher value of M_f^* than estimated by [89].

The shock potential energy is estimated to be

$$e\Delta\phi \approx \alpha(M_s,t)\frac{mv_{sh}^2}{2}, \tag{12}$$

where the factor $\alpha(M_s,t) \sim 1/2$ depends on M_s and varies with time [93, 94]. According to [28], during low states without the overshoot most of ions have $m_i v_x^2/2 > e\Delta\phi$ and advect downstream across the

29

shock, while in high states a substantial fraction of ions are reflected by the overshoot in $\Delta\phi$. This results in periodic bursts of back-streaming ions along the upstream parallel magnetic field. In addition, the reflected ions excite waves and amplify the transverse magnetic fields, which in turn changes the quasi-parallel background field to locally quasi-perpendicular fields (see Section "dependence on shock parameters"). Then incoming ions can be reflected by magnetic mirrors at those quasi-perpendicular parts of the shock transition [88, 95]. Obviously, shock reformation is closely related with the quasi-periodic growth and decay of the overshoot and ensuing ion reflection. It is expected that α decreases and the overshot does not develop for low Mach number 'subcritical' shocks.

Figure 7 compares the spatial structures of the shock potential and total magnetic field strength averaged over the transverse dimension for M2.0-2D and M3.2-2D models during $w_{pe}t = (0.8 - 1.2) \times 10^5$. The fluctuations in B are mainly due to the transverse waves (B_y and B_z), since the parallel component remains almost the same. M3.2-2D model displays the characteristics of supercritical shocks such as the overshoots in $\phi(x)$ and $B(x)$, self-reforming shock jump, and turbulent waves with $\langle \delta B^2 \rangle^{1/2}/B_0 \approx 1$. On the other hand, M2.0-2D model has much weaker turbulence, compared to M3.2-2D model, and it does not exhibit distinct overshoots.

Figure 8 compares the phase space distribution and the density of ions for M2.0-2D and M3.2-2D models at $w_{pe}t \approx 4.5 \times 10^4$. The presence of reflected ions moving along $+\hat{x}$ direction in the foreshock region is evident in the M3.2-2D model, while there is no beam of reflected ions in the shock upstream in the M2.0-2D model. In the M3.2-2D model most ions are advected and trapped in the downstream as thermal ions, while about $\sim 20\%$ are reflected back to the upstream flow. During the shock reformation cycle of M3.2-2D the shock discontinuity is almost steady for $\sim 5.4\Omega_{ci}^{-1}$, until the beam of reflected ions produce a new discontinuity $\sim 2.4r_{L,i}$ ahead of original discontinuity. The mean density in the far-downstream region is compressed by the expected factor, $r \approx 3.1$ in M3.2-2D and $r \approx 2.3$ in M2.0-2D.

Figures 9 (a) and (b) compare the ion spectra at $w_{pe}t = 1.3 \times 10^5$ ($\Omega_{ci}t \approx 35$) in M3.2 and M3.2-2D, and in M2.0 and M2.0-2D, respectively. They confirm that the results of 'almost' 1D simulations are consistent with those of 2D simulations. Since 2D simulations are computationally much more expensive, we therefore use 'almost' 1D simulations to investigate shocks with wide ranges of the model parameters as listed in Table 2.

As mentioned before, the reflected ions gain energy initially via multiple cycles of SDA and continue to be accelerated to nonthermal energies sufficient to diffuse across the shock. In the test-particle regime of DSA, the non-thermal momentum distribution in the downstream region becomes a power-law form

$$f(p) \approx f_N \left(\frac{p}{p_{\text{inj}}} \right)^{-q} \exp \left[-\left(\frac{p}{p_{\text{max}}} \right)^2 \right], \tag{13}$$

where $f_N(t)$ is the normalization factor, $q = 3r/(r-1)$, and $p_{\text{max}}(t)$ is the maximum momentum of CR protons that increases with the shock age [22, 96]. In the non-relativistic regime ($E = (\gamma - 1)m_i c^2 \approx p^2/2m_i$) the energy distribution function $f(E)$ can be approximated as $f(E) = 4\pi p^2 f(p)dp/dE \propto (\gamma - 1)^{-\frac{q-1}{2}}$.

Figure 9 (c) displays the time evolution of downstream ion spectra during $w_{pe}t \approx 4.5 \times 10^4 - 3.4 \times 10^5$ in the M3.2 model, proceeding from pre-energization and to the early-stage of DSA. As shown in

the red line, at $w_{pe}t_{end} \approx 3.4 \times 10^5$ the energy spectrum develops roughly a power-law tail, $dN/d\gamma \propto (\gamma - 1)^{-p}$, where $p \approx 1.72$ is consistent with the test-particle slope expected for a $M_s = 3.2$ shock. We also see that the downstream energy spectrum changes from Maxwellian to power-law distributions at $E_{inj} \approx 5.0 \times 10^{-3} m_i c^2 \approx 4.9 E_{th}$, where $E_{th} = (3/2)k_B T_2$ and T_2 is the downstream temperature. Here we designate E_{inj} as the injection energy, which corresponds to the so-called the injection momentum, p_{inj}, to mark the boundary between the thermal and nonthermal distributions. Then suprathermal particles are somewhat loosely defined as energized ions that belong to 'a superathermal bridge' between the thermal Maxwellian distribution and the nonthermal power-law population, as shown intuitively in Figure 2 of [26]. The parameter E_{inj} (or p_{inj}) should depend on both M_s and M_A as well as θ_{Bn}, because the ability of ions to cross the shock depends on the flow compression ratio, strength of self-generated magnetic waves, and magnetic field configuration at the shock transition zone. Our results at t_{end} for M3.2 model indicates $p_{inj}/p_{th} \approx 2.7$ (where $p_{th} = \sqrt{2m_i k_B T_2}$).

Long-term evolution of the downstream ion spectrum well into full Fermi-I acceleration regime is beyond the reach of our PIC simulations. However, 2D hybrid simulations of [26] that ran up to $\Omega_i t = 2500$ showed that the nonthermal power-law tail extends to increasingly higher $p_{max}(t)$ with time, and that $p_{inj}/p_{th} \approx 3.0 - 3.5$ at strong quasi-parallel shocks in $\beta \sim 1$ plasma. For the M3.2 model shown in Figure 9, the ratio, $p_{inj}/p_{th} \approx 2.7$, is smaller and the normalization factor f_N is higher than the values inferred from those hybrid simulations. Such differences may come from the different dimensionality (i.e. 1D versus 2D) and different physical models (with or without electron kinetic processes) of the two simulations as well as different shock parameters (i.e. M_s and β). Considering the trend during $w_{pe}t_{end} \approx (1.3 - 3.4) \times 10^5$ shown in Figure 9 (c), we expect the ratio p_{inj}/p_{th} increases and f_N decreases gradually with time as high energy particles well above p_{inj} undergo the full Fermi I acceleration.

Figure 10 shows ion energy spectra in three downstream regions, post-shock ($[0 - 1]r_{L,i}$ behind the shock), near downstream ($[1 - 2]r_{L,i}$), and far downstream ($[5 - 6]r_{L,i}$), at $\Omega_i t_{end} \approx 90$ of the 1D simulations for M2.0, M2.25, M2.5, and M3.2 models. The shock models with $M_s \geq 2.25$ develop a nonthermal power-law-like tail with a slope p, which is similar to that expected for a given sonic Mach number. On the other hand, the M2.0 model does not show nonthermal particles beyond the Maxwellian distribution. From these results, we can deduce that in $\beta \approx 100$ ICM plasma the fast first critical Mach number occurs at $M_f^* \approx 2.2$, which is higher than the values $M_f^* \approx 1.0 - 1.1$ for $\beta \sim 4$ quasi-parallel shocks estimated by [89]. In summary, at ICM shock with $M_s \gtrsim 2.2$ ions are reflected and injected into the Fermi I process, and then accelerated to high energy CRs.

Although our simulations have reached only very early stage of DSA, we attempt to estimate the ion injection fraction at $\Omega_i t_{end} \approx 90$ as the fraction of nonthermal ions with $p \gtrsim p_{inj}$ in the downstream ion energy spectrum,

$$\xi \equiv \frac{1}{n_2} \int_{p_{min}}^{p_{max}} 4\pi f(p)p^2 dp, \tag{14}$$

where $p_{min} = \sqrt{2}p_{inj}$. Figure 11 shows $\xi(t_{end}, M_s)$ for 1D models with $\theta_{Bn} = 13°$ and $M_s \approx 2.0 - 4.0$. As shown in the red line, it increases with the Mach number as $\xi(M_s) \propto M_s^{1.5}$ for $M_s \gtrsim 2.2$. Since the shock compression ratio decreases with decreasing M_s for weak shocks, the fractional energy gain at each
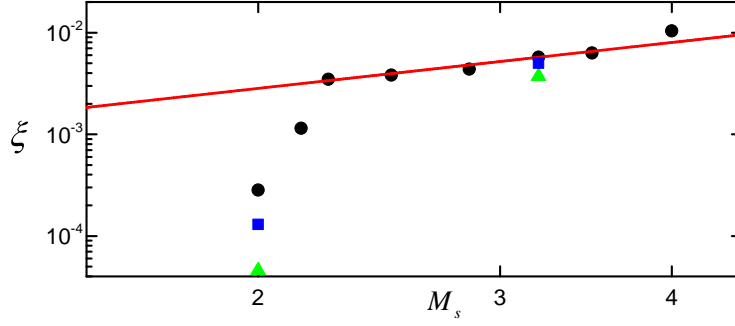
Figure 11: Injection fraction ξ as a function of M_s at t_{end} of 1D simulations for M2.0 - M4.0 models (black dots). The red line is a fitting line which follows a scaling relation, $\xi \propto M_{\mathrm{s}}^{1.5}$. The blue squares and green triangles are for $\beta = 50$ and $\beta = 30$ models, respectively.

shock-crossing cycle is smaller, and so ions need to undergo more cycles of reflection to gain energies sufficient for injection. Moreover, the size factor, $\alpha(M_{\mathrm{s}})$, of $\Delta\phi$ in Equation 12 should decreases with decreasing M_s. As a result, the injection fraction is expected to decrease at lower M_{s} shocks and drops rather abruptly to a small value for $M_{\mathrm{s}} < 2.2$. In the test-particle limit of weak shocks, the power-law slope q is greater than 4 and approximately constant. So the normalization factor, $f_N(t)$ determines $\xi(t)$ but the growth of $p_{\mathrm{max}}(t)$ with time does not increase ξ. In fact, both f_N and ξ decrease with time during $w_{\mathrm{pe}}t_{\mathrm{end}} \approx (1.3 - 3.4) \times 10^5$ in the M3.2 simulation, so in DSA regime ξ is expected to be much smaller than what is shown in Figure 11.

The blue squares and the green triangles in Figure 11 show the results for $\beta = 50$ and 30 cases, respectively. For higher β, the self-excited waves are stronger due to higher M_{A} (see Section "dependence on shock parameters"), which should facilitate ion injection, So the trend of higher ξ at higher β shown in Figure 11 is consistent with such expectation.

magnetic field amplification

As shown in Figures 7 and 8, at supercritical shocks ions are reflected by the shock potential barrier and stream upstream along the magnetic fields, which excite turbulent waves via CR-driven instabilities. To analyze the nature of the excited wave modes, we perform Fourier analysis of the self-generated components, $\delta B_y(k)$ and $\delta B_z(k)$, in a region of width $\sim 2 \times 10^3 c/w_{\mathrm{pe}}$ upstream of the shock transition, where $\delta\mathbf{B}(\mathbf{x}) = \mathbf{B}(\mathbf{x}) - \mathbf{B_0}$ with $B_{0y} = B_0 \sin\theta_{\mathrm{Bn}}$, and $B_{0z} = 0$.

Following [27], we consider the stationary equation for magnetic energy density of the Alfvén waves produced by resonant streaming instability [97]. The spectrum of the transverse component of self-generated magnetic turbulence, $\delta\mathbf{B}_\perp$, is represented by $\mathscr{F}(k)$, the magnetic energy density per unit logarithmic bandwidth of waves with wavenumber k, normalized to the initial energy density, $B_0^2/(8\pi)$. Using their Equations (7)-(8),

$$\mathscr{F}(k) \propto \mathscr{P}(p_k) \propto \frac{4\pi}{3} p_k^4 v(p_k) f(p_k), \tag{15}$$

32
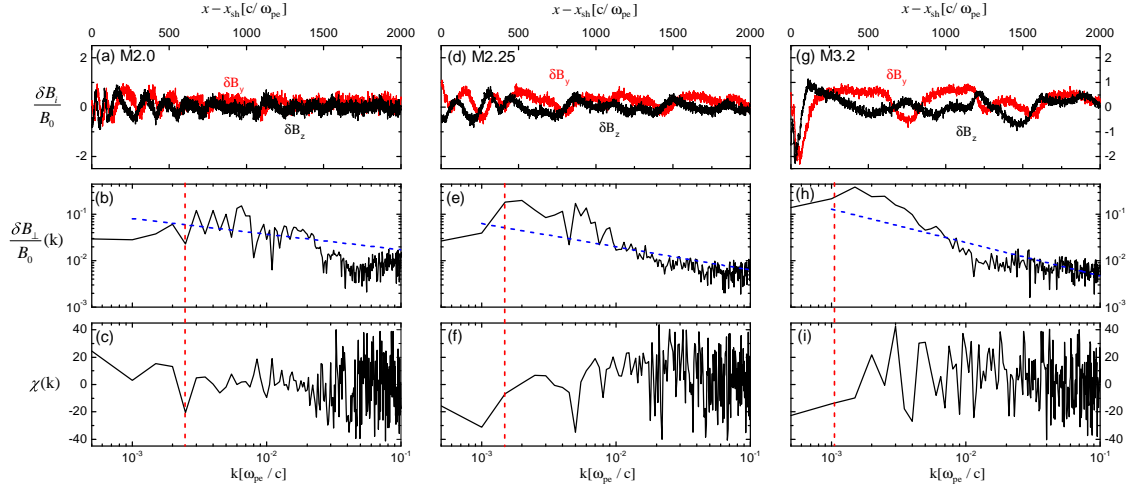
Figure 12: Self-excited magnetic field, $\delta B_\perp$, in the shock precursor ($0 < (x - x_s)w_{pe}/c < 2 \times 10^3$) at $w_{pe}t \approx 3.4 \times 10^5$ for M2.0, M2.25, and M3.2 models. Top panels: Spatial profiles of $\delta B_y(x)/B_0$ (Red) and $\delta B_z(x)/B_0$ (Black). Middle panels: Spectral distribution of $\delta B_\perp/B_0(k)$. Bottom panels: Polarization angle χ, where $+(-)$ sign corresponds to right-(left-)handed modes. The red dashed line indicates the inverse of the mean CR gyroradius, while the blue dashed line shows the characteristic power-law, $k^{(q-6)/2}$, due to the resonant streaming instability.

where $p_k = m\Omega_{ci}/k$ is the ion momentum resonant with waves of k and $\mathscr{P}(p_k)$ corresponds to the CR pressure per unit logarithmic momentum bandwith. For nonthermal ion distribution with the test-particle spectrum, $f(p) \propto p^{-q}$, the wave spectrum of turbulence driven by the resonant instability is expected to be

$$\mathscr{F}(k) = k(\frac{\delta B_\perp}{B_0})^2 \propto k^{q-5}, \tag{16}$$

where $\delta B_\perp^2 = \delta B_y(k)^2 + \delta B_z(k)^2$. Then, the Fourier transform of the self-excited magnetic field $\delta B_\perp$ becomes

$$\frac{\delta B_\perp}{B_0} \propto k^{\frac{q-6}{2}}, \tag{17}$$

which depends on the sonic Mach number, M_s. For strong shocks with $q = -4$, $\mathscr{F}(k) \propto k^{-1}$ and $\delta B_\perp/B_0 \propto k^{-1}$.

The polarization angle χ of a monochromatic, elliptically polarized wave of a given k can be calculated by

$$\chi(k) = \frac{1}{2}\sin^{-1}\left(\frac{V}{I}\right), \tag{18}$$

where $I(k)$ and $V(k)$ are the Stokes parameters for the two transverse magnetic field components in k-space. Positive (negative) values of χ indicate right-handed (left-handed) polarization of the excited waves. In particular, $\chi = +(-)45°$ corresponds to right-handed (left-handed) circularly polarized waves.

Figure 12 shows the spatial distribution of the transverse components, $\delta B_y(x)$ and $\delta B_z(x)$, and the Fourier analysis of $\delta B_\perp(k)$ with the polarization angle, $\chi(k)$ in the shock precursor ($0 < (x - x_s)w_{pe}/c <$
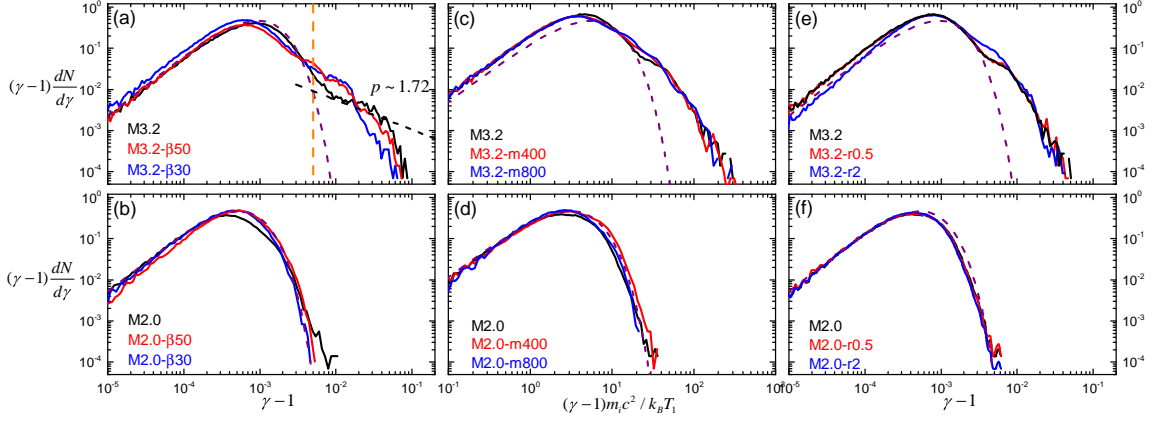
Figure 13: Downstream ion energy spectra for different models with $M_s \approx 3.2$ (upper panels) and 2.0 (lower panels). (a)-(b) Models with plasma $\beta = 30$, 50 and 100 at $w_{pe}t \approx 3.4 \times 10^5$ (c)-(d) Models with the mass ratio $m_i/m_e = 100$, 400, and 800 at $w_{pe}t \approx 8.4 \times 10^4$ (e)-(f) models with the resolution parameter $N = c/(w_{pe}\Delta x) = 5$, 10, and 20 at $w_{pe}t \approx 8.4 \times 10^4$. The purple dashed line shows the thermal Maxwellian distribution.

2×10^3) in M2.0 ($M_A \approx 18$), M2.25 ($M_A \approx 20$), and M3.2 ($M_A \approx 29$) models. In all three models, the excited waves due to CR ion-driven instabilities become marginally nonlinear with both $\delta B_y/B_0 \sim 1$ and $\delta B_z/B_0 \sim 1$ at t_{end}. The red vertical line marks $k_{CR} = 1/\rho_{CR}$, where ρ_{CR} is the average gyroradius of non-thermal ions in the upstream region of $(x - x_s)w_{pe}/c = [1.75 - 2.0] \times 10^3$ for each model. At higher M_s, ions are accelerated to higher energies, so ρ_{CR} is larger and the characteristic wavelength of resonant waves is longer, as shown in the top panels. Moreover, the blue dashed line shows the quasilinear turbulence spectrum, $k^{\frac{q-6}{2}}$, of the waves excited by the resonant streaming instability for each model. The magnetic energy spectrum. $\delta B(k)$, seems roughly consistent with the expected spectrum, except some excess power at large scales near $k \gtrsim k_{CR}$ in M2.25 and M3.2 models. This probably comes from nonlinear amplification due to the faster-growing nonresonant instability at higher M_A shocks. At higher M_s, higher flux of reflected ions induces stronger turbulence, so the amplitude of $\delta B(k)$ increases with increasing M_s.

Negative polarization angles near k_{CR} shown in the bottom panels of Figure 6 seem to agree with the fact that the resonant instability excites left-handed circularly polarized waves with $\chi = -45°$ in the quasilinear regime. On the other hand, the nonresonant instability is expected to excite right-handed circularly polarized waves with $\chi = +45°$ with higher growth rates on smaller scales at shocks with $M_A > 30$ [27]. Thus, the nonresonant instability becomes important for the M3.2 model with $M_A \approx 29$.

dependence on shock parameters

In this section, we investigate the dependence of the shock criticality on the shock obliquity angle and plasma beta. Figure 9 (d) compares the models with different θ_{Bn}. As shown in [26], ion injection and

acceleration depends only weakly on θ_{Bn} for quasi-parallel shocks, while it is severely suppressed for quasi-perpendicular shocks. The M3.2-θ63 model agree well with the model with $\theta_{\text{Bn}} = 63°$, $M_{\text{s}} = 3$, and $\beta = 20$, considered by [23]. The injection energy, E_{inj}, is higher at shocks with higher obliquity angles, so a larger number of SDA cycles is required for injection into DSA [28]. Despite that fact that at quasi-perpendicular shocks ions are reflected more efficiently and a significant fraction ($\sim 20\%$) of the downstream ions form a supra-thermal component, the reflected ions do not gain sufficient energies for injection to full Fermi I before they advect downstream behind the shock. Recently, [98] found a different behavior of perpendicular shocks using a combined PIC-MHD approach. Their results show that SDA can energize the non-thermal ions sufficiently that they can travel upstream where they excite long-wavelength fluctuations in the magnetic field. These fluctuations will eventually distort the shock and excite turbulence in the downstream medium. However, this result depends on having a much larger simulation domain in order to capture long-wavelength fluctuations. A computational domain of that size is not practical for pure PIC simulations.

Next, we explore the dependence on β in Figures 13 (a) and (b). Here $B_0 \propto \beta^{-1/2}$, while other shock parameters (i.e. n and T) are fixed. So the models with $\beta = 30$, and 50 have stronger B_0 and smaller M_A, compared to the fiducial model. So in the case of M3.2 models $M_A \approx 16, 21$, and 29 for $\beta = 30, 50$, and 100, respectively. Based on [27], it is expected that $\delta B/B_0 \propto M_A \propto \beta^{1/2}$, and so stronger turbulence is generated at higher β. Since the average gyroradius of nonthermal ions $\rho_{CR} \propto B_0^{-1}$, the resonant wavelength, $k_{\text{CR}}^{-1} \propto \beta^{1/2}$, increases with increasing β. One can see in the upper panels of Figures 12 and 14 that the characteristic wavelength of excited waves is longer at higher β. The middle panels of Figure 12 and the lower panels of Figure 14 show that the amplitude of the magnetic turbulent spectrum is higher at higher β. Stronger levels of magnetic turbulence at higher β are expected to lead to smaller injection fraction (smaller f_N), since reflected ions are more likely to advect downstream due to stronger interactions with excited waves. Comparison of M3.2 models with different β in Figure 13 (a), we may infer that DSA power-law is more mature at higher β. Comparison of Figures 13 (a) and (b) shows that a $M_{\text{s}} = 2.0$ shock do not reflect and accelerate ions at ICM plasma with $\beta = 30 - 100$.

dependence on simulation parameters

Finally, we examine how our findings depend on the simulation parameters such as the ion-to-electron mass ratio, m_i/m_e, and the spatial resolution parameter, $N = (c/w_{\text{pe}})/\Delta x$. Figures 13 (c) and (d) show that our simulation results do not depend sensitively on the mass ratio, so the critical Mach, $M_{\text{s}}^* \approx 2.2$ remains the same even for simulations with more realistic mass ratio. Figures 13 (e) and (f) explore the dependence of the ion energy spectra on the grid resolution of our PIC simulations. All three cases resolve essentially the same ion spectra at the given time, $\Omega_{ci}t \sim 22.3$. Figures 13 (c)-(f) confirm that in high β plasma the critical sonic Mach number is $M_{\text{s}}^* \sim 2.2$ for quasi-parallel obliquity. In summary, the main results of this study can be considered as being converged numerically in terms of m_i/m_e and N.
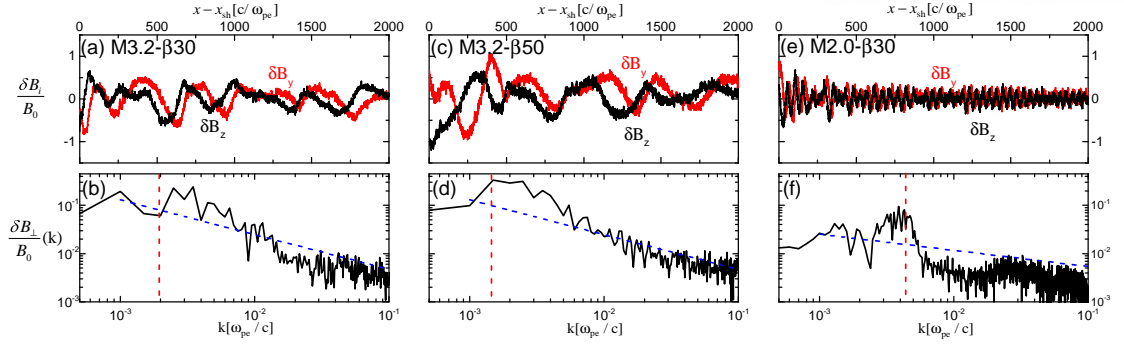
Figure 14: Self-excited magnetic field, $\delta B_\perp$, in the shock precursor $(0 < (x - x_s)w_{\rm pe}/c < 2 \times 10^3)$ at $w_{\rm pe}t \approx 3.4 \times 10^5$ for M3.2-β30, M3.2-β50, and M2.0-β30 models. Upper panels: Spatial profiles of $\delta B_y(x)/B_0$ (Red) and $\delta B_z(x)/B_0$ (Black). Lower panels: Spectral distribution of $\delta B_\perp/B_0(k)$. The red dashed line indicates the inverse of the mean CR gyroradius, while the blue dashed line shows the characteristic power-law, $k^{(q-6)/2}$, due to the resonant streaming instability.

3.3   Summary

At supercrical quasi-parallel shocks incoming ions are specularly reflected by the overshoot in the electrostatic shock potential and locally perpendicular magnetic field in the shock transition [29]. The reflected ions escaping upstream along the magnetic field excite left-handed (right-handed) circularly polarized waves via CR-driven resonant (nonresonant) instabilities, amplifying transverse components of the magnetic field [27]. This induces locally quasi-perpendicular fields in the shock ramp, which in turn facilitates the specular reflection of ions due to magnetic deflection and SDA due to drift along the motional electric field [88]. In $\beta \sim 1$ environment, the critical fast Mach number is expected to approach to $M_{\rm f}^* \approx 1.0 - 1.5$ for the shock obliquity angle $\theta_{\rm Bn} \lesssim 45°$ [89]. In this study, we study such plasma processes and estimate the critical sonic Mach number $M_{\rm s}^*$, above which ion reflection and acceleration is efficient, by performing PIC simulations for quasi-parallel shocks in $\beta \approx 100$ plasmas. A wide range of shock parameters are considered as summarized in Table 2.

The main results are summarized as follows:

1. We find that the critical Mach number is $M_{\rm s}^* \approx 2.2$ for quasi-parallel shocks at high β environment, which is higher than the values $M_{\rm f}^* \approx 1.0 - 1.1$ estimated from Rankine-Hugoniot relations by [89]. We conjecture that anomalous dissipation inside the shock transition due to wave generation and wave-particle interactions may provide the necessary shock dissipation at shocks with $M_{\rm s} \lesssim 2.2$, since high β plasma is more prone to self excitation of turbulent waves via CR-driven instabilities. Thus only at supercritical quasi-parallel shocks with $M_{\rm s} \gtrsim 2.2$ ions impinging on the shock ramp are reflected to upstream and gain sufficient energies via SDA to become nonthermal particles.

2. For high β (≈ 100), weak ICM shocks with $M_{\rm s} \approx 2 - 3$ have relatively large Alfvén Mach numbers, $M_{\rm A} \approx \sqrt{\beta}M_{\rm s} \approx 20 - 30$. Since $\delta B/B_0 \propto M_{\rm A} \propto \beta^{1/2}$ for Alfvén waves generated via resonant streaming instability, magnetic turbulence is stronger for higher β. According to [27], nonresonant Bell instability is predicted to grow faster than resonant instability for $M_{\rm A} \gtrsim 30$. In the M3.2 model with

$M_s \approx 3.2$ and $M_A \approx 29$, for instance, both instabilities must operate efficiently, while at the weaker shocks resonant streaming instability should be dominant.

3. We estimate the CR injection fraction, ξ, the number fraction of nonthermal ions with the kinetic energy $E \gtrsim 10E_{th}$ in the downstream ion spectrum at the end of the 1D simulations, which corresponds to the very early stage of DSA. For quasi-parallel shocks, it ranges $\xi(M_s) \sim 10^{-3} - 10^{-2}$ for $M_s \approx 2.2 - 4.0$ and increases with increasing M_s as $M_s^{1.5}$. Although a quantitative estimate of ξ in the full Fermi I regime is beyond the scope of this study, we expect $\xi(t)$ decreases on many ion gyration period and becomes be smaller than what is presented in Figure 11.

4. If quasi-parallel ICM shock with $M_s < 2.2$ were unable to generate CR protons as implied by this study, the level of gamma-ray flux due to shocks accelerated CR protons would be much lower than previously estimated [31]. This may explain non-detection of gamma-ray emission from galaxy clusters [87].

More follow-up works have been conducted to investigate proton acceleration at ICM shocks for longer timescale than the timescale considered in this work (e.g., [99–101]. While PIC simulation requires lots of computational memory to resolve the detailed shock structure in multi-dimensional space (i.e., 2D and 3D) for a sufficiently long time ($\sim \mathcal{O}(10^2)\Omega_{ci}^{-1}$, such follow-up works employ alternative numerical methods to overcome the computational challenge to simulate shocks in high β-regime. The first method is using hybrid simulation code, which treats ions kinetically while electrons are modeled as a fluid. With this method, computational cost for simulation is substantially reduced compared to the PIC simulation. [99] recently performed hybrid simulations to simulate ICM shocks with $M_s = 3.2$ and $\beta = 100$ and has examined ion acceleration process. Especially, the early injection and DSA process are consistent with the results presented in this Section and the spectral evolution via DSA beyond the early stage is identified. Moreover, some works implement new method to investigate particle acceleration process [100, 101]. Such works suggest a method combining PIC method and magnetohydrodynamics. Here, the thermal plasma is treated as a fluid and non-thermal particles are added and treated kinetically. Because the shock structure are fully generated by the thermal plasma and the CR-driven resonant (nonresonant) instabilities are induced by the injected non-thermal particles, so the microphysics for particle acceleration could be explored. In the parameter space for ICM shocks, $M_s = 2 - 4$ and $\beta = 100$, [100, 101] again confirmed that CR-driven instabilities are efficiently generated only at the supercritical shocks with $M_s \gtrsim 2.25$ and DSA operates only at such supercritical shocks as well. Based on those results, we interpret that the preacceleration physics described in this Section could be applicable even in the sufficiently long timescale.

Furthermore, while we investigate only proton acceleration in quasi-parallel ICM shocks with $M_s \sim 2 - 4$ and $\beta = 30 - 100$, [25] showed that proton and electron can be simultaneously energized through the DSA mediated by ion-beam driven instabilities in the quasi-parallel shock with $M_s \approx 20$ and $\beta \approx 1$. Further studies regarding electron acceleration at quasi-parallel ICM shocks should be required, however, we expect that electron acceleration efficiency at quasi-parallel ICM shock is much lower than that obtained at the quasi-parallel shocks in low-β medium. In order to operate electron DSA process, thermal electrons need to be preaccelerated at the shock surface through the motional electric field,

$|E| \propto v_0 B_0 \propto v_0/c_s/\sqrt{\beta} \propto M_s/\sqrt{\beta}$. Because the amount of energy gain via the motional electric field decreases as β increases or $M_s increases$, electron preacceleration process at low-M_s and high-β ICM shock becomes more ineffcient compared to the preacceleration at high-M_s and low-β shock.

Before closing this Section, we further comments about initial distribution function of upstream magnetized beam and turbulent nature of ICM. Firstly, while we considered only initial Maxwellian distribution for the upstream magnetized beam, realistic particle distribution may have a chance to deviate from Maxwellian due to the previous episodes of acceleration via shocks and/or turbulence. Such upstream condition may enhance the acceleration efficiency. Secondly, numerical studies including this work typically focus on the self-excited plasma waves, however, preexisting waves should exist as consequence of turbulence in the realistic ICM. It has been shown that the kinetic turbulence is possibly transferred energy up to the scale comparable to the gyroradii of thermal ion and electron (see e.g., [102, 103]), so the preexisting waves near the ICM shock surfaces could be scattering off the upstream ions. Further studies should be necessary to investigate the ingredients listed here.

IV   Gamma-ray and Neutrino Emissions due to Cosmic-ray Protons Accelerated at Intracluster Shocks in Galaxy Clusters

We have confirmed that protons are possibly energized at the ICM shocks through the mechanism mediated by plasma waves near the shock surface (Section III). As a follow-up work of the Section III, we followed long-term evolution of ICM shock produced by PIC simulation up to $\Omega_{ci}t \sim 270$, which is about 3 times longer than t_{end} of the simulation shown in this Section [104]. As we expected through this work, the injection fraction decreases as time increases. This tendency can be explained as follows: (1) The shock kinetic energy is continuously dissipated into CR acceleration and the post-shock region has cooled down as well. (2) As the post-shock temperature decreases, the ratio between injection momentum and post-shock thermal momentum increases, which is the key parameter to determine injection fraction (see [104] for more details). Adopting PIC simulation results, we then proposed a DSA model for ICM shocks based on the test-particle approach [96]. Since the dynamical feedback of CR is not substantial in the weak shock regime with low CR acceleration efficiency and injection fraction, the test-particle approach is reasonable way to conduct DSA model for ICM. In this Section, employing the DSA model, the detectability of γ-ray and neutrino emissions due to CR protons produced at ICM shocks is investigated. Note that all results shown here are originally presented in the paper (Ha, J.-H., Ryu, D., & Kang, H. 2020, The Astrophysical Journal, 892, 86; [105]).

If CRp are produced at ICM shocks, most of them are expected be accumulated in galaxy clusters because the lifetime of CRp could be longer than the age of current universe [106]. Then, inelastic collisions between CRp with $E \gtrsim 1.22$ GeV (i.e., the threshold of the reaction; corresponding kinetic energy threshold is ~ 0.78 GeV) and thermal protons (CRp-p collisions) in the ICM produce neutral and charged pions, which produce γ-ray and neutrino through the following channels [107]:

$$
\begin{aligned}
\pi^0 &\rightarrow \gamma\gamma, \\
\pi^\pm &\rightarrow \nu_\mu/\overline{\nu}_\mu + \mu^\pm \rightarrow \nu_e/\overline{\nu}_e + \nu_\mu + \overline{\nu}_\mu + e^\pm.
\end{aligned} \tag{19}
$$

The observation of diffuse cluster-wide *gamma*-ray emission caused by CRp-p collisions could thus give evidence for CRp production at ICM shocks. In this context, such emission has been estimated using galaxy clusters obtained by cosmological hydrodynamic simulations (see [31, 84, 85]). However, currently available telescopes like Fermi-LAT and Veritas have so far failed to detect γ-rays from clusters [87, 108] and thus future γ-ray observation should be required to explain CRp production inside galaxy clusters. The observation of high-energy neutrinos released by the same CRp-p collisions should be another evidence for CRp production at ICM shocks. For example, [109, 110] calculated neutrinos due to the CRp produced at AGNs and SNRs in the ICM and cluster galaxies. [111] and [112], on the other hand, stated that ICM shocks, as well as accretion shocks surrounding clusters, are unlikely to be substantial sources of CRp that contribute considerably to the IceCube neutrino flux with $E_\nu \gtrsim 10$ TeV. Moreover, detecting point neutrino source in the lower energy range, $E_\nu \lesssim 1$ TeV, is not straightforward because of atmospheric neutrino background (e.g., [113, 114]).

Based on fluid simulations of DSA where the time-dependent diffusion-convection equation for the isotropic part of CRp momentum distribution is solved along with a thermal leakage injection model, [76] suggested that η could be as large as ~ 0.1 for shocks with $M_s \simeq 5$. According to the hybrid simulations performed by [26], however, $\eta \approx 0.036$ for the $M_s \approx 6.3$ ($M = 5$ in their definition) shock in $\beta \sim 1$ plasmas. On the other hand, [31] argued that the overall efficiency of CRp acceleration at ICM shocks with $2 \lesssim M_s \lesssim 5$ should be limited to $\eta \lesssim 10^{-3}$, if the predicted γ-ray emissions from simulated clusters are to be consistent with the upper limits set by Fermi-LAT for observed clusters [108]. This apparent discrepancy between the theoretical expectation and the observational constraint remains to be further investigated and is the main focus of this work.

To resolve such discrepancy, in this work, we adopt the DSA model proposed in [104] including the detailed microphysics for proton acceleration by ICM shocks. We first estimate the CRp produced via fresh-injection DSA at ICM shocks in simulated sample clusters. Assuming that those CRp fill the cluster volume and serve as the preexisting CRp, and adopting a simplified model for reacceleration based on the "test-particle" solution, we also estimate the boost of the CRp energy due to the multiple passages of the ICM plasma through shocks. We then calculate γ-ray and neutrino emissions from simulated clusters using the approximate formalisms presented in [107] and [115]. The predicted γ-ray emissions are compared to the Fermi-LAT upper limits [108]. The neutrino fluxes from nearby clusters are compared with the IceCube flux [116] and the atmospheric neutrino flux [117].

4.1 CR protons in Simulated Clusters

Simulations and Galaxy Cluster Sample

Cluster samples used in this study were obtained from a set of cosmological hydrodynamic simulations as described in Section II. All parameters for ΛCDM cosmology are identical to that used in Section II, except the $\sigma_8 = 0.82$ value.

Because the cosmological simulation performed for this study is hydrodynamic simulation, so magnetic field modeling is necessary for differentiating between $Q_\parallel$ and $Q_\perp$-shocks (see Section "Shock Identification"). We here obtain the passively evolved magnetic field including the Biermann Battery mechanism at shocks [118]. Here, the Biermann Battery mechanism states the magnetic field amplification through the kinematic process induced by density and temperature gredients. In our simulations, the following equation along with the equations for fluid and gravity were solved:

$$\frac{\partial B}{\partial t} = \nabla \times (v \times B) + \frac{c \nabla p_e \times \nabla n_e}{n_e^2 e}, \tag{20}$$

where n_e and p_e are the electron number density and pressure, respectively, and v is the flow speed. The second term on the right hand side accounts for the Biermann battery mechanism. The passive evolution of B implies that the Lorenz force term in the momentum equation is ignored, so the magnetic field does not affect the fluid motions. Further detailed descriptions can be found in [119].

In the simulation box, the local peaks of X-ray emissivity are identified as the centers of clusters, and the total (baryons plus DM) mass, M_{200}, and the X-ray emission-weighted temperature, T_X, of
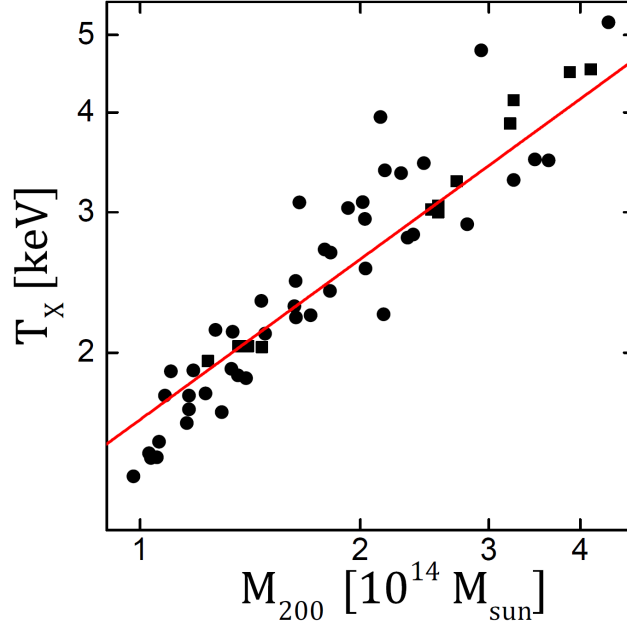
Figure 15: Mass versus temperature relation for 58 sample clusters at $z = 0$, found in a set of cosmological simulations for the LSS formation of the universe. The total (baryon plus DM) mass and the X-ray emission-weighted temperature inside the spherical volume of $r \leq r_{200}$ are shown. The filled squares denote 12 clusters used to show the shock energetics plotted in Figures 16. The virial scaling relation of $T_X \propto M_{200}^{2/3}$ is represented as the red solid line.

clusters inside r_{200} are calculated [120]. Here, r_{200} is the virial radius defined by the gas overdensity of $\rho_{\text{gas}}/\langle\rho_{\text{gas}}\rangle = 200$. From the $z = 0$ data of four simulations, a sample of 58 clusters with 1 keV $\lesssim$ $T_X \lesssim 5$ keV are found. They have $10^{14} M_\odot \lesssim M_{200} \lesssim 5 \times 10^{14} M_\odot$ and $r_{200} \approx 1 - 2h^{-1}$Mpc. Figure 15 shows the mass *versus* temperature relation of the sample clusters, which follows $T_X \propto M_{200}^{2/3}$, expected for virial equilibrium.

Shock Produced in Galaxy Cluster Sample

We identify ICM shocks formed inside simulated clusters through shock capturing method described in Section II. Shocks with $M_s \geq 1.5$ are identified, although only $Q_\parallel$-shocks with $M_s \geq 2.25$ are accounted for the CRp production. Typically, a shock surface consists of a number of shock zones, and the surface area is estimated assuming each shock zone contributes $s_{\text{sh}} = 1.19(\Delta l)^2$, which is the mean projected area of a zone for random shock normal orientation.

For shock zones, the shock obliquity angle is calculated as $\theta_{\text{Bn}} \equiv \cos^{-1}[|\Delta u \cdot B_1|/(|\Delta u||B_1|)]$, where $\Delta u = u_2 - u_1$ and B_1 is the preshock magnetic field. Inside $r \leq r_{200}$ of simulated clusters, typically $\sim 30\%$ of identified shock zones are $Q_\parallel$ with $\theta_{\text{Bn}} \leq 45°$, while the rest are $Q_\perp$ with $\theta_B > 45°$ [121].

Because the statistics of ICM shocks (see below) are insensitive on nongravitational effects such as radiative process [4], so such effects are not taken into account our simulations as argued in Section II. Although the CRp production in the core of galaxy clusters might affect nongravitational effects, we
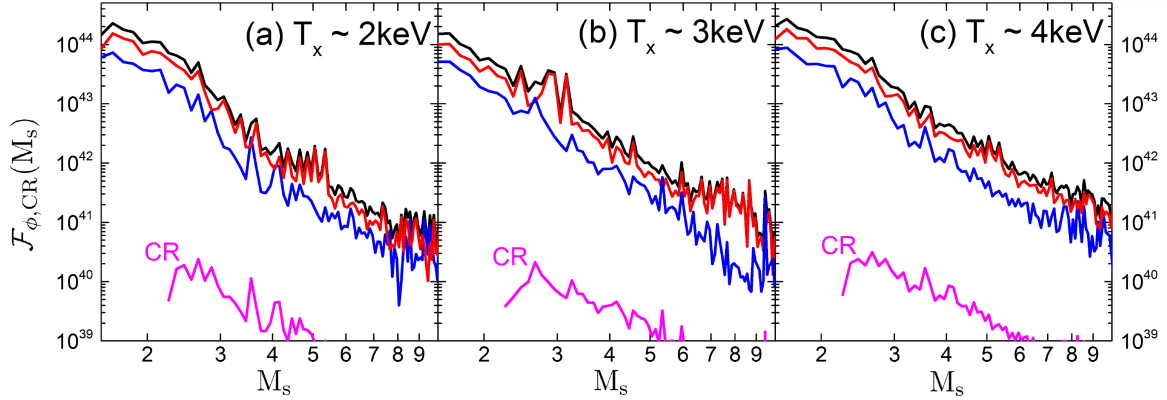
Figure 16: Kinetic energy flux, $\mathscr{F}_\phi$, and energy flux dissipated to CRp production, $\mathscr{F}_{CR}$, in units of erg s^{-1}(h^{-1}Mpc)$^{-3}$, as a function of M_s, processed through shock surfaces inside the sphere of r_{200} of sample clusters with the X-ray emission-weighted temperature (a) $T_X \sim 2$ keV, (b) $T_X \sim 3$ keV and (c) $T_X \sim 4$ keV. Each panel shows the fluxes averaged over 4 clusters with similar T_X, denoted with the filled squares in Figure 15. The black, red and blue solid lines show $\mathscr{F}_\phi$ through all the shocks, $Q_\perp$-shocks and $Q_\parallel$-shocks, respectively. In addition, $\mathscr{F}_{CR}$ produced by supercritical $Q_\parallel$-shocks is plotted as the magenta lines.

expect such CRp production gives only minor contribution because shocks in the core region of clusters are very weak and CR acceleration could be very inefficient [83].

CRp Production via Fresh-Injection DSA

To estimate the CRp produced via DSA, followed by *in insu* injection at shock zones from the background thermal plasma, we adopt the analytic model presented in Paper I. The main ideas of this model can be summarized as follows. (1) The proton injection and DSA are effective only at supercritical $Q_\parallel$-shocks with $M_s \gtrsim 2.25$. (2) At weak $Q_\parallel$-shocks with $M_s \lesssim 5$, the postshock CR distribution, $f_{CR}(p)$, follows the test-particle DSA power-law with the slope, $q = 3\chi/(\chi - 1)$, determined by the shock compression ratio, χ. (3) The transition from the postshock Maxwellian to the CRp power-law distribution occurs at the so-called injection momentum, p_{inj}. The amplitude of $f_{CR}(p)$ at p_{inj} is anchored at the thermal Maxwellian distribution. (4) As a fraction of the shock energy is transferred to CRp, the energy density of postshock thermal protons and hence the postshock temperature T_2 decrease self-consistently. At the same time, the normalization of $f_{CR}(p)$ reduces. The weakening of the subshock due to the dynamical feedback of the CR pressure to the shock structure and the resulting reduction of $f_{CR}(p)$ have been observed in numerical simulations [26, 83, 122]. (5) In the model, the CR energy density is kept to be less than 10 % of the shock kinetic energy density for shocks with $M_s \lesssim 5$, consistent with the test-particle treatment.

The analytic DSA model gives the momentum spectrum of CRp at shock zones as

$$f_{CR}(p) \approx n_2\, \pi^{-1.5}\, p_{th,p}^{-3} \exp(-Q_i^2) \left(\frac{p}{p_{inj}}\right)^{-q} \quad \text{for } p \geq p_{inj}, \tag{21}$$

for $Q_\parallel$-shocks with $M_s \geq 2.25$. Here, n_2 and $p_{\mathrm{th,p}} \equiv \sqrt{2m_p k_B T_2}$ are the postshock number density and momentum of thermal protons, respectively, and m_p is the proton mass, and k_B is the Boltzmann constant. The injection momentum, p_{inj}, is expressed in terms of the injection parameter, Q_i, as

$$p_{\mathrm{inj}} = Q_i \cdot p_{\mathrm{th,p}}. \tag{22}$$

In the model, $Q_i = Q_{i,0}/\sqrt{R_T}$ with a fixed initial $Q_{i,0}$ increases gradually, but approaches to an asymptotic value as the CR energy density increases. Considering the results from the hybrid simulations of [26] and [28] and the extended PIC simulation presented in Paper I, $Q_{i,0} \approx 3.3 - 3.5$ is suggested. R_T is the reduction factor of the postshock temperature, which depends on both M_s and $Q_{i,0}$. Here, we present the production of CRp with $Q_{i,0} = 3.5$, along with R_T from Figure 4 of Paper I (see below for discussions on the dependence on $Q_{i,0}$).

Then, the postshock energy density of CRp can be evaluated as

$$E_{\mathrm{CR}} = c \int_{p_{\min}}^{\infty} (\sqrt{p^2 + (m_p c)^2} - m_p c) f_{\mathrm{CR}}(p) \, 4\pi p^2 dp, \tag{23}$$

where c is the speed of light. For the lower bound of the integral, $p_{\min} = 0.78 \ \mathrm{GeV}/c$ is used, which is the threshold energy of π-production reaction. Note that $p_{\min}$ is much larger than p_{inj} of typical ICM shocks. For the shock with $M_s \sim 3$ propagating in the medium with $T \sim 10^8$ K, for instance, the injection momentum is roughly $p_{\mathrm{inj}} \sim 2.5 \times 10^{-2} \mathrm{GeV}/c$, so p_{inj} is more than an order of magnitude smaller than $p_{\min}$. The postshock CRp energy flux is given as $F_{\mathrm{CR}} = E_{\mathrm{CR}} u_2$.

With the shock kinetic energy flux, $F_\phi = (1/2)\rho_1 u_s^3$, the DSA efficiency, $\eta(M_s) \equiv F_{\mathrm{CR}}(M_s)/F_\phi(M_s)$ (see the introduction), is given. The analytic DSA model of Paper I, adopted in this paper, suggests $\eta(M_s) \approx 10^{-3} - 10^{-2}$ for $Q_\parallel$-shocks with $M_s = 2.25 - 5.0$. Here, F_{CR} at ICM shocks is estimated using Equations (21) and (23), rather than as $\eta(M_s)F_\phi$. However, for shocks with $M_s > 5$, which are beyond the Mach number range of the analytic DSA model (see Figure 4 of [104]), R_T is adjusted, so that $F_{\mathrm{CR}}(M_s)/F_\phi(M_s)$ is limited to 0.01. We note that the contribution from shocks with $M_s > 5$ in the ICM is rather insignificant (see Figure 16).

A few comments are in order. (1) In the case of weak shocks with low M_s, where the CRp spectrum is dominated by low-energy particles, the estimated F_{CR} depends rather sensitively on $p_{\min}$, although the π-production rate does not once $p_{\min} \leq 0.78 \ \mathrm{GeV}/c$. (2) If $Q_{i,0} = 3.3$, instead of $Q_{i,0} = 3.5$, is adopted, F_{CR} would be ~ 2 times larger. (3) As mentioned in the introduction, [76] suggested $\eta(M_s) \sim 0.1$ for $M_s \simeq 5$, while [26] presented $\eta \approx 0.036$ for $M_s \approx 6.3$. The analytic DSA model, adopted in this paper, assumes $\eta(M_s)$ and hence F_{CR}, which are about several to ten times smaller than those of [76] and [26].

To quantify the CRp production at ICM shocks, we evaluate the energy flux processed through shocks inside sample clusters, as a function of the shock Mach number, as

$$\mathscr{F}_A(M_s) \, d\log M_s = \frac{1}{V_{<r_{200}}} \sum s_{\mathrm{sh}} F_A(M_s), \tag{24}$$

where $A = \phi$ and $A = \mathrm{CR}$ are used to denote the shock kinetic energy flux and the CRp energy flux, respectively. The summation goes over the shock zones with the Mach number between $\log M_s$ and
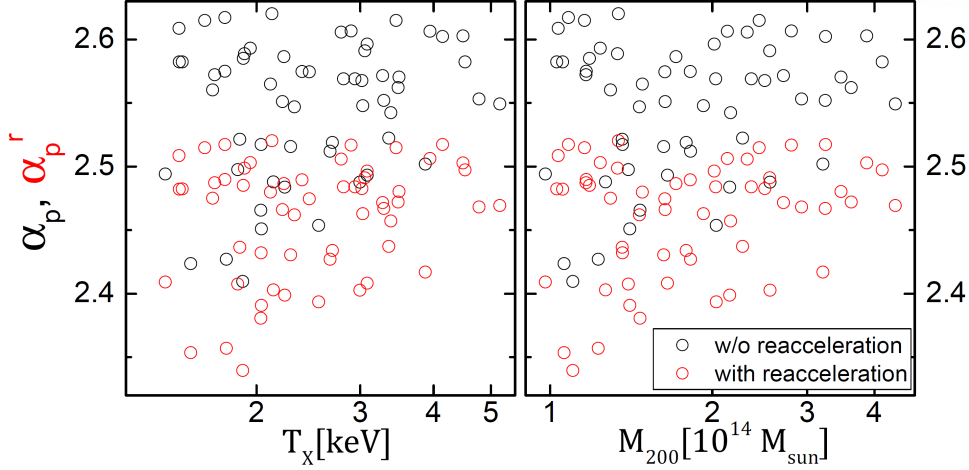
Figure 17: Slope of the volume-integrated CRp momentum spectrum, produced by all supercritical $Q_\parallel$-shocks inside the sphere of r_{200}, as a function of the X-ray emission-weighted temperature (left panel) and the total mass (right panel), for all 58 sample clusters. The black and red open circles draw the slopes without (α_p) and with (α_p^r) reacceleration process, respectively.

$\log M_s + d \log M_s$ inside r_{200}, $V_{<r_{200}} = (4\pi/3)r_{200}^3$, and s_{sh} is the area of each shock zone. Figure 16 shows $\mathscr{F}_\phi$ and $\mathscr{F}_{CR}$ at the present epoch ($z = 0$) for clusters with the X-ray emission-weighted temperature close to $T_X \sim 2$ keV, ~ 3 keV, and ~ 4 keV. Weaker shocks dissipate a larger amount of shock kinetic energy, as pointed in previous works [2,7]. Specifically, $\sim 97\%$ of $\mathscr{F}_\phi$ is processed through shocks with $M_s \lesssim 5$, and the fraction is not sensitive to cluster properties, such as T_X. We find that for all sample clusters, $\sim 30\%$ of $\mathscr{F}_\phi$ is processed through $Q_\parallel$-shocks (blue lines) and the rest through $Q_\perp$-shocks (red lines); the partitioning is about the same as that of the frequency of $Q_\parallel$ and $Q_\perp$-shocks. Moreover, $\sim 23\%$ of $\mathscr{F}_\phi$ associated with all $Q_\parallel$-shocks goes through supercritical shocks with $M_s \geq 2.25$. As a result, only $\sim 7\%$, or $\sim 6-8\%$ including the range for different clusters, of the shock kinetic energy is dissipated through supercritical $Q_\parallel$-shocks that are expected to accelerate CRp.

Figure 16 demonstrates that $\mathscr{F}_{CR}$ (magenta lines), produced by supercritical $Q_\parallel$-shocks, is several orders of magnitude smaller than $\mathscr{F}_\phi$. We find that for all sample clusters, the total $\mathscr{F}_{CR}$, integrated over M_s, is $\sim (1-2) \times 10^{-4}$ of the total $\mathscr{F}_\phi$. This can be understood as the average value of $\eta(M_s) \times \mathscr{F}_\phi(M_s)$, convoluted with the population of supercritical $Q_\parallel$-shocks. It means that the fraction of the shock kinetic energy transferred to CRp is estimated to be $\sim (1-2) \times 10^{-4}$, based on the analytic DSA model adopted in this paper. If $Q_{i,0} = 3.3$ is used (the results are not shown), $\mathscr{F}_{CR}$, and hence the amount of CRp produced, would be ~ 2 times larger.

The number of CRp in the momentum bin between p and $p + dp$, produced by ICM shocks, can be evaluated as follow:

$$\frac{d\mathscr{N}_{CR}(p)}{dt} dp = \sum_{Q_\parallel, M_s \geq 2.25} 4\pi s_{sh} u_2 f_{CR}(p) \, p^2 dp, \tag{25}$$

where the summation includes the entire population of supercritical $Q_\parallel$-shocks with $M_s \geq 2.25$ inside r_{200}. Note that $d\mathscr{N}_{CR}(p)/dt$ is defined in a way that $\int d\mathscr{N}_{CR}(p)/dtdp$ is the total rate of CRp production in the ICM. We fit it to a power-law, i.e., $d\mathscr{N}_{CR}(p)/dt \propto p^{-\alpha_p}$, with the volume-averaged slope α_p.

44

Figure 17 show the values of α_p, calculated for all 58 simulated galaxy clusters at $z = 0$ (black open circles). The slope spreads over a range of $\alpha_p \sim 2.4 - 2.6$, indicating that the average Mach number of the shocks of most efficient CRp production is in the range of $M_s \sim 2.8 - 3.3$, which is consistent with the Mach number range of large $\mathscr{F}_{\mathrm{CR}}$, $M_s \sim 2.5 - 3.5$, in Figure 16. We point that the slope in Figure 17 is a bit larger than the values presented in [8] (see their Figure 10, where $\bar{q} = \alpha_p + 2$). The difference can be understood with the difference in $\eta(M_s)$; $\eta(M_s = 5)/\eta(M_s = 2.25)$ is, for instance, ~ 10 in the analytic model adopted in this paper, while it is ~ 100 in the DSA efficiency model used in [8]. Hence, shocks with higher M_s are counted with larger weights for the calculation of α_p in [8].

CRp Distribution in Sample Clusters

Inside clusters, the CRp produced by ICM shocks are expected to be accumulated over the cosmological timescale, owing to their long lifetimes, as mentioned in the introduction. Although streaming and diffusion could be important for the transport of highest energy CRp, most of lower energy CRp should be advected along with the background plasma and magnetic fields [123–125]. Hence, the CRp distribution would be relaxed over the cluster volume via turbulent mixing on the typical dynamical timescale of the order of $\sim$ Gyr. Then, the total number of CRp in the momentum bin between p and $p + dp$ accumulated inside clusters can be evaluated as

$$\mathscr{N}_{\mathrm{CR}}(p) = \int \frac{d\mathscr{N}_{\mathrm{CR}}(p)}{dt} dt. \tag{26}$$

In our LSS formation simulations, we did not follow self-consistently in run-time the production of CRp at ICM shocks and their transport behind shocks. Instead, we identify shocks and calculate $f_{\mathrm{CR}}(p)$ at shock zones in the post-processing step. We here attempt to approximate the above integral as

$$\mathscr{N}_{\mathrm{CR}}(p) \approx \tau_{\mathrm{acc}} \frac{d\mathscr{N}_{\mathrm{CR}}(p)}{dt}, \tag{27}$$

with $d\mathscr{N}_{\mathrm{CR}}(p)/dt$ estimated at $z = 0$. Here, τ_{acc} is the mean acceleration time scale. Note that the estimation of $d\mathscr{N}_{\mathrm{CR}}(p)/dt$ at earlier epochs for a specific cluster found at $z = 0$ is not feasible in postprocessing, since the cluster has gone through a hierarchical formation history involving multiple mergers. Hence, in [2], [5], and [7], for instance, the shock population and the shock kinetic energy flux, $\mathscr{F}_\phi$, at different epochs were estimated, over the entire computational volume of LSS formation simulations, rather than inside the volume of a specific cluster. The Mach number distribution of $\mathscr{F}_\phi$ was presented in those studies; $\mathscr{F}_\phi(M)$ shows only a slow evolution from $z = 1$ to 0, whereas it is somewhat smaller at higher redshifts. By considering the time evolution of the shock population and the shock energy dissipation in LSS formation simulations, we use $\tau_{\mathrm{acc}} \sim 5$ Gyr for all sample clusters. This approximation should give reasonable estimates within a factor of two or so.

Previous studies, in which the generation and transport of CRp were followed in run-time in LSS formation simulations, on the other hand, showed that CRp are produced preferentially in the cluster outskirts and then mixed, leading to the radial profile of the CR pressure, $P_{\mathrm{CR}}(r)$, which is broader than that of the gas pressure, $P_{\mathrm{gas}}(r)$ [31, 126, 127]. This is partly because the shocks that can produce CRp

($M_s \gtrsim$ a few) are found mostly in the outskirts [8, 33], and also because the DSA efficiency is expected to increase with M_s in the DSA theory [76, 104]. Hence, we here employ an illustrative model for the radial profile of the CRp density that scales with the shell-averaged number density of gas particles as $n_{CR}(r, p) \propto \bar{n}_{gas}(r)^\delta$. We take $\delta = 0.5 - 1$, which covers most of the range suggested in the previous simulation studies cited above and observations [128]. Considering that the ICM is roughly isothermal, $\delta < 1$ results in the radial profile of P_{CR} broader than that of P_{gas}. For a smaller value of δ, n_{CR} is less centrally concentrated, so the rate of inelastic CRp-p collisions occurring in the inner part of the cluster volume with high n_{gas} is lower.

Energization of CRp through Reacceleration

The ICM plasma passes through ICM shocks more than once. In the medium with temperature, $T \sim 5 \times 10^7$ K, for instance, the sound speed is ~ 1000 km/s and the average velocity of $M_s = 2$ shock inside the sample cluster is roughly $\langle u_s \rangle \sim 2000$ km/s. During τ_{acc}, the shock swept up the volume, $\sim \tau_{acc} \times \langle u_s \rangle \sim 10$ Mpc, while the average diameter of the sample clusters are ~ 3.2 Mpc. Therefore, shocks inside clusters typically swept ~ 3.1 times during τ_{acc}. To estimate the number of shock passages during τ_{acc} more rigorously, we estimate the amount of volume swept through shocks within the virial radius during τ_{acc} as

$$N_{passage} = \frac{\tau_{acc}}{V_{<r_{200}}} \sum s_{sh} u_s. \tag{28}$$

Here, the summation goes over all the identified shock zones inside r_{200}. For all 58 sample clusters, $N_{passage}$ is in the range of $\sim 3 - 4$ and the averaged value is $\langle N_{passage} \rangle \approx 3.2$. Hence, the CRp produced via fresh-injection DSA during the first shock passage could be further energized by reacceleration, on average at two subsequent shock passages.

Here, we attempt to estimate the energization of CRp through reacceleration in the post-processing step, adopting the following "simplified model". It involves a number of assumptions, including the test-particle treatment for reacceleration, as follows. (1) The ICM plasma passes through ICM shocks "three times". The three shock passages occur in sequence during each period of $\tau_{acc}/3$, and hence the CRp production is a three-stage procedure. In the first stage, only fresh-injection DSA occurs. In the second and third stages, along with fresh-injection DSA, a fraction of the preexisting CRp, produced in the previous stages, is reaccelerated. (2) Reacceleration operates only at supercritical $Q_\parallel$-shocks with $M_s \geq 2.25$, as in the case of fresh-injection DSA. Even in the presence of preshock CRp, the reflection of protons at the shock front and the ensuing generation of upstream waves due to streaming protons is likely to be ineffective at subcritical shocks and $Q_\perp$-shocks. (See below for a discussion on the consequence of relaxing this assumption.) (3) If the preexisting CRp, upstream of shock, has a power-law spectrum, $f_{pre}(p) = f_0 \left(p/p_{inj}\right)^{-s}$, the reaccelerated, downstream spectrum is given as

$$f_{reacc}^{(1)}(p) = \begin{cases} [q/(q-s)] \left[1 - (p/p_{inj})^{-q+s}\right] f_{pre}(p), & \text{if } q \neq s, \\ q \ln(p/p_{inj}) f_{pre}(p), & \text{if } q = s, \end{cases}$$

$$\tag{29}$$

where $q = 3\chi/(\chi - 1)$ with the shock compression ratio, χ, is the test-particle power-law slope [129]. If the momentum spectrum of the preexisting CRp for the subsequent shock passage is taken as $f_{\mathrm{reacc}}^{(1)}$ in Equation (29), then, after the second reacceleration episode, the downstream spectrum has the following analytic form:

$$
f_{\mathrm{reacc}}^{(2)}(p) = \begin{cases} \{q^2/(q-s)^2 - [q^2/(q-s)\ln(p/p_{\mathrm{inj}}) \\ \quad - q^2/(q-s)^2](p/p_{\mathrm{inj}})^{-q+s}\}f_{\mathrm{pre}}(p), & \text{if } q \neq s, \\ q^2/2\,[\ln(p/p_{\mathrm{inj}})]^2 f_{\mathrm{pre}}(p), & \text{if } q = s. \end{cases}
$$

where q is again the test-particle power-law slope [22, 129]. In the case that $f_{\mathrm{pre}}(p)$ has a simple form, $f_{\mathrm{reacc}}(p)$ can be written down analytically. (4) During each acceleration stage, CRp are advected and spread over $V_{<r_{200}}$, and the radial profile of the CRp density is described as $n_{\mathrm{CR}}(r) \propto \bar{n}_{\mathrm{gas}}(r)^\delta$.

In the model, after the first stage, the CRp, produced solely via fresh-injection DSA and accumulated inside clusters, has the volume-integrated momentum distribution

$$
\mathcal{N}_{\mathrm{CR}}^{\mathrm{1st}}(p) \approx \frac{\tau_{\mathrm{acc}}}{3} \frac{d\mathcal{N}_{\mathrm{CR}}(p)}{dt}, \tag{30}
$$

where $d\mathcal{N}_{\mathrm{CR}}(p)/dt$ is the CRp production rate in Equation (25).

After the second stage, the volume-integrated CRp momentum distribution is given as

$$
\mathcal{N}_{\mathrm{CR}}^{\mathrm{2nd}}(p) \approx \left(\frac{2}{3} - \frac{\varphi}{3}\right) \tau_{\mathrm{acc}} \frac{d\mathcal{N}_{\mathrm{CR}}(p)}{dt} + \frac{\varphi}{3} \tau_{\mathrm{acc}} \frac{d\mathcal{N}_{\mathrm{reacc}}^{(1)}(p)}{dt}. \tag{31}
$$

Here, φ is the fraction of preexisting CRp that passes through supercritical $Q_\parallel$-shocks and hence is reaccelerated. It may be inferred as

$$
\varphi \approx \sum_{Q_\parallel,\, M_s \geq 2.25} s_{\mathrm{sh}}\rho_1 u_s \Big/ \sum s_{\mathrm{sh}}\rho_1 u_s, \tag{32}
$$

which is estimated to be $\varphi \sim 6 - 8\%$ for sample clusters. Note that φ is almost identical to the fraction of the shock kinetic energy dissipated at supercritical $Q_\parallel$-shocks. $d\mathcal{N}_{\mathrm{reacc}}^{(1)}(p)/dt$ incorporates the reacceleration of CRp, and is estimated as follows. Assuming that the preexisting CRp produced in the first stage have a power-law momentum distribution, $f_{\mathrm{pre}}(p) \propto (p/p_{\mathrm{inj}})^{-s}$, and the radial density profile of $\propto \bar{n}_{\mathrm{gas}}(r)^\delta$, $f_{\mathrm{reacc}}^{(1)}(p)$ in Equation (29) is calculated at each supercritical $Q_\parallel$-shock zone; then all the contributions of reacceleration from shocks inside r_{200} are added.

After the third, final stage, the volume-integrated CRp momentum distribution is given as

$$
\mathcal{N}_{\mathrm{CR}}^{\mathrm{3rd}}(p) \approx \left(1 - \varphi + \frac{\varphi^2}{3}\right) \tau_{\mathrm{acc}} \frac{d\mathcal{N}_{\mathrm{CR}}(p)}{dt} + \left(\varphi - \frac{2\varphi^2}{3}\right) \frac{d\mathcal{N}_{\mathrm{reacc}}^{(1)}(p)}{dt} + \frac{\varphi^2}{3} \tau_{\mathrm{acc}} \frac{d\mathcal{N}_{\mathrm{reacc}}^{(2)}(p)}{dt}. \tag{33}
$$

Here, $d\mathcal{N}_{\mathrm{reacc}}^{(2)}(p)/dt$ represents the CRp that undergo the reacceleration twice. Similarly to $d\mathcal{N}_{\mathrm{reacc}}^{(1)}/dt$, $d\mathcal{N}_{\mathrm{reacc}}^{(2)}/dt$ is evaluated with $f_{\mathrm{reacc}}^{(2)}(p)$ in Equation (30).

In Figure 18, the volume-integrated momentum distributions without (Equation (27)) and with (Equation (33)) the energization of reacceleration are compared for three simulated clusters at $z = 0$; $\delta = 0.75$ is used in the calculation of reacceleration contribution. Reacceleration conserves the number
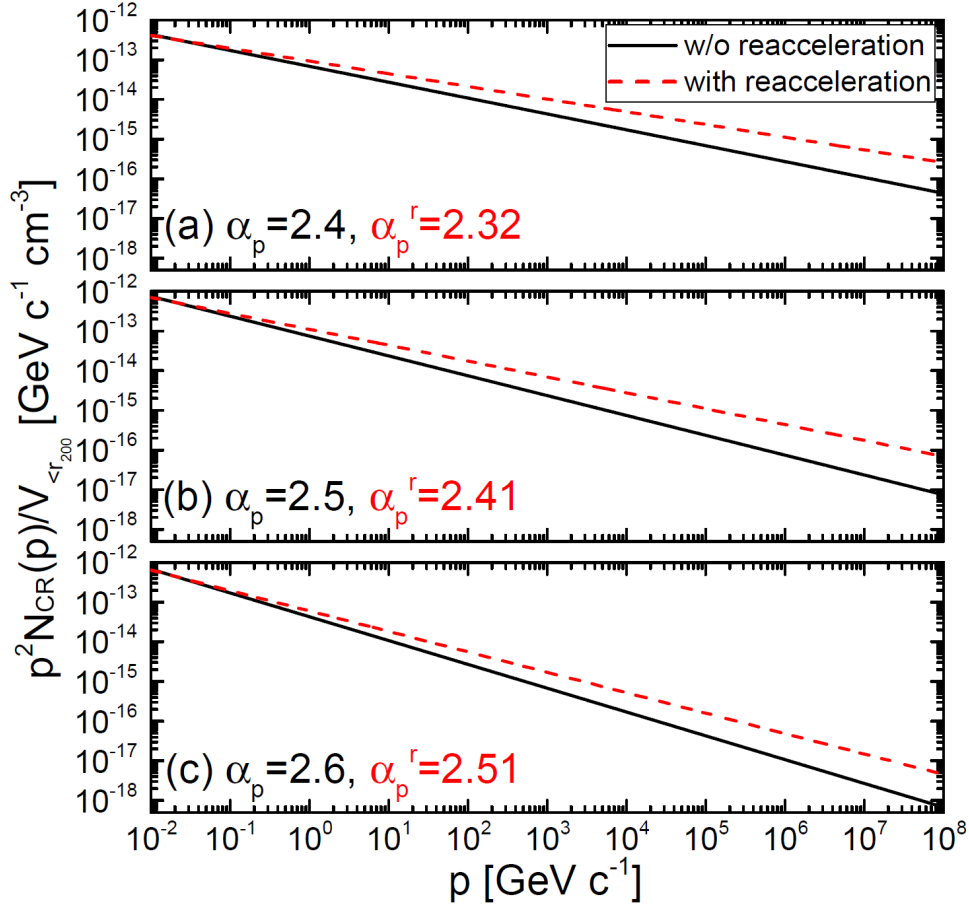
Figure 18: Volume-integrated CRp momentum spectrum, $\mathcal{N}_{CR}(p)$, produced by all supercritical $Q_\parallel$-shocks inside the sphere of r_{200}, without (black solid lines) and with (red dashed lines) the reacceleration process, for three simulated clusters. Here, $\delta = 0.75$ is adopted in the calculation of reacceleration. The volume-averaged slopes without and with reacceleration, α_p and α_p^r, are given in all three panels.
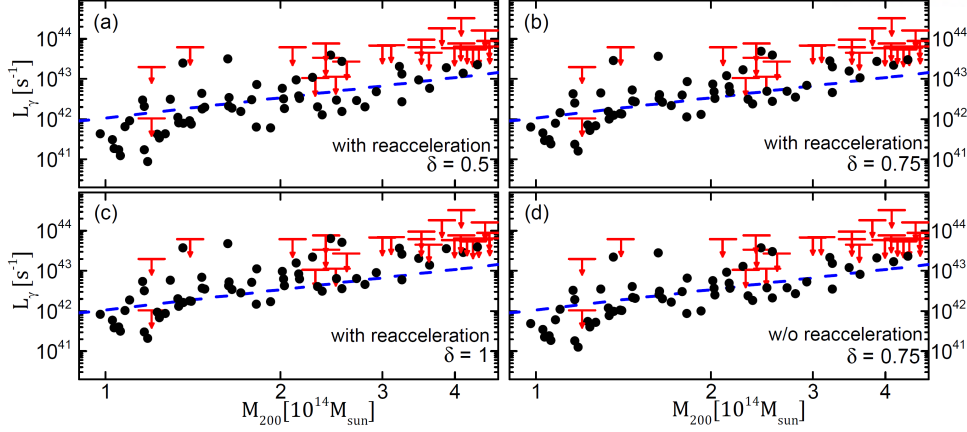
Figure 19: The amount of γ-ray photons produced per second in the energy band of [0.5, 200] GeV, L_γ, as a function of the total cluster mass, for all 58 sample clusters (black circles). The red symbols are the upper limits suggested by Fermi LAT for observed clusters. The blue dashed lines represent the mass-luminosity relation, $L_\gamma \propto M_{200}^{5/3}$, assuming virial equilibrium and a constant CRp-to-gas energy ratio. The panels (a) - (c) show L_γ estimated from the CRp production model with reacceleration process; the three panels are for the different spatial distribution models of CRp with different δ. Note that smaller δ indicates flatter spatial distribution). L_γ values from the CRp production model without reacceleration for $\delta = 0.75$ is displayed in the panel (d), for comparison.

of CRp, and hence, the total number of CRp, $\int \mathcal{N}_{CR}(p)dp$, remains the same. On the other hand, it makes the momentum spectrum harder, that is, $\mathcal{N}_{CR}(p)$ becomes flatter, as shown in Figure 18. For all sample clusters, $\mathcal{N}_{CR}(p)$ in Equation (33) including the energization of reacceleration is again fitted to a power-law form with the slope, α_p^r. In Figure 17, the estimated values of α_p^r are compared to those without reacceleration, α_p; $\alpha_p^r \sim 2.35 - 2.5$, while $\alpha_p \sim 2.4 - 2.6$, that is, the momentum spectrum flattens by $\sim 0.05 - 0.1$ due to reacceleration.

A flatter spectrum means a larger number of high energy CRp, and hence, the total energy contained in the CRp component (see Equation (23)) should be larger. We find that the total CRp energy increases due to reacceleration by $\sim 40 - 80\%$ with a mean value of $\sim 60\%$ when averaged for all clusters, if $\delta = 0.75$ is assumed; the averaged increment is $\sim 75\%$ and $\sim 50\%$ for $\delta = 0.5$ and 1, respectively. This number can be understood as follows. In Equation (33), the major contribution of reacceleration is included in the $\varphi d\mathcal{N}_{reacc}^{(1)}(p)/dt$ term. The boost of the CRp energy with Equation (29) is, for instance, $\lesssim 10$ for shocks with $M_s \sim 3$ [129], while $\varphi \sim 6 - 8\%$.

For completeness, a few additional numbers are given here. If reacceleration operates at all (both supercritical and subcritical) $Q_\parallel$-shocks, the total CRp energy contained in sample clusters increases by $\sim 90\%$ on average (when $\delta = 0.75$ is assumed). If reacceleration were to operate at all shocks, that is, both $Q_\parallel$ and $Q_\perp$-shocks, then the CRp energy would be increased by several times, which is probably too large to be compatible with the Fermi upper limits.

Below, for the estimations of γ-ray and neutrino emissions, we use the CRp expressed as

$$n_{\rm CR}(r,p)\,dp \approx n_{\rm CR0}\left[\frac{\bar{n}_{\rm gas}(r)}{n_{\rm gas}(0)}\right]^{\delta}\left(\frac{p}{{\rm GeV}/c}\right)^{-\alpha_p^r}\frac{dp}{{\rm GeV}/c}, \tag{34}$$

where $n_{\rm gas}(0)$ is the gas particle number density at the cluster center. The normalization factor, $n_{\rm CR0}$, is fixed by the condition

$$\int_{<r_{200}}\int n_{\rm CR}(r,p)\,dp\,dV = \int \mathcal{N}_{\rm CR}(p)\,dp, \tag{35}$$

where the volume integral is over the sphere inside r_{200}.

4.2 Gamma-Rays and Neutrinos from Simulated Clusters

In this section, we calculate γ-ray and neutrino emissions from simulated clusters, using $n_{\rm CR}(r,p)$ in Equation (34), which includes the energization due to reacceleration. To speculate the consequence of reacceleration, we first compare the numbers of CRp with and without reacceleration, in the three momentum ranges: (1) $p_{\rm inj} < p < p_{\rm min}$, (2) $p_{\rm min} < p < 10^3$ GeV/c ($p_{\rm min} = 0.78$ GeV/c) where most of the γ-rays observed by Fermi-LAT in the energy band of [0.5, 200] GeV are produced, and (3) $10^6 < p < 10^8$ GeV/c where most of the high-energy neutrinos detected by IceCube are produced (see below). Because the reacceleration process makes the CRp spectrum more flatter, so the number of CRp in $p_{\rm inj} < p < p_{\rm min}$ is increased when the reacceleration process is considered. In the higher momentum range, however, the flatter spectral slope due to the reacceleration is the main factor for increasing the CRp number fraction. The number of CRp is increased by $\sim 1.3 - 2.5$ times in $p_{\rm min} < p < 10^3$ GeV/c and that is increased by $\sim 4.1 - 6.8$ times in $10^6 < p < 10^8$ GeV/c. This indicates that the CRp number fraction in the higher momentum range depends more sensitively on the presence of reacceleration. In this context, reacceleration would have a limited consequence on the γ-rays observation with Fermi-LAT (see the results and relevant text of Figure 19). On the other hand, it substantially boosts high-energy neutrinos from clusters.

Gamma-Ray Emissions

The number density of γ-ray photons in the unit of GeV$^{-1}s^{-1}cm^{-3}$ as a function of the distance from the cluster center, r and the γ-ray energy, E_γ is estimated by employing the formula proposed in [107];

$$q_\gamma(r,E_\gamma)dE_\gamma dV \approx c\sigma_{\rm pp}\bar{n}_{\rm gas}(r)\tilde{n}_{\rm CR}(r)\frac{2^{4-\alpha_\gamma}}{3\alpha_\gamma}$$

$$\times\left(\frac{{\rm GeV}}{m_{\pi^0}c^2}\right)^{\alpha_\gamma}\left[\left(\frac{2E_\gamma}{m_{\pi^0}c^2}\right)^{\delta_\gamma}+\left(\frac{m_{\pi^0}c^2}{2E_\gamma}\right)^{\delta_\gamma}\right]^{-\frac{\alpha_\gamma}{\delta_\gamma}}$$

$$\times\frac{dE_\gamma}{{\rm GeV}}dV, \tag{36}$$

where $\alpha_\gamma = 4/3(\alpha_p^r - 1/2)$ is the slope of γ-ray spectrum, $\delta_\gamma = 0.14\alpha_\gamma^{-1.6} + 0.44$ is the shape parameter, $\sigma_{\rm pp} = 32\times(0.96 + e^{4.4-2.4\alpha_\gamma})$ mbarn is the effective cross-section of inelastic CRp-p collision, and m_{π^0} is the pion mass. In our model, $\tilde{n}_{\rm CR}(r) = n_{\rm CR0}[\bar{n}_{\rm gas}(r)/n_{\rm gas}(0)]^{\delta}$ is the shell-averaged number density

of CRp. Then, the number of γ-ray photons emitted per second per GeV from a cluster, dL_γ/dE_γ is calculated by integrating $q_\gamma(r, E_\gamma)$ over the cluster volume.

Using $\bar{n}_{\text{gas}}(r)$ and α_p^r calculated for simulated clusters with $\delta = 0.5, 0.75$, and 1, we estimate L_γ of 58 sample clusters. We integrate dL_γ/dE_γ in the energy band of $[E1, E2] = [0.5, 200]$ GeV to compare the estimates with the Fermi-LAT upper limits presented in [108]. Figure 5 shows the estimates for L_γ as a function of the cluster mass M_{200}, along with the Fermi-LAT upper limits. A few points are noted. (1) Because clusters with similar masses may undergo different dynamical evolutions, they could experience different shock formation histories and have different CRp productions. Hence, the $L_\gamma - M_{200}$ relation exhibits significant scatters. (2) Assuming virial equilibrium and a constant CRp-to-gas energy ratio, the mass-luminosity scaling relation, $L_\gamma \propto M_{200}^{5/3}$, is predicted [31, 84, 111]. Although there are substantial scatters, L_γ's for our sample clusters seem to roughly follow the predicted scaling relation. (3) Different CRp spatial distributions with different δ give different estimates for L_γ within a factor of two (see the panels (a), (b), and (c)). Being the most centrally concentrated, the model with $\delta = 1$ produces the largest amount of γ-ray emissions. (4) The panels (b) and (d) compare L_γ's from the CRp with and without reacceleration boost ($\delta = 0.75$). As speculated above, the difference in L_γ's is small, indicating that estimated L_γ is not sensitive to whether the reacceleration of CRp at ICM shocks is included or not.

All the models shown in Figure 19, including the one with reacceleration for $\delta = 1$, result in L_γ's that are mostly below the Fermi-LAT upper limits. Hence, although there are uncertainties in our estimation for the production of CRp at ICM shocks, we conclude that the DSA model proposed in Paper I is consistent with the Fermi-LAT upper limits.

We attempt to compare our results with the predictions made by [31], in particular, the one for their CS14 model of the DSA efficiency, $\eta_{\text{CS}14}(M_s)$, which adopted the efficiency based on the hybrid simulations of [26] for high M_s along with the fitting form of [76] for the M_s dependence in low M_s. For instance, the red triangles (labeled as CS14) in Figure 7 of [31] shows $L_\gamma \approx 2 - 4 \times 10^{43}$ photons s^{-1} for simulated clusters with $M_{200} \approx 2 - 3 \times 10^{14} M_\odot$, while our estimates for the model with $\delta = 0.75$ vary as $L_\gamma \approx 0.5 - 2 \times 10^{43}$ photons s^{-1} for the same mass range. The ICM shock population and energy dissipation should be similar in the two works [2, 7]; also the fraction of $Q_\parallel$-shocks is $\sim 30\%$ in both works. One of differences in the two modelings is that for subcritical $Q_\parallel$-shocks with $M_s < 2.25$, we assume no production of CRp at all, while $\eta_{\text{CS}14}(M_s)$ is not zero. However, this may not lead to a significant difference in the CRp production, since $\eta_{\text{CS}14}(M_s)$ sharply decreases with decreasing M_s in the regime of $M_s \lesssim 3$. On the other hand, with the DSA model adopted here, $\eta(M_s) \approx 10^{-3} - 10^{-2}$ for $M_s = 2.25 - 5$, which is lower by up to a factor of three to four times than $\eta_{\text{CS}14}(M_s)$, explaining the difference in the predicted L_γ in the two studies. To comfirm this argument, we estimated the amount of γ-ray photons produced by the CRp production through all $Q_\parallel$-shocks and have confirmed that the γ-ray production by the subcritical $Q_\parallel$-shocks with $M_s \lesssim 2.25$ increases the total γ-ray flux within a factor of two.

While we focus on the GeV-range γ-ray emission, our results could be extended to explain non-detection of γ-ray in the higher energy range such as TeV-range. Likewise Fermi-LAT, Veritas and HESS focusing on the TeV-range γ-ray have failed to detect diffuse cluster-wide γ-ray as well. For the case of
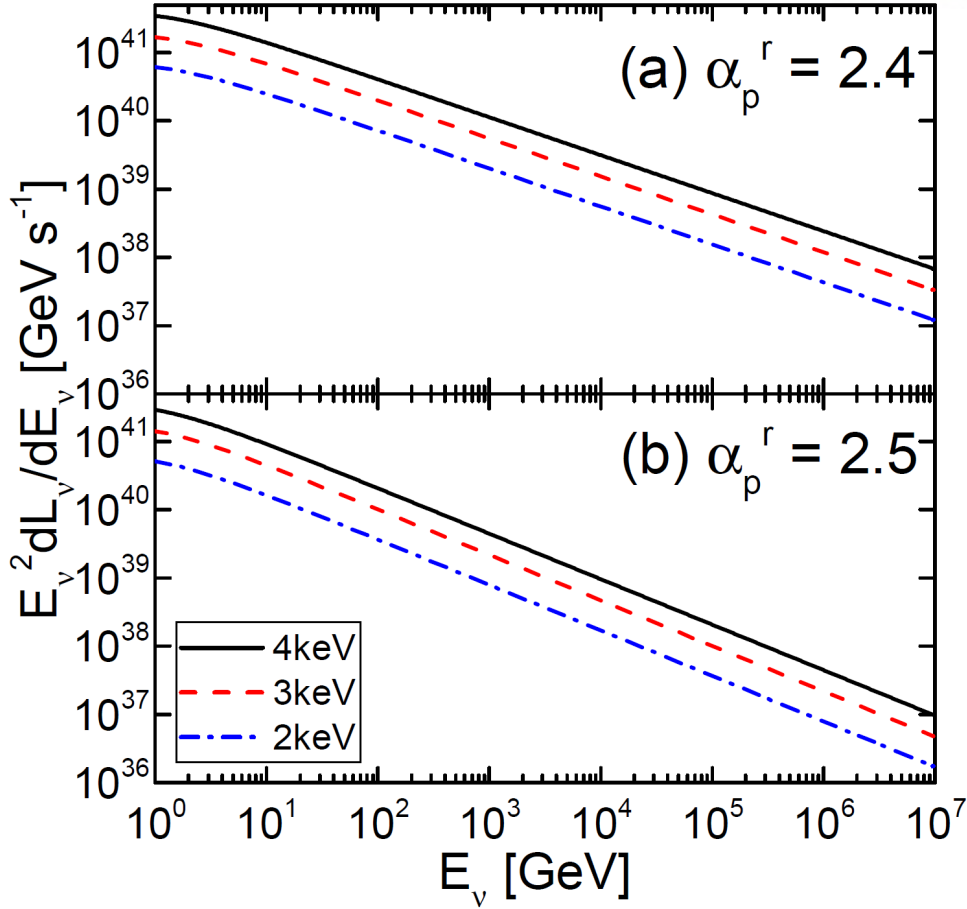
Figure 20: Neutrino energy spectra from the sample clusters of $T_X \sim 2\,\text{keV}$ (blue dashed dot lines), 3 keV (red dashed lines), and 4 keV (black solid lines). All the spectra shown here are obtained by averaging over 4 clusters with similar T_X. For the momentum distribution of CRp, $\alpha_p^r = 2.4$ and $\delta = 0.75$ are adopted in the upper panel, and $\alpha_p^r = 2.5$ and $\delta = 0.75$ in the lower panel, respectively.

shocks in supernova remnants, the shock-accelerated CRp spectrum may follow a broken power-law due to the nonlinear DSA process (see e.g., [130]) and such CRp spectrum enhances the TeV-range γ-ray emission. While the dynamical feedback and complex process due to the shock-produced CRp would be substantial in the very strong SNR shocks with $M_s \sim 100$ because of the efficient CRp acceleration (i.e., roughly $\sim 10\%$ of kinetic energy goes to CRp acceleration), CRp acceleration in ICM shocks is much inefficient and such nonlinear process due to the CRp feedback would be negligible. This aspect is also consistent with the test-particle assumption adopted in [104]. In this context, the cluster-wide γ-ray spectrum produced by weak ICM shocks is generally expected as a single power-law spectrum and our interpretation described through Figure 19 can be also applicable to explain non-detection of γ-ray in the higher energy range.

Neutrino Emissions

To calculate neutrino emissions from simulated clusters, we employ the analytic prescription described in [115]. Assuming that the pion source function as a function of pion energy E_π has a power-law form, $q_\pi(r, E_\pi) \propto E_\pi^{-\alpha_\gamma}$, the neutrino source function at the neutrino energy $E_\nu = E_\gamma$ is approximately related to the γ-ray source function as

$$q_\nu(r, E_\nu) = q_\gamma(r, E_\gamma)[Z_{\nu_\mu}(\alpha_\gamma) + Z_{\nu_e}(\alpha_\gamma)]. \tag{37}$$

Here,

$$
\begin{aligned}
Z_{\nu_\mu}(\alpha_\gamma) &= \frac{4[3 - 2k - k^{\alpha_\gamma}(3 - 2k + \alpha_\gamma - k\alpha_\gamma)]}{\alpha_\gamma(1-k)^2(\alpha_\gamma+2)(\alpha_\gamma+3)} \\
&+ (1-k)^{\alpha_\gamma-1}, \tag{38} \\
Z_{\nu_e}(\alpha_\gamma) &= \frac{24[(1-k)\alpha_\gamma - k(1 - k^{\alpha_\gamma})]}{\alpha_\gamma(1-k)^2(\alpha_\gamma+1)(\alpha_\gamma+2)(\alpha_\gamma+3)}, \tag{39}
\end{aligned}
$$

with $k = m_{\mu^\pm}^2/m_{\pi^\pm}^2 = 0.573$ account for the contributions of muon and electron neutrinos, respectively. Then, the energy spectrum of neutrons emitted per second from a cluster is estimated by

$$\frac{dL_\nu}{dE_\nu} = \int_{<r_{200}} q_\nu(r, E_\nu) \, dV. \tag{40}$$

Figure 20 plots $E_\nu^2 dL_\nu/dE_\nu$ as a function of E_ν for simulated clusters; the lines with different colors are for the sample clusters with T_X close to ~ 2 keV, ~ 3 keV, and ~ 4 keV, respectively. The upper and lower panels show the estimated spectra for the volume-averaged slope of CRp momentum distribution, $\alpha_p^r = 2.4$ and 2.5, respectively, which cover the range of α_p^r of simulated clusters (see Figure 3); for the spatial distribution of CRp, $\delta = 0.75$ is used. The spectrum has the energy dependence of $\propto E_\nu^{-2.53}$ for $\alpha_p^r \sim 2.4$ and $\propto E_\nu^{-2.67}$ for $\alpha_p^r \sim 2.5$, according to $\alpha_\gamma = 4/3(\alpha_p^r - 1/2)$. The number of neutrinos emitted from clusters of $T_X \sim 2 - 4$ keV is estimated to be $\sim 10^{33} - 10^{34}$ GeV^{-1}s^{-1} at $E_\nu \sim 1$ TeV and $\sim$ a few $\times (10^{24} - 10^{26})$ GeV^{-1}s^{-1} at $E_\nu \sim 1$ PeV.

We also try to assess neutrino fluxes from the five nearby clusters listed in Table 1. Due to the limited box size of the LSS formation simulations here, the parameters of our sample clusters (see Figure 1) do not cover those of some of the nearby clusters. Hence, we employ the scaling relation $L_\nu \propto T_X^{5/2}$, along with the neutrino energy spectrum for $\alpha_p^r = 2.4$ in the upper panel of Figure 19, to guess dL_ν/dE_ν for these nearby clusters. Then, the neutrino flux of each cluster can be calculated as

$$\frac{d\Phi_\nu}{dE_\nu} = \frac{1}{4\pi^2 R_{\rm vir}^2} \frac{dL_\nu}{dE_\nu}, \tag{41}$$

where $R_{\rm vir}$ is the virial radius of the cluster. Note that the above has the units of neutrinos GeV^{-1}cm^{-2}s^{-1} sr^{-1}.

Figure 21 shows $E_\nu^2 d\Phi_\nu/dE_\nu$ as a function of E_ν, predicted for the nearby clusters in Table 1, along with the IceCube flux [116] and the atmospheric muon and electron neutrino fluxes [117] for comparison. A few points are noticed. (1) Among the nearby clusters, the Coma, Perseus, and Ophiuchus clusters are expected to produce the largest fluxes. Yet, at $E_\nu = 1$ PeV, the predicted fluxes are $\lesssim 10^{-4}$ times smaller

Table 3: List of Nearby Clusters

	d [Mpc] [a]	T_X [keV] [b]	R_{vir} [Mpc] [b]
Virgo	16.5	2.3	1.08
Centaurus	41.3	3.69	1.32
Perseus	77.7	6.42	1.58
Coma	102	8.07	1.86
Ophiuchus	121	10.25	2.91

a: References for the cluster distances: [131] for the Virgo cluster, [132] for the Centaurus cluster, [133] for the Perseus cluster, [134] for the Coma cluster, and [135] for the Ophiuchus cluster.

b: The X-ray temperature and virial radius of the Virgo cluster are from [136]. Those of the Centaurus, Perseus, Coma, and Ophiuchus clusters are from [137].
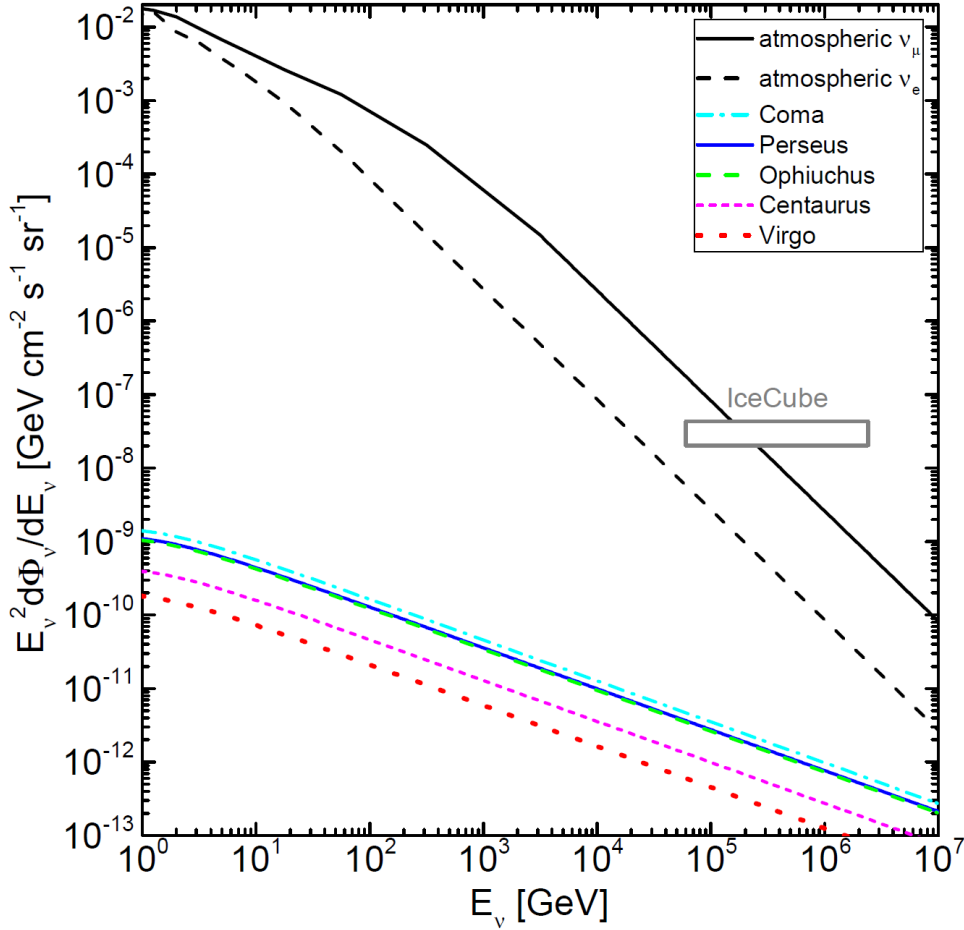
Figure 21: Predicted neutrino fluxes from five nearby clusters. For the momentum distribution of CRp, the model with $\alpha_p^r = 2.4$ and $\delta = 0.75$ is employed. The gray box shows the IceCube flux [116], and the black solid and dashed lines indicate the fluxes of atmospheric muon and electron neutrinos, respectively [117].

than the IceCube flux. Hence, it is unlikely that high-energy neutrinos from clusters would be reckoned with IceCube, even after the stacking of a large number of clusters is applied. (2) At the neutrino energy range of several GeV to TeV, for which the flux data of the Super-Kamiokande detector are available [113], the fluxes from nearby clusters are smaller by $\lesssim 10^{-6}$ times than the atmospheric muon neutrino flux and smaller by $\lesssim 10^{-4}$ times than the atmospheric electron neutrino flux. Hence, it is unlikely that the signature of neutrinos from galaxy clusters could be separated in the data of ground detectors such as Super-Kamiokande and future Hyper-Kamiokande [138]. (3) Our neutrino fluxes from nearby clusters are substantially smaller than the ones estimated in previous works. For instance, our estimates are $\sim 10^{-3}$ times smaller than those for $\alpha_p = 2.4$ at $E_\nu = 250$ TeV in Table 3 of [111]. This discrepancy comes about mainly because our DSA model has a smaller acceleration efficiency, compared to the efficiency model adopted in their work (see Section "CRp Production via Fresh-Injection DSA"), but also partly due to different approaches for modeling the CRp production in simulated clusters.

4.3   Summary and Discussion

In this Section, we investigated the production of CRp in galaxy clusters as well as the possibility of detecting γ-ray and neutrino emissions from galaxy clusters. The main results of our study can be summarized as follows:

1) Inside simulated clusters, ~ 30 % of identified shocks are $Q_\parallel$, and ~ 23 % of the shock kinetic energy flux at $Q_\parallel$-shocks is dissipated by supercritical shocks with $M_s \geq 2.25$. As a result, only ~ 7 % of the kinetic energy flux of the entire shock population is dissipated by the supercritical $Q_\parallel$-shocks that are expected to accelerate CRp. The fraction of the shock kinetic energy transferred to CRp via fresh-injection DSA is estimated to be $\sim (1-2) \times 10^{-4}$.

2) The CRp, produced via fresh-injection DSA at supercritical $Q_\parallel$-shocks, have the momentum distribution, well fitted to a power-law. The volume-averaged power-law slope is $\alpha_p \sim 2.4 - 2.6$, indicating that the average Mach number of CRp-producing shocks is $M_s \sim 2.8 - 3.3$, which is typical for shocks in the cluster outskirts.

3) Reacceleration due to the multiple shock passages of the ICM plasma makes the CRp spectrum harder. After the energization through reacceleration is incorporated in our model, the volume-averaged power-law slope reduces to $\alpha_p^r \sim 2.35 - 2.5$, that is, the CRp spectrum flattens by $\sim 0.05 - 0.1$ in slope. At the same time, the total amount of CRp energy contained in sample clusters increases by $\sim 40 - 80\%$.

4) The predicted γ-ray emissions from simulated clusters are mostly below the Fermi-LAT upper limits for observed clusters [108]. Our estimates are lower than those of [31] based on the DSA model of [26], because our DSA efficiency, η, is smaller than their η_{CS14} in the range of $M_s = 2.25 - 5$. In addition, we believe future γ-ray observation could provide the evidence of CRp production and further refine the DSA model of ICM shocks as well.

5) The predicted neutrino fluxes from nearby clusters are smaller by $\lesssim 10^{-4}$ times than the IceCube flux at $E_\nu = 1$ PeV [116] and smaller by $\lesssim 10^{-6}$ times than the atmospheric neutrino flux in the range of $E_\nu \leq 1$ TeV [117]. Hence, it is unlikely that they will be observed with ground facilities such as

IceCube, Super-Kamiokande, and future Hyper-Kamiokande.

While hadronic originated γ-ray emission due to the π^0 decay is only considered in this work, leptonic originated γ-ray emission could be also emitted due to the CRp. As explained above, the inelastic collisions between CRp and background thermal protons could produce both neutral and charged pions and charged pions are decayed into neutrinos and electrons. Such electrons are the so-called secondary electrons and inverse-Compton (IC) emissions could be emitted in the γ-ray energy range as consequence of interaction between secondary electrons and cosmic macrowave background photons. In the ICM, the γ-ray emission produced by π^0-decay is expected to dominate over the γ-ray emission due to the IC via secondary electrons. [107], for instance, showed that the γ-ray flux produced by IC is more than an order of magnitude smaller than that produced by π^0-decay and thus the contribution of IC is negligible.

In addition, while we only consider the CRp production inside clusters via ICM shocks, it would be interesting if CRp produced around cluster by cluster accretion shocks are advected into the cluster virial radius. Because the radiative timescale of CRp is longer than the cosmological age, so CRp can be sufficiently advected several Mpc scales. In such cases, the number density of CRp inside cluster could be increased. We interpret that such contribution could be negligible because the gas density around galaxy clusters is roughly two order of magnitude lower than the mean gas density inside clusters so the CRp density produced around clusters is expected to be lower than that produced inside clusters as well.

V Electron Preacceleration at Weak Quasi-perpendicular Shocks in Intracluster Medium: 1. Plasma Instabilities in Shock Upstream

As argued in the previous kinetic plasma simulation studies, the electron acceleration process at the shocks in various astrophysical environments is mediated by the microinstabilities near the shock surface (e.g., [23–27, 139–141]). Again, the radio observations have provided the evidence of electron acceleration at the ICM shocks, however, the detailed acceleration mechanism has yet to be understood. From observations of the so-called radio relics [39, 44], in particular, the electron acceleration is inferred to operate in low Mach number, quasi-perpendicular ($Q_\perp$, hereafter) shocks with $\theta_{\mathrm{Bn}} \gtrsim 45°$ in the hot ICM [142]. Here, θ_{Bn} is the obliquity angle between the background magnetic field and the shock normal. In this regards, from this Section to Section VIII, we examine the electron acceleration including microinstabilities at the ICM $Q_\perp$-shocks using PIC simulations. In particular, we here study the properties plasma instability driven at the shock upstream due to the dynamics of shock reflected electrons through linear stability analysis and PIC simulation (the results shown in this section are presented in the paper (Kim, S., Ha, J.-H., Ryu, D., & Kang, H. 2020, The Astrophysical Journal, 892, 85; [143])).

According to prevous numerical works for simulating $Q_\perp$-shocks [144, 145], self-excited waves in the shock upstream are essential. The upstream waves could be induced by the following process: (1) the upstream ions and electrons are reflected due to the magnetic mirror deflection at the shock surface, (2) the reflected particles are energized through the motional electric field at the shock (i.e., shock drift acceleration (SDA, hereafter)), (3) because the reflected and SDA energzied electrons are backstreaming along the upstream magnetic field, such SDA energized electrons drive upstream plasma waves. Depending on the plasma conditions, electrostatic waves or electromagnetic waves are generated. (4) Through the wave-particle mediated by such upstream waves, electrons can undergo multiple SDA cycles [23, 24, 139, 140, 146–148]. The injection problem can be followed from first principles only through particle-in-cell (PIC) simulations, which fully treat kinetic microinstabilities and wave-particle interactions on both ion and electron scales around the shock transition.

More precisely, the shock-reflected electrons stated above can drive plasma instabilities because they could generate anisotropy in electron velocity space. Regarding the growth of such plasma instabilities, the following parameters would be substantial: the plasma beta, $\beta = P_{\mathrm{gas}}/P_{\mathrm{B}}$ (the ratio of the gas to magnetic pressures), the sonic Mach number M_{s}, the Alfvén Mach numbers, M_{A} ($M_{\mathrm{A}} = \sqrt{\beta\Gamma/2}M_{\mathrm{s}}$ where $\Gamma = 5/3$ is the gas adiabatic index), the obliquity angle, θ_{Bn}, and the adopted ion-to-electron mass ration, m_p/m_e [149, 150]. Those parameter effects could be understood as follows: (1) higher Mach number generates larger density and magnetic field jumps and thus the number fraction of shock-reflected ions and electrons typically increases as Mach number increases when the shock surface potential is small enough. (2) If magnetic field is strong (i.e., low β plasma), plasma system is easily stabilized because large magnetic pressure suppress plasma instability. In high β plasma, on the other hand, plasma instability could be easily induced because the system is almost independent of magnetic suppression.

To understand the electron acceleration at ICM shocks, [23, 24, 140] performed two-dimensional

(2D) PIC simulations of $M_s = 2 - 3$, $Q_\perp$-shocks in $\beta = 6 - 200$ plasmas with $k_B T = 8.6 - 86$ keV. They argued that the temperature anisotropy ($T_{e\parallel} > T_{e\perp}$) due to reflected electrons, backstreaming along the background magnetic fields with small pitch angles, derives the electron firehose instability (EFI, hereafter), which excites mainly nonpropagating oblique waves in the shock upstream. Here, $T_{e\parallel}$ and $T_{e\perp}$ are the electron temperatures, parallel and perpendicular to the background magnetic field, respectively. The SDA-reflected electrons are scattered back and forth between the magnetic mirror at the shock ramp and the EFI-driven upstream waves, but they are still suprathermal and do not have sufficient energies to diffuse downstream across the shock transition. On the other hand, [151] and [141] have recently shown through 2D and 3D plasma simulations of supercritcal $Q_\perp$-shocks that shock surface ripplings generate multi-scale perturbations that can facilitate the electron acceleration beyond the injection momentum. In the following Section VI, we seperately present the results regarding multi-scale perturbations in the shock transition layer and in this Section, we focus only on the EFI waves driven in shock upstream.

The EFI in homogeneous, magnetized, collisionless plasmas has been extensively studied in the space-physics community as a key mechanism that constrains the electron anisotropy in the solar wind [152]. It comes in the following two varieties: (1) the electron temperature-anisotropy firehose instability (ETAFI, hereafter), driven by a temperature anisotropy, $T_{e\parallel} > T_{e\perp}$ [153–155], and (2) the electron beam firehose instability (EBFI, hereafter), also known as the electron heat flux instability, induced by a drifting beam of electrons [156–158]. In the EBFI, the bulk kinetic energy of electrons is the free energy that drives the instability. In the linear analyses of these instabilities, typically ions are represented by an isotropic Maxwellian velocity distribution function (VDF, hereafter) with T_p, while electrons have different distributions, that is, either a single anisotropic bi-Maxwellian VDF with $T_{e\parallel} > T_{e\perp}$ for the ETAFI, or two isotropic Maxwellian VDFs (i.e., the core with T_c and the beam with T_b) with a relative drift speed, u_{rel}, for the EBFI.

[24] and [140] (KRH19, hereafter) argued that the upstream waves in the shock foot in their PIC simulations have the characteristics consistent with the nonprogating oblique waves excited by the ETAFI. Considering that backstreaming electrons would behave like a drifting beam, however, it would have been more appropriate to interpret the operating instability as the EBFI. So we here consider and compare the two instabilities, in order to understand the nature of the upstream waves in $Q_\perp$-shocks in high-β plasmas. Another reason why we study this problem is that the ETAFI and EBFI in high-β plasmas have not been examined before. In particular, we study the instabilities at both parallel and oblique propagations through the kinetic Vlasov linear theory and 2D PIC simulations, focusing on the kinetic properties of the EFI in high-β ($\beta_p \approx 50$ and $\beta_e \approx 50$) plasmas relevant for the ICM.

5.1 Linear Analysis of ETAFI and EBFI

The ETAFI and EBFI in a homogeneous, collisionless, magnetized plasma are considered. For the case of the ETAFI, the anisotropic bi-Maxwellian distribution of electrons is assumed with the parameter describing the temperature anisotropy, $\mathscr{A} = T_{e\parallel}/T_{e\perp}$, whearease the ion population follows Maxwellian with a single temperature. For the case of the EBFI, two population of electrons are assumed (i.e.,

the core and beam populations) and the core and beam populations are drifting along the background magnetic field with drift speeds of u_c and u_b, respectively. The ion Maxwellian is simply placed with zero drift speed. We employ the realistic proton-to-electron mass ratio, $m_p/m_e = 1836$ as a fiducial model. For the sake of comparing with a corresponding PIC simulation results, reduced mass ratios, $m_p/m_e = 100$ and 400 are adopted as well.

The VDF of a drifting bi-Maxwellian population is given by the following form,

$$f_a(v_\perp, v_\parallel) = \frac{n_a}{n_0} \frac{\pi^{-3/2}}{\alpha_{a\perp}^2 \alpha_{a\parallel}} \exp\left[-\frac{v_\perp^2}{\alpha_{a\perp}^2} - \frac{(v_\parallel - u_a)^2}{\alpha_{a\parallel}^2} \right]. \tag{42}$$

The subscript a denotes the population of core electrons (c), beam electrons (b), or ions (p). Here, n_a and u_a are the number density and the drift speed of the particle species a, respectively. Note that the charge neutrality condition ($n_0 = n_c + n_b = n_p$) and the zero net current condition ($n_c u_c + n_b u_b - n_p u_p = 0$) are satisfied. The thermal velocities are $\alpha_{a\parallel} = \sqrt{2k_B T_{a\parallel}/m_a}$ and $\alpha_{a\perp} = \sqrt{2k_B T_{a\perp}/m_a}$, respectively. The variables for describing plasma system and normalization factors are defiend as follows: the plasma beta, $\beta_a = 8\pi n_0 k_B T_a/B_0^2$, the plasma frequency, $\omega_{pa}^2 = 4\pi n_0 e^2/m_a$, and the gyro-frequency, $\Omega_a = eB_0/m_a c$. The Alfvén speed, given as $v_A = (B_0^2/4\pi n_0 m_p)^{1/2}$, is also used. Note that for the ion (proton) population, $T_{p\parallel} = T_{p\perp} = T_p$ in the ETAFI analysis, while $u_p = 0$ in the EBFI analysis in the following subsections.

To examine the linear properties of EM modes for the ETAFI and EBFI, we solve the linear dispersion relation (see [159, 160] for more details) which is given as

$$\det\left(\varepsilon_{ij} - \frac{c^2 k^2}{\omega^2}\left(\delta_{ij} - \frac{k_i k_j}{k^2}\right) \right) = 0, \tag{43}$$

with the dielectric tensor, ε_{ij}, where k_i and k_j are the components of the wavevector $\mathbf{k}$. Then, the complex frequency, $\omega = \omega_r + i\gamma$, can be expressed as a function of the wave number, k, and the propagation angle, θ. Note that [143] provides the dielectric tensor for the general VDF. Here, both the background magnetic field $\mathbf{B}_0 = B_0 \hat{z}$ and $\mathbf{k}$ lie in the $z - x$ plane, the components of ε_{ij} for the VDF in Equation (42) is obtained by using the Equation (3) in [143].

Electron Temperature Anisotropy Firehose Instability (ETAFI)

We first examine the ETAFI in the ICM environment, triggered by the temperature anisotropy of electrons; hence, $T_{e\parallel} > T_{e\perp}$, while $T_{p\parallel} = T_{p\perp}$, and $u_c = u_b = 0$ (no drift of electrons). For the anisotropic distribution of electrons in Equation (42), the plasma beta is given as $\beta_{e\perp} = \beta_{e\parallel}/\mathscr{A}$ and $\beta_e = (\beta_{e\parallel} + 2\beta_{e\perp})/3 = \beta_{e\parallel}(1 + 2/\mathscr{A})/3$. We restrict the analysis to the case of $\beta_e = \beta_p$, because $\beta_e = \beta_p$ (or $T_e = T_i$) is expected to be generally satisfied in shock upstream. Then, the analysis is reduced to a problem of five parameters, for instance, $T_{e\parallel}$, $T_{e\perp}$, n_0, B_0 and m_p/m_e. We specify the problem with four dimensionless quantities, $\mathscr{A} = T_{e\parallel}/T_{e\perp}$, $\beta = \beta_e + \beta_p$, v_A/c, and m_p/m_e, and use ω_{pe} to normalize k. We then calculate $\omega_r/\Omega_e + i\gamma/\Omega_e$ as a function of ck/ω_{pe} and θ. Note that Ω_e is given as a combination of other quantities, $\Omega_e = \omega_{pe}(v_A/c)(m_p/m_e)^{1/2}$. Considering that $n_0 \sim 10^{-4}$ cm^{-3}, and $T_e \sim T_p \sim 10^8$ K (8.6 keV), and B_0 is of the order of μG in the ICM (see the introduction), we adopt $\beta = 100$ and $v_A/c = [(2/\beta_p)(k_B T/m_p c^2)]^{1/2} \equiv 6 \times 10^{-4}/[(m_p/m_e)/1836]^{1/2}$ as fiducial values.
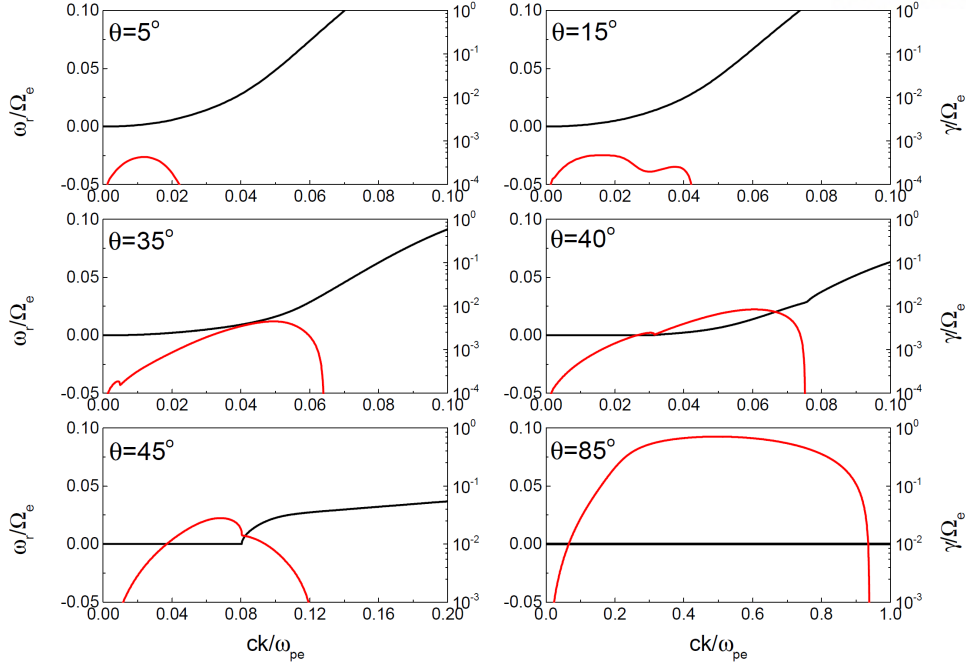
Figure 22: Real frequency, ω_r (black), and imaginary frequency (i.e., growth rate), γ (red), of the ETAFI as a function of wavenumber, k, for different propagation angle θ, the angle between the wavevector and the background magnetic field. Here, the following parameters are employed: $\beta = 100$ (i.e., $\beta_{e\parallel} = 72.3$, $\beta_{e\perp} = 38.9$, and $\beta_p = 50$), $\mathscr{A} = T_{e\parallel}/T_{e\perp} = 1.86$, $v_A/c = 6 \times 10^{-4}$, and $m_p/m_e = 1836$.

Figure 22 shows the analysis results of the ETAFI for the model of $\mathscr{A} = 1.86$, $\beta = 100$, $v_A/c = 6 \times 10^{-4}$, and $m_p/m_e = 1836$. The normalized real frequency, ω_r/Ω_e (black line), and the normalized growth rate, γ/Ω_e (red line), are plotted as a function of ck/ω_{pe} for different θ. At small, quasi-parallel angles ($\theta < 35°$), the propagating mode with $\omega_r \neq 0$ dominates over the nonpropagating mode with $\omega_r = 0$ in all the range of k. As θ increases, γ of both the modes increase, but γ of the nonpropagating mode increases more rapidly than that of the propagating mode (see the panels of $\theta = 35°$, $40°$, and $45°$). As θ increases further, the nonpropagating mode dominates in all the range of k (see the panel of $85°$). The maximum growth rate, γ_m, appears at $ck_m/\omega_{pe} \approx 0.49$ and $\theta_m \approx 85°$, while nonpropagating modes with a broad range of $ck/\omega_{pe} \sim 0.2 - 0.8$ have similar γ. This agrees with the previous finding that the ETAFI predominantly generates oblique phase-standing waves (see the introduction).

Figure 23 shows the analysis results for different parameters. The left panels exhibit the dependence on $\beta_{e\parallel}$ with $\beta_{e\parallel} = 5$, 25, and 50 for a fixed $\mathscr{A} = 1.67$; then, $\beta = 7.33$, 36.6, and 73.3, respectively, and other parameters are $v_A/c = 10^{-4}$ and $m_p/m_e = 1836$. The maximum growth rate, γ_m, and the corresponding wavenumber, k_m, for given θ, are plotted as a function of θ for both the propagating (dashed line) and nonpropagating (solid line) modes. The results of the $\beta_{e\parallel} = 5$ model are in perfect agreement with the solutions provided by [153] (see their Figure 2), demonstrating the reliability of our analysis. The peak of γ_m occrus at the nonpropagating mode, again indicating that the fastest-growing mode is nonpropagating, regardless of β. For higher β, the peak is higher and appears at larger θ and smaller k; that is, for higher β, the ETAFI grows faster, and the fastest-growing mode has a longer
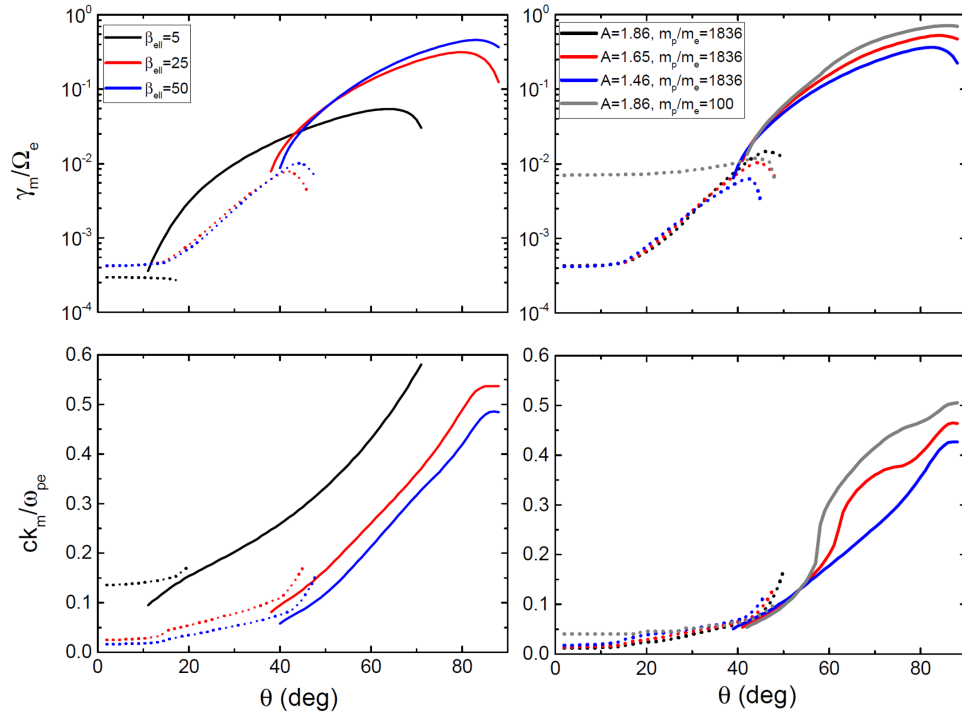
Figure 23: Maximum growth rate, γ_m (top), and wavenumber, k_m (bottom), for the propagating (dashed line) and nonpropagating (solid line) modes of the ETAFI, as a function of θ. The left panels show dependence on the $\beta_{e\parallel}$ values with a set of fixed parameters: $\mathscr{A} = 1.67$; $\beta = 2\beta_{e\parallel}(1+2/\mathscr{A})/3$, $v_A/c = 10^{-4}$, and $m_p/m_e = 1836$. The right panels present dependence on $\mathscr{A}$ and m_p/m_e with a set of fixed parameters: $\beta = 100$ and $v_A/c = 6 \times 10^{-4}/[(m_p/m_e)/1836]^{1/2}$ In the right panels, the gray solid lines almost completely overlap with the black solid lines.

Table 4: Model Parameters for the Linear Analysis of the EBFI

	$\beta_e = \beta_p$	n_b/n_0	u_c/c	u_b/c	$\mathscr{A}_{\text{eff}}$	v_A/c	m_p/m_e	γ_m/Ω_e	θ_m	ck_m/ω_{pe}
Lu0.22	50	0.2	0.044	-0.176	1.46	6×10^{-4}	1836	0.17	79°	0.31
Lu0.26	50	0.2	0.052	-0.208	1.65	6×10^{-4}	1836	0.21	80°	0.34
Lu0.3	50	0.2	0.06	-0.24	1.86	6×10^{-4}	1836	0.24	81°	0.38
Lu0.3β50	25	0.2	0.06	-0.24	1.86	8.5×10^{-4}	1836	0.21	79°	0.41
Lu0.3m100	50	0.2	0.06	-0.24	1.86	2.6×10^{-3}	100	0.24	81°	0.38
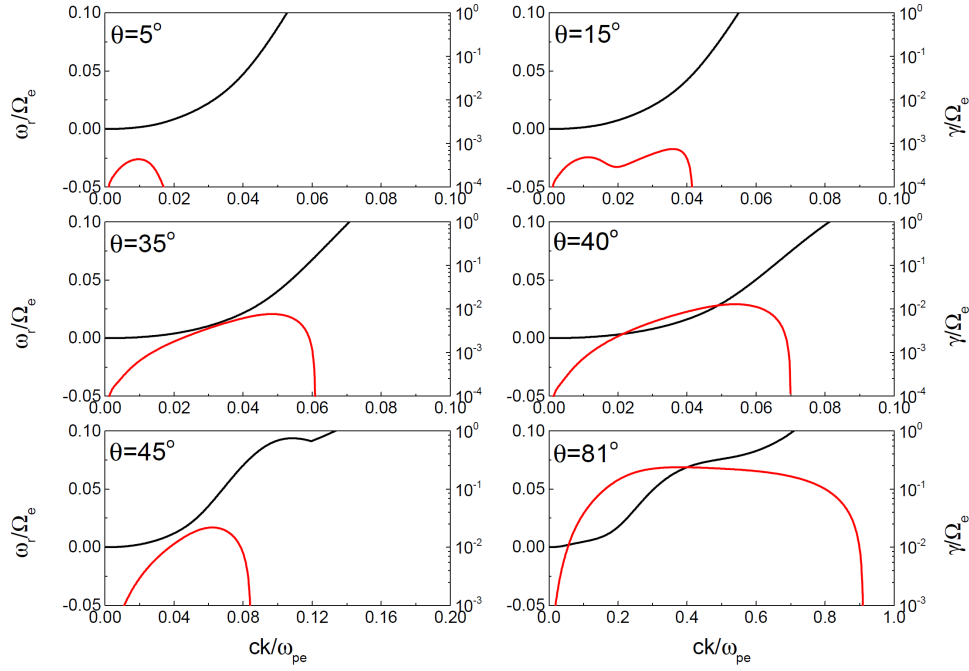
Figure 24: Real frequency, ω_r (black), and growth rate, γ (red), of the EBFI for the Lu0.3 model in Table 1, as a function of wavenumber, k, for different propagation angle, θ. Here, modes have a nonpropagating characteristics when γ is larger than ω.

wavelength and a larger propagation angle.

The right panels of Figure 23 examine the dependence on $\mathscr{A}$ in the range of $\mathscr{A} = 1.46 - 1.86$ for a fixed $\beta = 100$; then, $\beta_{e\parallel} = 63.3 - 72.3$, and other parameters are $v_A/c = 6 \times 10^{-4}$ and $m_p/m_e = 1836$. For larger $\mathscr{A}$, the peak of γ_m is higher and appears at larger θ and larger k; that is, for larger $\mathscr{A}$, the ETAFI grows faster, and the fastest-growing mode has a shorter wavelength and a larger propagation angle. The right panels also compare the models of $m_p/m_e = 1836$ and 100 for $\mathscr{A} = 1.86$. While the growth rate of the propagating mode strongly depends on m_p/m_e, the characteristics of the nonpropagating mode is insensitive to m_p/m_e once m_p/m_e is sufficiently large. This is consistent with the findings of [153].
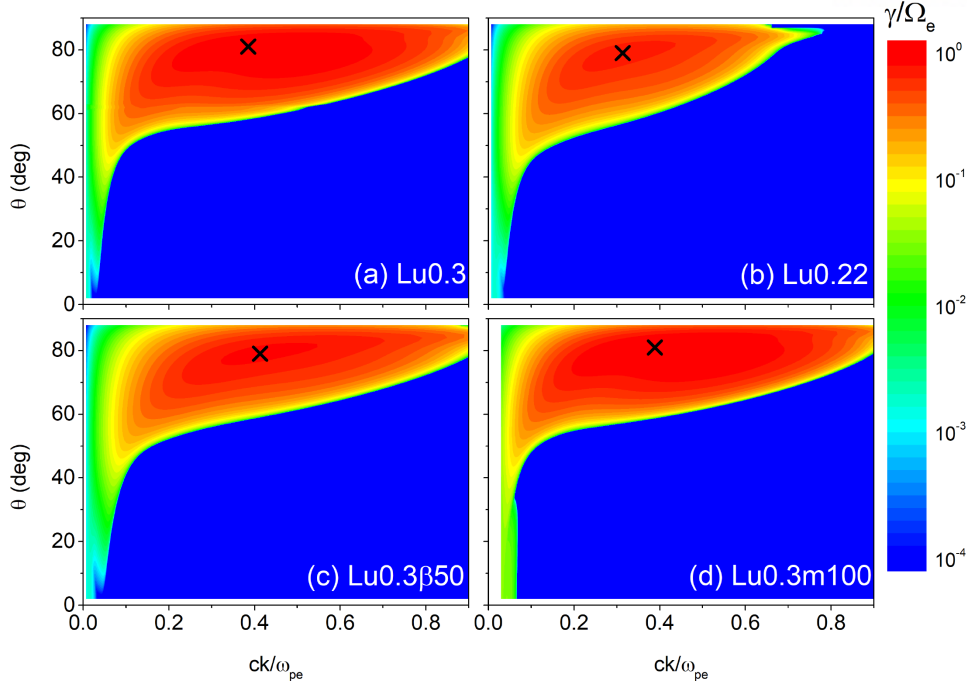
Figure 25: The growth rate, γ, of the EBFI for four models is displayed in the wavenumber k versus wave propagating angle θ space, (a) Lu0.3, (b) Lu0.22, (c) Lu0.3β50, and (d) Lu0.3m100, in Table 1. The symbol X marks the location of the maximum growth rate in the k-θ space.

Electron Beam Firehose Instability (EBFI)

In this subsection, we examine the EBFI in the ICM environment, induced by a drifting beam of electrons. Three populations of core electrons, beam electrons, and ions are involved, and we assume that all follow isotropic Maxwellian VDFs. We again restrict the analysis to the case of $\beta_e = \beta_p$, or equivalently $T_e = T_p$. Then, with the charge neutarlity and zero net current conditions, the analysis is reduced to a problem of six parameters, for instance, T_e, n_c, n_b, $u_{\rm rel} \equiv u_c - b_b$, B_0, and m_p/m_e. We specify the problem with five dimensionless quantities, β, n_b/n_0, $u_{\rm rel}/c$, v_A/c, and m_p/m_e, again using ω_{pe} to normalize k.

Emulating backstreaming electrons in the foot of a simulated shock in the ICM environment, specifically, the M3.0 model shock ($M_s = 3.0$, $\beta = 100$) of KRH19, we adopt the model of $\beta = 100$, $n_b/n_0 = 0.2$ (then, $n_c/n_0 = 0.8$), $u_{\rm rel}/c = 0.3$ ($u_c = 0.06$ and $u_b = -0.24$), $v_A/c = 6 \times 10^{-4}$, and $m_p/m_e = 1836$ as the fiducial model. We also consider four additional models to explore the dependence of the EBFI on $u_{\rm rel}/c$, β, and m_p/m_e, as listed in Table 4. The model name in the table has the following meaning. The first character 'L' stands for 'linear analysis'. The letter 'u' is followed by $u_{\rm rel}/c$; the Lu0.3 model in the third row is the fiducial case. The models in the last two rows are appended by a character for the specific parameter and its value that is different from the fiducial value; the Lu0.3β50 model has $\beta = 50$, and the Lu0.3m100 model has $m_p/m_e = 100$. The last three columns of the table show γ_m, θ_m and k_m of the fastest-growing mode.

To compare the characteristics of the EBFI with those of the ETAFI, we define an "effective" tem-

Table 5: Model Parameters for the PIC Simulations of the EBFI

	$\beta_e = \beta_p$	n_b/n_0	u_c/c	u_b/c	$\mathscr{A}_{\text{eff}}$	$T_e = T_p[\text{K(keV)}]$	m_p/m_e	$L_x = L_y[c/\omega_{pe}]$
Su0.22	50	0.2	0.044	-0.176	1.46	$10^8(8.6)$	100	100
Su0.26	50	0.2	0.052	-0.208	1.65	$10^8(8.6)$	100	100
Su0.3	50	0.2	0.06	-0.24	1.86	$10^8(8.6)$	100	100
Su0.3β50	25	0.2	0.06	-0.24	1.86	$10^8(8.6)$	100	100
Su0.3m400	50	0.2	0.06	-0.24	1.86	$10^8(8.6)$	400	100

perature anisotropy as follows. The "effective" parallel and perpendicular temperatures of the total (core plus beam) electron population are estimated as

$$
\begin{aligned}
T_{e\parallel}^{\text{eff}} &= \frac{m_e}{k_B n_0} \int d^3v \left(v_\parallel - \langle v_\parallel \rangle\right)^2 f_e \\
&= T_e + \frac{m_e}{k_B} \left(u_c^2 \frac{n_c}{n_0} + u_b^2 \frac{n_b}{n_0}\right), \\
T_{e\perp}^{\text{eff}} &= \frac{m_e}{k_B n_0} \int d^3v \frac{v_\perp^2}{2} f_e = T_e,
\end{aligned}
\tag{44}
$$

where $f_e = f_c + f_b$. Note that

$$
\langle v_{e\parallel} \rangle = \frac{1}{n_0} \int d^3v \, v_\parallel f_e = \frac{n_c}{n_0} u_c + \frac{n_b}{n_0} u_b = 0,
\tag{45}
$$

with the zero net current condition in the ion rest frame. Then, the effective temperature anisotropy, arsing from the drift of electrons, is given as $\mathscr{A}_{\text{eff}} = T_{e\parallel}^{\text{eff}}/T_{e\perp}^{\text{eff}}$; it is listed in the sixth column of Table 4.

Figure 24 shows the normalized real frequency, ω_r/Ω_e (black line), and the normalized growth rate, γ/Ω_e (red line), for the Lu0.3 model of the EBFI, as a function of ck/ω_{pe} for different θ. This model has $\mathscr{A}_{\text{eff}} = 1.86$, which is the same as $\mathscr{A}$ of the ETAFI model of Figure 1. The magnitude of γ and the unstable wavenumber range in Figure 24 are comparable to those in Figure 1, and in both the figures, γ increases with increasing θ. For the Lu0.3 model, the maximum growth, $\gamma_m/\Omega_e = 0.24$, appears at $\theta_m \approx 81°$, and at this angle, modes with a broad range of $ck/\omega_{pe} \sim 0.2 - 0.8$ have γ close to γ_m. The wavenumber of γ_m is $ck_m/\omega_{pe} \approx 0.38$ for the Lu0.3 model, smaller than $ck_m/\omega_{pe} \approx 0.49$ at $\theta_m \approx 85°$ in Figure 1. The more notable difference is that fast-growing oblique modes of the EBFI have $\omega_r \neq 0$, while those of the ETAFI have $\omega_r = 0$. However, $\omega_r < \gamma$, for most of the modes; for the Lu0.3 model, $\gamma_m/\Omega_e \approx 0.24$ and $\omega_r/\Omega_e \approx 0.06$ at k_m and θ_m, and hence, $(\omega_r/k_m)/\gamma_m \approx 0.66 \, c/\omega_{pe} \ll \lambda_m (\equiv 2\pi/k_m) \approx 16.5 \, c/\omega_{pe}$, that is, the fastest-growing mode propagates the distance much smaller than its wavelength during the linear grow time of $1/\gamma_m$. It means that EM fluctuations grow much faster than they propagate. Thus, the oblique mode of the EBFI may be regarded as "nearly phase-standing", while the oblique mode of the ETAFI is truly nonpropagating.

Figure 25 demonstrates the effects of u_{rel}/c, β, and m_p/m_e on the growth rate, γ, of the EBFI in the k-θ plane. The black "X" denotes the location (k_m, θ_m) of the fastest-growing mode. The comparison of the Lu0.22 and Lu0.3 (also Lu0.26, although not shown) models indicates that for larger u_{rel} (i.e.,
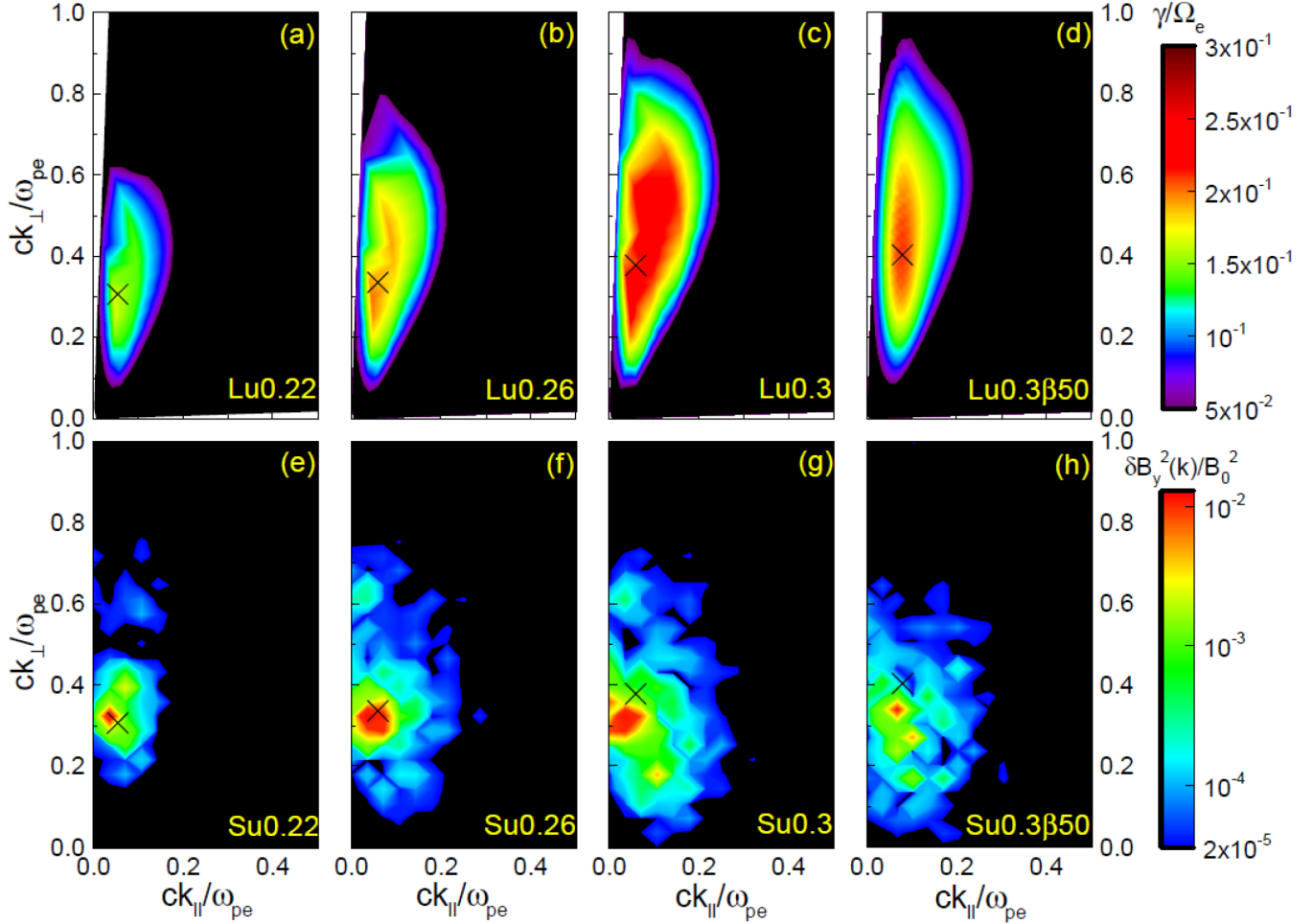
Figure 26: Top panels: the growth rate of the EBFI, $\gamma(\mathbf{k})/\Omega_e$, in the $k_\parallel$-$k_\perp$ space for four models in Table 1, obtained by the linear analysis. Bottom panels: the magnetic energy density, $\delta B_y^2(\mathbf{k})/B_0^2$, in the $k_\parallel$-$k_\perp$ space for four models in Table 2, estimated at $\Omega_e t = 5$, from PIC simulations. Note that $\gamma(\mathbf{k})/\Omega_e$ is displayed in the linear scale, while the colorbar of $\delta B_y^2(\mathbf{k})/B_0^2$ is in the logarithmic scale (see the corresponding text for more details). The parameters of Su models are identical to those of their respective Lu models, except that $m_p/m_e = 100$ for Su models while $m_p/m_e = 1836$ for Lu models. The symbol X marks the wavenumber of the maximum linear growth rate, γ_m, of the Lu models.
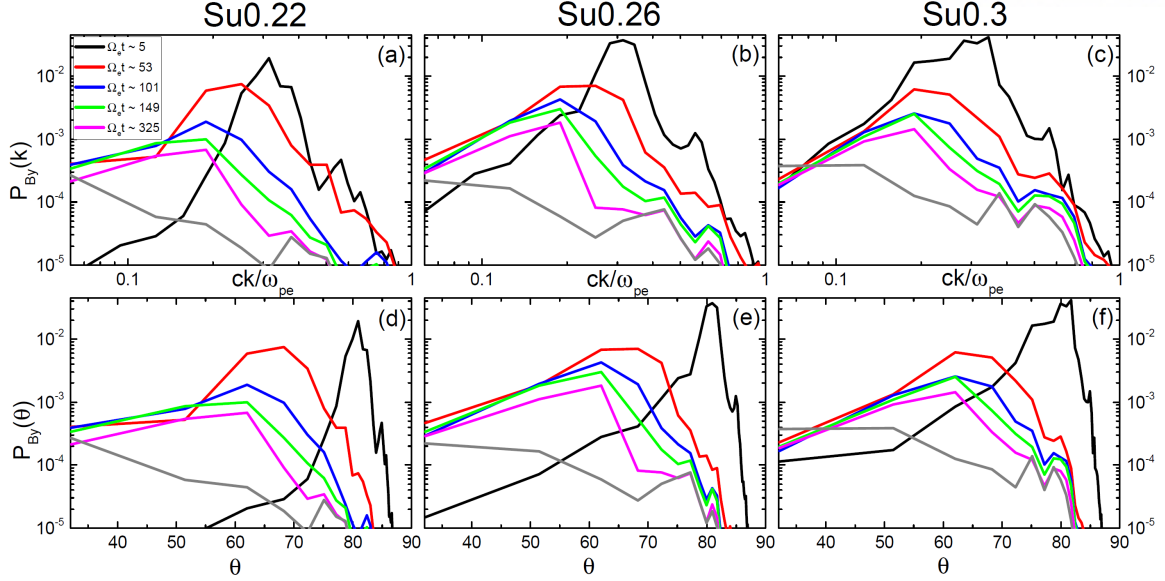
Figure 27: Time evolution of magnetic field power spectra (top panels: $P_{B_y}(k)$; bottom panels: $P_{B_y}(\theta)$) as a function of k and θ, at different times in the PIC simulations for the Su0.22, Su0.26 and Su0.3 models in Table 5. The gray lines show the power spectrum at a later time, $\Omega_e t \sim 500$.

larger $\mathscr{A}_{\mathrm{eff}}$), γ peaks at larger k_m and larger θ_m. This is consistent with the result of the ETAFI, shown in the right panels of Figure 23. The panels (a) and (c), which compare the Lu0.3 and Lu0.3β50 models, illustrate that for smaller β, k_m is larger, while θ_m is smaller. Such β dependence is also seen in the case of the ETAFI, shown in the left panels of Figure 2. The panels (a) and (d), which compare the Lu0.3 and Lu0.3m100 models, manifest that m_p/m_e is not important, especially at high oblique angles of $\theta \gtrsim 40°$, as in the ETAFI. In summary, these characteristics of the EBFI are similar to those of the ETAFI. Hence, we expect that the EBFI would behave similarly to the ETAFI.

5.2 PIC Simulations of EBFI

Simulation Setup

To further explore the development and evolution of the EBFI in the foot of weak $Q_\perp$-shocks in the ICM, we study the instability through 2D PIC simulations. We consider the setup equivalent to that of linear analysis; electrons, described with an isotropic Maxwellian VDF, drift along the direction of the background magnetic field, $\mathbf{B}_0 = B_0 \hat{z}$. In fact, [24] performed similar PIC simulations to describe the triggering instability and the properties of excited upstream waves, seen in their shock study. The difference is that in their simulations, the beam electrons are drifting within the maximum pitch angle and have a power-law energy distribution.

The PIC simulations were performed using TRISTAN-MP, a parallelized EM PIC code [91, 92]. All the three components of the particle velocity and the EM fields are calculated within a periodic box. The background plasma consists of core electrons, beam electrons, and ions. The core and beam electron populations drift, satisfying the zero net current condition, while the ion population is at rest.
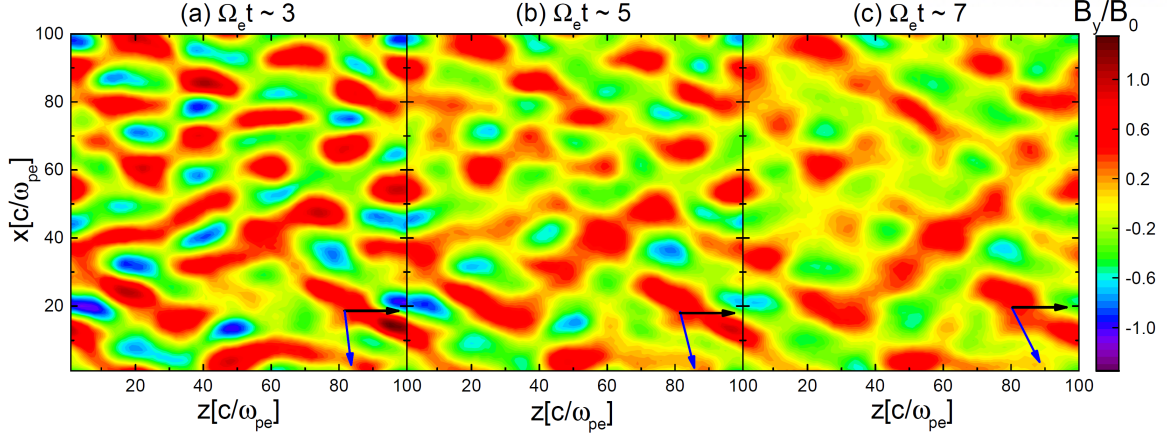
Figure 28: Two-dimensional slices of magnetic field fluctuation, $\delta B_y/B_0$, at three different times in the PIC simulation for the Su0.3 model. The black arrows draw the direction of background magnetic field, while the blue arrows indicates the wavevector corresponding to the peak of power spectrum, $P_{B_y}(\mathbf{k})$.

The simulation domain is in the $z - x$ plane. Again, the case of $\beta_e = \beta_p$, or equivalently $T_e = T_p$, is considered.

Parallel to the models for the linear analysis shown in the previous section, we ran simulations for the five models listed in Table 5. The model name in the first column has the same meaning as that in Table 4, except that the first character 'S' stands for 'simulation'. Su0.3 in the third row is the fiducial model; $\beta = 100$, $n_b/n_0 = 0.2$, $u_{\rm rel}/c = 0.3$, $T_e = T_p = 8.6$ keV, and $m_p/m_e = 100$. Again, this model is to intended to reproduce the upstream condition of the M3.0 model shock of KRH19. Note that here $m_p/m_e = 100$ is used to speed up the simulations, but the early, linear-stage evolution of fast-growing oblique modes should be insensitive to the mass ratio, as mentioned above. Four additional models are considered to explore the dependence on $u_{\rm rel}/c$, β, and m_p/m_e.

The simulation domain is represented by a square grid of size $L_z = L_x = 100\ c/\omega_{pe}$, which consists of cells of $\Delta z = \Delta x = 0.1\ c/\omega_{pe}$. In each cell, 200 particles (100 for electrons and 100 for ions) are placed. The time step is $\Delta t = 0.045\ [\omega_{pe}^{-1}]$, and the simulations ran up to $t_{\rm end} = 1000\ \Omega_{\rm e}^{-1}$.

Simulations Results

As in the ETAFI (see the introduction), for fast-growing oblique modes of the EBFI, the magnetic field fluctuations are induced predominantly along the direction perpendicular to both $\mathbf{k}$ and $\mathbf{B_0}$, i.e., along the y axis in our geometry. Hence, below, we present the simulation results associated with δB_y to describe the evolution of the EBFI. With its Fourier transformation, $\delta B_y(\mathbf{k})$, we first compare $\ln(\delta B_y^2(\mathbf{k})/B_0^2)$, calculated in the PIC simulations, with the linear growth rate, $\gamma(\mathbf{k})$, since $\delta B_y(\mathbf{k}) \propto \exp(\gamma(\mathbf{k}))$ in the linear regime. Figure 26 shows such comparison between $\gamma(\mathbf{k})$ of the linear analysis models in Table 4 (top panels) and $\delta B_y^2(\mathbf{k})/B_0^2$ of their respective simulation models in Table 5 (bottom panels). Here, $\delta B_y(\mathbf{k})$ is at $\Omega_e t = 5$, close to the linear growth time of the fastest-growing mode, Ω_e/γ_m. In the linear analysis, the fastest-growing mode occurs at $k_m c/\omega_{pe} \sim 0.31 - 0.41$ and $\theta_m \sim 79° - 81°$ (see Table 5), which corresponds to the positions of the black "X" marks in the figure. The figure
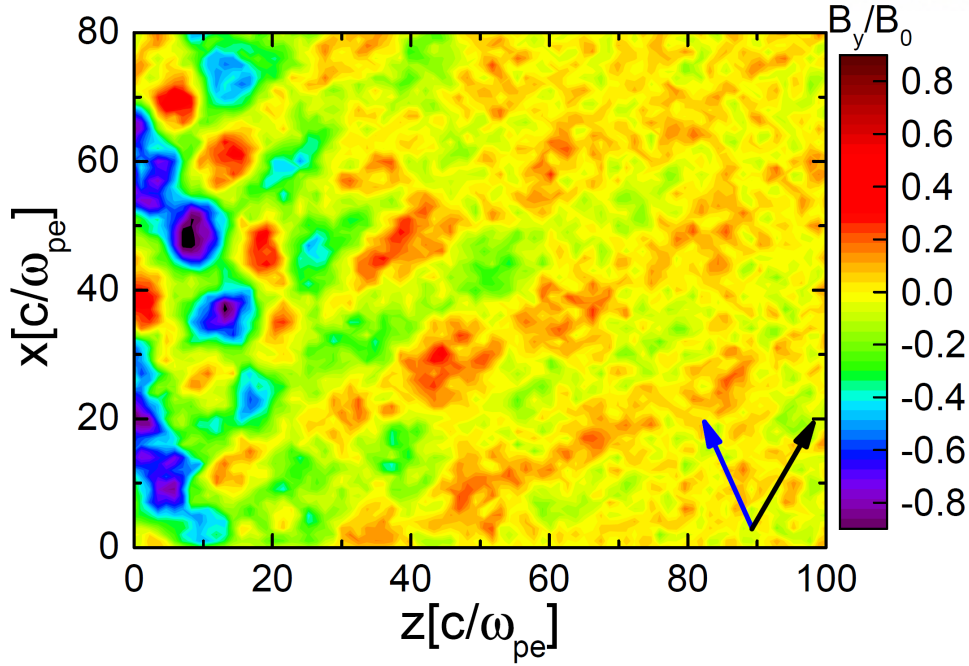
Figure 29: Two-dimensional slice of y-magnetic field, $\delta B_y/B_0$, at $\Omega_e t \sim 5000$ in the PIC simulation of the M3.0 model shock of KRH19. The black arrow draw the direction of background magnetic field, while the blue arrow points the wavevector corresponding to the peak of power spectrum, $P_{B_y}(\mathbf{k})$.

demonstrates a fair consistency between the simulations and the linear analysis. The bottom panels show that $\ln(\delta B_y^2(\mathbf{k})/B_0^2)$ is substantial in the portion of the $k_\parallel$-$k_\perp$ plane where the growth rate is substantial. In the Su0.22 and Su0.26 models, the peak of $\delta B_y^2(\mathbf{k})/B_0^2$ agrees reasonably well with the location of the X mark. In the Su0.3 and and Su0.3β50 models, on the other hand, the peak shifts a little to the lower left direction of the X mark, possibly a consequence of the nonlinear evolution of the instability (see below).

Although the Su0.3m400 model is not presented in Figure 26, we find that the distribution of $\ln(\delta B_y^2(\mathbf{k})/B_0^2)$ in the $k_\parallel$-$k_\perp$ plane coincides well with that of the Su0.3 model. This confirms that the development of the EBFI is not sensitive to m_p/m_e in the nonlinear regime as well as in the linear regime.

As described in the introduction, previous studies of the ETAFI have shown that as the instability develops, the magnetic field fluctuations inversely cascade toward longer wavelengths and smaller θ, and that the scattering of electrons by excited waves reduces the temperature anisotropy and the ETAFI-induced waves decay [154, 155]. We expect a similar inverse cascade for the EBFI-driven magnetic field fluctuations as well. In addition, excited waves will disperse the electron beam, resulting in the decrease of the relative drift speed and eventually leading to the damping of the magnetic field fluctuations with time.

To describe the evolution of the EBFI, we examine the magnetic power spectra, $P_{B_y}(k)$ and $P_{B_y}(\theta)$,

defined with the following relations,

$$\frac{\delta B_y^2}{B_0^2} = \int P_{B_y}(k)d\ln k = \int P_{B_y}(\theta)d\theta. \tag{46}$$

Note that $P_{B_y}(k) = (\delta B_y^2(k)/B_0^2)k^2$. Figure 27 shows the time evolution of $P_{B_y}(k)$ and $P_{B_y}(\theta)$ for three Su models. We first see that at the early time of $\Omega_e t = 5$, the peaks of $P_{B_y}(k)$ and $P_{B_y}(\theta)$ occur at the values close to those predicted in the linear analysis, k_m and θ_m (see the discussion above). The figure also demonstrates that the magnetic power transfers to smaller k and smaller θ; such inverse cascade continues to $kc/\omega_{pe} \sim 0.2$ (corresponding wavelength is $\lambda \sim 30c/\omega_{pe}$) and $\theta \sim 60°$ at $\Omega_e t \sim 300$. Eventually, the magnetic power decays away in the timescale of $\Omega_e t \sim 500$, indicating that the modes of long wavelengths with $\lambda \gg \lambda_m$ are not produced by the EBFI.

A similar evolutionary behavior of the magnetic field fluctuations, that is, the inverse cascade followed by the decay, was observed in the simulations of weak $Q_\perp$-shocks in the high-β ICM plasmas presented by KRH19. In the shocks, however, the beam of SDA-reflected electrons is, although fluctuating, continuously supplied from the shock ramp, persistently inducing the instability. As a consequence, the magnetic field fluctuations exhibit an oscillatory behavior, showing the rise of the instability, followed by the inverse cascade of the magnetic power, and then the decay of turbulence (see Figure 9 of KRH19). The period of such oscillations is $\Omega_e t \sim 500 - 1000$, close to the decay time scale of the EBFI. Even in the shocks with a continuous stream of reflected electrons, the modes of long wavelengths ($\lambda \gg \lambda_m$) do not develop, as shown in KRH19.

The linear analysis of the EBFI indicates that fast-growing oblique modes, although they are propagating with $\omega_r \neq 0$, have mostly $\omega_r < \gamma$. So these modes are "effectively" phase-standing, similar to the oblique nonpropgating modes excited by the ETAFI. Figure 28 shows the spatial distribution of $\delta B_y/B_0$ at three different times covering almost one linear growth time in the PIC simulation for the Su0.3 model. The figure demonstrates that the oblique modes induced by the EBFI are indeed almost nonpropgating. It also illustrates visually that the peak of $P_{B_y}(k)$ shifts gradually toward longer wavelength and smaller θ, while the magnetic field fluctuations decay.

Figure 29 shows the spatial distribution of $\delta B_y/B_0$ in the foot of a shock, which is taken from the PIC simulation for the M3.0 model shock ($M_s = 3.0$, $\theta_{Bn} = 63°$) reported by KRH19. The strong waves in the shock ramp at the left-hand side of the figure are whistlers excited by reflected ions; obviously they are absent in our periodic-box simulations for the EBFI. The oblique waves in the region, $z/[c/\omega_{pe}] > 30$, on the other hand, are well compared with those in Figure 28. In particular, the wavelength and θ of the peak of P_{B_y} are comparable to those in Figure 28(c). By considering the origin of the instability and also the similarity between Figures 28 and 29, we conduce that it should be the EBFI due to the beam of SDA-reflected electrons that operates in the foot of $Q_\perp$-shocks in the ICM. We also argue that the upstream waves excited by the EBFI, although they have non-zero ω_r, can be regarded as almost phase-standing.

In this work, we explore EFI in weak $Q_\perp$ ICM shocks using linear analysis and corresponding PIC simulations. However, the nature of the foot of a shock may break the assumption of linear analysis. A few points are noted. First of all, we assumed the isotropic maxwellian ions in linear analysis. In

the shock front, however, the ion temperature anisotrpy can be triggered due to the SDA-reflected ions. Indeed, the ion anisotropy in the shock ramp region at the left-hand side of figure 8 is $T_{p\parallel}/T_{p\perp} \sim 0.7 - 1$. Such ion temperature anisotropy is induced as consequence of the dynamics of shock-reflected ions. In the region, $z/[c/\omega_{\mathrm{pe}}] > 30$, on the other hand, the ion temperature anisotropy is weak, $T_{p\parallel}/T_{p\perp} \sim 1$, because the shock reflected ions in the $Q_\perp$-shocks are advected back to the shock downstream. This results are in agreement with the hybrid simulation results proposed in [26]. Because ion reflection at shock surface becomes inefficient in $Q_\perp$-shock, the generation of ion-scale waves in the shock upstream is suppressed in $Q_\perp$-shock. Hence, to investigate EFI found in the shock front, the isotropic maxwellian ions can be applicable. In the following Section VI, we present the plasma instability induced by ion temperature anisotropy, $T_{p\parallel}/T_{p\perp} \lesssim$ in the shock ramp and downstream. Secondly, the current may exist in the shock foot. The average current, j in the region, $z/[c/\omega_{\mathrm{pe}}] < 100$ is $j/[B_0\omega_{\mathrm{pe}}/4\pi] \sim 10^{-2}$. Then, the magnetic field due to the current, B_{curn} can be written as $B_{\mathrm{curn}} \sim 4\pi j/ck_{\mathrm{m}} \sim 0.03 B_0$. Since B_{curn} is much smaller than the magnetic field strength, $|B_{\mathrm{y}}| \sim 0.3 B_0$ in the region, $z/[c/\omega_{\mathrm{pe}}] > 30$ shown in figure 29, we interpret that the current in the shock foot make only a minor contribution to magnetic field generation.

5.3   Summary and Discussion

To describe the nature of the upstream waves excited in the shock foot, we here studied the EFI in two different forms: (1) the ETAFI induced by the electrons of a bi-Maxwellian VDF with the temperature anisotropy, $\mathscr{A} = T_{e\parallel}/T_{e\perp} > 1$, and (2) the EBFI induced by the electrons of a drifting beam with an isotropic Maxwellian VDF and the relative drift speed, u_{rel}. We carried out the kinetic linear analysis of both types of the EFI and the 2D PIC simulations of the EBFI. In particular, the PIC simulations of the EBFI show that the time evolution of the magnetic field fluctuations induced by this instability is consistent with the prediction of the linear analysis and also with the results for the ETAFI reported by [154] and [155]. The oblique, almost nonpropagating modes inverse-cascade in time to the modes with smaller wavenumbers, k, and smaller propagation angles, θ. The scattering of electrons by these waves reduces the beam strength, which in turn leads to the damping of the waves. As a result, the modes of long wavelengths with $\lambda \gg \lambda_m \sim 15 - 20 c/\omega_{pe}$ are not produced by the EBFI.

Before closing this Section, we provide comments about two ingredients: (1) buneman and modified two-stream instabilities driven by the electron beam and (2) plasma instabilities driven by ion temperature anisotropy.

In this Section, we particularly focus on the electromagnetic EFI-induced waves. However, depending on the plasma parameters such as plasma β, the presence of electron beam could enhance more instabilities. For instance, buneman instability could be induced in the shock upstream by the interaction between incoming ions and shock-reflected electrons [91]. The waves induced by buneman waves are electrostatic waves and electrons can be trapped into the shock upstream and continuously energized through the motional electric field in the shock upstream (e.g., [146]). In addition, it has been argued through PIC simulations (see also Section III) that a substantial fraction of ions can be reflected at $Q_\perp$-

shock and thus the modified two-stream instability (MTSI) can be induced in the shock upstream by the relative modtion between electrons and ions. Through MTSI, oblique whistler waves are generated and those waves efficiently confine and enhance electron preacceleration (e.g., [139]). As we pointed in the main text of this Section, shock reflected beam is backstreaming along the upstream magnetic field, so it is likely to consider the generation of bunemann instability and MTSI as well. However, both bunemann instability and MTSI are induced only at the low β plasma. In the low β plasma, the drift velocity of beam is much larger than the background thermal velocity. In the high β plasma, on the other hand, the thermal effects become substantial, so the drift motion of shock-reflected beam is easily stabilized. For this reason, it is unlikely to observe buneman instability and MTSI in the ICM shocks.

Furthermore, while we focus on the instability driven by the dynamics of shock-reflected electrons, additional plasma waves can be generated due to ion temperature anisotropy near the shock surface. Particularly in the shock transition zone, Alfvén-Ion Cyclotron and/or ion mirror instabilities could be induced due to the $T_{p\parallel}/T_{p\perp} < 1$. The waves driven by such instabilities have the wavelength longer than EFI waves, and thus play significant role in wave-particle interaction for particle acceleration. In the shock upstream, on the other hand, it is unlikely to generate effective temperature anisotropy because of absense of shock-reflected ion beam, so the longer wavelength waves beyond EFI waves would not be induced. In this regards, in the following Sections VI and VII, we present the recent linear analysis and PIC simulation results regarding the various instabilities in the shock transition zone.

VI Electron Preacceleration at Weak Quasi-perpendicular Shocks in Intracluster Medium: 2. Plasma Instabilities in the Shock Downstream

In Section V, the properties of plasma instability induced at the shock upstream due to the shock reflected electrons are described including linear stability analysis and corresponding PIC simulation results. The electron preacceleration has been a key outstanding problem in understanding the production of CR electrons in weak ICM shocks. Previous studies have shown that, in low-M_s, high-β, $Q_\perp$-shocks, thermal electrons could be preaccelerated primarily through the Fermi-like acceleration in the shock foot [23, 24, 140, 147] and the stochastic shock drift acceleration (SSDA) in the shock transition region [141, 151, 161–163]. While we focused on the kinetic plasma process in the shock upstream to support the Fermi-like acceleration, it is expected that the various microinstabilities driven by the dynamics of ions and electrons in the shock transition region and shock downstream are also important to explain the SSDA at ICM $Q_\perp$-shocks (e.g., [141, 162, 163]). Hence, in this Section, we perform linear stability analysis and PIC simulations to investigate such microinstabilities (Kim, S., Ha, J.-H., Ryu, D., & Kang, H. 2021, The Astrophysical Journal, 913, 35; [164]).

The two preacceleration mechanisms mentioned above rely on the various microinstabilities triggered by the ion and electron temperature anisotropies in the shock structure [152]. If $T_{e\parallel} > T_{e\perp}$, for example, the electron firehose instability (EFI) can grow with the following two branches: the nonresonant, parallel-propagating mode with left-hand circular polarization, and the resonant, nonpropagating, oblique mode [153]. Hereafter, the subscripts $\parallel$ and $\perp$ denote the parallel and perpendicular directions to the background magnetic field, $\mathbf{B}_0$, respectively. Under the condition of $T_{e\perp} > T_{e\parallel}$, by contrast, the whistler instability and the electron-mirror (e-mirror) instability can be triggered [165–167]. The most unstable whistler mode propagates in the direction parallel to $\mathbf{B}_0$ with right-hand circular polarization, while the e-mirror mode is nonpropagating and has the maximum growth rate at the wavevector direction oblique with respect to $\mathbf{B}_0$. In the case of $T_{i\perp} > T_{i\parallel}$, the Alfvén ion cyclotron instability (AIC, or the proton cyclotron instability) and the ion-mirror (i-mirror) instability may become unstable [152, 168–170]. The fastest-growing mode of the AIC instability propagates in the direction parallel to $\mathbf{B}_0$ with left-hand circular polarization, while the i-mirror mode is non-propagating and has the maximum growth rate at the wavevector direction oblique with respect to $\mathbf{B}_0$. Table 6 summarizes these linear properties of the instabilities driven by perpendicular temperature anisotropies, which are relevant for the present study.

In this Section, adopting the numerical estimates for the temperature anisotropies in the transition region of the simulated shocks shown in the following Section VII, we first perform a linear stability analysis for the microinstabilities for wide ranges of parameters such as $M_s = 2-3$, $\beta = 1-100$, and the ion-to-electron mass ratio, $m_i/m_e = 50-1836$. In addition, adopting the same setup as in the linear analysis but only for the models with $\beta = 50$ and $m_i/m_e = 50$, we carry out 2D PIC simulations with periodic boundary conditions (periodic-box simulations, hereafter) to study the nonlinear evolution of the plasma waves excited by such microinstabilities.

Table 6: Linear Properties of the Instabilities driven by Perpendicular Temperature Anisotropies

instability	AIC	whistler	ion-mirror	electron-mirror
free energy source	$T_{i\perp} > T_{i\parallel}$	$T_{e\perp} > T_{e\parallel}$	$T_{i\perp} > T_{i\parallel}$	$T_{e\perp} > T_{e\parallel}$
propagation angle with $\gamma_m{}^a$	parallel	parallel	oblique	oblique
wavenumber	$ck/\omega_{pi} \leq 1$	$ck/\omega_{pe} \leq 1$	$ck/\omega_{pi} \leq 1$	$ck/\omega_{pe} \leq 1$
wave frequency	$0 < \omega_r < \Omega_{ci}$	$\Omega_{ci} < \omega_r < \Omega_{ce}$	$\omega_r = 0$	$\omega_r = 0$
wave polarization	LHCP^b	RHCP^b	Non-propagating	Non-propagating

a: γ_m is the maximum growth rate.

b: LHCP (RHCP) stands for left-hand (right-hand) circular polarization.
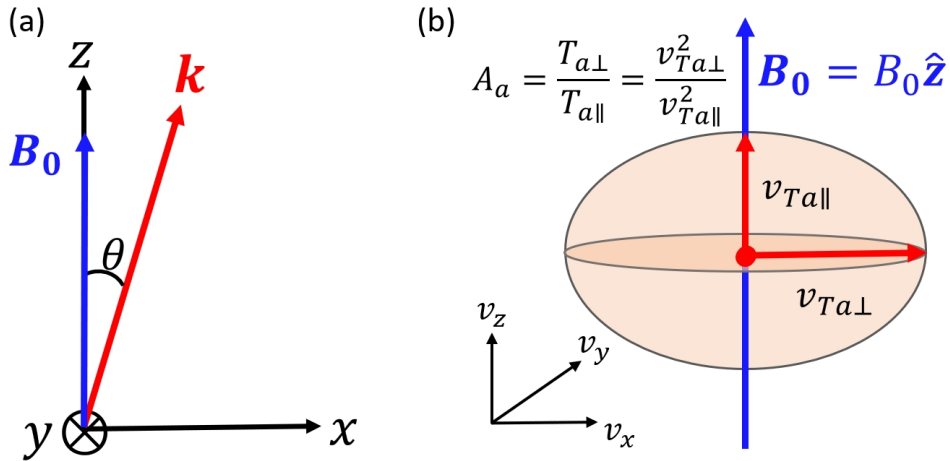
Figure 30: (a) In this study, the background magnetic field, $\mathbf{B}_0 = B_0\hat{z}$, and the wavevector, $\mathbf{k} = k_x\hat{x} + k_z\hat{z}$, lie in the x-z plane. The angle θ, is defined as the angle between $\mathbf{B}_0$ and $\mathbf{k}$. (b) Schematic figure showing the velocity anisotropy (or temperature anisotropy) of a bi-Maxwellian VDF with $\mathscr{A}_a$, where a denotes either 'ion' or 'electron'.

6.1 Linear Analysis

We study the linear properties of the microinstabilities induced by the ion and electron temperature anisotropies through linear stability analysis. The basic equations for solving the linear dispersion relation of electromagnetic modes and the particle velocity distribution functions are the same as the equations used in Section V. The schematic diagram for the coordinates of this work is displayed in Figure 30(a). Here, the background magnetic field is along the $+z$ direction ($\mathbf{B}_0 = B_0\hat{z}$) and the wavevector, $\mathbf{k} = k_x\hat{x} + k_z\hat{z}$ lies in the x-z plane. The values such as n_0, $\mathbf{B}_0$, $T_{a\parallel}$, and $T_{a\perp}$ measured at the shock transition region of the model shown in Section VII are employed and the upstream conditions for those shock simulations are specified with the typical parameters of ICM, $n_{\text{ICM}} = 10^{-4}\text{cm}^{-3}$, $k_B T_{\text{ICM}} = (k_B T_i + k_B T_e)/2 = 8.6$ KeV, and $\beta_{\text{ICM}} = \beta_i + \beta_e = 20 - 100$.

Plasma waves are characterized with the growth rate, γ, and the real frequency, ω_r, which are calculated by solving the dispersion relation for wavevector $\mathbf{k}$. If the propagation angle of the wave with the maximum growth rate, γ_m, is $\theta_m \approx 0°$, the wave mode is called 'parallel-propagating'. If $\theta_m \gg 0°$, it is 'oblique-propagating'. If the wave frequency, $\omega_r \approx 0$, the mode is 'non-propagating'. The wave polarization, P, can be estimated also using the solution of the dispersion relation as follows:

$$P \equiv \text{sign}(\omega_r)\frac{|\delta E_+| - |\delta E_-|}{|\delta E_+| + |\delta E_-|}, \tag{47}$$

where $\delta E_\pm \equiv \delta E^x_{\mathbf{k},\omega} \mp i\delta E^y_{\mathbf{k},\omega}$ [171]. The left-hand circular polarization (LHCP) corresponds to $P = -1$, whereas the right-hand circular polarization (RHCP) corresponds to $P = +1$. Waves are in general elliptically polarized with $P \neq \pm 1$. In the case of non-propagating mode ($\omega_r = 0$), $P = 0$ (see Table 6).

Linear Properties of AIC, Whistler and Mirror Instabilities

In this section, we report the results of the linear stability analysis for the microinstabilities triggered by the ion and electron temperature anisotropies in the transition region of high-β, $Q_\perp$-shocks. Parameters for the linear stability analysis are given in Table 7. For the models of $\beta \approx 20 - 100$ and the mass ration $m_i/m_e = 50$, they are obtained with n_0, $\mathbf{B}_0$, $T_{a\parallel}$, and $T_{a\perp}$ estimated by averaging the numerical values over the transition region in the simulated shocks with $M_s = 2 - 3$ and $\beta^{\text{up}} = 20 - 100$ of Section VII. Considering the uncertainties in averaging over nonlinear structures with overshoot/undershoot oscillations, they are given only up to two significant figures.

For the models with higher mass ratios, LM3.0β50-m100 with $m_i/m_e = 100$ and LM3.0β50-m1836 with $m_i/m_e = 1836$, the parameters for the LM3.0β50 model ($\beta_e = 19$, $\beta_i = 31$, $\mathscr{A}_e = 1.2$, and $\mathscr{A}_i = 2.0$) are used only for the linear analysis. Also we carried out two additional shock simulations for M3.0β1 with $\beta = 1$ and M3.0β5 with $\beta = 5$, which were not considered in HKRK2021, in order to obtain the parameters to be used for LM3.0β1 and LM3.0β5. Our fiducial models have $m_i/m_e = 50$, which is adopted in order to ease the requirements of computational resources for the periodic-box PIC simulations that will be described in the following Section.

The linear predictions for the AIC, whistler, i-mirror, and e-mirror instabilities are given in the $8 - 11$ columns of Table 7. The three numbers inside each parenthesis present the linear properties of the fastest

Table 7: Model Parameters and Linear Predictions

	M_s	β_e^a	β_i^a	$\mathscr{A}_e^a$	$\mathscr{A}_i^a$	m_i/m_e	AIC[b]	whistler[c]	ion-mirror[b]	electron-mirror[c]
LM2.0β20	2.0	9.7	10.3	1.1	1.1	50	stable	stable	stable	stable
LM2.0β50	2.0	24	26	1.1	1.2	50	stable	(0.013,0.20,0)	quasi-stable	(0.0029,0.14,69)
LM2.0β100	2.0	48	52	1.1	1.2	50	quasi-stable	(0.035,0.20,0)	(0.015,0.14,62)	(0.008,0.15,56)
LM2.3β20	2.3	8.4	12	1.1	1.5	50	(0.041,0.21,0)	(0.0016,0.26,0)	(0.04,0.28,63)	stable
LM2.3β50	2.3	22	28	1.2	1.5	50	(0.048,0.15,0)	(0.03,0.24,0)	(0.054,0.21,61)	(0.0074,0.18,67)
LM2.3β100	2.3	44	56	1.2	1.5	50	(0.053,0.11,0)	(0.056,0.24,0)	(0.063,0.16,58)	(0.016,0.17,61)
LM3.0β1	3.0	0.48	0.52	1.2	1.2	50	stable	stable	stable	stable
LM3.0β5	3.0	1.9	3.1	1.2	2.0	50	(0.065,0.40,0)	(0.005,0.39,0)	(0.032,0.41,63)	stable
LM3.0β20	3.0	7.5	13	1.2	2.0	50	(0.127,0.29,0)	(0.0156,0.30,0)	(0.094,0.32,56)	(0.0016,0.17,74)
LM3.0β50	3.0	19	31	1.2	2.0	50	(0.145,0.20,0)	(0.059,0.29,0)	(0.11,0.23,55)	(0.015,0.22,64)
LM3.0β100	3.0	38	62	1.2	2.0	50	(0.156,0.15,0)	(0.10,0.29,0)	(0.12,0.18,54)	(0.03,0.21,56)
LM3.0β50-m100	3.0	19	31	1.2	2.0	100	(0.145,0.20,0)	(0.065,0.29,0)	(0.11,0.23,55)	(0.016,0.22,64)
LM3.0β50-m1836	3.0	19	31	1.2	2.0	1836	(0.145,0.20,0)	(0.072,0.29,0)	(0.12,0.24,55)	(0.016,0.22,64)

a: The quantities, β_e, β_i, $\mathscr{A}_e \equiv T_{e\perp}/T_{e\parallel}$, and $\mathscr{A}_i \equiv T_{i\perp}/T_{i\parallel}$, are obtained by averaging numerical values over the transition zone in the simulated $Q_\perp$-shocks presented in Section VII.

b: Linear predictions for the fastest growing mode of the ion-driven instabilities, $(\gamma_m/\Omega_{ci}, ck_m/\omega_{pi}, \theta_m)$, normalized with the ion gyro and plasma frequencies. θ_m is given in units of degree.

c: Linear predictions for the fastest growing mode of the electron-driven instabilities, $(\gamma_m/\Omega_{ce}, ck_m/\omega_{pe}, \theta_m)$, normalized with the electron gyro and plasma frequencies. θ_m is given in units of degree.
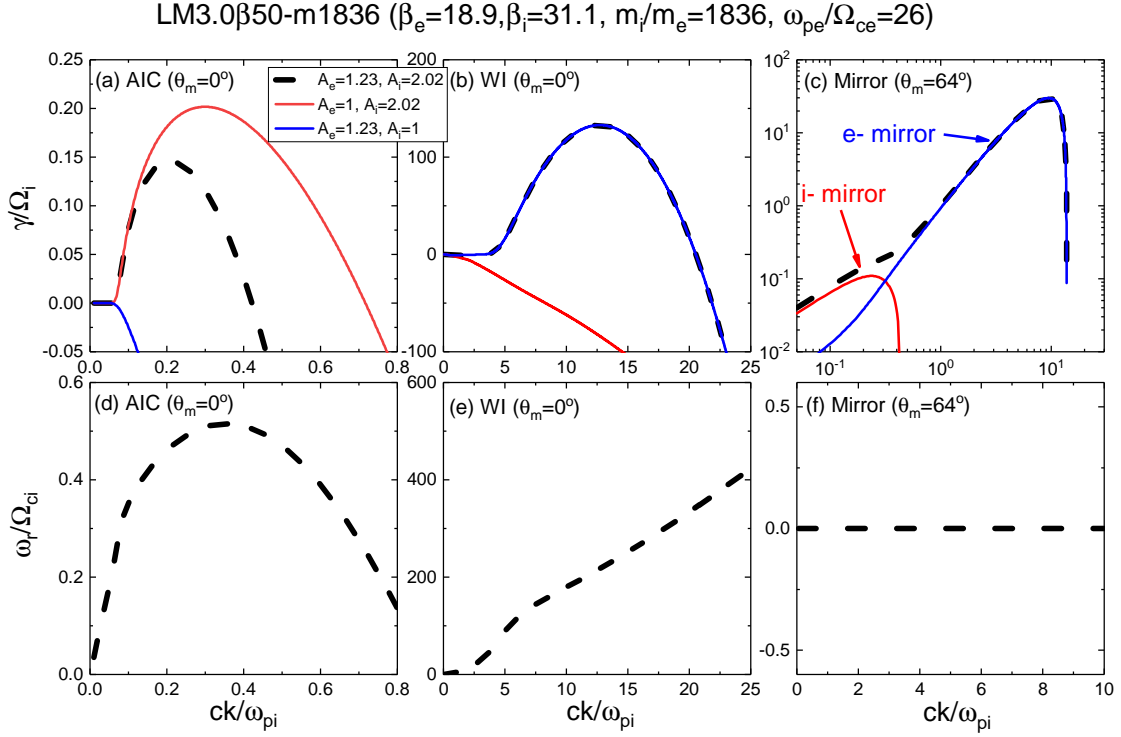
Figure 31: (a)-(c): Linear growth rate, γ, at the propagation angle of the fastest growing mode, θ_m, for the AIC, whistler, and mirror modes, respectively, as a function of the wavenumber k for the LM3.0β50-m1836 model. To examine separately the electron mode (blue) and the ion mode (red), the cases of $\mathscr{A}_e = 1.2$ and $\mathscr{A}_i = 1.0$ (blue) and $\mathscr{A}_e = 1.0$ and $\mathscr{A}_i = 2.0$ (red) are shown. The black dashed lines show the mixed mode case, in which $\mathscr{A}_e = 1.2$ and $\mathscr{A}_i = 2.0$. In panel (c) both γ and k are plotted in logarithmic scales. (d)-(f): Real frequency, ω_r, for the same case as the black dashed lines in the upper panels. Note that γ and ω_r are normalized with Ω_{ci} and k is normalized with ω_{pi}/c, uniformly for both the ion and electron modes.
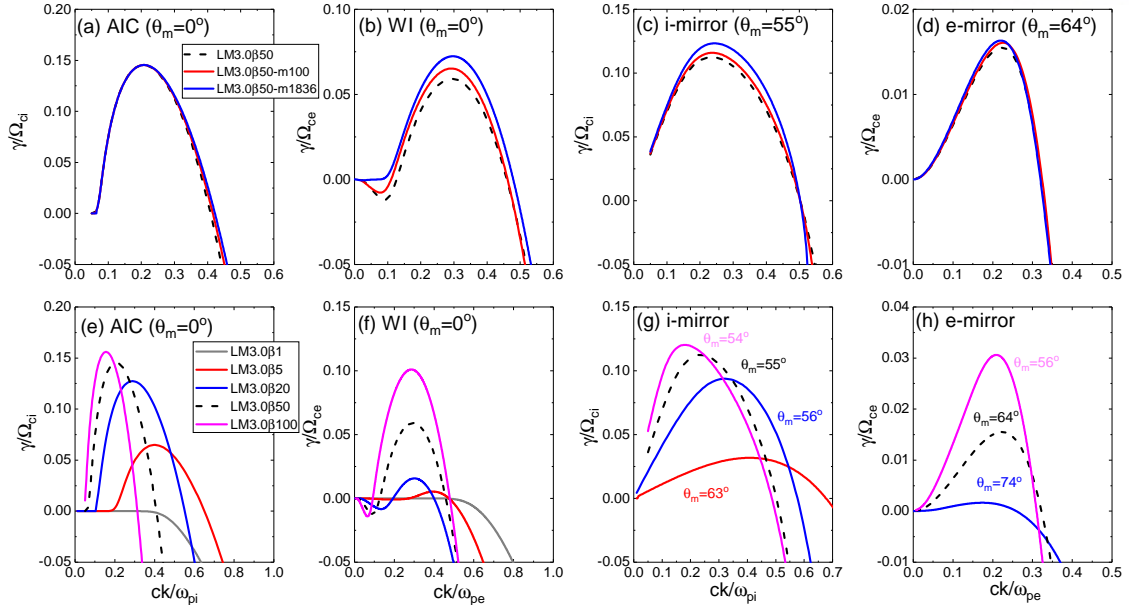
Figure 32: Dependence of the linear growth rate, γ, on m_i/m_e (top) and β (bottom); γ at the propagation angle of the fastest growing mode, θ_m, is given as a function of the wavenumber k. The model parameters are listed in Table 7. Note that for the mirror modes, θ_m depends on β, but not on m_i/m_e.

growing mode: $(\gamma_m/\Omega_{ci}, ck_m/\omega_{pi}, \theta_m)$ for the AIC and i-mirror instabilities, and $(\gamma_m/\Omega_{ce}, ck_m/\omega_{pe}, \theta_m)$ for the whistler and e-mirror instabilities. Here, k_m is the wavenumber that has the maximum growth rate γ_m at θ_m, and θ_m is given in units of degree. For a clear distinction between the ion and electron mirror modes, in the $10 - 11$ columns, γ_m of each mirror mode, obtained with either isotropic electrons (i.e., $\mathscr{A}_e = 1, \mathscr{A}_i > 1$) or isotropic ions (i.e., $\mathscr{A}_i = 1, \mathscr{A}_e > 1$), is shown. Note that 'stable' means that waves cannot grow because $\gamma_m < 0$, and 'quasi-stable' corresponds to $\gamma_m/\Omega_{ci} < 10^{-2}$.

Figure 31 shows the linear analysis results for the LM3.0β50-m1836 model. For the adopted parameters, $\omega_{pe}/\Omega_{ce} = 26$. Panels (a)-(c) display the growth (or damping) rate at θ_m of the AIC, whistler, and mirror instabilities, respectively, as a function of the wavenumber. To make a uniform comparison, γ and k are normalized with Ω_{ci} and ω_{pi}/c, respectively, for both the ion-driven and electron-driven instabilities. Note that in panel (c) both γ and k are given in logarithmic scales, in order to show both the i-mirror and e-mirror modes in the same panel. To examine the effects of $\mathscr{A}_i$ and $\mathscr{A}_e$ separately and also their combination, we present the black dashed lines for the case with both the ion and electron anisotropies, the red solid lines with the ion anisotropy only, and the blue solid lines with the electron anisotropy only.

The AIC instability induces quasi-parallel modes with $\theta_m = 0°$. Although $\mathscr{A}_i > 1$ is the main free energy source which drives the AIC instability, we find that $\mathscr{A}_e > 1$ reduces the growth rate (see the red and black lines in panel (a) and also [172]). By contrast, the whistler instability is unstable for $\mathscr{A}_e > 1$, and the growth rate is independent of $\mathscr{A}_i$. The whistler mode is also quasi-parallel propagating with $\theta_m = 0°$. The mirror modes, on the other hand, are highly oblique with $\theta_m = 64°$ for LM3.0β50-m1836. The e-mirror mode (blue) at high-k ($ck/\omega_{pi} > 0.3$) grows much faster than the i-mirror mode (red) at

77

low-k ($ck/\omega_{pi} < 0.3$). With both $\mathscr{A}_i > 1$ and $\mathscr{A}_e > 1$, a mixture of the two mirror modes appears in the intermediate-k regime ($ck/\omega_{pi} \sim 0.3$).

In the LM3.0β50-m1836 model, the maximum growth rates are given in the following order:

$$\gamma_{WI} \gg \gamma_{E-M} \gg \gamma_{AIC} > \gamma_{I-M}, \tag{48}$$

where γ_{WI}, γ_{E-M}, γ_{AIC} and γ_{I-M} are the maximum growth rates of the whistler, e-mirror, AIC and i-mirror instabilities, respectively. Note that in general $\gamma_{WI} > \gamma_{E-M}$ [173], and $\gamma_{AIC} > \gamma_{I-M}$ under space plasma conditions with low-β and large temperature anisotropies [152, 166].

The real frequency, ω_r/Ω_{ci}, at θ_m for the mixed case ($\mathscr{A}_e = 1.2$ and $\mathscr{A}_i = 2.0$) are shown in panels (d)-(f) of Figure 31. The AIC-driven mode has $\omega_r/\Omega_{ci} \sim 0.25 - 0.5$ for $ck/\omega_{pi} \sim 0.1 - 0.4$, while the whistler mode has $\omega_r/\Omega_{ci} \sim 80 - 350$ for $ck/\omega_{pi} \sim 5 - 20$. The mirror modes are nonpropagating or purely growing with $\omega_r = 0$. Moreover, the polarization, calculated using the solutions of the dispersion relation, is $P = -1, +1$, and 0 for the AIC, whistler, and mirror instabilities, respectively, as expected.

Parameter Dependence of Linear Properties

As listed in Table 7, we consider a number of models to explore the dependence on m_i/m_e and β. The upper panels of Figure 32 show the linear predictions for the models with $M_s = 3$, $\beta = 50$, and $m_i/m_e = 50 - 1836$, while the lower panels are for the models with $M_s = 3$, $m_i/m_e = 50$, and $\beta = 1 - 100$. For a higher mass ratio, electrons go through more gyro-motions per the ion gyro-time, Ω_{ci}^{-1}. Nevertheless, γ_{AIC} and γ_{E-M} are almost independent of m_i/m_e. In the case of the whistler and i-mirror instabilities, on the other hand, overall, the growth rates are slightly lower for smaller m_i/m_e. Also the damping rate for the whistler instability is slightly higher for smaller m_i/m_e in the small wavenumber regime ($ck/\omega_{pe} \sim 0.1$). As a result, the growth of the whistler and i-mirror instabilities may be somewhat suppressed in the shock simulations with reduced mass ratios. However, even in the case of $m_i/m_e = 50$, this effect is expected to be only minor, because the inequality in Equation (48) is still valid and the changes of k_m and θ_m are negligible (see the table 7).

The plasma beta is another important parameter that affects the stability of the system. Note that the anisotropy parameters, $\mathscr{A}_e$ and $\mathscr{A}_i$, are almost independent of β for $\beta \approx 20 - 100$, the range relevant for ICM shocks (see Table 7), although they tend to increase slightly with increasing β in the second digit to the right of the decimal point. In the low-β case (LM3.0β1), $\mathscr{A}_i = 1.2$ is significantly smaller than those of other high-β models due to the strong magnetization of ions. This is because $\mathscr{A}_i$ in the shock transition is closely related to the fraction of reflected ions. On the other hand, $\mathscr{A}_e$ in the shock transition is not substantially affected by β, because it is mainly determined by the magnetic field compression rather than the fraction of reflected electrons. Given the same temperature anisotropies, the growth of the instabilities tends to be suppressed by strong magnetic fields at low-β plasmas. As can be seen in the lower panels of Figure 32, the peak values of either γ_m/Ω_{ci} for the ion-driven modes or γ_m/Ω_{ce} for the electron-driven modes increase with increasing β. For the AIC, whistler, and i-mirror instabilities, γ_m/Ω_{ci} or γ_m/Ω_{ce} occurs at smaller ck/ω_{pi} or ck/ω_{pe}, for higher β. But such a trend is not obvious in the case of the e-mirror mode.
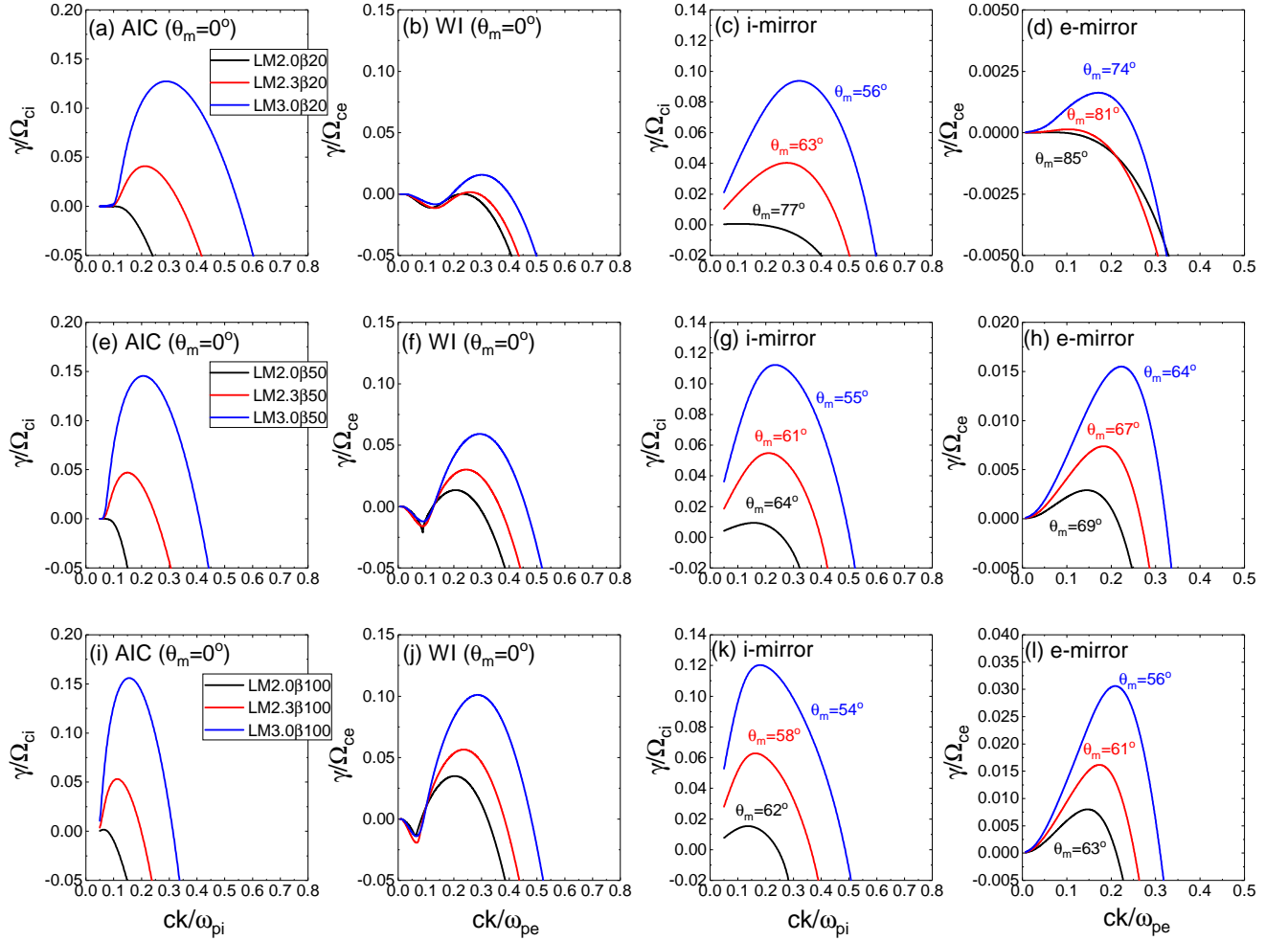
Figure 33: Dependence of the linear growth rate, γ, on M_s and β; γ at the propagation angle of the fastest growing mode, θ_m, is given as a function of the wavenumber k. In each panel, the black, red, and blue lines show the results for $M_s = 2.0$, 2.3, and 3.0, respectively. The plasma beta varies as $\beta = 20$ (top), 50 (middle), and 100 (bottom). The model parameters are listed in Table 7. Note that for the mirror modes, θ_m depends on β.
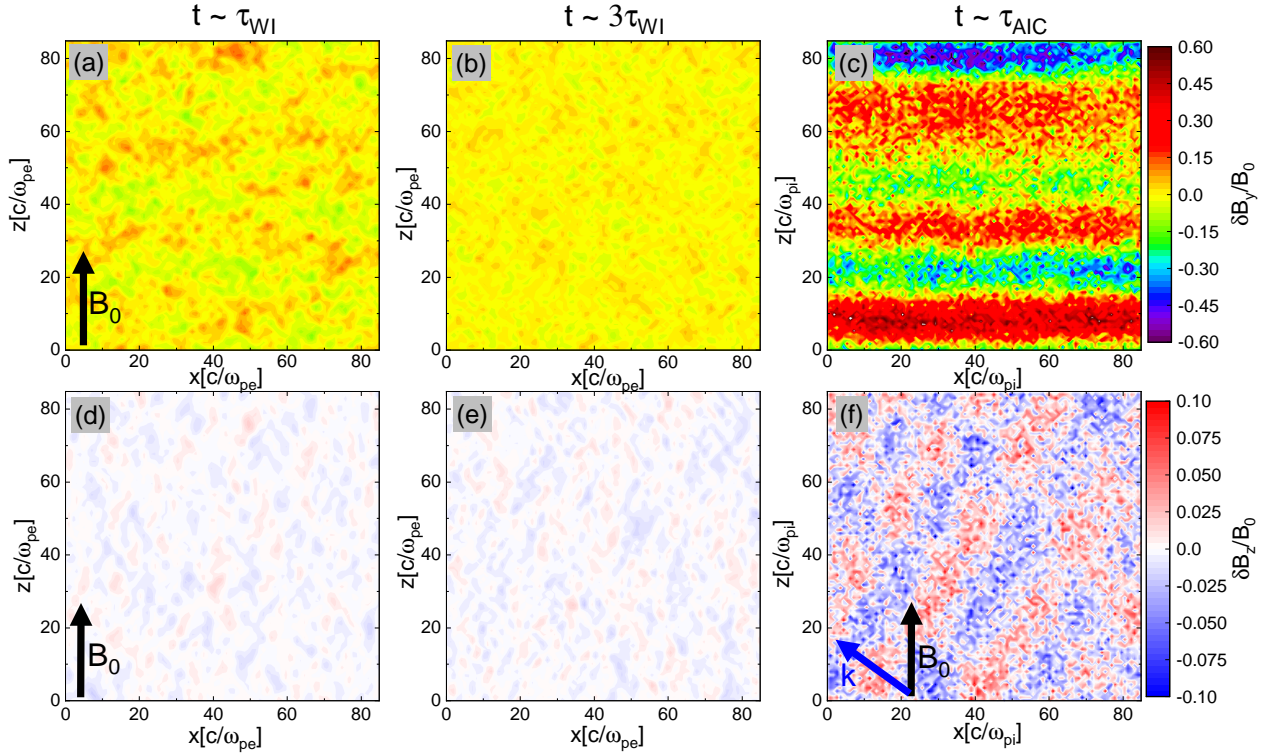
Figure 34: Magnetic field fluctuations, δB_y (top) and δB_z (bottom), in the periodic-box simulation for the LM3.0β50 model, plotted in the x-z plane. At early times, $t \sim 1 - 3\tau_{\text{WI}}$, shown in panels (a)-(b) and (d)-(e), electron-scale waves are excited by the whistler and e-mirror instabilities, while ion-scale waves are generated by the AIC and i-mirror instabilities at $t \sim \tau_{\text{AIC}}$ shown in panels (c) and (f). Note that the 2D domain with $[84.8 \times 84.8](c/\omega_{\text{pe}})^2$ is shown in panels (a)-(b) and (d)-(e), while the 2D domain with $[84.8 \times 84.8](c/\omega_{\text{pi}})^2$ is shown in panels (c) and (f). The black arrows indicate the direction of the background magnetic field, $\mathbf{B}_0$, while the blue arrow in panel (f) shows the direction of the wave propagation, $\mathbf{k}$, for the i-mirror mode with the maximum growth rate.

In the high-β cases ($\beta \approx 20 - 100$) with $M_s = 3$, all the AIC, whistler, i-mirror and e-mirror waves can be triggered, as shown in the lower panels of Figure 32, leading to the generation of multi-scale waves from electron to ion scales. On the other hand, in the LM3.0β5 model (red solid lines), the e-mirror mode is stable, but other modes are unstable. In the LM3.0β1 model (gray solid lines), all the instabilities are stable with negative growth rates.

The sonic Mach number, M_s, is the key parameter that determines the temperature anisotropies in the transition of high-β ICM shocks ($\beta \approx 20 - 100$), since the ion reflection fraction and the magnetic field compression are closely related to M_s. Figure 33 shows the growth rates of the instabilities for $M_s = 2.0$ (black), 2.3 (red), and 3.0 (blue), in the cases of $\beta = 20$ (top), 50 (middle) and 100 (bottom). As M_s increases, both $\mathscr{A}_e$ and $\mathscr{A}_i$ increase, so all the modes grow faster and k_m shifts towards larger k, regardless of β.

Note that the AIC and whistler modes have γ_m at $\theta_m = 0$ independent of M_s, whereas θ_m decreases with increasing M_s for the i-mirror and e-mirror modes (see also Table 7). In LM2.0β50 and LM2.0β100, the AIC instability is stable or quasi-stable, while the whistler and mirror modes can grow. In the case of LM2.0β20, all the instabilities are stable (see black lines in top panels). In the models with $M_s = 2.3 - 3$ (red and blue lines), on the other hand, the four instabilities are unstable, and hence multi-scale plasma waves can be generated.

6.2 Nonlinear Evolution of Induced Waves in Periodic-Box Simulations

Numerical Setup

To investigate the development and nonlinear evolution of the instabilities, we performed 2D PIC simulations with periodic boundary conditions for the three fiducial models, LM2.0β50, LM2.3β50 and LM3.0β50, with the same setup of the linear analysis. The electrons and ions are prescribed with bi-Maxwellian VDFs with β_e, β_i, $\mathscr{A}_e$, $\mathscr{A}_i$ given in Table 7. As noted before, here $m_i/m_e = 50$ is employed due to the computational limitations, but at least the early, linear-stage development of the plasma instabilities under consideration is expected to depend rather weakly on the mass ratio.

The simulations were carried out using a parallelized EM PIC code, TRISTAN-MP [91, 92]. The simulation domain is a square of box size $L_x = L_z = 84.8c/\omega_{pi} = 600c/\omega_{pe}$ in the x-z plane, which consists of the grid cells of $\Delta x = \Delta z = 0.1c/\omega_{pe}$. In each cell, 32 particles (16 for ions and 16 for electrons) are placed. The time step of the simulations is $\Delta t = 0.045\omega_{pe}^{-1}$, and the simulations were run up to $t_{end} = 130\Omega_{ci}^{-1}$.

Results of Periodic-Box Simulations

With the inequality in Equation (48), we expect that the whistler mode grows much faster than the other modes, resulting in the relaxation of $\mathscr{A}_e$ during the early stage. As the whistler and e-mirror modes grow and then decay on the time scale of $\tau_{WI} \equiv 1/\gamma_{WI}$, the AIC and i-mirror modes become dominant later on the time scale of $\tau_{AIC} \equiv 1/\gamma_{AIC}$.
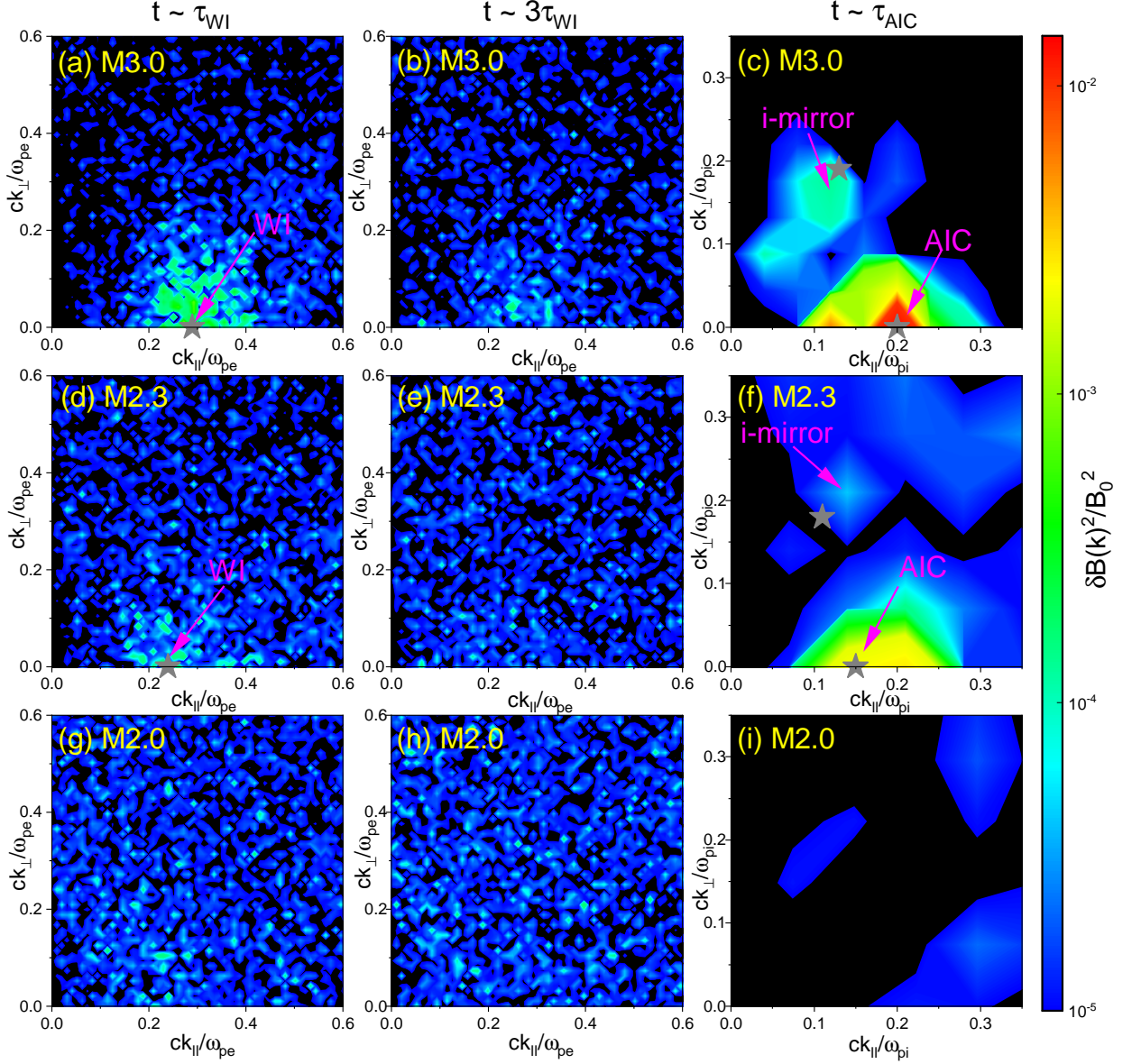
Figure 35: Power spectra of the magnetic field fluctuations, $\delta B_y^2(\mathbf{k})$, in the period-box simulations for LM3.0β50 (top), LM2.3β50 (middle), and LM2.0β50 (bottom), plotted in the $k_\parallel$-$k_\perp$ (that is, $k_z - k_x$) plane. The results are shown at $t \sim \tau_{WI}$ (left), $t \sim 3\tau_{WI}$ (middle), and $t \sim \tau_{AIC}$ (right). See the text for the remarks on τ_{AIC} for LM2.0β50. The gray star symbol marks the location of the maximum linear growth rate, γ_m, estimated from the linear analysis. In the models with $M_s \geq 2.3$, AIC, whistler and i-mirror waves appear, while those waves do not grow substantially in the model with $M_s = 2$.

Figure 34 shows the magnetic field fluctuations, δB_y (upper panels) and δB_z (lower panels), in the x-z plane (simulation plane) at three different times in the LM3.0β50 model. Here, the growth time scales, τ_{WI} and τ_{AIC}, are estimated by γ_m of each mode in Table 7. At $t \sim \tau_{\mathrm{WI}}$, the transverse component, δB_y, appears on electron scales and the waves containing it propagate parallel to $\mathbf{B}_0$ in panel (a), but the longitudinal component, δB_z, does not grow significantly in panel (d). In this early stage, the dominant mode is the whistler mode, while the e-mirror mode is much weak to be clearly manifested. As $\mathscr{A}_{\mathrm{e}}$ decreases in time due to the electron scattering off the excited waves, the whistler waves decay as shown in panel (b). On the time scale of τ_{AIC}, both the AIC and i-mirror instabilities grow and become dominant. It is clear that the AIC-driven waves, shown in panel (c), are parallel-propagating, while the i-mirror-driven waves, shown in panel (f), are oblique-propagating; the blue arrow in the bottom-left corner of panel (f) denotes the wavevector of the i-mirror-driven mode with the maximum growth rate.

Figure 35 shows the time evolution of the power spectrum for the magnetic field fluctuations, $\delta B_y^2(\mathbf{k})$, for LM2.0β50, LM2.3β50, and LM3.0β50 at $t \sim \tau_{\mathrm{WI}}$, $t \sim 3\tau_{\mathrm{WI}}$, and $t \sim \tau_{\mathrm{AIC}}$. Again, the growth time scale of each mode is estimated with γ_m listed in Table 7, except for the LM2.0β50 model, in which the AIC instability is stable, and so the output time of panel (i) is chosen at the evolutionary stage similar to that of LM2.3β50. In the cases of $M_s = 2.3$ and 3, whistler waves are excited dominantly at quasi-parallel propagating angles at $t \sim \tau_{\mathrm{WI}}$. After the initial linear stage, the energy of the whistler waves is transferred to smaller wavenumbers and the waves gradually decay, as shown in panels (b) and (e). On the time scale of $\sim \tau_{\mathrm{AIC}}$, AIC waves and i-mirror waves appear dominantly at quasi-parallel and highly oblique angles, respectively, as shown in panels (c) and (f). This is consistent with the evolutionary behavior which we have described with Figure 34. For the AIC and whistler instabilities, the linear predictions for $\mathbf{k_m}$ with the maximum growth rate (gray star symbols) agree reasonably well with the peak locations of the magnetic power spectrum realized in the PIC simulations. But the linear estimates for the i-mirror mode are slightly off, because γ_m is obtained without the electron anisotropy, as stated through the linear analysis results in the previous section. In summary, the results of the periodic-box simulations are quite consistent with the linear predictions described earlier. Also we note that the results of our PIC simulations are in good agreement with those of [172], in which PIC simulations were carried out to explore the evolution of the instabilities due to the temperature anisotropies in space plasmas with $\beta \sim 1$. The bottom panels of Figure 35 confirm that waves do not grow noticeably in the LM2.0β50 model.

In these periodic-box simulations, the electron-scale waves develop first and then decay as $\mathscr{A}_{\mathrm{e}}$ is relaxed in the early stage, followed by the growth of the ion-scale waves due to $\mathscr{A}_{\mathrm{i}}$. In the shock transition region, by contrast, temperature anisotropies are to be supplied continuously by newly reflected-gyrating ions and magnetic field compression, hence multi-scale plasma waves from electron to ion scales are expected to be simultaneously present.

Table 8: Shock Criticality of the Simulated Shock Models and Stability of the Linear Analysis Models

Simulated Shock Model	Shock Criticality	Linear Analysis Model	AIC	WI	ion-mirror	electron-mirror
M2.0β20	sub	LM2.0β20	stable	stable	stable	stable
M2.0β50	sub	LM2.0β50	stable	unstable	quasi-stable	unstable
M2.0β100	sub	LM2.0β100	quasi-stable	unstable	unstable	unstable
M2.3β20	super	LM2.3β20	unstable	unstable	unstable	stable
M2.3β50	super	LM2.3β50	unstable	unstable	unstable	unstable
M2.3β100	super	LM2.3β100	unstable	unstable	unstable	unstable
M3.0β1	sub	LM3.0β1	stable	stable	stable	stable
M3.0β5	super	LM3.0β5	unstable	unstable	unstable	stable
M3.0β20	super	LM3.0β20	unstable	unstable	unstable	unstable
M3.0β50	super	LM3.0β50	unstable	unstable	unstable	unstable
M3.0β100	super	LM3.0β100	unstable	unstable	unstable	unstable

6.3   Implications for Shock Simulations

Shock Criticality

As mentioned in the introduction, the Fermi-like acceleration, which relies on the upstream waves excited by the EFI, is effective only for supercritical shocks with $M_s \geq M_{EFI}^* \approx 2.3$ in $\beta \approx 20 - 100$ plasma [24, 140]. The SSDA, which depends on the multi-scale waves excited mainly by the AIC and whistler instabilities, is thought to occur in supercritical shocks with $M_s \geq M_{AIC}^* \approx 3.5$ in $\beta \approx 1$ plasmas [151] and $M_s \geq M_{AIC}^* \approx 2.3$ in $\beta \approx 20 - 100$ plasmas (HKRK2021). We suggest that both M_{EFI}^* and M_{AIC}^* are related to the sonic critical Mach number, M_s^*, for ion reflection, since the structure of collisionless shocks is governed primarily by the dynamics of shock-reflected ions.

Table 8 summarizes the shock criticality of the simulated shock models and the stability of the linear analysis models. The first column lists the name of the simulated shock models considered in HKRK2021, and the two additional models for low-β shocks performed for this study. The shock criticality of each model is given in the second column. The name of the corresponding linear analysis models is given in the third column, while the last four columns show the stability for the four instabilities (see also Table 7). We note that the name of the shock models includes β^{up} in the preshock, upstream plasmas, while that of the linear analysis models includes β in the shock transition zone given in Table 7.

According to the results obtained by linear analysis and corresponding PIC simulations, in $\beta \approx 20 - 100$ plasmas, the AIC instability operates for $M_s \gtrsim 2.3$, while whistler waves are induced regardless of M_s. In the M3.0β5 model, the e-mirror mode is stable, while the other three modes are unstable. This is in good agreement with the 2D simulation of a $M_s = 5$ and $\beta = 5$ shock reported earlier by [141]. In the M3.0β1 model, by contrast, $\mathscr{A}_i$ is smaller than that of high-β models, and all the four instability modes are suppressed by strong magnetization. This is consistent with the results of $M_{AIC}^* \approx 3.5$ for shocks with $\beta \approx 1$ presented by [151].

Shock Surface Rippling

Another important feature of the supercritical shocks above M_{AIC}^* is the shock surface rippling. According to previous shock simulations [141, 151, 174, 175], the rippling has the characters of AIC waves with the fastest growing mode at $\theta_m \sim 0$, the propagation speed close to the local Alfvén speed, and the wavelengths of $\sim \lambda_{AIC}$ ($\approx 30c/\omega_{pi}$).

The parallel-propagating AIC and whistler waves in homogeneous plasmas are purely electromagnetic and incompressible with both the electric and magnetic wave vectors pointing normal to $\mathbf{B}_0$. The fluctuating magnetic fields of oblique mirror modes, on the other hand, have a substantial longitudinal component, that is, $\delta\mathbf{B}$ has a significant component parallel to $\mathbf{B}_0$ [152]. Since the density fluctuations are proportional to the parallel electric and magnetic field fluctuations [176], we expect to see only weak ion density fluctuations due to the i-mirror mode in our 2D periodic-box simulations.

Panel (b) of Figure 36 displays the variations of the ion density, $[\langle n_i - n_0 \rangle_{x,avg}/n_0] \approx \pm 0.01$, aver-

aged over the x-direction in the periodic-box simulation for the LM3.0β50 model. Panel (a) shows the fluctuations of the transverse component of $\mathbf{B}_0$, $[\langle B_y - B_0 \rangle_{\mathrm{x,avg}}/B_0] \approx \pm 0.4$, which have a relatively large amplitude due to the AIC-driven waves. It shows that even after the AIC-driven waves have fully grown, they have little effects on the ion density fluctuations.

However, the ion density fluctuations of the rippling waves propagating along the shock surface behind the shock ramp are rather significant in the shock simulation for the M3.0β50 model in HKRK2021. Panel (c) shows that both the variations of $[\langle n_i - n_0 \rangle_{\mathrm{x,avg}}/n_0] \approx \pm 0.1$ and $[\langle B_y - B_0 \rangle_{\mathrm{x,avg}}/B_0] \approx \pm 0.1$ have similar amplitudes; the fluctuations of n_i are much larger than those of the linear prediction expected for the parallel-propagating AIC mode. Note that here the quantities are averaged along the x-direction over the shock transition zone including the first and second overshoot oscillations behind the ramp. Hence, the basic assumptions of the linear theory, such as the homogeneous background, charge neutrality, and zero net-current, are likely to be violated in this region.

We point that such large-amplitude fluctuations of n_i, comparable to the fluctuations of B_y, were previously recognized in the 2D hybrid simulations of supercritical, perpendicular shocks presented in [168]. The authors suggested that large compressive waves might result from nonlinear effects in addition to oblique i-mirror modes. The effects due to nonlinear couplings between various wave modes could be significant as well [177–179]. Therefore, the pure AIC-driven waves in the shock transition could have been modified by such possible nonlinearities, leading to the enhancement of ion density fluctuations.

6.4 Summary

In this work, adopting the numerical estimates for the ion and electron temperature anisotropies found in the 2D PIC simulations of $Q_\perp$-shocks with $M_s = 2 - 3$ (see Table 7), we have carried out the kinetic linear analysis of the microinstabilities for wide ranges of parameters, $\beta = 1 - 100$ and $m_i/m_e = 50 - 1836$. The linear predictions for the fastest growing mode, γ_m, k_m, θ_m, of each instability are given in Table 7. In addition, in order to investigate the development and nonlinear evolution of the waves induced by the microinstabilities, we have performed the 2D PIC simulations with periodic boundary conditions for the three fiducial models, LM2.0β50, LM2.3β50, and LM3.0β50. Finally, the results were also compared with the 2D PIC simulations for ICM shocks reported in the following Section VII.

According to the linear analysis results, the generation of microinstabilities depends on M_s, because $\mathscr{A}_e$ and $\mathscr{A}_i$ increase as M_s increases. Especially, AIC can be induced only at the shocks with $M_s \gtrsim 2.3$ (see also Section VII). In addition, the maximum growth rates of the four instabilities have the following order: $\gamma_{\mathrm{WI}} \gg \gamma_{\mathrm{E-M}} \gg \gamma_{\mathrm{AIC}} > \gamma_{\mathrm{I-M}}$ (Figure 31). Hence, the parallel-propagating AIC and whistler waves are expected to be more dominant than the oblique-propagating mirror waves. Based on the parameter dependence presented in this work, the generation of multi-scale plasma waves and relevant physics for that could be applicable in the realistic ICM environments with $m_i/m_e = 1836$.

The 2D periodic-box simulations confirm the linear predictions. In the early stage of $\sim \tau_{\mathrm{WI}}$, electron-
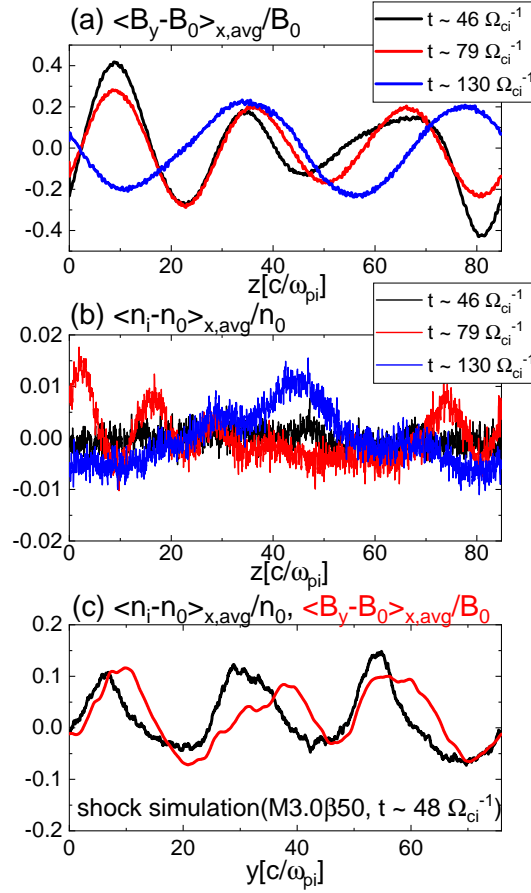
Figure 36: (a)-(b): Variations in the transverse component of magnetic field, $\langle B_y - B_0 \rangle_{\mathrm{x,avg}}/B_0$, and the ion-density, $\langle n_{\mathrm{i}} - n_0 \rangle_{\mathrm{x,avg}}/n_0$, averaged over the x-domain in the 2D periodic-box simulation for the LM3.0β50 model, plotted along $\mathbf{B}_0$ (z-direction) at three different times. (c): Variations in the longitudinal component of magnetic field, $\langle B_y - B_0 \rangle_{\mathrm{x,avg}}/B_0$ (red), and the ion-density, $\langle n_{\mathrm{i}} - n_0 \rangle_{\mathrm{x,avg}}/n_0$ (black), averaged along the x-direction over the shock transition zone in the 2D shock simulation for the M3.0β50 model in HKRK2021, plotted along the y-direction. Note that the preshock magnetic field, $\mathbf{B}_0^{\mathrm{up}}$, lies in the x-y plane, and the obliquity angle between $\mathbf{B}_0^{\mathrm{up}}$ and the y-axis is $\theta_{\mathrm{Bn}} = 63°$ in the shock simulation.

scale waves develop and then decay as $\mathscr{A}_{\mathrm{e}}$ is relaxed, followed by the growth of ion-scale waves on the time scale of $\sim \tau_{\mathrm{AIC}}$ (Figures 34 and 35). In addition, The rippling waves propagating along the shock surface have the characteristics of the AIC waves. Although the AIC waves are parallel-propagating, electromagnetic, incompressible in the linear regime, the amplitudes of the longitudinal magnetic field and ion-density fluctuations associated with the overshoots in the shock transition are similar and of the order of 10% according to the shock simulation for the M3.0β50 model (Figure 36). It is expected that the inhomogeneity in the shock transition and the nonlinear effects could lead to the generation of such large-amplitude fluctuations of the ion-density along the shock surface.

In conclusion, our results well support the suggestion for the generation of multi-scale plasma waves via various microinstabilities in the transition region of high-β, supercritical, $Q_{\perp}$-shocks [141, 151, 161, 181]. A detailed description of the shock structure and the electron preacceleration in such ICM shocks, realized in 2D PIC simulations, is reported in the following Section VII.

VII Electron Preacceleration at Weak Quasi-perpendicular Shocks in Intracluster Medium: 3. Preacceleration Mechanisms

As noted in the previous sections, the acceleration of nonthermal particles at collisionless shocks in tenuous astrophysical plasmas involves a very broad spectrum of complex kinetic plasma processes [22, 32, 150] and so the microinstabilities covered in Section V and VI could play an important role in electron acceleration at the ICM shocks. The acceleration process depends on various parameters including the sonic Mach number, M_s, the plasma beta, $\beta = P_{\text{gas}}/P_B$ (the ratio of thermal to magnetic pressures), and the obliquity angle, θ_{Bn}, between the upstream background magnetic field direction and the shock normal. In this Section, we study the detailed electron acceleration mechanism at the ICM shocks by performing PIC simulations with the relevant parameters (M_s, β, & T) for ICM (Ha, J.-H., Kim, S., Ryu, D., & Kang, H. 2021, The Astrophysical Journal, 915, 18; [163]).

7.1 Basic Physics of $Q_\perp$-Shocks

The physics of kinetic plasma processes in collisionless, $Q_\perp$-shocks is complex. For comprehensive reviews, readers are referred to [150] and [182]. A brief overview of some key problems that are relevant for this study can be found in [140] (KRH2019, hereafter).

The structures and ensuing excitation of microinstabilities are primarily governed by the dynamics of shock-reflected ions and electrons. Figure 37 illustrates the typical structures of a supercritical $Q_\perp$-shock: (1) the shock foot emerges due to the upstream gyration of reflected ions, and (2) overshoot/undershoot oscillations develop due to the downstream gyration of those reflected ions in the shock transition zone. The figure also depicts that the EFI is excited in the preshock region by the SDA-reflected electrons backstreaming along the background magnetic field [24], whereas the AIC and whistler instabilities are excited along the first and second overshoots, leading to the shock surface rippling [141, 151].

Electron Reflection and Shock Drift Acceleration

We here describe the basic physics regarding electron reflection and Shock Drift Acceleration (SDA) at the shock surface. Note that while we particularly focus on the acceleration physics at shocks in the ICM, the physics described here can be applied in general astrophysical shocks.

The electron reflection at the shock surface is governed by the magnetic mirror reflection. Because magnetic field is compressed at the shock, a substantial fraction of electrons can be reflected if the upstream electrons meet the condition for reflection. If the electrons are satisfied the reflection condition, they gain energy simultaneously through the motional electric field which is generated by the upstream bulk magnetized flow and move back to the shock upstream. Such acceleration cycle is the so-called SDA. In Section III, we describe the reflection of upstream protons (or ions) and preacceleration mediated by SDA at $Q_\parallel$-shocks. Regarding protons, the shock reflection is mainly governed by the shock potential, while magnetic mirror reflection makes only minor contribution for that. However, the shock
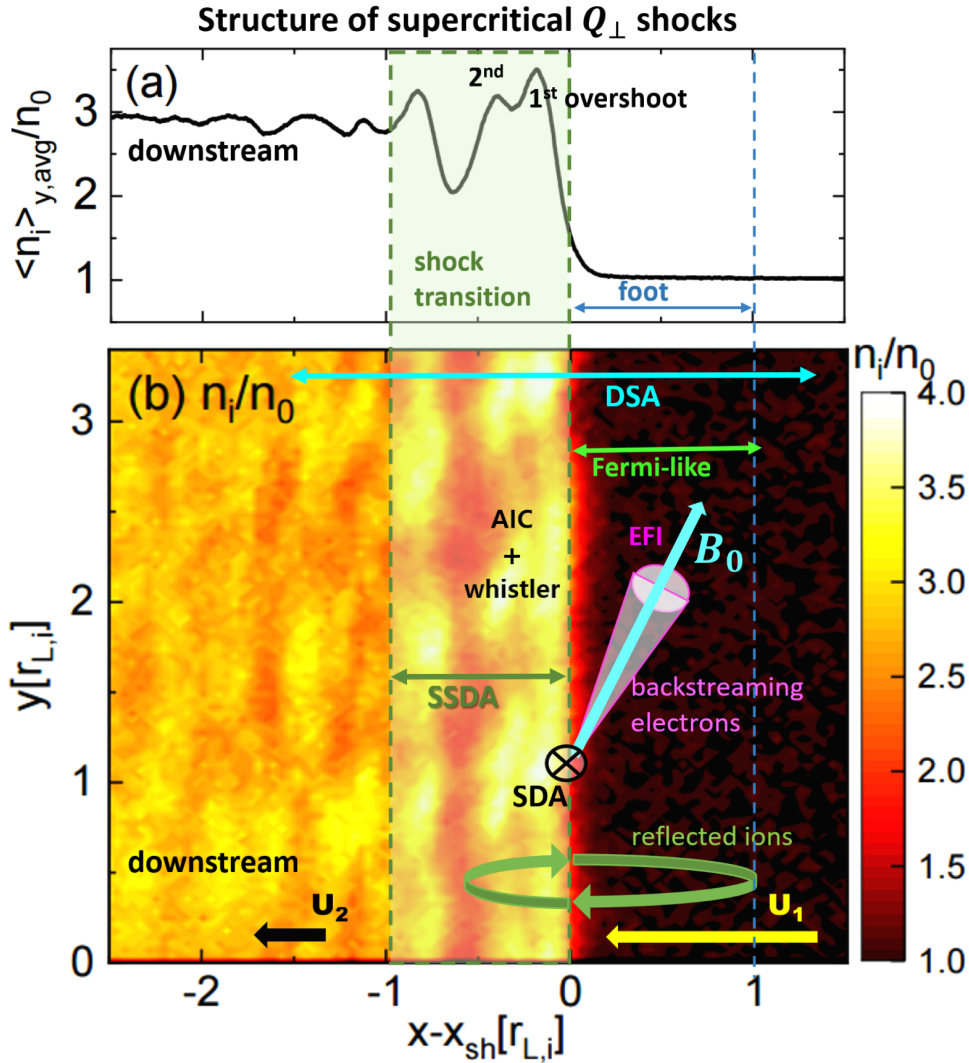
Figure 37: (a) Ion number density, $\langle n_i \rangle_{y,\text{avg}}/n_0$, averaged over the y-direction, normalized to the upstream ion number density, n_0, for a supercritical $Q_\perp$-shock (M3.0 model). (b) Ion number density, $n_i(x,y)/n_0$, in the $x-y$ plane for the same model. 2D PIC simulation results are shown in the region of $-2.5 \leq (x-x_{\text{sh}})/r_{\text{L,i}} \leq 1.5$ at $\Omega_{\text{ci}}t \sim 32$, where x_{sh} is the shock position. The gyromotion of reflected ions (green circular arrows) generates the overshoot/undershoot structure in the shock transition, while the backstreaming of SDA-reflected electrons (magenta cone) induces the temperature anisotropy and the EFI in the the preshock region. The colored arrows indicate the regions where DSA (cyan), SSDA (dark green), and Fermi-like acceleration (light green) operate. The labels for the three instabilities, AIC, whistler, and EFI, are placed in the regions where the respective instabilities are excited. During a SDA cycle, electrons drift in the negative z-direction (into the paper here) anti-parallel to the convection electric field $\vec{E}_{\text{conv}} = -(1/c)\vec{U}_1 \times \vec{B}_0$.

potential suppresses the electron reflection because it drags the upstream electrons to the shock downstream. Hence, to treat electron reflection at the shock, the effects of both magnetic mirror and shock potential should be rigorously considered.

A theory of SDA considering a shock surface as a magnetic mirror has been used in previous works regarding electron acceleration (e.g., [23, 24, 140]). That theory mainly describes the criteria for electron reflection at the magnetic mirror (i.e., the conditions that electrons are not in the loss-cone). To build a magnetic mirror model for a shock, it is necessary to chosse proper frame for that. There are three frames which are typically adopted in the shock simulation: (1) downstream rest frame: downstream has zero velocity so both shock surface and upstream flow have velocity (i.e., the simulation frame adopted in the thesis). (2) upstream rest frame: upstream has zero velocity, so shock surface and downstream have the same velocity to move, (3) shock rest frame: downstream and upstream flows have speed and the upstream flow speed is faster than the downstream flow speed as a factor of shock compression ratio. In such frames, acceleration via motional electric fields in shock upstream/downstream should be considered simultaneously while considering the mirror reflection condition. Because the strength of motional electric field is just determined by the shock Mach number, M_s, so it would be better if we can treat the reflection and energy gain via motional electric field, seperately. In this context, previous works (e.g., [23, 24, 140]) typically employ de Hoffmann-Teller (HT, hereafter) frame. HT frame has zero motional electric field in both shock upstream and downstream because the background magnetic field is parallel to the flow velocity [183]. In the HT frame, the flow speed measured in the upstream is $u_{\mathrm{t,HT}} = u_{\mathrm{sh}}/\cos\theta_{\mathrm{Bn}}$ where u_{sh} stands for the shock speed measured in the upstream rest frame.

[23] proposed a relativistic SDA theory. Using the reflection conditions in the HT frame given in the Equations (13) & (14) of [23], KRH2019 rewrites the conditions in the upstream rest frame, which are given as follows,

$$v_\parallel < u_{\mathrm{t,HT}} \tag{49}$$

(the same as the Equation (19) of [23]), and

$$v_\perp \gtrsim \gamma_{\mathrm{t,HT}}\tan\alpha_0[(v_\parallel - u_{\mathrm{t,HT}})^2 + 2c^2\cos^2\alpha_0\Delta\phi\left(1 - \frac{v_\parallel u_{\mathrm{t,HT}}}{c^2}\right)^2\left(1 - \frac{(v_\parallel - u_{\mathrm{t,HT}})^2}{(1 - v_\parallel u_{\mathrm{t,HT}}/c^2)^2 c^2\cos^2\alpha_0}\right)^{1/2}$$
$$+ (c^2\cos^2\alpha_0\left(1 - \frac{v_\parallel u_{\mathrm{t,HT}}}{c^2}\right)^2 - (v_\parallel - u_{\mathrm{t,HT}})^2)\Delta\phi^2]^{1/2}. \tag{50}$$

Here, $v_\parallel$ and $v_\perp$ denotes the parallel and perpendicular velocities with respect to the background magnetic field, $\gamma_{\mathrm{t,HT}}$ is the Lorentz factor of $u_{\mathrm{t,HT}}$, $\Delta\phi/m_e c^2$ is the electrostatic shock potential and $\alpha_0 \equiv \sin^{-1}(1/\sqrt{r})$ is the pith angle of mirror reflection with the shock compression ratio, r. Note that the equation for $v_\perp$ is obtained by assuming very small shock potential in the ICM with $T \sim 10^8$ K, $\Delta\phi/m_e c^2 \ll 1$.

Based on the criteria described above, [24] and KRH2019 calculated the electron reflection fraction with various parameters relevant for ICM shocks, $T = 10^8$K, $\beta = 100$, $M_s \approx 2 - 3$ and $\theta_{\mathrm{Bn}} = 13° - 63°$. The main findings are summarized as follows. (1) The reflection fraction increases with M_s because the magnetic compression ratio at the shock also increases with M_s. Note that the shock with larger

M_s has larger the shock potential, $\Delta\phi$, so such effect could suppress the electron reflection. In this sense, the reflection fraction could decrease as M_s increases. However, the contribution of the shock potential is negligible in the ICM enviroments, $\Delta\phi/m_e c^2 \ll 1$, therefore, more electrons are reflected at larger M_s shock. (2) The reflection fraction at $Q_\perp$-shock is larger than that of $Q_\parallel$-shock because such the magnetic field strength at the shock is larger with larger θ_{Bn}. (3) Because the motional electric field is larger at larger M_s, the average energy gain through SDA increases as M_s. (4) The reflection fraction becomes dropped if the shock speed in the HT frame is larger than the speed of thermal electron, $v_{\mathrm{th,e}} = \sqrt{2k_B T_e/m_e}$ (i.e., $u_{\mathrm{t,HT}} = u_{\mathrm{sh}}/\cos\theta_{\mathrm{Bn}} > v_{\mathrm{th,e}}$ or $\theta_{\mathrm{Bn}} \lesssim \cos^{-1}(M_s\sqrt{m_e/m_i})$). This is because, a substantial fraction of electrons moves slower than $v_{\mathrm{th,e}}$ in the HT frame. For the shock with $m_i/m_e = 50$ and $M_s = 3$, for example, the minimum value for efficient electron reflection is $\theta_{\mathrm{limit}} \approx 65°$ and θ_{limit} is larger at the shocks with smaller M_s. (5) If the shock speed in the HT frame is larger than the speed of light (i.e., $u_{\mathrm{t,HT}} = u_{\mathrm{sh}}/\cos\theta_{\mathrm{Bn}} > c$), the electron reflection at the shock becomes impossible, because electrons cannot move faster than the speed of light. For nonrelativistic shocks with $u_{\mathrm{sh}} \ll c$, shock with large θ_{Bn} becomes superluminal shock. In case of the shock with $m_i/m_e = 50$ and $M_s = 3$, for instance, the minimum obliquity angle for superluminal shock is $\theta_{\mathrm{sl}} \approx 84°$ and θ_{sl} increases as M_s decreases.

Shock Criticality

As described above, the reflection of upstream electrons is mainly governed by the magnetic mirror effect due to the magnetic compression at the shock, whereas the shock potential is mainly responsible for the reflection of upstream ions. While only *fast first critical Mach number*, M_{f}^* is introduced in Section III [89], there are a few varieties of critical Mach numbers, including the *second and third whistler critical Mach numbers*, which are related to the emission of dispersive whistler waves and quasi-periodic shock-reformation [184, 185]. Obviously, these processes depend on the shock obliquity angle, θ_{Bn}, and the plasma β, because ion reflection is affected by anomalous resistivity and microinstabilities in the shock transition.

In [83] and KRH2019, examining the shock structure, energy spectra of ions and electrons, and self-excited waves in shock models with $M_s \approx 2 - 3$, it was suggested that, in high-β (~ 100) ICM plasmas, the first critical Mach number for ion reflection is $M_s^* \sim 2.3$ for both $Q_\parallel$ and $Q_\perp$ shocks, while the EFI critical Mach number for the excitation of the EFI is also $M_{\mathrm{ef}}^* \sim 2.3$ for $Q_\perp$-shocks. These two critical Mach numbers are closely related, since the oscillations in the shock transition due to ion reflection enhance the magnetic mirror and electron reflection. The critical mach number M_s^* is higher than the fast first critical Mach number, $M_{\mathrm{f}}^* \sim 1$, estimated for $\beta \sim 4$ by [89] using the fluid description, in which kinetic processes such as wave excitations and wave-particle interactions were not accounted for.

Note that $M_A \gg M_s \approx M_f$ in $\beta \gg 1$ plasmas. In KRH2019, we argued that the critical Mach number for weak ICM shocks should be characterized with M_s, instead of M_A, since primarily the sonic Mach number controls both the shock electrostatic potential drop relevant for ion reflection and the magnetic field compression relevant for electron reflection.

In this work, we explore the shock criticality in terms of the shock surface rippling triggered by the

AIC instability, using 2D PIC simulations with a transverse dimension large enough to include ion-scale fluctuations.

Fermi-like Preacceleration in Shock Foot

[23, 24] and KRH2019 demonstrated that thermal electrons could be preaccelerated via a Fermi-like acceleration in the foot of $M_s = 3$ shocks in $\beta = 20$ ICM plasmas. The key processes involved in this preacceleration include the following: (1) a fraction ($\sim 20\%$) of incoming thermal electrons are reflected and energized through the standard SDA at the shock ramp, (2) the SDA-reflected electrons backstreaming along the background magnetic field generate oblique waves via the EFI due to the electron temperature anisotropy ($T_{e\parallel}/T_{e\perp} > 1$), and (3) some electrons are scattered back and forth between the shock ramp and the EFI-driven upstream waves, gaining energy further through multiple cycles of SDA. Although the EFI-driven waves can be generated broadly in the upstream region, depending on $T_{e\parallel}/T_{e\perp}$, the Fermi-like acceleration occurs primarily within the shock foot. In the course of this Fermi-like acceleration, electrons stay in the upstream region of the shock, hence they are energized mainly through the gradient-drift along the motional electric field at the shock ramp. The authors showed that this acceleration is effective for $\beta \gtrsim 20$ shocks, whereas the EFI is suppressed at low-β plasmas due to strong magnetization of electrons. Moreover, the EFI is known to be almost independent of the mass ratio, m_i/m_e. (4) KRH2019 found that nonpropagating oblique waves in the shock upstream with $\lambda \sim 15 - 20c/\omega_{pe}$ are dominantly excited, and that the scattering of electrons by those waves reduces the temperature anisotropy and stabilize the EFI. Thus, we suggested that the preacceleration of electrons by the Fermi-like acceleration involving multiple cycles of SDA may not proceed all the way to DSA in weak ICM shocks. This calls for additional mechanisms that could energize electrons beyond the point where the Fermi-like acceleration ceases to operate.

Stochastic Shock Drift Acceleration in Shock Transition

[161] proposed that the electron preacceleration via SDA could be extended by stochastic pitch-angle scattering off these multi-scale waves, because electrons are trapped much longer in the shock transition zone. They coined the term "stochastic shock drift acceleration (SSDA)" for such acceleration. Then, [141, 162] performed a 2D PIC simulation for $M_s = 3$ shock with $\beta = 5$, $\theta_{Bn} = 75°$ and $m_i/m_e = 100$. They observed the emergence of shock surface rippling, accompanied by the plasma waves driven by the various microinstabilities (AIC and whistler) in the shock transition, as well as the EFI-driven obliques waves in the preshock region. They also saw the development of suprathermal tails in both the upstream and downstream energy spectra of electrons that extend slightly beyond p_{inj} by the end of their simulations.

Furthermore, [151] performed 2D and 3D hybrid simulations with test-particle electrons for $Q_\perp$-shocks with $M_s = 2.9 - 6.6$, $\beta \approx 1$, and $\theta_{Bn} = 80° - 87°$. In typical hybrid simulations, ions are treated kinetically, while electrons are treated as a charge-neutralizing fluid. So this type of simulations cannot properly capture electron-driven instabilities. With that caveat, they observed that shock surface fluctu-

Table 9: Model Parameters for PIC Simulations

	M_s	M_A	θ_{Bn}	β	$T_{e0} = T_{i0}$[K(keV)]	m_i/m_e	$L_x[c/\omega_{pe}]$	$L_y[c/\omega_{pe}]$	$\Delta x[c/\omega_{pe}]$
M2.0	2.0	12.9	63°	50	10^8(8.6)	50	3200	310	0.1
M2.15	2.15	13.9	63°	50	10^8(8.6)	50	3200	310	0.1
M2.3	2.3	14.8	63°	50	10^8(8.6)	50	3200	310	0.1
M2.5	2.5	16.1	63°	50	10^8(8.6)	50	3200	310	0.1
M2.8	2.8	18.1	63°	50	10^8(8.6)	50	3200	310	0.1
M3.0	3.0	19.4	63°	50	10^8(8.6)	50	3200	310	0.1
M2.0-m100	2.0	12.9	63°	50	10^8(8.6)	100	2000	440	0.1
M2.3-m100	2.3	14.8	63°	50	10^8(8.6)	100	2000	440	0.1
M3.0-m100	3.0	19.4	63°	50	10^8(8.6)	100	2000	440	0.1
M2.0-β20	2.0	8.2	63°	20	10^8(8.6)	50	3200	200	0.1
M2.3-β20	2.3	9.4	63°	20	10^8(8.6)	50	3200	200	0.1
M3.0-β20	3.0	12.3	63°	20	10^8(8.6)	50	3200	200	0.1
M2.0-β100	2.0	18.2	63°	100	10^8(8.6)	50	2000	440	0.1
M2.3-β100	2.3	21.0	63°	100	10^8(8.6)	50	2000	440	0.1
M3.0-β100	3.0	27.4	63°	100	10^8(8.6)	50	2000	440	0.1
M2.0-θ53	2.0	12.9	53°	50	10^8(8.6)	50	3200	310	0.1
M2.0-θ73	2.0	12.9	73°	50	10^8(8.6)	50	3200	310	0.1
M2.3-θ53	2.3	14.8	53°	50	10^8(8.6)	50	3200	310	0.1
M2.3-θ73	2.3	14.8	73°	50	10^8(8.6)	50	3200	310	0.1
M3.0-θ53	3.0	19.4	53°	50	10^8(8.6)	50	3200	310	0.1
M3.0-θ73	3.0	19.4	73°	50	10^8(8.6)	50	4000	310	0.1

ations develop on ion scales, and that test-particles electrons could be preaccelerated well beyond p_{inj} at supercritical shocks with the Alfvénic Mach number greater than the critical Mach number, $M_{A,crit} \approx 3.5$. Note that they considered $\beta \approx 1$ shocks, so $M_{s,crit} \approx M_{A,crit}$.

7.2 Numerics

2D PIC simulations were performed to generate collisionless shocks by adopting the same numerical setup described in Section III, except that here the transverse box size in unit of $r_{L,i}$ is much larger than that used in Section III. For all simulation models considered here, the transverse box size is larger than $\sim 3.4 r_{L,i}$ to resolve the plasma waves induced as consequence of the ion dynamics at the shock. The model parameters are given in Table 9. Models with different M_s are named with the combination of the letter "M" and sonic Mach numbers (e.g., the M3.0 model has $M_s = 3.0$). Six models, M2.0-M3.0, in the top group represent our 'fiducial' models with $\beta = 50$, $\theta_{Bn} = 63°$, and $m_i/m_e = 50$. Models with the parameters different from the fiducial values have the names that are appended by a character for

the specific parameter and its value. For example, the M3.0-m100 model has $m_i/m_e = 100$, while the M3.0-θ53 model has $\theta_{\mathrm{Bn}} = 53°$.

7.3 Results

Shock Criticality and Surface Rippling

To understand the shock structures, we first look at the 2D spatial distributions of the ion number density and magnetic field strength for the M2.0 (subcritical) and M3.0 (supercritical) models in Figure 38(a)-(d). In the M3.0 model, overshoot/undershoot oscillations develop and ripples appear in the shock transition zone along the shock surface, while the overall shock structure is relatively smooth in the M2.0 model. Panels (e) and (f) of Figure 38 show that the ion temperature anisotropy, $\mathscr{A}_i > 1$, is generated in the shock transition due to the shock-reflected ions in the M3.0 model, while $\mathscr{A}_i \approx 1$ due to inefficient ion reflection in the M2.0 model.

Based on the findings of KHRK2021 and previous studies [141, 151, 174, 175], we interpret that the ripples along the shock surface are induced by the AIC instability. In the fiducial M3.0 model, the characteristic length of the ripples is $\lambda_{\mathrm{ripple}} \sim 14 c/\omega_{\mathrm{pi}} \sim 1.1 r_{\mathrm{L,i}} \sim 0.8\lambda_{\mathrm{AIC}}$, where $\lambda_{\mathrm{AIC}} \sim 18 c/\omega_{\mathrm{pi}} \sim 1.4 r_{\mathrm{L,i}}$ is the wavelength of the AIC-driven waves with the maximum growth rate. The simulation domain is periodic in the y-direction and the transverse dimension of all the $M_{\mathrm{s}} = 3.0$ models in Table 1 is $L_{\mathrm{y}} \approx 3.4 r_{\mathrm{L,i}} \sim 2.4 - 2.6\lambda_{\mathrm{AIC}}$. Hence, on average about 2-3 waves are expected to develop along the y-direction (see also Figure 44(g)-(i)), resulting in $\lambda_{\mathrm{ripple}} \sim 0.8 - 1.3\lambda_{\mathrm{AIC}}$. In addition, the rippling waves propagate along the shock surface with the Alfvén speed in the shock overshoot, $v_{\mathrm{A,os}} = B_{\mathrm{os}}/\sqrt{4\pi n_{\mathrm{os}} m_{\mathrm{i}}} \sim 0.009 c$, where B_{os} and n_{os} are the magnetic field strength and the ion number density of the shock overshoot, respectively. Hence, we regard that the rippling waves have the characteristics of the waves driven by the AIC instability [174].

Using both linear theory and hybrid simulations, [169] presented the instability condition for the AIC instability:

$$I_{\mathrm{AIC}} = \frac{T_{\mathrm{i}\perp}}{T_{\mathrm{i}\parallel}} - 1 - \frac{S_p}{\beta_{\mathrm{i}\parallel}^{\alpha_p}} > 0, \tag{51}$$

where $\beta_{\mathrm{i}\parallel} = 8\pi n_{\mathrm{i}} k_{\mathrm{B}} T_{\mathrm{i}\parallel}/B_0^2$ is the ion β parallel to the magnetic field. The fitting parameters are $\alpha_p \approx 0.72$ and $S_p \approx 1.6$ for $\beta_{\mathrm{i}\parallel} \approx 5 - 50$ (see their Figure 8). This condition signifies that the AIC instability tends to be stabilized at lower $\beta_{\mathrm{i}\parallel}$ due to the stronger magnetization of ions. For a given value of $\beta_{\mathrm{i}\parallel}$, the AIC growth rate increases with increasing $\mathscr{A}_i$, which in turn depends on the fraction of reflected ions. Sine the ion temperature anisotropy is higher at stronger shocks, the transition zone is expected to be more unstable against the AIC instability in shocks with higher M_{s}.

Here, using the simulation results for the anisotropy $\mathscr{A}_i$, we calculate the instability parameter, I_{AIC}, which is shown in Figure 39(a). For $M_{\mathrm{s}} = 2$, $I_{\mathrm{AIC}} \lesssim 0$, so the AIC instability is stable, which is consistent with the smooth shock structure shown in Figure 38. The instability parameter increases steeply around $M_{\mathrm{s}} \sim 2.2 - 2.4$. Considering also the simulation results described in the next section, we suggest that the critical Mach number to trigger the AIC instability is $M_{\mathrm{AIC}}^* \approx 2.3$ in these high-β shocks. We note
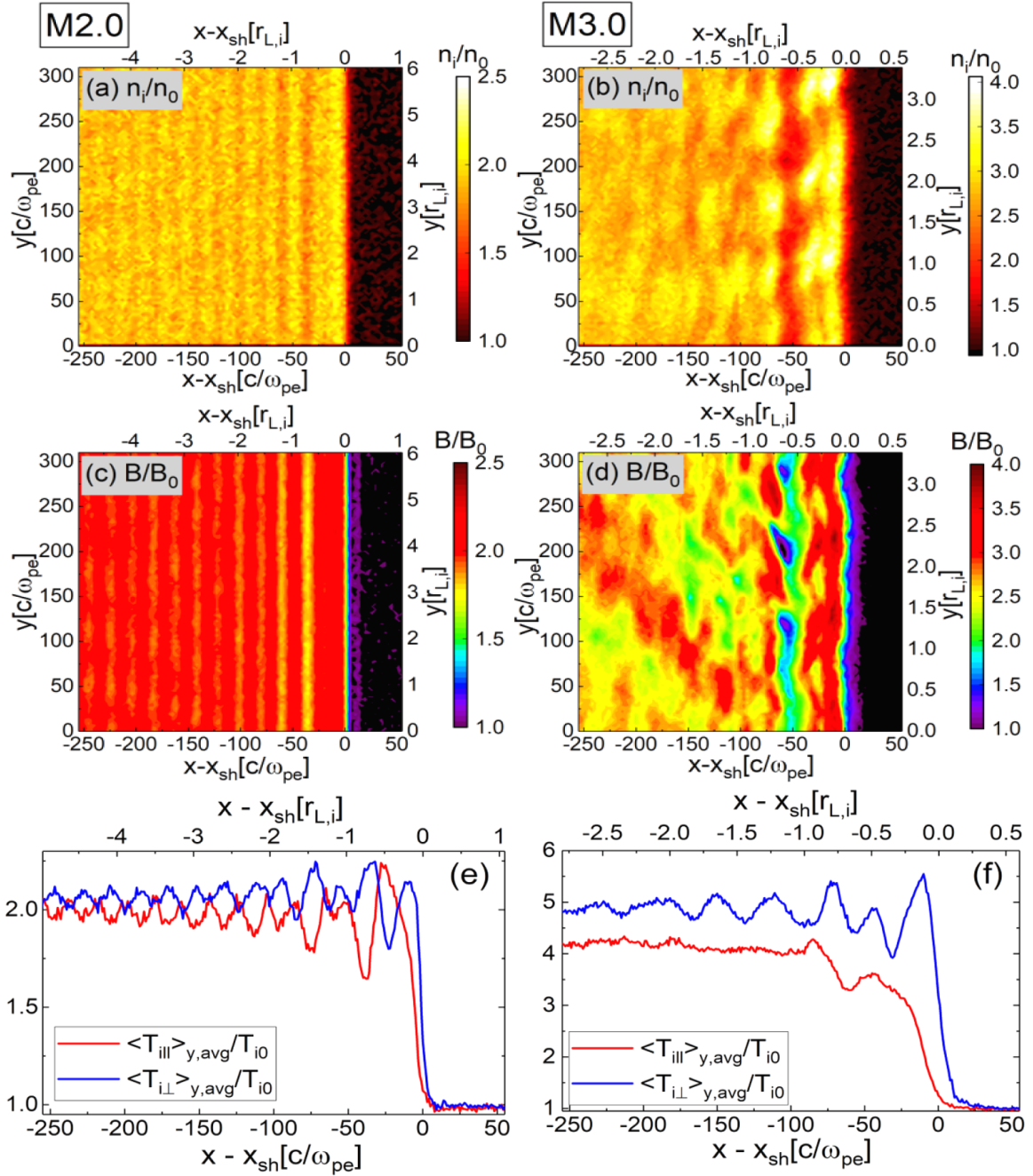
Figure 38: Shock structure in the M2.0 and M3.0 models in the region of $-255 \leq (x - x_{\mathrm{sh}})\omega_{\mathrm{pe}}/c \leq 55$ at $\Omega_{\mathrm{ci}}t \sim 32$. Panels (a)-(b) show the ion number density, n_{i}/n_0. Panels (c)-(d) show the magnetic field strength, B/B_0. Panels (e)-(f) show the ion temperature, $\langle T_{\mathrm{i}\|}\rangle_{y,\mathrm{avg}}/T_{\mathrm{i}0}$ (red), and $\langle T_{\mathrm{i}\perp}\rangle_{y,\mathrm{avg}}/T_{\mathrm{i}0}$ (blue), averaged over the y-direction. Here $r_{\mathrm{L,i}} \approx 91(c/\omega_{\mathrm{pe}}) \cdot (M_{\mathrm{s}}/3)$.
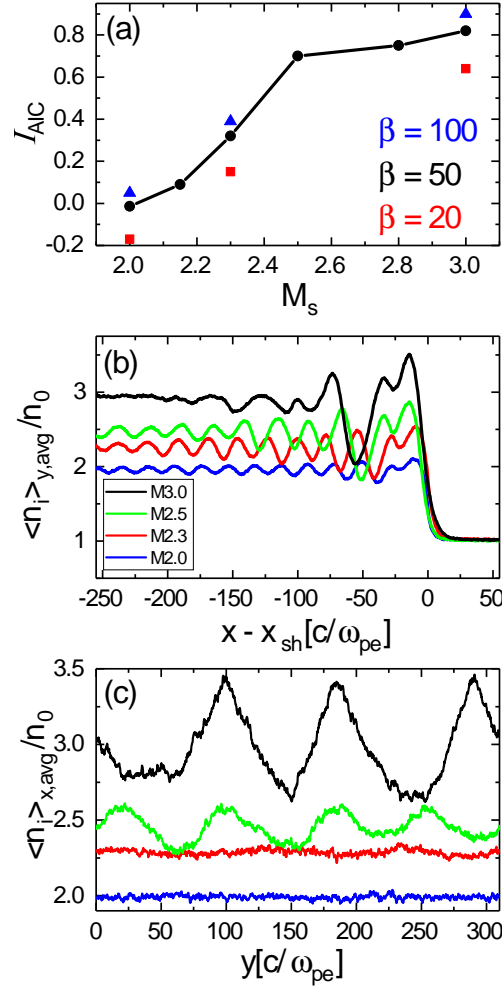
Figure 39: (a) Instability parameter, I_{AIC}, in Equation (51), estimated using the mean temperature and plasma beta, $\langle T_{\mathrm{i}\perp}\rangle$, $\langle T_{\mathrm{i}\parallel}\rangle$ and $\langle \beta_{\mathrm{i}\parallel}\rangle$, in the region of $(x - x_{\mathrm{sh}})\omega_{\mathrm{pe}}/c = [-50, 0]$ and $y\omega_{\mathrm{pe}}/c = [0, 310]$. The results for the fiducial models with $\beta = 50$ are shown by the black circles connected with the black line, while the models with $\beta = 100$ and 20 are presented by the blue triangles and red squares, respectively. (b) Ion number density, $\langle n_{\mathrm{i}}\rangle_{y,\mathrm{avg}}(x)$, averaged for $y\omega_{\mathrm{pe}}/c = [0, 310]$ in the fiducial models, M2.0(blue), M2.3 (red), M2.5 (green), and M3.0 (black). (c) Ion number density, $\langle n_{\mathrm{i}}\rangle_{x,\mathrm{avg}}(y)$, averaged for $(x - x_{\mathrm{sh}})\omega_{\mathrm{pe}}/c = [-50, 0]$ in the same fiducial models as in panel (b). For all the quantities, the simulation results at $\Omega_{\mathrm{ci}}t \sim 32$ are used.

that this is similar to the critical Mach number for ion reflection, M_s^*, reported in KRH2019, because the AIC instability is triggered by the shock-reflected ions.

As can be inferred from Equation (51), Figure 39(a) shows that with similar anisotropy $\mathscr{A}_i$'s, I_{AIC} decreases as β decreases from 100 (blue triangles) to 20 (red squares) owing to stronger magnetization at lower β. Thus, we expect that the AIC critical Mach number would be somewhat higher at lower-β shocks. For example, [180] estimated $M_{\mathrm{AIC}}^* \sim 4$ for $\beta \approx 1$, using hybrid simulations. [151] obtained a similar value, $M_{\mathrm{AIC}}^* \sim 3.5$ also for $\beta \approx 1$, as mentioned before.

Figure 39(b) shows the y-averaged ion number density profile, $\langle n_i \rangle_{y,\mathrm{avg}}(x)$, for the models with $M_s = 2 - 3$. It demonstrates that the shock becomes supercritical for $M_s \gtrsim 2.3$, developing substantial overshoot/undershoot oscillations in the shock transition. Figure 39(c), on the other hand, shows the ion number density profile, $\langle n_i \rangle_{x,\mathrm{avg}}(y)$, averaged over the shock transition zone in the x-direction, along the y axis (parallel to the shock surface) for the same four models. The mean wavelengths of the shock surface ripples are $\lambda \sim 100c/\omega_{\mathrm{pe}} \sim r_{\mathrm{L,i}}$ for the M3.0 model (black), while $\lambda \sim 75c/\omega_{\mathrm{pe}} \sim r_{\mathrm{L,i}}$ for for the M2.5 model (green). Note that here the Larmor radius of incoming ions, $r_{\mathrm{L,i}} \propto u_0 \propto M_s$, scales approximately with the shock Mach number. The variation of $\langle n_i \rangle_{x,\mathrm{avg}}$ along the shock surface is insignificant for $M_s \lesssim 2.3$.

Plasma Waves in Shock Transition

As discussed above, in the shock transition region of supercritical shocks, the ion temperature anisotropy ($\mathscr{A}_i$) can trigger the AIC and ion-mirror instabilities, while the electron temperature anisotropy ($\mathscr{A}_e$) can induce the whistler and electron-mirror instabilities. Due to the large mass ratio, typically electron-driven waves grow much faster on much smaller scales, compared to ion-driven waves (see also, [164]).

Panels (a)-(c) of Figure 40 show B_z/B_0 for three shock models. In the M3.0 model, we observe multi-scale waves with the wavelengths ranging from electron to ion scales in the shock transition region, $(x - x_{\mathrm{sh}})/r_{\mathrm{L,i}} \approx [-1, 0]$. Based on the linear analysis results shown in Section VI, in this supercritical shock we interpret that ion-scale fluctuations are induced dominantly by the AIC instability, while electron-scale waves are induced mainly by the whistler instability. In Figure 40(c) we can identify such AIC-driven waves propagating mainly in the direction parallel to $\mathbf{B_0}$. For comparison, the M3.0β50 model ($\beta = 50$, $m_i/m_e = 100$) of KRH2019 is shown in panel (g), which shows pronounced features on smaller scales. In the M2.3 model, on the other hand, the AIC mode is not observed, whereas oblique waves driven by the ion-mirror instability appear in the far downstream region ($x - x_{\mathrm{sh}} < -2.0r_{\mathrm{L,i}}$). In the M2.0 model shown in Figure 40(a), primarily electron-scale waves with small amplitudes are observed in the shock transition, while weak oblique waves probably due to the ion-mirror instability appear in the far downstream region.

The black lines in Figure 40(d)-(f) show the magnetic power spectra, P_{B_z}, in the shock transition region shown in the upper panels (a)-(c). In the M3.0 model, P_{B_z} indicates the presence of multi-scale waves in the wide range of wavenumbers, $k_y/2\pi \sim [0.009 - 0.9]\omega_{\mathrm{pe}}/c$, corresponding to $\lambda \sim [11.1 - 111]c/\omega_{\mathrm{pe}}$. In particular, the wavelength of the ion-scale waves driven by the AIC instability,
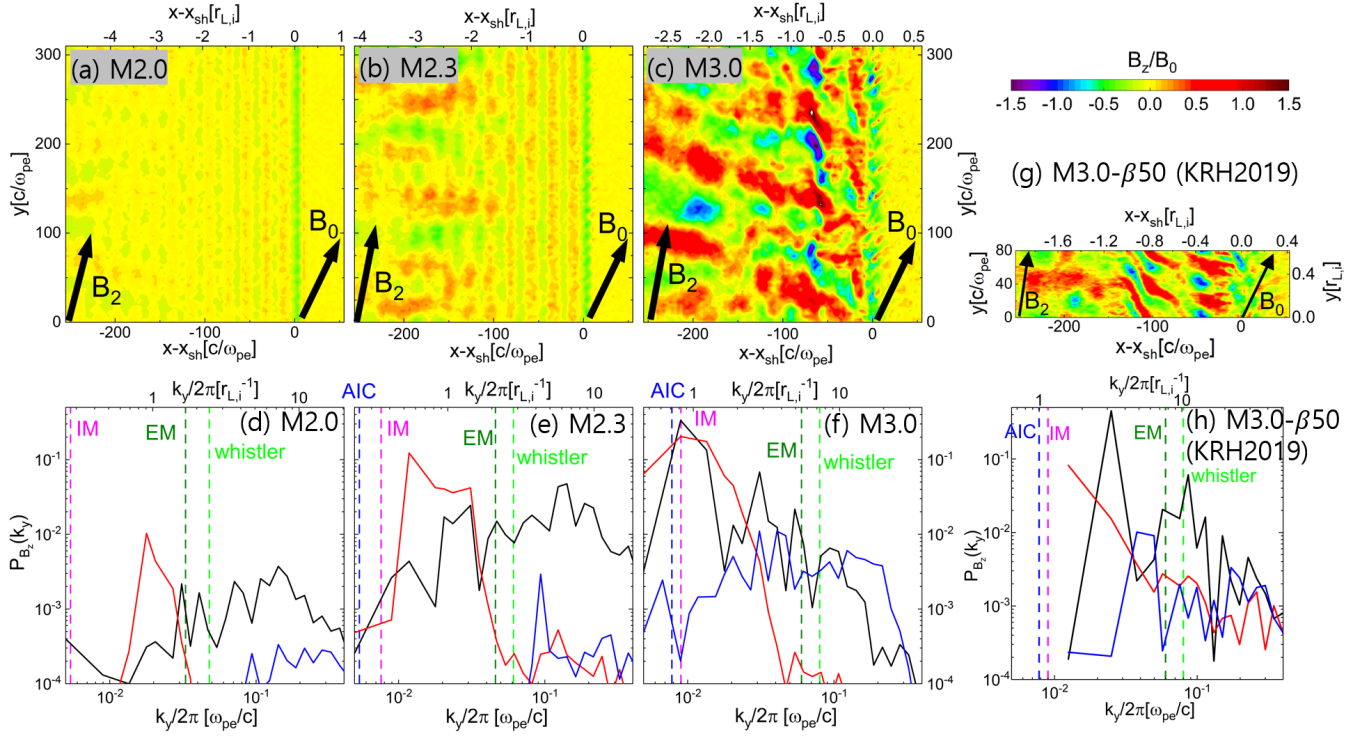
Figure 40: Panels (a)-(c): Magnetic field fluctuations, B_z/B_0, in the region of $(x - x_{\text{sh}})\omega_{\text{pe}}/c = [-255, +55]$ at $\Omega_{\text{ci}}t \sim 32$ for the fiducial models with $M_{\text{s}} = 2, 2.3$, and 3. The black arrows indicate the directions of the preshock and postshock magnetic field vectors, $\mathbf{B_0}$ and $\mathbf{B_2}$, respectively. Panels (d)-(f): Magnetic power spectrum, $P_{B_z}(k_y) \propto (k_y/2\pi)(\delta B_z(k_y)^2/B_0^2)$, is calculated for the shock transition region of $(x - x_{\text{sh}})/r_{\text{L,i}} \approx [-1.0, 0.0]$ (black), the far downstream region of $(x - x_{\text{sh}})/r_{\text{L,i}} \approx [-2.8, -1.8]$ (red), and the upstream region of $(x - x_{\text{sh}})/r_{\text{L,i}} \approx [0.2, 1.2]$ (blue) at $\Omega_{\text{ci}}t \sim 32$. The blue, bright green, magenta, and dark green vertical lines denote the wavenumbers with the maximum growth rates for the AIC, whistler, i-mirror, and e-mirror instabilities, respectively. Panels (g)-(h): Magnetic field fluctuations and power spectrum of the M3.0 model in KRH2019. For the models in the figure, $r_{\text{L,i}} \approx 91(c/\omega_{\text{pe}}) \cdot (M_{\text{s}}/3)\sqrt{\beta/50}\sqrt{(m_i/m_e)/50}$.
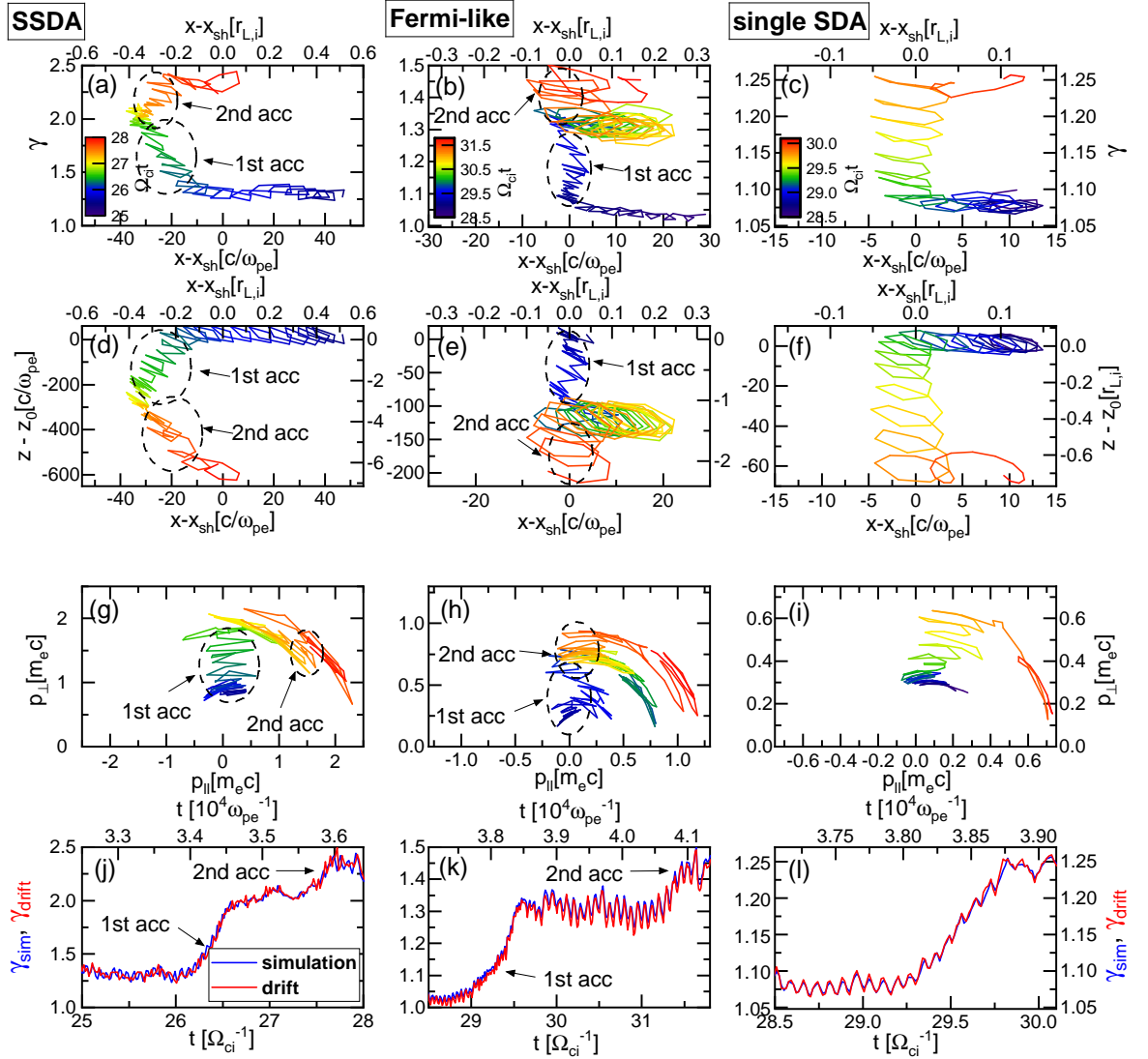
Figure 41: Left panels: Trajectory of a selected electron that undergoes the SSDA during $\Omega_{ci}t \sim 25 - 29.5$. Middle panels: Trajectory of a selected electron that undergoes the Fermi-like acceleration during $\Omega_{ci}t \sim 28 - 32$. Right Panels: Trajectory of a selected electron that undergoes a single SDA during $\Omega_{ci}t \sim 28.5 - 30.1$. Note that the trajectories in the shock rest frame are shown. They are taken from the M3.0 model simulation. In panels (g)-(i), the trajectories along the $p_\perp$-direction show the energy gain due to the gradient-B drift along the motional electric field, while trajectories along the arcs in the $p_\parallel - p_\perp$ space represent pitch-angle scattering. In panels (j)-(l), the blue lines show the evolution of the Lorentz factor, γ_{sim}, in the simulation frame, while the red lines show the energy gain, $\gamma_{drift} = -(e/m_e c^2) \int E_z dz$, estimated using the motional electric field in the shock transition zone.

$\lambda \sim 111 c/\omega_{\mathrm{pe}} \sim 1.2 r_{\mathrm{L,i}}$, is similar to the size of shock surface surface ripples, $\lambda_{\mathrm{ripple}}$, as shown in Figure 38. P_{B_z} shows substantial powers also on the electron-scale waves with $k_y/2\pi \sim 0.09\omega_{\mathrm{pe}}/c$ ($\lambda \sim 11.1 c/\omega_{\mathrm{pe}}$) driven by the whistler instability. Again, for comparison, P_{B_z} for the M3.0β50 model of KRH2019 is shown in Figure 40(h). Due to the smaller transverse domain, the powers on small wavenumbers, $k_y/2\pi \lesssim 10^{-2}\omega_{\mathrm{pe}}/c$, are not present. In the M2.3 model in panel (e), the electron-scale waves are relatively more dominant than the ion-scale waves, while the ion-scale waves are driven mainly by the ion-mirror instability as indicated in panel (b). In the M2.0 model in panel (d), the ion-scale waves are almost absent. These results are consistent with the fact that multi-scale plasma waves can be triggered by the AIC instability only in supercritical shocks with $M_{\mathrm{s}} \gtrsim 2.3$.

The plasma waves induced in the shock transition undergo nonlinear evolution, while being advected further downstream. In order to investigate such nonlinear evolution, in Figure 40(d)-(f), we also show P_{B_z} (red lines) in the far downstream region of $(x - x_{\mathrm{sh}})/r_{\mathrm{L,i}} \approx [-2.8, -1.8]$. A few points are noted: (1) The whistler waves are excited in the transition region immediately behind the ramp, and then undergo rapid damping via electron scattering, leading to the reduction of $\mathscr{A}_e$ in the far downstream region. So the magnetic power of electron-scale waves is significantly reduced there as well. (2) In Figure 40(f), P_{B_z} on ion-scale waves remains relatively substantial in the far downstream, even after experiencing nonlinear evolution. (3) In Figure 40(d)-(e), P_{B_z} on small k's is mainly due to the oblique waves excited by the ion-mirror instability in the far downstream region, which can be seen in Figure 40(a)-(b).

We point that the presence of shock surface ripples could enhance or supress the electron reflection at the shock surface. In the case of the shock with $M_{\mathrm{s}} = 3$, $T = 5 \times 10^8$ K, $m_i/m_e = 100$ and $\theta_{\mathrm{Bn}} = 73°$ [141], the electron reflection is initially ineffective, since the shock speed measured in the HT frame is larger than the electron thermal velocity, i.e., $u_{\mathrm{tmHT}} \sim 1.5 v_{\mathrm{th,e}}$. After $t \gtrsim \tau_{\mathrm{AIC}}$, the shock surface rippling produces the locally smaller θ_{Bn} portions and the electron reflection is enhanced (see their Figure 2) because the shock speeds in the HT frame in such local parts become smaller than the electron thermal velocity. In case of the our fiducial model with $M_{\mathrm{s}} = 3$ and $\theta_{\mathrm{Bn}} = 63°$, on the other hand, $u_{\mathrm{t,HT}} \sim v_{\mathrm{th,e}}$ and the fraction of reflection electrons is substantial ($\sim 23\%$) regardless of the presence of shock surface ripples (see Fig. 1 of KRH2019). In fact, the enhancement of the electron reflection fraction and the ensuing EFI-driven waves in the upstream region due to the shock ripples is only a few % (also compare the blue lines in panels (f) and (h) of Figure 40). Although the fraction of suprathermal electrons is increased slightly by the addition of the SSDA in the new simulations (see Figure 42), the impacts on the self-excited upstream waves seem only marginal possibly due to the limited integration time.

Electron Preacceleration via SSDA

To understand the preacceleration mechanism in our simulations, we examine how electrons gain energy in the M3.0 model shock. Figure 41 shows the trajectories of three selected electrons that gain energy via the SSDA (left panels), the Fermi-like acceleration (middle panels), and a single SDA (right panels). Note that the trajectories in the shock rest frame are shown, so that the region of $(x - x_{\mathrm{sh}})\omega_{\mathrm{pe}}/c \approx [-5, 5]$ corresponds to the shock ramp, while the downstream region of $(x - x_{\mathrm{sh}})\omega_{\mathrm{pe}}/c \approx [-50, 0]$ contains both
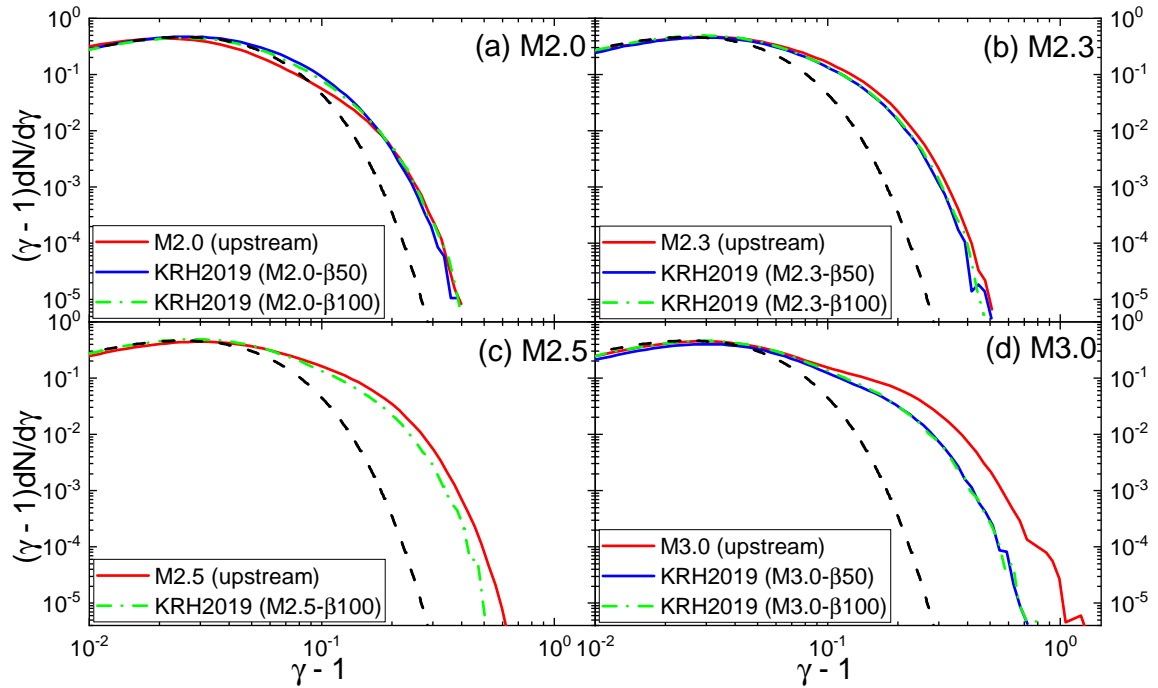
Figure 42: Upstream electron energy spectra (red solid lines) at $\Omega_{\mathrm{ci}}t \sim 32$ in the fiducial models with $M_{\mathrm{s}} = 2 - 3$. The spectra are taken from the region of $(x - x_{\mathrm{sh}})/r_{\mathrm{L,i}} = [0, +1]$ and the black dashed lines show the Maxwellian distributions in the upstream. The blue solid ($\beta = 50$) and green dot-dashed ($\beta = 100$) lines show the upstream electron energy spectra at $\Omega_{\mathrm{ci}}t \sim 30$ for the models in KRH2019, in which the transverse domain, $L_y/r_{\mathrm{L,i}}$, is about 8 times smaller than that of the simulations in this study.

the first and second overshoots in the transition zone (see Figure 2(b)). The trajectories in panels (a) and (d) show that this electron is confined within the transition zone during $\Omega_{ci}t \sim 26 - 28$, and undergoes the first (green) and second (orange) stages of the gradient-B drift along the $-z$-direction, illustrating the SSDA. Panels (b) and (e) show that the electron experiences the Fermi-like acceleration by going through the first (blue) and second (orange) stages of the SDA, while being reflected at the ramp and scattered by upstream waves. Panels (c) and (f) show that the electron undergoes only a single cycle of the standard SDA. In panels (g)-(i), the trajectories roughly parallel to the $p_\perp$-direction show the energy gain due to the drift along the motional electric field, while the trajectories following the arcs in the $p_\parallel - p_\perp$ space represent pitch-angle scattering. In panels (g) and (h), the electrons experience two episodes of acceleration, as indicated by the ellipses and arrows.

The bottom panels, (j)-(l), compare the variation of the Lorentz factor in the simulation (blue line) with the energy gain of $\gamma_{drift} = -(e/m_e c^2) \int E_z dz$ (red line), which is expected to accumulate from the drift along the motional electric field in the shock transition zone. We confirm that the preacceleration realized in the simulated shock is consistent with the SSDA mechanism proposed by previous studies [141, 161]. Although electrons can be energized by both the Fermi-like acceleration and SSDA, the most energetic electrons are produced mainly by the SSDA.

Figure 42 compares the upstream electron energy spectra in the fiducial models of the current study (red lines) with the corresponding spectra for the models with $\beta = 50$ (blue lines) and $\beta = 100$ (green lines) reported in KRH2019. Note that $m_i/m_e = 100$ in KRH2019, but the simulations were insensitive to the mass ratio [24]. As mentioned before, in KRH2019, the 2D simulation domain was too small in the transverse direction to include the emergence of the shock surface rippling via the AIC instability. As a result, the SDA-reflected electrons gain energy only through the Fermi-like acceleration in that study. The figure clearly demonstrates that in the case of supercritical shocks, through the SSDA, electrons can be accelerated further to higher energies in the new simulations than in the simulations of KRH2019. In subcritical shocks, on the other hand, the AIC instability is not triggered and the ensuing SSDA does not occur even in the new simulations with a larger simulation domain.

The PIC simulation of a $\beta \approx 5$ shock by [141] and the hybrid simulations of $\beta \approx 1$ shocks by [151] showed that electrons could be preaccelerated well above the injection momentum through the SSDA in supercritical shocks. In [141], for instance, the highest electron energy of $\gamma_{max} \approx 60$ was achieved by several phases of the SSDA for the simulation duration of $\Omega_{ci}t_{max} \approx 79$, while $\gamma_{inj} \approx 25$ for their shock parameters. By contrast, Figure 41 shows only two phases of the SSDA for the M3.0 model, resulting in $\gamma_{max} \sim 2.5$. So the electron energy spectra even in the new simulations (red) are extended to the energy below the injection momentum ($\gamma_{inj} \sim 7$), as shown in Figure 42(d). This is because the required computational resources for the PIC simulations of such high-β shocks are quite demanding. In fact, simulating electron energization all the way to injection to DSA in $\beta \approx 100$ shocks would require much larger simulation domains and much longer simulation times. However, we expect that the SSDA would continue to reach $p > p_{inj}$, as long as the electrons are confined within the shock transition region by scattering due to multi-scale waves.

Dependence on the Model Parameters

In this section, we examine how our findings depend on the simulation parameters such as β, m_i/m_e and θ_{Bn}.

In Figure 43 we compare the ion density distributions in the six M3.0 models with different parameters. Here the length scales are normalized with $r_{\mathrm{L,i}} \propto \sqrt{\beta}\sqrt{(m_i/m_e)}$. Panels (g)-(i) show the ion number density, $\langle n_i \rangle_{x,\mathrm{avg}}$, averaged for $(x-x_{\mathrm{sh}})/r_{\mathrm{L,i}} = [-0.6, 0]$ at $\Omega_{\mathrm{ci}}t \sim 8-20$. According to the linear predictions given in Table 2, $\lambda_{\mathrm{AIC}}/r_{\mathrm{L,i}} \propto (\lambda_{\mathrm{AIC}}\omega_{\mathrm{pi}}/c)/\sqrt{\beta}$, is independent of m_i/m_e, but it decreases only slightly with β, i.e., $\lambda_{\mathrm{AIC}}/r_{\mathrm{L,i}} \sim 1.5$, 1.4, and 1.3 for $\beta = 20$, 50, and 100, respectively. We expect that, due to the periodic boundary condition, about 2-3 ripples would appear along the y-direction in all the six panels with $y/r_{\mathrm{L,i}} = [0, 3.4]$ in Figure 43. In the M3.0-m100 model (magenta lines), for example, the two dominant modes with $\lambda \sim L_y/2$ and $L_y/3$ can be identified. We note that $\Omega_{\mathrm{ci}}t \sim 8-20$ is much longer than the growth time scale of the AIC, $\Omega_{\mathrm{ci}}\tau_{\mathrm{AIC}} = 2.6$, 2.3, and 2.1 for $\beta = 20$, 50, and 100, respectively. Hence, panels (g)-(i) illustrates the time-varying density configuration in fully developed, nonlinear stages of the AIC. We find that the amplitude of the dominant modes do not exactly match the linear predictions possible due to nonlinear effects described above. For instance, the M3.0 model with $\beta = 50$ (black) shows the greater amplitude, compared to the two models with $\beta = 20$ (red) and 100 (blue), although $\gamma_{\mathrm{AIC}}/\Omega_{\mathrm{ci}}$ increases with increasing β.

Several points are noted: (1) For all the models, the length scale of induced ripples ranges $\lambda_{\mathrm{ripple}} \sim 1.0 - 1.2 r_{\mathrm{L,i}}$ ($\sim 14 - 21 c/\omega_{\mathrm{pi}}$), which agrees reasonably well with $\lambda_{\mathrm{AIC}} \sim 1.3 - 1.5 r_{\mathrm{L,i}}$ from the linear analysis. (2) Comparing the three models with different β in the upper panels, we see some traces of ion-scale ripples linger further downstream in the $\beta = 20$ case, whereas they are mostly erased by the thermal motions in the $\beta = 100$ case. (3) Comparing the three models with different θ_{Bn}, we find that the shock ripples exhibit more fluctuations in the models with higher θ_{Bn}. This is mainly because the motional electric field is stronger for higher θ_{Bn}, and so the SDA-reflected ions are more energetic. (4) The AIC instability is insensitive to m_i/m_e, so the two models with $m_i/m_e = 50$ and 100 produce similar results. In panels (a) and (d), about three ripples are visible along the y-direction, although the second ripple is less pronounced than the first and third ripples in panel (d) for the M3.0-m100 model.

Figure 44 compares the magnetic field power spectra for the M3.0 and M2.0 models with different values of β, m_i/m_e and θ_{Bn}. In all the models with $M_s = 3$ (upper panels), multi-scale waves in the range of $k_y r_{\mathrm{L,i}}/2\pi \sim [0.7 - 10]$ ($\lambda \sim [0.1 - 1.5]r_{\mathrm{L,i}}$) are induced for the considered ranges of parameters. In all the models with $M_s = 2$ (lower panels), by contrast, mainly electron-scale waves are excited, as expected.

In Figure 45, we examine the upstream electron energy spectra for the same set of the models shown in Figure 44. The figure shows that the preacceleration depends only weakly on β and m_i/m_e, while it is more efficient with larger θ_{Bn} due to the stronger motional electric field. In the M3.0-θ73 model, in which the simulation was carried out for a longer time, $\Omega_{\mathrm{ci}}t \sim 50$ (magenta line in Figure 45(c)), some of the most energetic electrons were accelerated to $p_{\mathrm{inj}} \sim 3p_{\mathrm{th,i}}$ ($\gamma_{\mathrm{inj}} \sim 7$). This implies that the preacceleration via the SSDA could be a feasible mechanism for electron injection to the full DSA
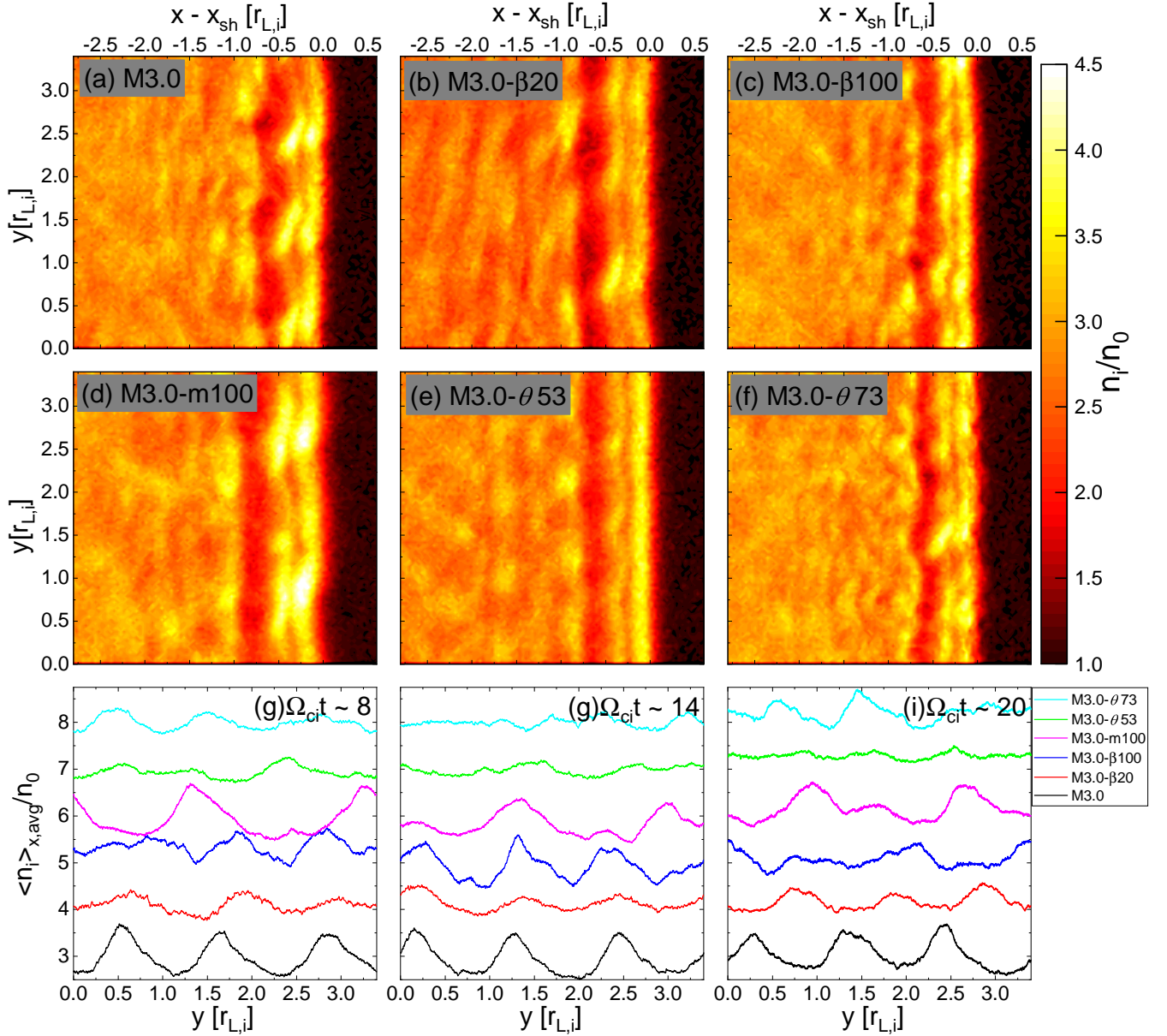
Figure 43: Panels (a)-(f): Ion number density, $n_i(x,y)/n_0$, in the region of $(x - x_{sh})/r_{L,i} = [-2.8, 0.6]$ and $y/r_{L,i} = [0, 3.4]$ at $\Omega_{ci}t \sim 20$ in the six M3.0 models with different values of β, m_i/m_e, and θ_{Bn}. The fiducial M3.0 model has $M_s = 3$, $\beta = 50$, $m_i/m_e = 50$, and $\theta_{Bn} = 63°$. See Table 1 for the parameters of other models. Panels (g)-(i): Ion number density, $\langle n_i \rangle_{x,avg}(y)$, averaged for $(x - x_{sh})/r_{L,i} = [-0.6, 0]$ at $\Omega_{ci}t \sim 8 - 20$ for the same set of the models. The line color for each model is given in the small box. Each line is shifted vertically by $+1$ for the purpose of clarity. Note that the growth time scale for the AIC is $\Omega_{ci}\tau_{AIC} = 2.1 - 2.6$, so the density configurations shown here display fluctuations in nonlinear stages.
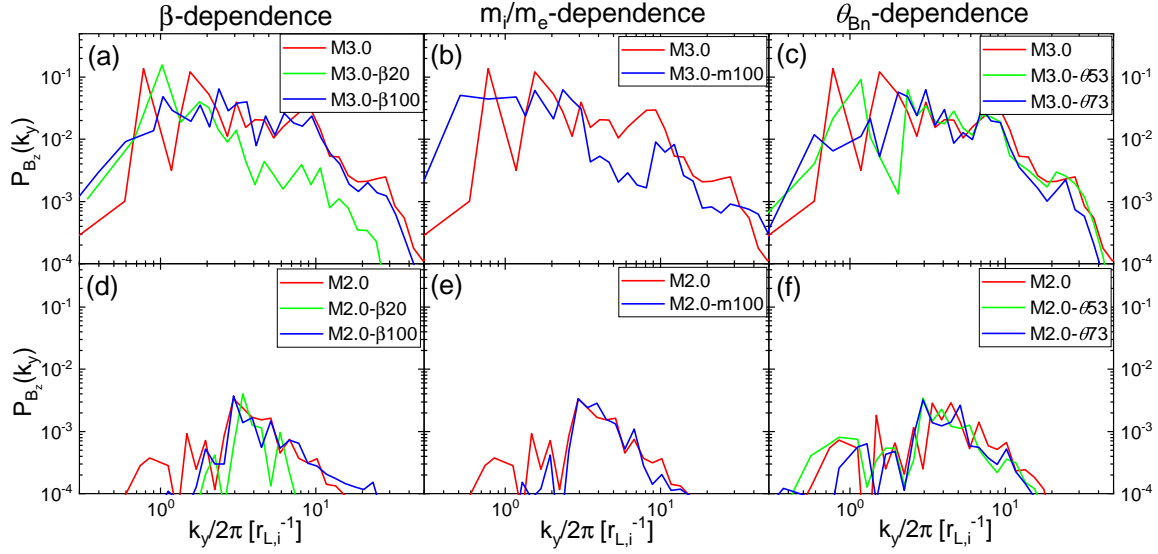
Figure 44: Magnetic power spectra, $P_{B_z}(k_y) \propto (k_y/2\pi)(\delta B_z(k_y)^2/B_0^2)$, averaged over the time period of $\Omega_{\mathrm{ci}}t = [8, 20]$, for the M3.0 models (upper panels) and the M2.0 models (lower panels) with different parameters in the transition region of $(x - x_{\mathrm{sh}})/r_{\mathrm{L,i}} = [-1.0, 0.0]$. In the fiducial M2.0 and M3.0 models, $M_{\mathrm{s}} = 3$, $\beta = 50$, $m_i/m_e = 50$, and $\theta_{\mathrm{Bn}} = 63°$. See Table 9 for the parameters of other models. Note that here the wavenumber k_y is normalized with the Larmor radius for incoming ions, $r_{\mathrm{L,i}} \approx 91(c/\omega_{\mathrm{pe}}) \cdot (M_{\mathrm{s}}/3)\sqrt{\beta/50}\sqrt{(m_i/m_e)/50}$.

process in high-β supercritical shocks, as previously shown for lower β shocks in [141] and [151]. In all the models with $M_{\mathrm{s}} = 2$, however, the energy spectra seem consistent with the single SDA cycle [24], and neither the Fermi-like acceleration nor the SSDA are effective.

Based on the results described in this section, we conclude that the preacceleration of electrons and the shock criticality are almost independent of m_i/m_e, but depend somewhat weakly on β ($\approx 20 - 100$) for the ranges of values considered here. Furthermore, the preacceleration would be more effective at larger θ_{Bn}, as long as the shock parameters satisfy the subluminal condition, i.e., $\theta_{\mathrm{Bn}} \leq \arccos(u_{\mathrm{sh}}/c)$ (see KRH2019).

7.4 Summary

In this work, we examine the electron preacceleration process via SSDA and Fermi-like acceleration in the ICM shocks through 2D PIC simulations. The main results can be summarized as follows:

1. Adopting the numerical values for $T_{i\perp}$, $T_{i\parallel}$, and $\beta_{i\parallel}$ in the shock transition zone of the simulated models with $M_{\mathrm{s}} = 2 - 3$, we estimated the instability parameter, I_{AIC}, defined in Equation (51). Considering both the behavior of I_{AIC} and the PIC simulation results, we suggest that the critical Mach number above which the AIC mode becomes unstable is $M_{\mathrm{AIC}}^* \approx 2.3$ for $\beta \approx 20 - 100$. Note that in this study the critical Mach numbers are defined in terms of the sonic Mach number rather than the Alfvénic Mach number, since both ion and electron reflections are controlled mainly by the shock compression.

2. The simulations confirmed that overshoot/under-shoot oscillations and shock surface rippling become
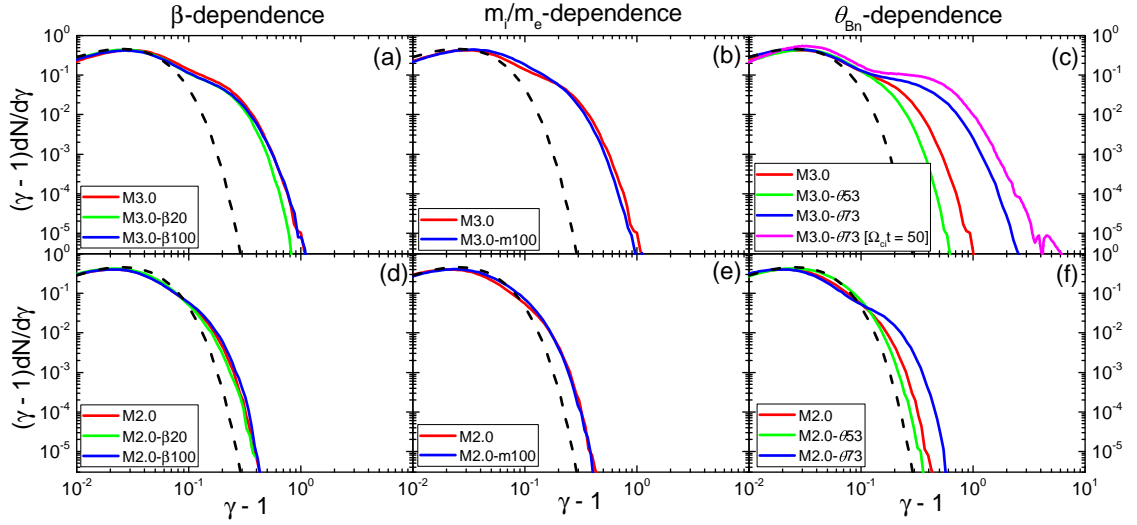
Figure 45: Upstream electron energy spectra at $\Omega_{\mathrm{ci}}t \sim 20$ for the M3.0 models (upper panels) and the M2.0 models (lower panels) with different parameters. The spectra are taken from the region of $(x - x_{\mathrm{sh}})/r_{\mathrm{L,i}} = [0, +1]$ and the black dashed lines show the Maxwellian distributions in the upstream. In the fiducial M2.0 and M3.0 models, $\beta = 50$, $m_i/m_e = 50$, and $\theta_{\mathrm{Bn}} = 63°$. See Table 9 for the parameters of other models. In panel (c) the magenta line shows the energy spectrum at $\Omega_{\mathrm{ci}}t \sim 50$ for the M3.0-θ73 model.

increasingly more evident for higher M_{s} in supercritical shocks with $M_{\mathrm{s}} \gtrsim M_{\mathrm{AIC}}^*$, while the shock structures seem relatively smooth for subcritical shocks.

3. In the transition zone of supercritical shocks, ion-scale waves can be generated by the AIC and ion-mirror instabilities due to the ion temperature anisotropy ($T_{\mathrm{i}\perp}/T_{\mathrm{i}\parallel} > 1$), while electron-scale waves can be generated by the whistler and electron-mirror instabilities due to the electron temperature anisotropy ($T_{\mathrm{e}\perp}/T_{\mathrm{e}\parallel} > 1$). Both the linear analysis and periodic-box PIC simulations presented in KHRK2021 indicate that the AIC and whistler instabilities are dominant over the ion and electron mirror instabilities, respectively, in high-β plasma under consideration. In the case of subcritical shocks with small anisotropies, on the other hand, primarily electron-scale waves are induced by the whistler instability, while ion-scale waves with small amplitudes could be excited by the ion-mirror instability.

4. In $\beta \approx 20 - 100$ supercritical shocks, electrons are confined within the shock transition for an extended period and gain energy by the SSDA, as suggested by previous studies for $\beta \sim 1 - 5$ shocks [141, 151]. Although we could not see electron preacceleration all the way to injection to DSA in our PIC simulations due to the limited simulation domain and time, we suggest that the combination of the Fermi-like acceleration and the SSDA could energize thermal electrons to the full DSA regime in supercritical, $Q_\perp$, shocks in the ICM.

5. The shock criticality in terms of triggering the AIC instability (or shock surface rippling) depends rather weakly on the simulation parameters such as m_i/m_e and θ_{Bn} for the ranges of values considered here. However, the critical Mach number, M_{AIC}^*, tends to be somewhat higher at lower β (~ 1) owing

to the stronger magnetization of ions [151]. In addition, the preacceleration of electrons is relatively insensitive to β ($\sim 20 - 100$) and m_i/m_e, while its efficiency increases with increasing θ_{Bn}, as long as the shock remains subluminal. Therefore, we infer that our findings about the shock criticality and the preacceleration can be applied generally to $Q_\perp$-shocks in the ICM.

Although this study focus on the electron acceleration mediated by various microinstabilities, it has been shown that such various microinstabilities play an important role in particle heating at the post-shock region [181, 186]. The previous works, [181, 186] investigated electron heating mechanism at purely perpendicular shock with $\theta_{\mathrm{Bn}} = 90°$. However, the dynamics of particles and pre-acceleration efficiency depend on the upstream magnetic field configurations and so the properties of various microinstabilities depend on θ_{Bn} as well. In this context, more numerical studies with a wide θ_{Bn} would be required to understand the detailed heating process in the outskirts of galaxy clusters.

VIII   Electron Preacceleration at Weak Quasi-perpendicular Shocks in Intracluster Medium: 4. Effects of Preexisting Nonthermal Electrons

PIC simulations have been performed for $Q_\perp$-shocks with $M_s \lesssim$ several in plasmas of $\beta \approx 20 - 100$ to study the electron preacceleration at ICM shocks [23, 24, 140, 141, 147, 162, 163, 175]. In particular, according to the results shown in Section VII, the electron preacceleration mechanisms mediated by the multi-scale plasma waves near the shock surface are inefficient at the subcritical shocks with $M_s \lesssim 2.3$. As a possible solution for radio relics with low M_s shocks, the so-called "reacceleration model" was suggested, where preexisting relativistic fossil electrons are injected to DSA and further accelerated [187–191]. Those fossil electrons could enhance the acceleration efficiency, especially at weak shocks with $M_s \lesssim 3$ [129]. The presence of relativistic electron populations in the ICM is expected, possibly being supplied by radio jets of AGNs or produced through previous episodes of shock/turbulence acceleration [50, 191]. As a matter of fact, some radio relics are observed to be associated with nearby radio galaxies [192], and low-frequency observations indicate the possibility of preexisting nonthermal electrons [193]. However, the reacceleration scenario at weak shocks would operate, only if preexisting nonthermal electrons with $p \gtrsim p_{\rm inj}$ could be scattered diffusively across the shock transition. It requires either the triggering of microinstabilities and the self-generation of scattering waves or the presence of preexisting kinetic waves in the turbulent ICM.

In this Section, we revisit our previous work of PIC simulations for weak $Q_\perp$ ICM shocks, described in Section VII, by including power-law nonthermal electrons in addition to Maxwellian thermal electrons in the upstream plasma (Ha, J.-H., Ryu, D., Kang, H., & Kim, S. 2022, The Astrophysical Journal, 925, 88; [194]). Due to the limitation of computational capacities, the power-law component extends only up to the Lorenz factor of $\gamma \approx$ several, representing a suprathermal population, rather than the bonafide nonthermal population that continues to $\gamma \gg 1$. We study the effects of the preexisting suprathermal electrons on kinetic plasma processes in high-β $Q_\perp$-shocks. Especially, we examine whether the suprathermal electrons could enhance the microinstabilities that generate multiscale waves, leading to the preacceleration of electrons up to $p_{\rm inj}$, even in subcritical shocks with $M_s \lesssim 2.3$.

8.1   Numerics

We performed a set of two-dimensional PIC simulations with the numerical setup used in Sections III and VII. The main difference between this work and Section VII lies in the inclusion of preexisting power-law electrons (PPEs, hereafter). In this work, we add a nonthermal electron population of "isotropic" power-law distribution, $f(p) \propto p^{-\alpha}$, to the background thermal plasma, reducing the amount of thermal electrons accordingly. The power-law slope we consider covers the range of $\alpha = 4 - 4.5$, and the number fraction of PPEs ranges $n_p/n_0 = 0.01 - 0.1$. For the fiducial model, $\alpha = 4.2$ is adopted, assuming that the preexisting nonthermal electrons are produced by relativistic shocks such as those in radio jets [195, 196]. The minimum and maximum (or cutoff) Lorenz factors of the nonthermal component are $\gamma_{\rm min} = 1.15$

Table 10: Model Parameters for Simulations

	M_s	M_A	u_0/c	θ_{Bn}	β	m_i/m_e	α	n_p/n_0	γ_{cut}	$L_x[\lambda_{se}]$	$L_y[\lambda_{se}]$	$t_{end}[\Omega_{ci}^{-1}]$
M2.0	2.0	8.2	0.038	63°	20	50	4.2	0.01	5	2000	200	22
M2.3	2.3	9.4	0.046	63°	20	50	4.2	0.01	5	2000	200	22
M2.5	2.5	10.2	0.053	63°	20	50	4.2	0.01	5	2000	200	22
M3.0	3.0	12.3	0.068	63°	20	50	4.2	0.01	5	2000	200	22
M2.0-α4	2.0	8.2	0.038	63°	20	50	4	0.01	5	2000	200	22
M2.0-α4.5	2.0	8.2	0.038	63°	20	50	4.5	0.01	5	2000	200	22
M2.0-np0.1	2.0	8.2	0.038	63°	20	50	4.2	0.1	5	2000	200	22
M2.0-γcut10	2.0	8.2	0.038	63°	20	50	4.2	0.01	10	2000	200	22
M2.0-m25	2.0	8.2	0.053	63°	20	25	4.2	0.01	5	2000	140	22
M2.0-β50-m25	2.0	12.9	0.053	63°	50	25	4.2	0.01	5	2000	225	22
M3.0-α4	3.0	12.3	0.068	63°	20	50	4	0.01	5	2000	200	22
M3.0-α4.5	3.0	12.3	0.068	63°	20	50	4.5	0.01	5	2000	200	22
M3.0-np0.1	3.0	12.3	0.068	63°	20	50	4.2	0.1	5	2000	200	22
M3.0-γcut10	3.0	12.3	0.068	63°	20	50	4.2	0.01	10	2000	200	22
M3.0-m25	3.0	12.3	0.096	63°	20	25	4.2	0.01	5	2000	140	22
M3.0-β50-m25	3.0	19.4	0.096	63°	50	25	4.2	0.01	5	2000	225	22
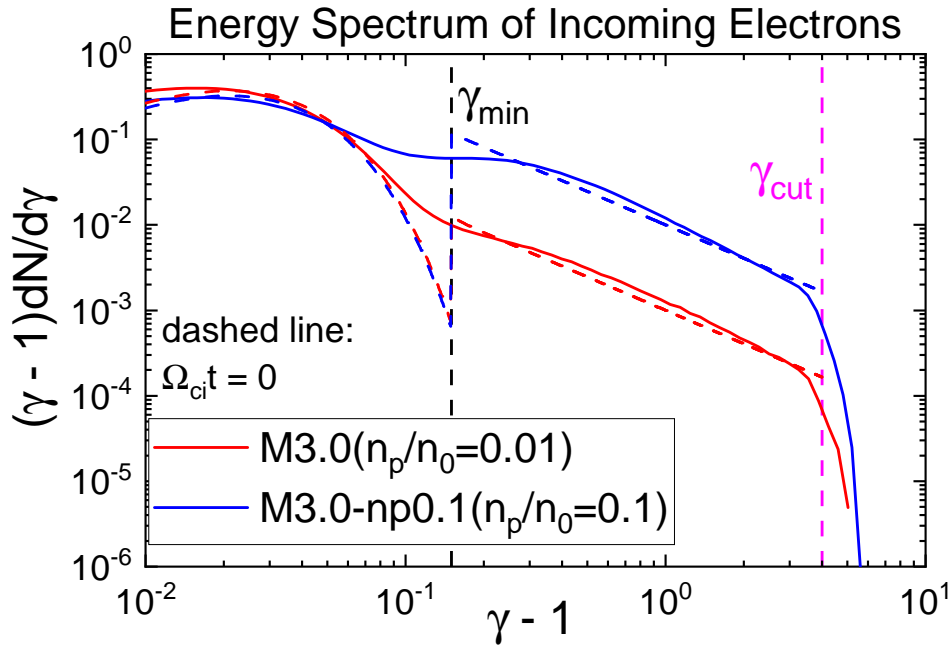
Figure 46: Energy spectra of electrons in the far upstream region $10 \leq (x - x_{sh})/r_{L,i} \leq 11$ (solid lines) and in the initial incoming plasmas (dashed lines) for two models M3.0 and M3.0-np0.1 (see Table 10). Here, x_{sh} is the shock position, and $r_{L,i} \approx 57\lambda_{se}$. The energy spectrum, $dN/d\gamma$, is related to the momentum spectrum, $f(p) \propto p^{-\alpha}$, as $4\pi f(p)p^2 dp/dE \propto dN/d\gamma \propto (\gamma-1)^{-s}$, where $s = \alpha - 2$.

110
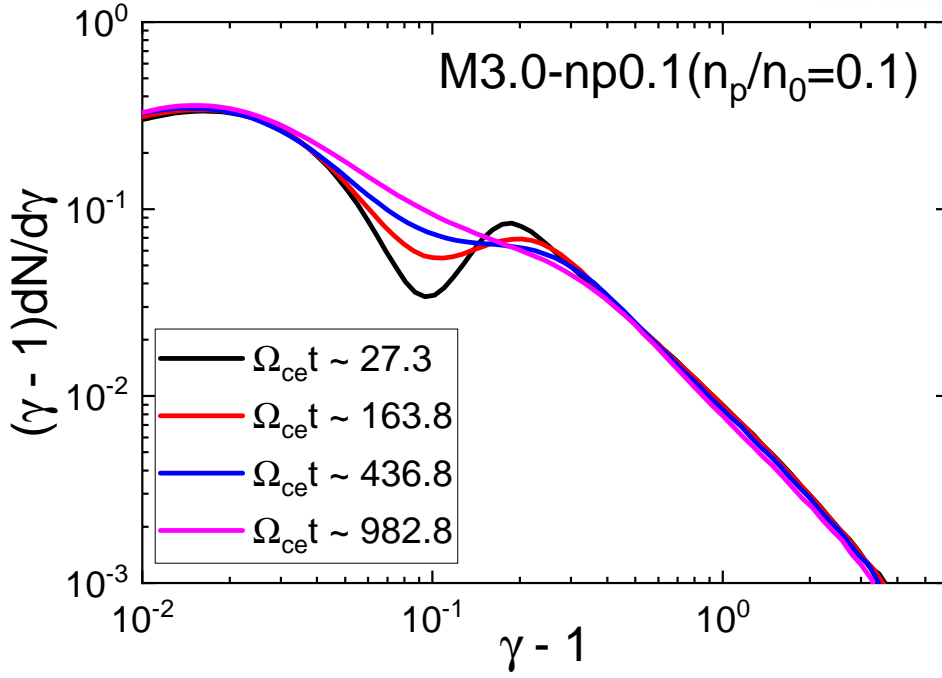
Figure 47: Energy spectra of electrons taken from the periodic box simulation Here, $r_{L,i} \approx 57\lambda_{se}$ and the number fraction of PPEs is the same as the shock model, $M3.0 - np0.1$.

(corresponding to the velocity $\sim 0.5c$) and $\gamma_{cut} = 5 - 10$, respectively. Figure 46 shows the energy spectra of electrons measured in the far upstream region of $10 \leq (x - x_{sh})/r_{L,i} \leq 11$ at $\Omega_{ci}t \sim 3$, and compares them with those of the initial incoming plasmas. Here, x_{sh} denotes the position of the shock.

In PIC simulations, the limited number of particles induces numerical dissipations [197], and hence a sufficiently large number of particles is required to maintain the power-law distribution of electrons for a sufficiently long time. In this work, 120 particles per cell (60 ions + 60 electrons) are placed, which are much larger than 32 particles per cell (16 per species) used in Sections III and VII. Even with this number of particles, $\gamma_{cut} = 5 - 10$ is the maximum value that we can accommodate. We point that this value of γ_{cut} is set by the computational limitation, rather than the physical argument. With $\gamma_{cut} = 5 - 10$, the PPE component should be regarded in effect as a suprathermal population.

The model parameters of our simulations are given in Table 10. Models with different M_s are named with the combination of the letter 'M' and the sonic Mach number (for instance, the M3.0 model has $M_s = 3$). The four models in the top group are the fiducial models, which have $\beta = 20$, $m_i/m_e = 50$, $\alpha = 4.2$, $n_p/n_0 = 0.01$, and $\gamma_{cut} = 5$. Models with parameters different from those of the fiducial models have the names that are appended by a character for the specific parameter and its value; for example, the M3.0-np0.1 model has $n_p/n_0 = 0.1$, while the M3.0-α4 has the power-law slope $\alpha = 4$. For the box size, L_x and L_y, the end time of simulations, t_{end}, and β, we adopt the values somewhat smaller than those of Section VII to compensate the longer computational time due to the larger number of particles. Yet, the adopted values of these parameters should be pertinent enough to capture the main results of this work. In the next section, the fiducial models in the current work will be compared with the models with $\beta = 20$ in Section VII (without PPEs).

111

In Figure 46, a smoothing in the upstream electron spectra at $\gamma \sim \gamma_{min}$ is observed as consequence of wave-particle interactions. This is because the PPEs generate resonant waves for scattering off electrons with the energy, $\gamma \sim \gamma_{min}$. To examine such effects of PPEs, we separately performed a 2D PIC simulations corresponding to the model, $M3.0 - np0.1$ with the periodic boundary conditions for both particle and electromagnetic fields. The box size is $L_x = L_y = 100c/\omega_{pe}$ to resolve the waves with the long enough wavelengths up to $\sim r_{L,i} \approx 57c/\omega_{pe}$. In addition, to keep consistency with the corresponding shock simulation model, 120 particles (60 ions + 60 electrons) are distributed per each grid zone and the grid resolution is identical to the all shock simulations shown in this thesis. The temperature and plasma beta are also relevant for the ICM parameters, $T = 10^8$ K and $\beta = 20 \gg 1$.

The electron energy spectra in the entire periodic box is shown in Figure 47. As noted in the shock simulation model, we recognize the electron energy spectrum undergoes smoothing process at $\gamma \sim \gamma_{min}$ due to the interactions mediated by the PPEs and the saturation timescale is roughly $\sim 1000\Omega_{ce}^{-1} = 20\Omega_{ci}^{-1}$. The timescale for saturation indicates the spectrum smoothing occurs simultaneously with electron preacceleration process near the shock surface because the preacceleration timescale is also roughly $\mathcal{O}(10)\Omega_{ci}^{-1}$. Although the smoothing of electron spectrum increases the number fraction of suprathermal electrons with $\gamma \sim \gamma_{min}$, we interpret that such effects would not be substantial for the detailed electron preacceleration process, because the number fraction of suprathermal electrons produced by electron is larger than the suprathermal fraction of saturated spectrum (see Figure 52-(c) and the descriptions for that Figure).

To understand the properties of plasma waves induced by the presence of PPEs, we examined the self-excited magnetic field, B_z. Figure 48 shows the 2D structures of B_z for four different time epochs. We first identify the waves are induced at $\Omega_{ce}t \sim 163.8$ and the wave energy decreases as time increases. In particular, the wavelength, $\lambda \sim 20c/\omega_{pe}$ is corresponding to the gyroradius of electrons with $\gamma \sim \gamma_{min}$ and the waves are propagating along the background magnetic field. We interpret that the wave observed here is the right-handed whistler wave. The growth rate of this wave is approximately $\sim 0.006\Omega_{ce}$. According to the linear analysis results presented in Sections V and VI, the growth rates of oblique firehose waves in the shock upstream and the whistler waves in the shock transition zone are $\sim 0.21\Omega_{ce}$ and $\sim 0.0156\Omega_{ce}$, respectively. This indicates that the wave generation due to the dynamics of electron near the shock surface is much faster than the wave generation mediated by the PPEs in the shock upstream. In this context, the wave-particle interaction mediated by whistler waves produced by the PPEs would not be important in electron preacceleration. In addition, the waves undergo inverse cascade and this is partly because the simulation is performed in 2D domain.

8.2 Results

Particle Reflection and Temperature Anisotropies

According to the relativistic SDA theory described in the Section VII, the reflection fraction is expected to increase, if PPEs with higher velocities are added to the Maxwellian distribution. This is because particle distribution existing in the wider velocity space contains more particles which are satisfying the
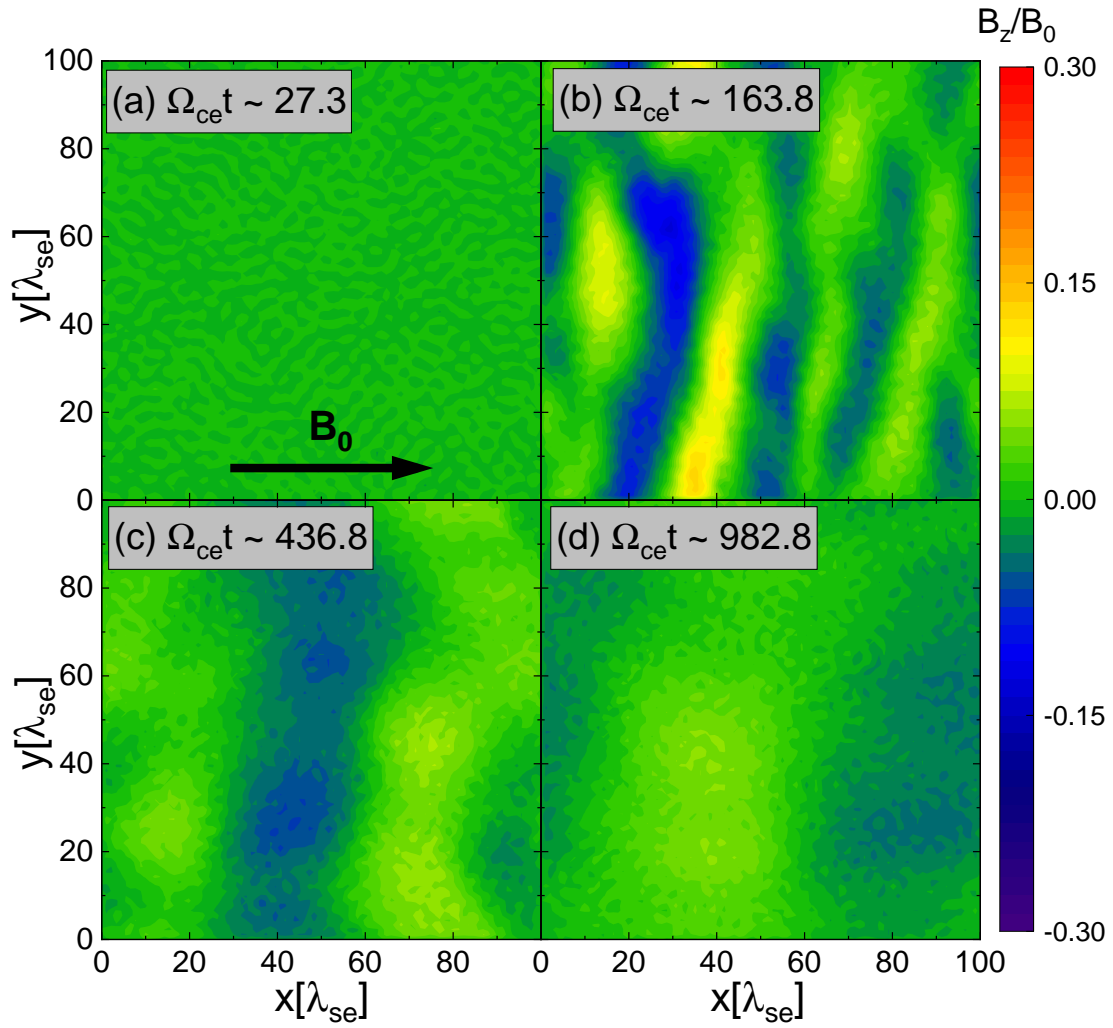
Figure 48: 2D slices of z-direction magnetic field, B_z. Black arrow displayed at panel (a) indicates the direction of background magnetic fields.
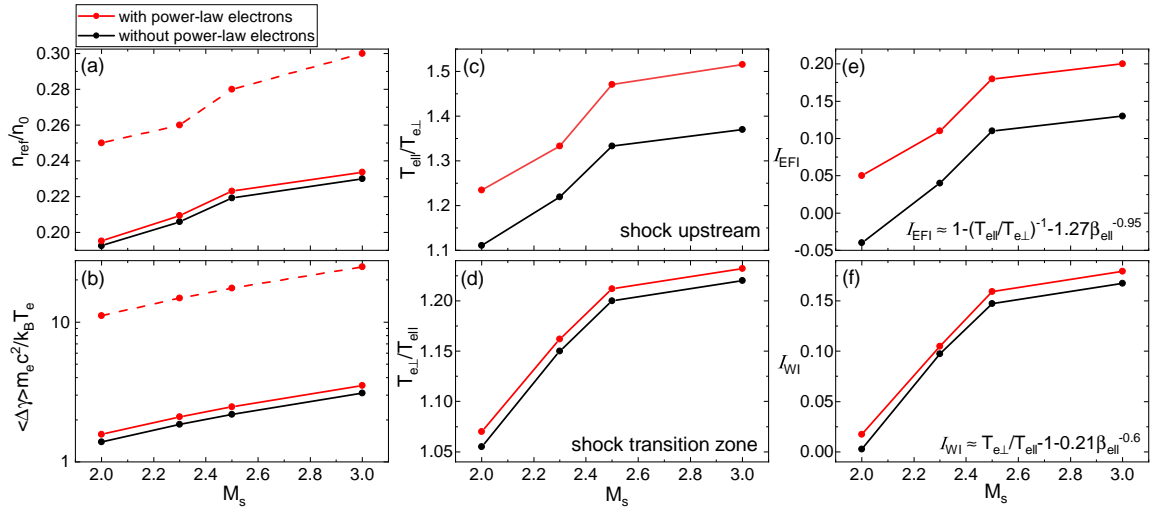
Figure 49: Fraction of reflected electrons (panel (a)) and average energy gained by reflected electrons in a single cycle of SDA (panel (b)), based on the relativistic SDA description [23, 140]. Electron temperature anisotropy, $T_{e\parallel}/T_{e\perp}$, estimated in the immediate upstream region, $0 \leq (x - x_{\text{sh}})/r_{L,i} \leq 1$ (panel (c)), and $T_{e\perp}/T_{e\parallel}$ estimated in the immediate downstream region, $-1 \leq (x - x_{\text{sh}})/r_{L,i} \leq 0$ (panel (d)). Instability parameters for the EFI, I_{EFI} (panel (e)), and for the WI, I_{WI} (panel (f)). The red solid lines draw the fiducial models with PPEs, while the black solid lines draw the corresponding models without PPEs from Paper I, at $\Omega_{ci}t \sim 22$. The red dashed lines in panels (a) and (b) show the quantities estimated only with PPEs, that is, the fraction of reflected PPEs and the average energy gained by reflected PPEs in a single cycle of SDA.

condition for mirror reflection. To examine such effects of PPEs on the SDA at the shock surface, we first calculate the reflection fractions and the average energy gain through a cycle of SDA which are shown in Figure 49-(a) & (b). As expected, the fraction of reflected PPEs (red dashed line) is larger than that of reflected thermal electrons (black solid line), so the fraction of total reflected electrons in the models with PPEs (red solid line) is larger than the fraction without PPEs (black solid line) as well. The average energy gained by reflected PPEs in a single SDA cycle is also larger than that of thermal electrons, because electrons with larger γ drift longer distances along the shock surface and the amount of energy gain through the motional electric field becomes larger. Hence, with PPEs, the electron temperature anisotropies, $T_{e\parallel}/T_{e\perp}$, estimated in the shock upstream, $0 \leq (x - x_{\mathrm{sh}})/r_{L,i} \leq 1$, increase (Figure 49(c)), and then based on the instability condition for the EFI, $I_{\mathrm{EFI}} \approx 1 - (T_{\mathrm{e}\parallel}/T_{\mathrm{e}\perp})^{-1} - 1.27\beta_{\mathrm{e}\parallel}^{-0.95} > 0$ [140], the growth of the EFI is expected to be enhanced in the upstream region (Figure 49(e)). On the other hand, the SDA-accelerated electrons and PPEs, which are advected downstream, would lead to a slight increase of the electron temperature anisotropy, $T_{e\perp}/T_{e\parallel}$, in the shock transition zone, $-1 \leq (x - x_{\mathrm{sh}})/r_{L,i} \leq 0$ (Figure 49(d)). Then, according to the instability condition for the WI, $I_{\mathrm{WI}} \approx T_{\mathrm{e}\perp}/T_{\mathrm{e}\parallel} - 1 - 0.21\beta_{\mathrm{e}\parallel}^{-0.6} > 0$ [181], the growth of the WI would be slightly enhanced in the transition zone (Figure 49(f)).

The instability condition for the AIC, $I_{\mathrm{AIC}} \approx (T_{\mathrm{i}\perp}/T_{\mathrm{i}\parallel}) - 1 - 1.6\beta_{\mathrm{i}\parallel}^{-0.72} > 0$ (Section VII), depends on the temperature anisotropy of ions, which is induced by the gyrating reflected ions in the plane perpendicular to the shock-compressed magnetic field [181]. Obviously, the presence of PPEs would not affect the ion reflection, so we expect that it would not increase the ion temperature anisotropy, nor enhance the growth of the AIC in the shock transition zone.

Generation of Waves by Microinstabilities

Figure 50 shows the distributions of the ion number density, n_i (top panels), and the self-excited magnetic field, B_z (bottom panels), around the shock for the M2.0 and M3.0 models with and without PPEs. Oblique waves with $\lambda \sim 20 - 30\lambda_{se}$ are generated in the preshock region of the M2.0 model with PPEs (Figure 50(e)), while such waves are absent in the M2.0 model without PPEs (Figure 50(f)). They are expected to be induced by the EFI, and present also in the upstream region of the M3.0 models both with and without PPEs (Figure 50(g, h)). [140] demonstrated that the fraction of reflected, backstreaming electrons, the energy gain via SDA, and the temperature anisotropy, $T_{e\parallel}/T_{e\perp}$, are large enough to trigger the EFI only in supercritical shocks with $M_s \gtrsim 2.3$. If PPEs are added to the incoming plasma, on the other hand, the fraction of reflected electrons and $T_{e\parallel}/T_{e\perp}$ increase as shown in Figure 49(a,c), and thus the EFI is excited even in the subcritical shock with $M_s = 2$ (Figure 50(e)). Moreover, the comparison of the models with and without PPEs reveals that electron-scale waves along the overshoot, excited by the WI, are somewhat enhanced by PPEs as well.

In Section VII, it was shown that in supercritical shocks, the AIC instability due to the ion temperature anisotropy could excite ion-scale waves with $\lambda_{\mathrm{ripple}} \sim 70\lambda_{se}$, leading to ripples propagating along the shock surface (Figure 50 (c,d)). As a result, multiscale plasma waves, ranging from electron to ion scales, appear in the supercritical M3.0 models (Figure 50 (g,h)). On the contrary, the emergence of
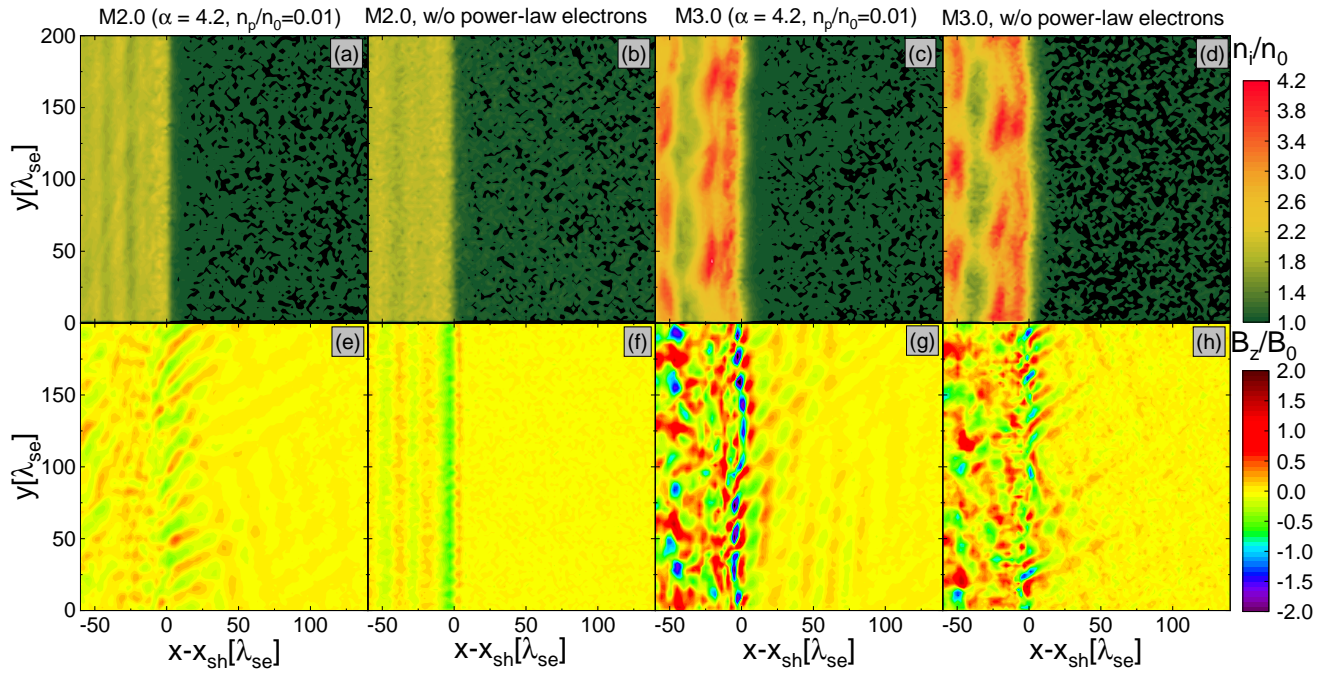
Figure 50: Ion number density (top panels), n_i, normalized to the upstream ion number density, n_0, and z-magnetic field (bottom panels), B_z, normalized to the upstream magnetic field, B_0, in the region of $-60 \leq (x - x_{sh})/\lambda_{se} \leq 140$ around the shock at $\Omega_{ci}t \sim 22$. Here, x_{sh} is the shock position. The fiducial M2.0 and M3.0 models with $\alpha = 4.2$ and $n_p/n_0 = 0.01$ (panels (a), (e), (c), (g)) are compared to the corresponding models without PPEs from Section VII (panels (b), (f), (d), (h)).
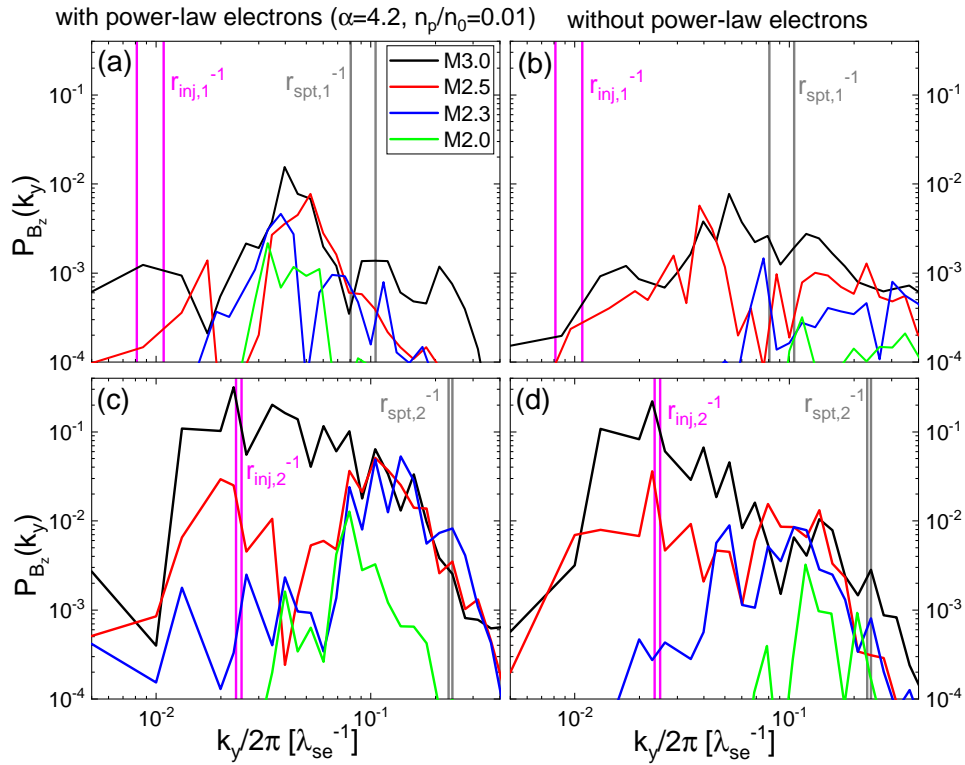
Figure 51: Magnetic field power spectra, $P_{B_z}(k_y) \propto (k_y/2\pi)(\delta B_z(k_y)^2/B_0^2)$, in the immediate upstream region, $0 \le (x-x_{\rm sh})/r_{L,i} \le 1$ (top panels), and the immediate downstream region, $-1 \le (x-x_{\rm sh})/r_{L,i} \le 0$ (bottom panels), at $\Omega_{ci}t \sim 22$, for the models with PPEs (left panels) and without PPEs (right panels). Here, $x_{\rm sh}$ is the shock position, and $r_{L,i} \approx 57\lambda_{se} \cdot (M_s/3)$. The magenta and gray boxes denote the ranges of the gyroradius of electrons with $p_{\rm inj}$ and $p_{\rm spt} \equiv \sqrt{m_e/m_i}\, p_{\rm inj}$, respectively, in the upstream and downstream regions.
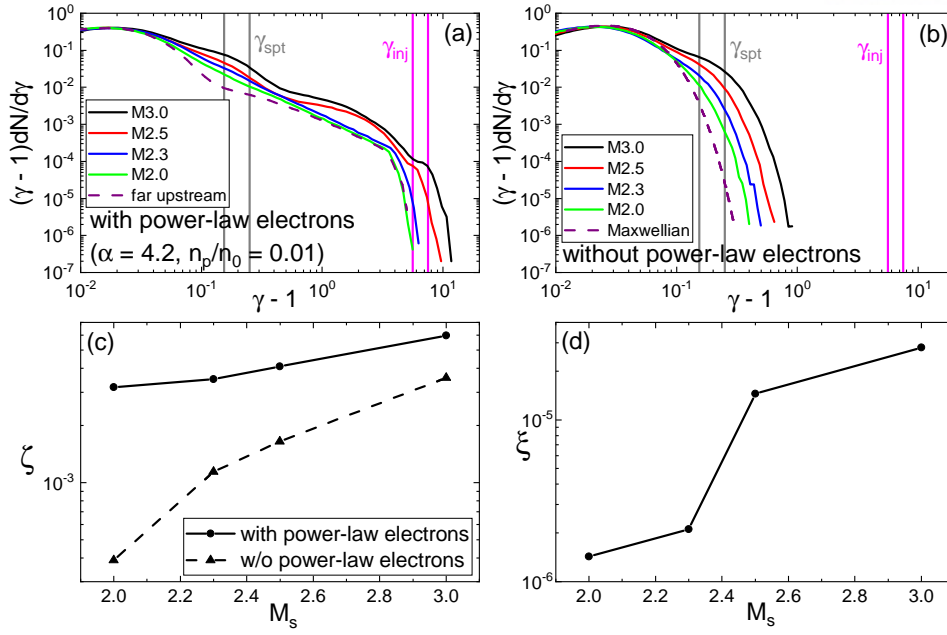
Figure 52: Upstream electron energy spectra (panels (a) and (b)), the suprathermal fraction, ζ (panel (c)) and the injection fraction, ξ (panel (d)) are estimated in the region of $0 \leq (x - x_{\mathrm{sh}})/r_{L,i} \leq 1$ at $\Omega_{\mathrm{ci}} t \sim 22$. Here, the four models (M2.0, M2.3, M2.5, M3.0) are employed in the panel (a), while the four models without a power-law tail are used in the panel (b) for comparison. The injection energy, γ_{inj} and the suprathermal energy, $\gamma_{\mathrm{spt}} = 1.25$ are marked as gray and magenta solid lines, respectively. Here, $r_{\mathrm{L,i}} \approx 57 \lambda_{\mathrm{se}} \cdot (M_{\mathrm{s}}/3)$.

such ripples and ion-scale waves are not observed in the subcritical M2.0 models, regardless of PPEs (Figure 50 (a,b)).

The presence of plasma waves on relevant kinetic scales is essential for electron preacceleration and subsequent injection to DSA. This is because for electron energization up to p_{inj}, wave-particle interactions mediated by waves with wavelengths as long as the gyroradius of electrons with p_{inj} are required. The injection momentum ranges $p_{\mathrm{inj}} \approx 3\sqrt{2m_i k_B T_2} \approx 5.6 - 7.5 m_e c$ (or $\gamma_{\mathrm{inj}} \approx 5.6 - 7.5$) for the fiducial models with $M_s = 2 - 3$, $T_1 = 10^8$ K, and $m_i/m_e = 50$. Hence, the gyroradius of electrons with γ_{inj} is $r_{\mathrm{inj},1} \equiv \gamma_{\mathrm{inj}} c/\Omega_{ce,1} \approx 92 - 123 \lambda_{se}$ and $r_{\mathrm{inj},2} \equiv \gamma_{\mathrm{inj}} c/\Omega_{ce,2} \approx 40 - 41 \lambda_{se}$ in the preshock and postshock regions, respectively. Here, $\Omega_{ce,1}$ and $\Omega_{ce,2}$ are the gyrofrequencies of electrons. Figure 50 demonstrates that in subcritical shocks, such ion-scale waves with $\lambda \sim r_{\mathrm{inj},1}$ or $r_{\mathrm{inj},2}$ are not excited by the addition of PPEs (Figure 50(a,e)).

For the further characterization of waves, the power spectra of B_z, P_{B_z}, in the immediate upstream (top panels) and downstream (bottom panels) regions of the shock are shown in Figure 51, for all the fiducial models with PPEs in Table 10 (left panels) and the corresponding models without PPEs (right panels). The ranges of r_{inj} (magenta) and the gyroradius, r_{spt}, for the suprathermal momentum, $p_{\mathrm{spt}} \equiv \sqrt{m_e/m_i}\, p_{\mathrm{inj}}$, (gray) are plotted for reference. Note that p_{spt} roughly marks the momentum above which electrons change from thermal to suprathermal distributions [140]. The comparison of the subcritical shocks (green and blue lines) with and without PPEs shows that PPEs enhance waves mainly with $\lambda \sim$

$20 - 30\lambda_{se} \ll r_{\text{inj},1}, r_{\text{inj},2}$, which cannot mediate the energization of electrons up to p_{inj}. The downstream waves with $r_{\text{spt},2} < \lambda < r_{\text{inj},2}$ appear partly due to the WI at the shock transition and partly via the advection of upstream waves.

On the other hand, waves with $\lambda \gtrsim r_{\text{inj},2}$ are produced only in the supercritical shocks (black and red lines), regardless of the presence of PPEs. An interesting point is that in the marginally critical shock of $M_s = 2.3$, waves with $\lambda \gtrsim r_{\text{inj},2}$ are enhanced slightly with PPEs, possibly owing to the modification of magnetic field fluctuations by the EFI mode. Again, Figure 51 confirms that the multiscale plasma waves that can resonate with electrons of $p_{\text{spt}} \lesssim p \lesssim p_{\text{inj}}$ are produced only at supercritical shocks with $M_s \gtrsim 2.3$.

Energy Spectrum and Injection Fraction

The consequences of wave-particle interactions should be manifested in the electron energy spectra. Figure 52 shows the spectra measured in the shock upstream for all the models with PPEs (Figure 52 (a)) and without PPEs (Figure 52 (b)). The spectra in Figure 52(b) are basically the same as those in Paper I. In the M2.0 model without PPEs (green line in Figure 52(b)), the EFI is not triggered, and so only a single SDA cycle occurs. In the M3.0 model without PPEs (black line in Figure 52(b)), on the other hand, thermal electrons are energized up to $\gamma \sim 2$ via the Fermi-like acceleration and SSDA.

In the spectra for the models with PPEs in Figure 52(a), two points are noted. (1) The suprathermal population grows in all the models, even in the M2.0 model. Especially, the population with $\gamma \lesssim 1.5$ represents the incoming thermal electrons energized via the Fermi-like acceleration mediated by EFI-driven waves. (2) In the supercritical models, the spectra stretch beyond γ_{inj} through the SSDA mediated by multiscale waves. However, in the M2.0 model, the high-energy end of the spectrum does not change, because PPEs do not aid the excitation of AIC-driven ion-scale waves. These results demonstrate that the presence of PPEs alone does not modify the critical Mach number, $M_{\text{crit}} \approx 2.3$, for electron preacceleration and subsequent injection to DSA.

In PIC simulations, the maximum energy of electrons is limited by computational constraints; hence, with a larger simulation box and a longer integration time, the spectra would extend to higher energies, as noted in Paper I. Previously, [151] performed hybrid simulations, implemented with test-particle electrons of initially kappa distributions. In their work, electron-scale waves, induced by the EFI and whistler modes, are not present due to the lack of electron dynamics. Yet, they showed that in supercritical shocks, electrons could be energized well above p_{inj} through interactions with multiscale waves, which are accompanied by the shock surface rippling triggered by the ion dynamics.

To estimate the electron acceleration efficiency quantitatively, we define the suprathermal fraction, ζ for the electron preacceleration process mediated by the electron-scale waves (i.e., EFI-induced wave in the shock upstream and whistler wave in the transition region) and the injection fraction ξ for counting the electrons with $\gamma \gtrsim \gamma_{\text{inj}}$. Those quantities are defined as follows:

$$\zeta \equiv \frac{1}{N_2} \int_{\gamma_{\text{spt}}}^{\gamma_{\text{inj}}} \frac{dN}{d\gamma} d\gamma, \tag{52}$$

$$\xi \equiv \frac{1}{N_2} \int_{\gamma_{\text{inj}}}^{\gamma_{\text{max}}} \frac{dN}{d\gamma} d\gamma, \tag{53}$$

where γ_{spt} is a free parameter for the minimum value for suprathermal electrons. For both ζ and ξ, the upstream energy spectrum is used, because the electrons accelerated at the shock upstream and transition region are well included in the shock upstream region. The panels (c) and (d) of figure 52 plots ζ and ξ for the four different shock models. Since the preexisting power-law electrons enhance the electron-scale waves, so ζ obtained from the model with PPEs is larger than that obtained from the model without PPEs. The M_{s} dependence of ξ indicates that electrons could reach the injection energy only in the supercritical shocks, as shown in the energy spectra (figure 52-(a)). Moreover, we interpret that at the supercritical shocks with $M_{\text{s}} \gtrsim 2.3$, the suprathermal electrons with $\gamma \lesssim 1.5$ are energized via SSDA and eventually inject into DSA on substantially longer timescales. In this context, the enhancement of suprathermal fraction, ζ may increase the injection fraction, ξ. However, at the subcritical shocks with $M_{\text{s}} \lesssim 2.3$, due to the lack of longer wavelength waves (i.e., $\lambda_{\text{EFI}} \ll r_{\text{inj,1}}$, $\lambda_{\text{WI}} \ll r_{\text{inj.2}}$), the suprathermal electrons are not expected to gain the injection energy. So, the enhancement of suprathermal fraction, ζ may not enough to explain electron injection, even on the longer timescales.

Note that the ξ defined in this Section is not directly corresponding to the injection fraction of DSA in the realistic ICM shocks, because the simulation performed within the very short timescale and thus the full physics of preacceleration and DSA is not fully exmained. In spite of such limitations, we point that the injection into the DSA in the subcritical shocks still remains as an open question, regardless of the contribution of PPEs for microphysics in the shock structure.

Dependence on Parameters

We next examine how our findings depend on the parameters that specify PPEs, such as n_p/n_0, α, and γ_{max}, as well as the simulation parameters, such as m_i/m_e and β. Figure 53 shows the magnetic field power spectra, P_{B_z}, in the immediate downstream, for the M2.0 models in the second group (Figure 53(a)) and the M3.0 models in the third group (Figure 6(b)) of Table 10. The comparison of all the lines in Figure 53(b) with the black line in Figure 51(c) indicates that the generation of waves does not strongly depend on these parameters in the case of the supercritical shocks with $M_s = 3$. In all the M3.0 models, P_{B_z} for $r_{\text{spt,2}} \lesssim \lambda \lesssim r_{\text{inj,2}}$ is substantial. By contrast, there are some differences in the case of the subcritical M2.0 models. For instance, in the M2.0-np0.1 model (green line in Figure 53(a)), with n_p/n_0 ten times larger than that of the fiducial model (green line in Figure 51(a)), the excitation of waves is enhanced. In the M2.0-β50-m25 model (orange line in Figure 53(a)), with a weaker background magnetic field, waves with longer wavelengths appear. As noted above, waves in the M2.0 models are mostly electron-scale waves, induced by the EFI and whistler modes.

Finally, Figure 54 compares the electron energy spectra in the immediate upstream for the M2.0 models in the second group (upper panels) and the M3.0 models in the third group (lower panels) of Table 10. The energy spectra extend up to $\gamma - 1 \sim 10$ in all the M3.0 models, independent of the parameters. This is because the ripples along the shock surface have $\lambda_{\text{ripple}} \sim 70\lambda_{se}$ (see Figure 50(c,d)), which marks the longest wavelength of AIC-driven waves. Hence, the maximum energy in the spectra is

Figure 53: Magnetic field power spectra, $P_{B_z}(k_y) \propto (k_y/2\pi)(\delta B_z(k_y)^2/B_0^2)$, in the immediate downstream region, $-1 \leq (x - x_{sh})/r_{L,i} \leq 0$, at $\Omega_{ci}t \sim 22$, for the M2.0 (top) and M3.0 (bottom) models with different parameters (see Table 10). Here, x_{sh} is the shock position, and $r_{L,i} \approx 57\lambda_{se} \cdot (M_s/3)\sqrt{\beta/20}\sqrt{(m_i/m_e)/50}$. The magenta and gray boxes denote the ranges of the gyroradius of electrons with p_{inj} and p_{spt}, respectively, in the downstream region.
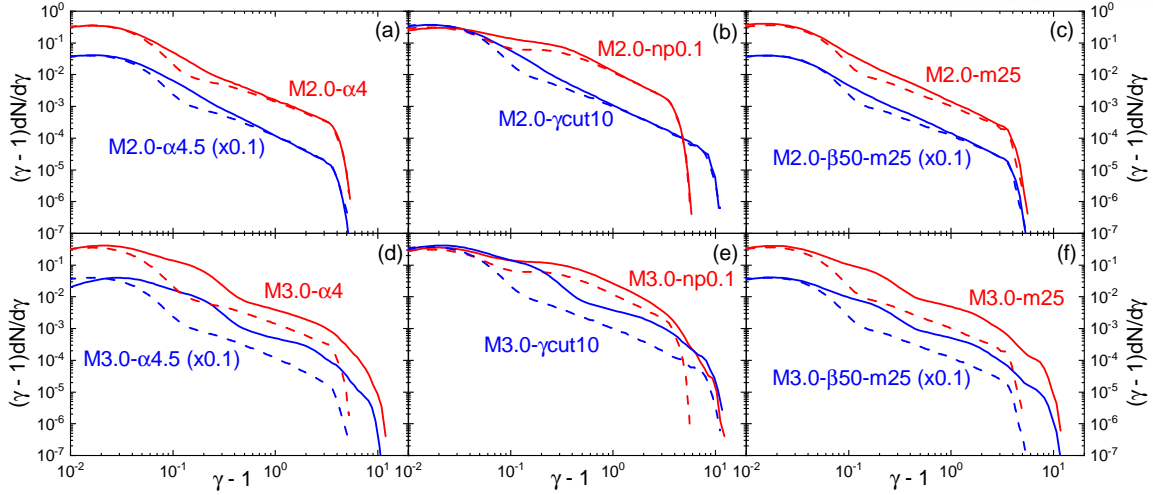
Figure 54: Electron energy spectra in the immediate upstream region, $0 \leq (x - x_{sh})/r_{L,i} \leq 1$, at $\Omega_{ci}t \sim 22$, for the M2.0 (upper panels) and M3.0 (lower panels) models with different parameters (see Table 10). The dashed lines draw the electron energy spectra in the far upstream region, $10 \leq (x - x_{sh})/r_{L,i} \leq 11$, at $\Omega_{ci}t \sim 3$, for comparison. Here, x_{sh} is the shock position, and $r_{L,i} \approx 57\lambda_{se} \cdot (M_s/3)\sqrt{\beta/20}\sqrt{(m_i/m_e)/50}$. Some of the blue solid and dashed lines marked by ($\times 0.1$) are shifted vertically for clarity.

given as $\gamma_{max} \approx \lambda_{ripple}\Omega_{ce,2}/c \approx 11$, in our simulations. Again, the main results described in the previous subsection remain valid, independent of the model parameters.

Effects of Preexisting CR Ions

While the effects of preexisting relativistic electrons are mainly considered in this work, it is likely to predict the presence of CR ions (mostly protons) in the ICM, although the evidence of CR ions still need to be confirmed through the diffuse γ-ray obervations. Based on the current upper-limits from currently available telescopes such as Fermi-LAT, the farction of CR ions is expected to be very small and corresponding numerical studies suggested that the CR fraction averaged over a typical cluster volume is roughly $10^{-4} - 10^{-3}$ [104, 105, 198]. In spite of such uncertainty, it has been shown that proton acceleration mechanism can be operated at ICM shocks, like most the astrophysical shocks such as shocks in front of supernova remnants (see Section III). In this regards, it is necessary to confirm the effects of preexisting CR ions at the ICM shocks through the detailed PIC simulations.

By adopting the same setup used for the shock model, M3.0-np0.1, we additionally run a simulation including both 10 % of CR electrons and CR ions. Note that the number of CR ions used here is much larger than the fraction suggested by the Fermi-LAT upper limits, so the model considered here is very optimistic case. With this model, the larger fraction of CR ions could generate more prominent features mediated by CR ions near the shock surfaces.

We first compare the magnetic field structures for the model with power-law ions and without power-law ions. Figure 55 shows 2D slices of magnetic fields along y and z directions. According to the structure of B_z, the multi-scale plasma waves for electron preacceleration are efficiently induced regardless
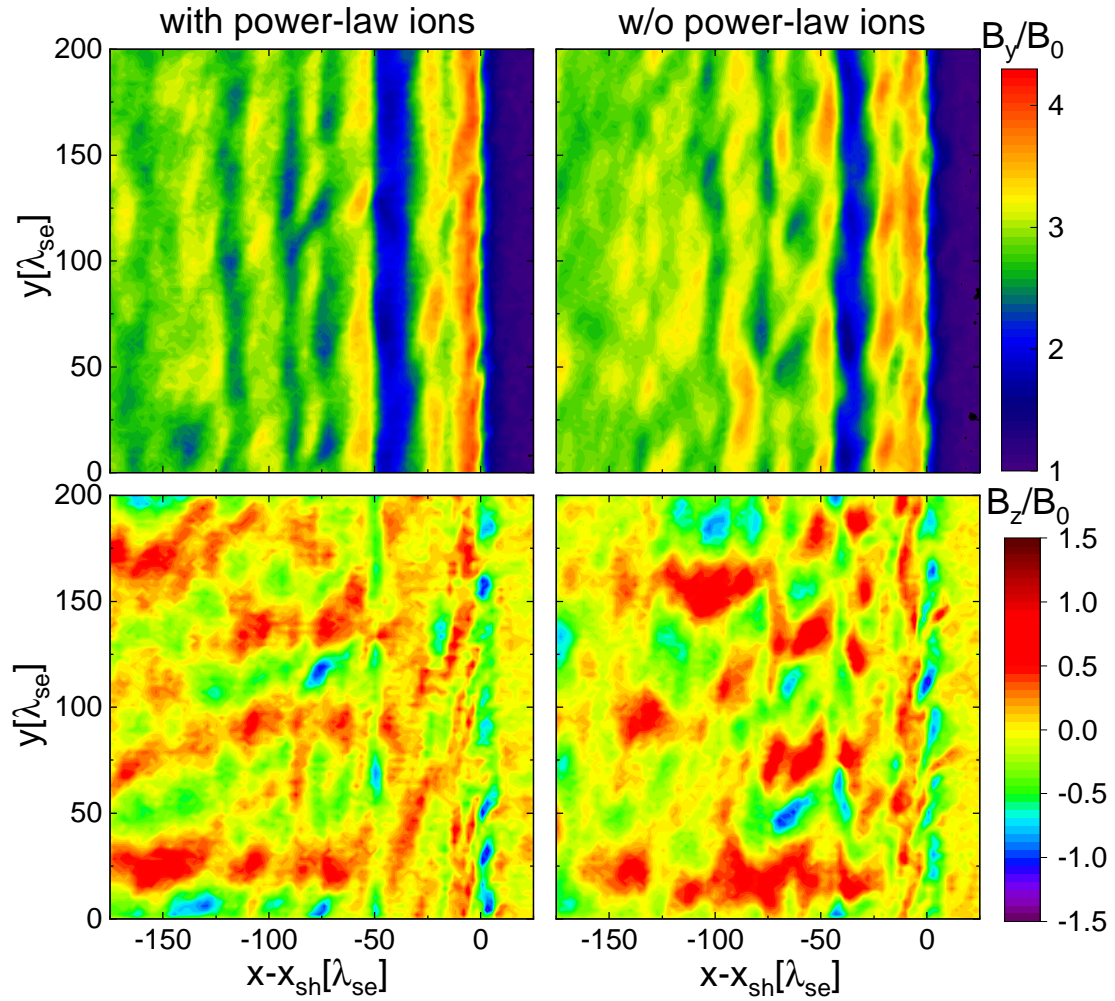
Figure 55: 2D slices of B_y (top panels) and B_z (bottom panels) are displayed at $\Omega_{ci}t \sim 18$. Left panels include the power-law ions, whereas right panels are obtained by the model without the power-law ions (i.e., the model, M3.0-np0.1 in table 10.
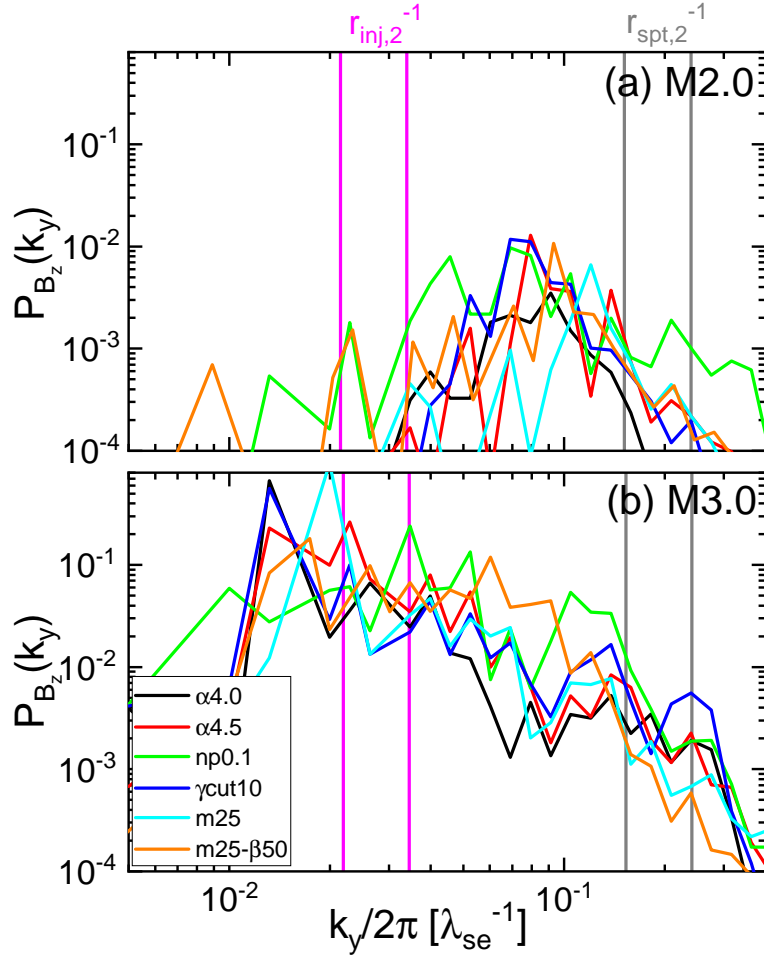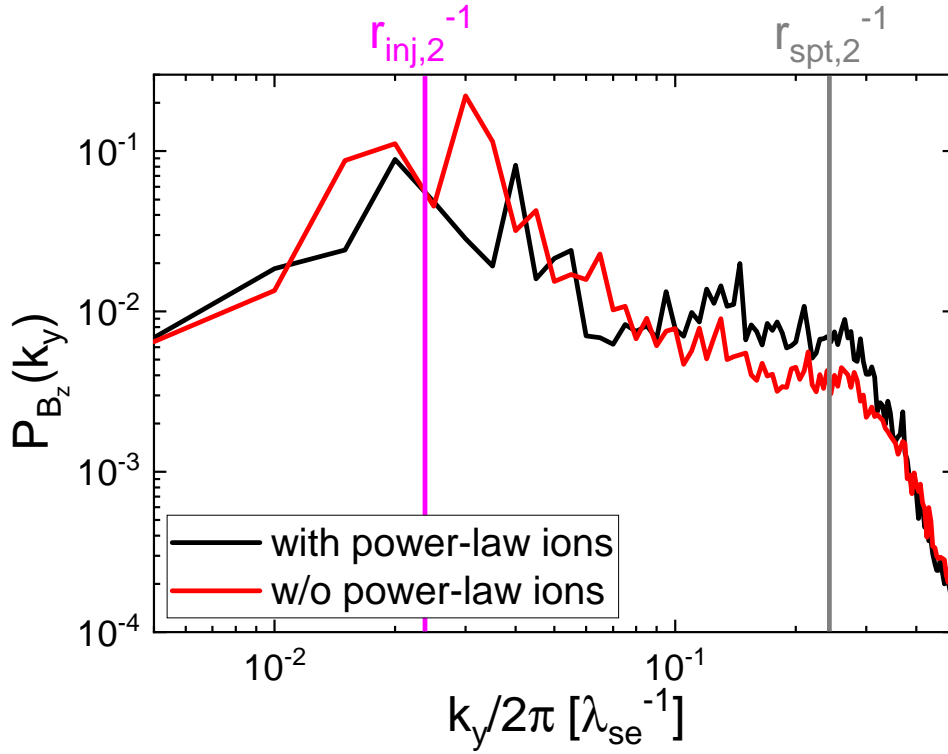
Figure 56: Magnetic field power spectra, $P_{B_z}(k_y) \propto (k_y/2\pi)(\delta B_z(k_y)^2/B_0^2)$, in the immediate downstream region, $-1 \le (x-x_{\text{sh}})/r_{L,i} \le 0$, at $\Omega_{ci}t \sim 18$, for the model with the power-law ions (black) and the model without the power-law ions (red). The magenta and gray solid lines display the gyroradius of electrons in the downstream region with p_{inj} and p_{spt}, respectively. Here, $r_{\text{L,i}} \approx 57\lambda_{\text{se}}$.
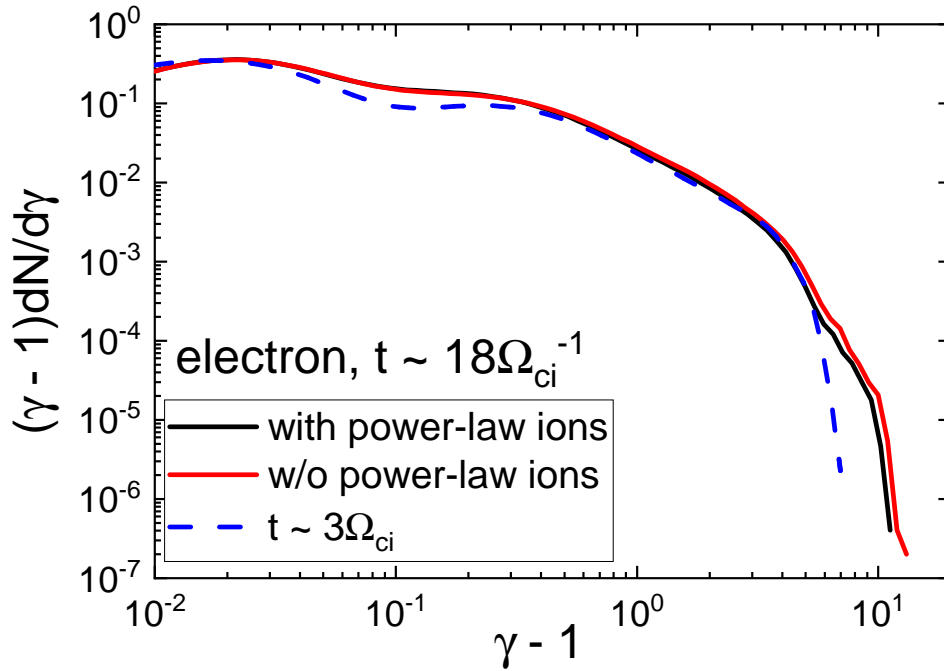
Figure 57: Upstream electron energy spectrum measured in the region of $0 \le (x-x_{\text{sh}})/r_{L,i} \le 1$ at $\Omega_{ci}t \sim 18$. Blue dashed line shows the far upstream spectrum measured at $\Omega_{ci}t \sim 3$. Here, $r_{\text{L,i}} \approx 57\lambda_{\text{se}}$.

of the presence of power-law ions. However, according to the structure of B_y at $x - x_{\rm sh} = [-50, 0]\lambda_{\rm se}$, the generation of shock surface rippling is slightly suppressed by the power-law ions. To confirm the suppression of generating ion-scale waves, we compute the magnetic power spectrum, P_{B_z} at the shock transition region, $x - x_{\rm sh} = [-50, 0]\lambda_{\rm se}$. Around the scale, $k_y/2\pi \sim r_{\rm inj,2}^{-1}$, the amplitude of power spectrum without the power-law ions is indeed larger than that with the power-law ions. The effects of power-law ions can be explained by the physics of ion reflection at the shock. Because the ions are mainly reflected by the shock potential, so ions with smaller kinetic energy are more likely to be reflected compared to the high energy ions. In other words, the high energy power-law ions just pass the shock surface and advect to downstream and thus, the presence of power-law ions reduces the ion temperature anisotropy, $T_{i\perp}/T_{i\parallel}$ at the shock transition zone. As described in Section VI, the growth rate of AIC (i.e., the instability responsible for the shock surface rippling) decreases as $T_{i\perp}/T_{i\parallel}$ decreases. In this regards, the presence of power-law ions does not play an important role in wave generation for electron preacceleration.

Upstream electron energy spectra for two different models (the model with and without the power-law ions) are plotted in Figure 57. Because the power-law ions does not enhance the multi-scale waves near the shock surface, the resulting energy spectra are insenstive to the presence of the power-law ions.Thus, we conclude that the CR ions in the upstream plasma does not change the results of this work.

8.3   Summary and Discussion

Merger-driven shocks in the ICM are collisionless and thought to produce CRs through DSA (e.g., [22]). The CR electrons responsible for the synchrotron radiation from observed radio relics, for instance, are expected to be accelerated at the $Q_\perp$-part of merger shocks (e.g., [144]). DSA involves a broad range of kinetic processes, including the generation of plasma waves and the interaction of waves and particles (e.g., [150]). In particular, one of the key issues for the DSA of electrons is preacceleration and subsequent injection to DSA, since thermal electrons have the momentum too small to cross the shock transition. Previously, two processes for preacceleration of electrons have been identified, the SDA mediated by upstream EFI-induced waves (e.g., [23, 24, 140]) and the SSDA mediated by multiscale waves in the shock transition (e.g., Section VII, [141, 162]). It was shown that those processes operate only in supercritical shocks. In the ICM, while supercritical shocks have $M_s \gtrsim 2.3$, some radio relics are observed to be associated with merger shocks with $M_s < 2.3$ (e.g., [48, 199, 200]).

As an effort to explain the production of CR electrons via DSA in radio relics with subcritical shocks, in this study, we have performed 2D PIC simulations for $Q_\perp$-shocks of $M_s = 2 - 3$ in high-β plasmas, with power-law nonthermal electrons preexisting in the shock upstream, in addition to Maxwellian thermal electrons. The nonthermal electrons intend to mimic relativistic electrons in the ICM. However, with limited computational capacities, the nonthermal component actually extends only up to $\gamma_{\rm cut} = 5 - 10$ in our simulations, representing a suprathermal population.

The main findings are summarized as follows. (1) The presence of PPEs enhances the EFI owing

to the increased fraction of the electrons reflected at the shock ramp. As a result, waves with $\lambda \sim 20 - 30\lambda_{se}$, generated by the EFI, appear even in the upstream region of the subcritical shocks in our M2.0 models. At the same time, the suprathermal population increases through the preacceleration via the Fermi-like acceleration mediated by the EFI waves in the M2.0 models, as well as in other models with supercritical shocks. (2) Ion-scale waves with $\lambda \gtrsim r_{L,i} \approx 57\lambda_{se} \cdot (M_s/3)$ are excited only in the supercritical shocks of the M2.3 - M3.0 models, as the consequence of the AIC instability, regardless of the presence of PPEs. In those models, the energy spectrum of electrons continues beyond p_{inj} via the SSDA mediated by multiscale waves ranging from electron to ion scales. On the other hand, ion-scale waves are not produced in the subcritical M2.0 models, since PPEs do not facilitate the excitation of ion-scale waves via the AIC instability. Hence, in the M2.0 models, the high-energy end of the electron energy spectrum does not change even with PPEs.

We further comment on the potential effects of the three ingredients that are not fully accounted for in our simulations: (1) realistic preexisting nonthermal electrons and (2) preexisting kinetic turbulence in the ICM.

As noted above, while the preexisting power-law component of electrons extends only up to $\gamma \lesssim \gamma_{\mathrm{inj}}$ in our simulations due to limited computational capacities, the nonthermal population in the ICM is expected to stretch to higher energies of $\gamma \sim 10^2 - 10^3$, considering the physical condition there [193,201]. Hence, in reality, some of the electrons reflected at the shock ramp may have energies higher than those reproduced in our simulations. On the other hand, the properties of the EFI induced by the reflected electrons, such as the wavelength and growth rate of the fastest growing mode, are not very sensitive to the characteristics of the electron beam that induces the instability [143]; as long as the bulk of the beam energy resides in the low-energy part of the power-law distribution, most of the EFI-induced waves would be still on electron scales. Although the details should be further investigated, we suspect that the power-law nonthermal electrons that extend to higher energies would not resolve the issue of the generation of ion-scale waves in subcritical shocks.

A more promising possibility would be the presence of broadband magnetic fluctuations, possibly produced by the turbulence in the ICM. Preexisting nonthermal electrons with energies up to $\gamma \sim 10^2 - 10^3$ could be directly injected into DSA via resonant scatterings off those preexisting turbulent waves. As a matter of fact, previous studies using test-particle simulations for electrons showed that electrons could be accelerated via SDA and DSA, regardless of the shock obliquity angle, by interacting with preexisting large-amplitude magnetic fluctuations in interplanetary shocks [202,203]. While such acceleration requires efficient wave-particle interactions in the ICM environment, the details of involved processes should be investigated through further simulations.

Additionally, we point that cosmological hydrodynamic simulations showed that radio relics, formed in the turbulent ICM, normally consist of shock surfaces with varying M_s and θ_{Bn} [33,48,52,121]. As suggested by several previous papers including Paper I, it would be interesting to consider a scenario, in which nonthermal electrons, accelerated in the locally supercritical portions of the shock surface, are injected to DSA at subcritical portions. Furthermore, the variation of θ_{Bn} in the shock surface could contribute to the generation of the large-scale modulation in the surface. In the interplanetary shocks, for

instance, the surface ripplings on scales larger than the AIC-induced waves have been detected [204], which are thought to be generated due to the upstream magnetic field fluctuations produced by the backstreaming ions at $Q_{\parallel}$-portions.

Finally, we thus conjecture that there is still the possibility of electron DSA in radio relics with subcritical shocks, when additional processes and/or ingredients other than those considered in this work are included. The investigation of such elements is beyond the scope of this article, so we leave it for future work. For now, we conclude that the presence of nonthermal electrons in the ICM "alone" would not resolve the issue of electron preacceleration and injection into DSA, and hence could not explain the production of CR electrons in radio relics with subcritical shocks.

IX Conclusion

Inside galaxy clusters, shocks are induced due to the supersonic flow motions and among such shocks, merger shocks induced by two clump mergers are the most energetically important. Indeed, the merger shocks have been detected through X-ray and radio observations and the radio synchrotron emission from such shocks have been recognized as a evidence of particle acceleration via DSA. Through the detailed numerical simulations, we have studied properties of merger-driven shocks and particle acceleration mechanism by such shocks in the galaxy clusters as well. We believe that our results are helpful to understand high energy phenomena due to the particle acceleration in the galaxy clusters (i.e., two outstanding problems described in Introduction). Through a set of PIC simulations for ICM $Q_\parallel$-shocks, we first examine the proton acceleration physics including the relevant plasma instabilities [83] and build a DSA model at ICM $Q_\parallel$-shocks as well [104]. According to that DSA model, the expected γ-ray emission from galaxy clusters are well below the upper limit suggested by Fermi-LAT. Future γ-ray observations could confirm whether the DSA model using in this thesis is reliable or not. Moreover, we partially resolve the issue about the origin of observed radio relics in the outskirts of galaxy clusters. In particular, the acceleration mechanisms mediated by microinstabilities in the transition region of shock could explain the electron acceleration at the ICM shocks with $M_s \gtrsim 2.3$. As pointed in the Sections VII and VIII, the electron acceleration at the very weak shocks with $M_s \lesssim 2.3$ should be investigated to understand the radio observations of such weak shocks. We will conduct more theoretical/numerical studies using PIC simulations as future works. For instance, it would be interesting if we can implement the turbulent upstream medium in our PIC simulation to consider more realistic turbulent ICM.

While this thesis mainly describes the physics of particle acceleration and relevant high energy phenomena inside galaxy clusters, it is likely to investigate particle acceleration around galaxy clusters. As explained in Introduction, kinetic energy flux dissipated through shocks around galaxy clusters is much smaller than that through shocks inside galaxy clusters, because external accretion shocks propagate in very low density medium. In spite of that, external accretion shocks may accelerate particles efficiently because of their large Mach number, $M_s \sim 10-100$. In this regards, external accretion shocks have been considered as CR accelerator (e.g., [205–211]). It is expected that Weibel instability plays an important role in shock formation when upstream bulk kinetic energy is much larger than upstream mangetic energy, and thus external accertion shocks could be also Weibel-mediated shocks. The detailed particle acceleration process in such shocks could be different from that in ICM shocks, so further numerical studies should be required to examine the detailed acceleration mechanism.

References

[1] F. Miniati, D. Ryu, H. Kang, T. W. Jones, R. Cen, and J. P. Ostriker, "Properties of Cosmic Shock Waves in Large-Scale Structure Formation," , vol. 542, no. 2, pp. 608–621, Oct. 2000.

[2] D. Ryu, H. Kang, E. Hallman, and T. W. Jones, "Cosmological Shock Waves and Their Role in the Large-Scale Structure of the Universe," , vol. 593, no. 2, pp. 599–610, Aug. 2003.

[3] C. Pfrommer, V. Springel, T. A. Enßlin, and M. Jubelgas, "Detecting shock waves in cosmological smoothed particle hydrodynamics simulations," , vol. 367, no. 1, pp. 113–131, Mar. 2006.

[4] H. Kang, D. Ryu, R. Cen, and J. P. Ostriker, "Cosmological Shock Waves in the Large-Scale Structure of the Universe: Nongravitational Effects," , vol. 669, no. 2, pp. 729–740, Nov. 2007.

[5] S. W. Skillman, B. W. O'Shea, E. J. Hallman, J. O. Burns, and M. L. Norman, "Cosmological Shocks in Adaptive Mesh Refinement Simulations and the Acceleration of Cosmic Rays," , vol. 689, no. 2, pp. 1063–1077, Dec. 2008.

[6] M. Hoeft, M. Brüggen, G. Yepes, S. Gottlöber, and A. Schwope, "Diffuse radio emission from clusters in the MareNostrum Universe simulation," , vol. 391, no. 4, pp. 1511–1526, Dec. 2008.

[7] F. Vazza, G. Brunetti, and C. Gheller, "Shock waves in Eulerian cosmological simulations: main properties and acceleration of cosmic rays," , vol. 395, no. 3, pp. 1333–1354, May 2009.

[8] S. E. Hong, D. Ryu, H. Kang, and R. Cen, "Shock Waves and Cosmic Ray Acceleration in the Outskirts of Galaxy Clusters," , vol. 785, no. 2, p. 133, Apr. 2014.

[9] K. Schaal and V. Springel, "Shock finding on a moving mesh - I. Shock statistics in non-radiative cosmological simulations," , vol. 446, no. 4, pp. 3992–4007, Feb. 2015.

[10] D. H. Porter, T. W. Jones, and D. Ryu, "Vorticity, Shocks, and Magnetic Fields in Subsonic, ICM-like Turbulence," , vol. 810, no. 2, p. 93, Sep. 2015.

[11] D. Ryu, H. Kang, J. Cho, and S. Das, "Turbulence and Magnetic Fields in the Large-Scale Structure of the Universe," *Science*, vol. 320, no. 5878, p. 909, May 2008.

[12] F. Vazza, G. Brunetti, C. Gheller, R. Brunino, and M. Brüggen, "Massive and refined. II. The statistical properties of turbulent motions in massive galaxy clusters with high spatial resolution," , vol. 529, p. A17, May 2011.

[13] F. Miniati, "The Matryoshka Run: A Eulerian Refinement Strategy to Study the Statistics of Turbulence in Virialized Cosmic Structures," , vol. 782, no. 1, p. 21, Feb. 2014.

[14] G. Brunetti and T. W. Jones, "Cosmic Rays in Galaxy Clusters and Their Nonthermal Emission," *International Journal of Modern Physics D*, vol. 23, no. 4, pp. 1 430 007–98, Mar. 2014.

[15] F. Vazza, T. W. Jones, M. Brüggen, G. Brunetti, C. Gheller, D. Porter, and D. Ryu, "Turbulence and vorticity in Galaxy clusters generated by structure formation," , vol. 464, no. 1, pp. 210–230, Jan. 2017.

[16] S. Brown and L. Rudnick, "Diffuse radio emission in/around the Coma cluster: beyond simple accretion," , vol. 412, no. 1, pp. 2–12, Mar. 2011.

[17] C. Pfrommer and T. W. Jones, "Radio Galaxy NGC 1265 Unveils the Accretion Shock Onto the Perseus Galaxy Cluster," , vol. 730, no. 1, p. 22, Mar. 2011.

[18] G. A. Ogrean and M. Brüggen, "First X-ray evidence for a shock at the Coma relic," , vol. 433, no. 2, pp. 1701–1708, Aug. 2013.

[19] M. Markevitch and A. Vikhlinin, "Shocks and cold fronts in galaxy clusters," , vol. 443, no. 1, pp. 1–53, May 2007.

[20] A. R. Bell, "The acceleration of cosmic rays in shock fronts - I." , vol. 182, pp. 147–156, Jan. 1978.

[21] R. D. Blandford and J. P. Ostriker, "Particle acceleration by astrophysical shocks." , vol. 221, pp. L29–L32, Apr. 1978.

[22] L. O. Drury, "REVIEW ARTICLE: An introduction to the theory of diffusive shock acceleration of energetic particles in tenuous plasmas," *Reports on Progress in Physics*, vol. 46, no. 8, pp. 973–1027, Aug. 1983.

[23] X. Guo, L. Sironi, and R. Narayan, "Non-thermal Electron Acceleration in Low Mach Number Collisionless Shocks. I. Particle Energy Spectra and Acceleration Mechanism," , vol. 794, no. 2, p. 153, Oct. 2014.

[24] ——, "Non-thermal Electron Acceleration in Low Mach Number Collisionless Shocks. II. Firehose-mediated Fermi Acceleration and its Dependence on Pre-shock Conditions," , vol. 797, no. 1, p. 47, Dec. 2014.

[25] J. Park, D. Caprioli, and A. Spitkovsky, "Simultaneous Acceleration of Protons and Electrons at Nonrelativistic Quasiparallel Collisionless Shocks," , vol. 114, no. 8, p. 085003, Feb. 2015.

[26] D. Caprioli and A. Spitkovsky, "Simulations of Ion Acceleration at Non-relativistic Shocks. I. Acceleration Efficiency," , vol. 783, no. 2, p. 91, Mar. 2014.

[27] ——, "Simulations of Ion Acceleration at Non-relativistic Shocks. II. Magnetic Field Amplification," , vol. 794, no. 1, p. 46, Oct. 2014.

[28] D. Caprioli, A.-R. Pop, and A. Spitkovsky, "Simulations and Theory of Ion Injection at Non-relativistic Collisionless Shocks," , vol. 798, no. 2, p. L28, Jan. 2015.

[29] R. A. Treumann, "Fundamentals of collisionless shocks for astrophysical application, 1. Non-relativistic shocks," , vol. 17, no. 4, pp. 409–535, Dec. 2009.

[30] D. Krauss-Varban and N. Omidi, "Structure of medium mach number quasi-parallel shocks: Upstream and downstream waves," , vol. 96, no. A10, pp. 17 715–17 731, Oct. 1991.

[31] F. Vazza, M. Brüggen, D. Wittor, C. Gheller, D. Eckert, and M. Stubbe, "Constraining the efficiency of cosmic ray acceleration by cluster shocks," , vol. 459, no. 1, pp. 70–83, Jun. 2016.

[32] A. Marcowith, A. Bret, A. Bykov, M. E. Dieckman, L. O'C Drury, B. Lembège, M. Lemoine, G. Morlino, G. Murphy, G. Pelletier, I. Plotnikov, B. Reville, M. Riquelme, L. Sironi, and A. Stockem Novo, "The microphysics of collisionless shock waves," *Reports on Progress in Physics*, vol. 79, no. 4, p. 046901, Apr. 2016.

[33] J.-H. Ha, D. Ryu, and H. Kang, "Properties of Merger Shocks in Merging Galaxy Clusters," , vol. 857, no. 1, p. 26, Apr. 2018.

[34] M. Markevitch, F. Govoni, G. Brunetti, and D. Jerius, "Bow Shock and Radio Halo in the Merging Cluster A520," , vol. 627, no. 2, pp. 733–738, Jul. 2005.

[35] G. A. Ogrean, M. Brüggen, R. van Weeren, H. Röttgering, A. Simionescu, M. Hoeft, and J. H. Croston, "Multiple density discontinuities in the merging galaxy cluster CIZA J2242.8+5301," , vol. 440, no. 4, pp. 3416–3425, Jun. 2014.

[36] M. Itahana, M. Takizawa, H. Akamatsu, T. Ohashi, Y. Ishisaki, H. Kawahara, and R. J. van Weeren, "Suzaku observations of the galaxy cluster 1RXS J0603.3+4214: Implications of particle acceleration processes in the "Toothbrush" radio relic," , vol. 67, no. 6, p. 113, Dec. 2015.

[37] S. Dasadia, M. Sun, C. Sarazin, A. Morandi, M. Markevitch, D. Wik, L. Feretti, G. Giovannini, F. Govoni, and V. Vacca, "A Strong Merger Shock in Abell 665," , vol. 820, no. 1, p. L20, Mar. 2016.

[38] M. Markevitch, A. H. Gonzalez, L. David, A. Vikhlinin, S. Murray, W. Forman, C. Jones, and W. Tucker, "A Textbook Example of a Bow Shock in the Merging Galaxy Cluster 1E 0657-56," , vol. 567, no. 1, pp. L27–L31, Mar. 2002.

[39] R. J. van Weeren, H. J. A. Röttgering, M. Brüggen, and M. Hoeft, "Particle Acceleration on Megaparsec Scales in a Merging Galaxy Cluster," *Science*, vol. 330, no. 6002, p. 347, Oct. 2010.

[40] A. Stroe, R. J. van Weeren, H. T. Intema, H. J. A. Röttgering, M. Brüggen, and M. Hoeft, "Discovery of spectral curvature in the shock downstream region: CIZA J2242.8+5301," , vol. 555, p. A110, Jul. 2013.

[41] R. J. van Weeren, M. Hoeft, H. J. A. Röttgering, M. Brüggen, H. T. Intema, and S. van Velzen, "A double radio relic in the merging galaxy cluster ZwCl 0008.8+5215," , vol. 528, p. A38, Apr. 2011.

[42] J. Bagchi, S. K. Sirothia, N. Werner, M. B. Pandge, N. G. Kantharia, C. H. Ishwara-Chandra, Gopal-Krishna, S. Paul, and S. Joshi, "Discovery of the First Giant Double Radio Relic in a Galaxy Cluster Found in the Planck Sunyaev-Zel'dovich Cluster Survey: PLCK G287.0+32.9," , vol. 736, no. 1, p. L8, Jul. 2011.

[43] A. Bonafede, H. T. Intema, M. Brüggen, M. Girardi, M. Nonino, N. Kantharia, R. J. van Weeren, and H. J. A. Röttgering, "Evidence for Particle Re-acceleration in the Radio Relic in the Galaxy Cluster PLCKG287.0+32.9," , vol. 785, no. 1, p. 1, Apr. 2014.

[44] R. J. van Weeren, H. J. A. Röttgering, H. T. Intema, L. Rudnick, M. Brüggen, M. Hoeft, and J. B. R. Oonk, "The "toothbrush-relic": evidence for a coherent linear 2-Mpc scale shock wave in a massive merging galaxy cluster?" , vol. 546, p. A124, Oct. 2012.

[45] R. J. van Weeren, G. Brunetti, M. Brüggen, F. Andrade-Santos, G. A. Ogrean, W. L. Williams, H. J. A. Röttgering, W. A. Dawson, W. R. Forman, F. de Gasperin, M. J. Hardcastle, C. Jones, G. K. Miley, D. A. Rafferty, L. Rudnick, J. Sabater, C. L. Sarazin, T. W. Shimwell, A. Bonafede, P. N. Best, L. Bîrzan, R. Cassano, K. T. Chyży, J. H. Croston, T. J. Dijkema, T. Enßlin, C. Ferrari, G. Heald, M. Hoeft, C. Horellou, M. J. Jarvis, R. P. Kraft, M. Mevius, H. T. Intema, S. S. Murray, E. Orrú, R. Pizzo, S. S. Sridhar, A. Simionescu, A. Stroe, S. van der Tol, and G. J. White, "LOFAR, VLA, and Chandra Observations of the Toothbrush Galaxy Cluster," , vol. 818, no. 2, p. 204, Feb. 2016.

[46] L. Feretti, G. Giovannini, F. Govoni, and M. Murgia, "Clusters of galaxies: observational properties of the diffuse radio emission," , vol. 20, p. 54, May 2012.

[47] M. Brüggen, A. Bykov, D. Ryu, and H. Röttgering, "Magnetic Fields, Relativistic Particles, and Shock Waves in Cluster Outskirts," , vol. 166, no. 1-4, pp. 187–213, May 2012.

[48] D. Wittor, S. Ettori, F. Vazza, K. Rajpurohit, M. Hoeft, and P. Domínguez-Fernández, "Exploring the spectral properties of radio relics - I: integrated spectral index and Mach number," , vol. 506, no. 1, pp. 396–414, Sep. 2021.

[49] H. Akamatsu, R. J. van Weeren, G. A. Ogrean, H. Kawahara, A. Stroe, D. Sobral, M. Hoeft, H. Röttgering, M. Brüggen, and J. S. Kaastra, "Suzaku X-ray study of the double radio relic galaxy cluster CIZA J2242.8+5301," , vol. 582, p. A87, Oct. 2015.

[50] H. Kang and D. Ryu, "Curved Radio Spectra of Weak Cluster Shocks,", vol. 809, no. 2, p. 186, Aug. 2015.

[51] H. Kang, D. Ryu, and T. W. Jones, "Shock Acceleration Model for the Toothbrush Radio Relic,", vol. 840, no. 1, p. 42, May 2017.

[52] S. E. Hong, H. Kang, and D. Ryu, "Radio and X-Ray Shocks in Clusters of Galaxies,", vol. 812, no. 1, p. 49, Oct. 2015.

[53] D. Clowe, A. Gonzalez, and M. Markevitch, "Weak-Lensing Mass Reconstruction of the Interacting Cluster 1E 0657-558: Direct Evidence for the Existence of Dark Matter,", vol. 604, no. 2, pp. 596–603, Apr. 2004.

[54] M. J. Jee, A. Stroe, W. Dawson, D. Wittman, H. Hoekstra, M. Brüggen, H. Röttgering, D. Sobral, and R. J. van Weeren, "MC ^{2}: Constraining the Dark Matter Distribution of the Violent Merging Galaxy Cluster CIZA J2242.8+5301 by Piercing through the Milky Way,", vol. 802, no. 1, p. 46, Mar. 2015.

[55] N. Okabe, H. Akamatsu, J. Kakuwa, Y. Fujita, Y. Zhang, M. Tanaka, and K. Umetsu, "Radio relics tracing the projected mass distribution in CIZA J2242.8+5301*,", vol. 67, no. 6, p. 114, Dec. 2015.

[56] N. Golovich, R. J. van Weeren, W. A. Dawson, M. J. Jee, and D. Wittman, "MC^2: Multiwavelength and Dynamical Analysis of the Merging Galaxy Cluster ZwCl 0008.8+5215: An Older and Less Massive Bullet Cluster,", vol. 838, no. 2, p. 110, Apr. 2017.

[57] M. J. Jee, W. A. Dawson, A. Stroe, D. Wittman, R. J. van Weeren, M. Brüggen, M. Bradač, and H. Röttgering, "MC2: Mapping the Dark Matter Distribution of the "Toothbrush" Cluster RX J0603.3+4214 with Hubble Space Telescope and Subaru Weak Lensing,", vol. 817, no. 2, p. 179, Feb. 2016.

[58] K. Finner, M. J. Jee, N. Golovich, D. Wittman, W. Dawson, D. Gruen, A. M. Koekemoer, B. C. Lemaux, and S. Seitz, "MC^2: Subaru and Hubble Space Telescope Weak-lensing Analysis of the Double Radio Relic Galaxy Cluster PLCK G287.0+32.9,", vol. 851, no. 1, p. 46, Dec. 2017.

[59] M. Markevitch, T. J. Ponman, P. E. J. Nulsen, M. W. Bautz, D. J. Burke, L. P. David, D. Davis, R. H. Donnelly, W. R. Forman, C. Jones, J. Kaastra, E. Kellogg, D. W. Kim, J. Kolodziejczak, P. Mazzotta, A. Pagliaro, S. Patel, L. Van Speybroeck, A. Vikhlinin, J. Vrtilek, M. Wise, and P. Zhao, "Chandra Observation of Abell 2142: Survival of Dense Subcluster Cores in a Merger,", vol. 541, no. 2, pp. 542–549, Oct. 2000.

[60] A. Vikhlinin, M. Markevitch, and S. S. Murray, "A Moving Cold Front in the Intergalactic Medium of A3667,", vol. 551, no. 1, pp. 160–171, Apr. 2001.

[61] H. Bourdin, P. Mazzotta, M. Markevitch, S. Giacintucci, and G. Brunetti, "Shock Heating of the Merging Galaxy Cluster A521," , vol. 764, no. 1, p. 82, Feb. 2013.

[62] J. A. ZuHone, M. Markevitch, and R. E. Johnson, "Stirring Up the Pot: Can Cooling Flows in Galaxy Clusters be Quenched by Gas Sloshing?" , vol. 717, no. 2, pp. 908–928, Jul. 2010.

[63] D. L. Emery, Á. Bogdán, R. P. Kraft, F. Andrade-Santos, W. R. Forman, M. J. Hardcastle, and C. Jones, "A Spectacular Bow Shock in the 11 keV Galaxy Cluster Around 3C 438," , vol. 834, no. 2, p. 159, Jan. 2017.

[64] D. Clowe, M. Bradač, A. H. Gonzalez, M. Markevitch, S. W. Randall, C. Jones, and D. Zaritsky, "A Direct Empirical Proof of the Existence of Dark Matter," , vol. 648, no. 2, pp. L109–L113, Sep. 2006.

[65] N. Okabe and K. Umetsu, "Subaru Weak Lensing Study of Seven Merging Clusters: Distributions of Mass and Baryons," , vol. 60, p. 345, Apr. 2008.

[66] V. Springel and G. R. Farrar, "The speed of the 'bullet' in the merging galaxy cluster 1E0657-56," , vol. 380, no. 3, pp. 911–925, Sep. 2007.

[67] R. J. van Weeren, M. Brüggen, H. J. A. Röttgering, and M. Hoeft, "Using double radio relics to constrain galaxy cluster mergers: a model of double radio relics in CIZA J2242.8+5301," , vol. 418, no. 1, pp. 230–243, Nov. 2011.

[68] S. M. Molnar and T. Broadhurst, "Shocks and Tides Quantified in the "Sausage" Cluster, CIZA J2242.8+5301 Using N-body/Hydrodynamical Simulations," , vol. 841, no. 1, p. 46, May 2017.

[69] ——, "Multi-phenomena Modeling of the New Bullet-like Cluster ZwCl 008.8+52 Using N-body/Hydrodynamical Simulations," , vol. 862, no. 2, p. 112, Aug. 2018.

[70] W. Schmidt, C. Byrohl, J. F. Engels, C. Behrens, and J. C. Niemeyer, "Viscosity, pressure and support of the gas in simulations of merging cool-core clusters," , vol. 470, no. 1, pp. 142–156, Sep. 2017.

[71] E. Komatsu, K. M. Smith, J. Dunkley, C. L. Bennett, B. Gold, G. Hinshaw, N. Jarosik, D. Larson, M. R. Nolta, L. Page, D. N. Spergel, M. Halpern, R. S. Hill, A. Kogut, M. Limon, S. S. Meyer, N. Odegard, G. S. Tucker, J. L. Weiland, E. Wollack, and E. L. Wright, "Seven-year Wilkinson Microwave Anisotropy Probe (WMAP) Observations: Cosmological Interpretation," , vol. 192, no. 2, p. 18, Feb. 2011.

[72] P. A. Thomas, J. M. Colberg, H. M. P. Couchman, G. P. Efstathiou, C. S. Frenk, A. R. Jenkins, A. H. Nelson, R. M. Hutchings, J. A. Peacock, F. R. Pearce, S. D. M. White, and Virgo Consortium, "The structure of galaxy clusters in various cosmologies," , vol. 296, no. 4, pp. 1061–1071, Jun. 1998.

[73] D. Ryu, J. P. Ostriker, H. Kang, and R. Cen, "A Cosmological Hydrodynamic Code Based on the Total Variation Diminishing Scheme," , vol. 414, p. 1, Sep. 1993.

[74] G. A. Ogrean, M. Brüggen, R. J. van Weeren, H. Röttgering, J. H. Croston, and M. Hoeft, "Challenges to our understanding of radio relics: X-ray observations of the Toothbrush cluster," , vol. 433, no. 1, pp. 812–824, Jul. 2013.

[75] F. Vazza, K. Dolag, D. Ryu, G. Brunetti, C. Gheller, H. Kang, and C. Pfrommer, "A comparison of cosmological codes: properties of thermal gas and shock waves in large-scale structures," , vol. 418, no. 2, pp. 960–985, Dec. 2011.

[76] H. Kang and D. Ryu, "Diffusive Shock Acceleration at Cosmological Shock Waves," , vol. 764, no. 1, p. 95, Feb. 2013.

[77] C. Rumsey, Y. C. Perrott, M. Olamaie, R. D. E. Saunders, M. P. Hobson, A. Stroe, M. P. Schammel, and K. J. B. Grainge, "AMI SZ observation of galaxy-cluster merger CIZA J2242+5301: perpendicular flows of gas and dark matter," , vol. 470, no. 4, pp. 4638–4645, Oct. 2017.

[78] H. Akamatsu, Y. Fujita, T. Akahori, Y. Ishisaki, K. Hayashida, A. Hoshino, F. Mernier, K. Yoshikawa, K. Sato, and J. S. Kaastra, "Properties of the cosmological filament between two clusters: A possible detection of a large-scale accretion shock by Suzaku," , vol. 606, p. A1, Sep. 2017.

[79] D. Ryu and E. T. Vishniac, "The Dynamic Instability of Adiabatic Blast Waves," , vol. 368, p. 411, Feb. 1991.

[80] A. Botteon, T. W. Shimwell, A. Bonafede, D. Dallacasa, G. Brunetti, S. Mandal, R. J. van Weeren, M. Brüggen, R. Cassano, F. de Gasperin, D. N. Hoang, M. Hoeft, H. J. A. Röttgering, F. Savini, G. J. White, A. Wilber, and T. Venturi, "LOFAR discovery of a double radio halo system in Abell 1758 and radio/X-ray study of the cluster pair," , vol. 478, no. 1, pp. 885–898, Jul. 2018.

[81] L. Gu, H. Akamatsu, T. W. Shimwell, H. T. Intema, R. J. van Weeren, F. de Gasperin, F. Mernier, J. Mao, I. Urdampilleta, J. de Plaa, V. Parekh, H. J. A. Röttgering, and J. S. Kaastra, "Observations of a pre-merger shock in colliding clusters of galaxies," *Nature Astronomy*, vol. 3, pp. 838–843, Jun. 2019.

[82] S. Gabici and P. Blasi, "Nonthermal Radiation from Clusters of Galaxies: The Role of Merger Shocks in Particle Acceleration," , vol. 583, no. 2, pp. 695–705, Feb. 2003.

[83] J.-H. Ha, D. Ryu, H. Kang, and A. J. van Marle, "Proton Acceleration in Weak Quasi-parallel Intracluster Shocks: Injection and Early Acceleration," , vol. 864, no. 2, p. 105, Sep. 2018.

[84] A. Pinzke and C. Pfrommer, "Simulating the γ-ray emission from galaxy clusters: a universal cosmic ray spectrum and spatial distribution," , vol. 409, no. 2, pp. 449–480, Dec. 2010.

[85] F. Zandanel and S. Ando, "Constraints on diffuse gamma-ray emission from structure formation processes in the Coma cluster," , vol. 440, no. 1, pp. 663–671, May 2014.

[86] H. Kang and D. Ryu, "Effects of Alfvénic Drift on Diffusive Shock Acceleration at Weak Cluster Shocks," , vol. 856, no. 1, p. 33, Mar. 2018.

[87] M. Ackermann, M. Ajello, A. Albert, W. B. Atwood, L. Baldini, J. Ballet, G. Barbiellini, D. Bastieri, K. Bechtol, R. Bellazzini, E. Bissaldi, R. D. Blandford, E. D. Bloom, R. Bonino, E. Bottacini, J. Bregeon, P. Bruel, R. Buehler, G. A. Caliandro, R. A. Cameron, M. Caragiulo, P. A. Caraveo, J. M. Casandjian, E. Cavazzuti, C. Cecchi, E. Charles, A. Chekhtman, G. Chiaro, S. Ciprini, J. Cohen-Tanugi, J. Conrad, S. Cutini, F. D'Ammando, A. de Angelis, F. de Palma, R. Desiante, S. W. Digel, L. Di Venere, P. S. Drell, C. Favuzzi, S. J. Fegan, Y. Fukazawa, S. Funk, P. Fusco, F. Gargano, D. Gasparrini, N. Giglietto, F. Giordano, M. Giroletti, G. Godfrey, D. Green, I. A. Grenier, S. Guiriec, E. Hays, J. W. Hewitt, D. Horan, G. Jóhannesson, M. Kuss, S. Larsson, L. Latronico, J. Li, L. Li, F. Longo, F. Loparco, M. N. Lovellette, P. Lubrano, G. M. Madejski, S. Maldera, A. Manfreda, M. Mayer, M. N. Mazziotta, P. F. Michelson, W. Mitthumsiri, T. Mizuno, M. E. Monzani, A. Morselli, I. V. Moskalenko, S. Murgia, E. Nuss, T. Ohsugi, M. Orienti, E. Orlando, J. F. Ormes, D. Paneque, M. Pesce-Rollins, V. Petrosian, F. Piron, G. Pivato, T. A. Porter, S. Rainò, R. Rando, M. Razzano, A. Reimer, O. Reimer, M. Sánchez-Conde, C. Sgrò, E. J. Siskind, F. Spada, G. Spandre, P. Spinelli, H. Tajima, H. Takahashi, J. B. Thayer, L. Tibaldo, D. F. Torres, G. Tosti, E. Troja, G. Vianello, K. S. Wood, S. Zimmer, Fermi-LAT Collaboration, and Y. Rephaeli, "Search for Gamma-Ray Emission from the Coma Cluster with Six Years of Fermi-LAT Data," , vol. 819, no. 2, p. 149, Mar. 2016.

[88] T. Sundberg, C. T. Haynes, D. Burgess, and C. X. Mazelle, "Ion Acceleration at the Quasi-parallel Bow Shock: Decoding the Signature of Injection," , vol. 820, no. 1, p. 21, Mar. 2016.

[89] J. P. Edmiston and C. F. Kennel, "A parametric survey of the first critical Mach number for a fast MHD shock," *Journal of Plasma Physics*, vol. 32, no. 3, pp. 429–441, Dec. 1984.

[90] A. R. Bell, "Turbulent amplification of magnetic field and diffusive shock acceleration of cosmic rays," , vol. 353, no. 2, pp. 550–558, Sep. 2004.

[91] O. Buneman, "Computer space plasma physics," *in Computer Space Plasma Physics: Simulation Techniques and Software, ed. H. Matsumoto & Y. Omura*, p. 67, 1993.

[92] A. Spitkovsky, "Simulations of relativistic collisionless shocks: shock structure and particle acceleration," *in AIP Conf. Proc., Astrophysical Sources of High Energy Particles and Radiation, ed. T. Bulik, B. Rudak, & G. Madejski (New York: AIP)*, vol. 801, no. 1, pp. 345–350, 2005. [Online]. Available: https://aip.scitation.org/doi/abs/10.1063/1.2141897

[93] M. M. Leroy, D. Winske, C. C. Goodrich, C. S. Wu, and K. Papadopoulos, "The structure of perpendicular bow shocks," , vol. 87, no. A7, pp. 5081–5094, Jul. 1982.

[94] D. Burgess and S. J. Schwartz, "The dynamics and upstream distributions of ions reflected at the earth's bow shock," , vol. 89, no. A9, pp. 7407–7422, Sep. 1984.

[95] R. A. Treumann and C. H. Jaroschek, "Fundamentals of Non-relativistic Collisionless Shock Physics: II. Basic Equations and Models," *arXiv e-prints*, p. arXiv:0805.2162, May 2008.

[96] H. Kang and D. Ryu, "Diffusive Shock Acceleration in Test-particle Regime," , vol. 721, no. 1, pp. 886–892, Sep. 2010.

[97] J. F. McKenzie and H. J. Voelk, "Non-linear theory of cosmic ray shocks including self-generated Alfven waves," , vol. 116, no. 2, pp. 191–200, Dec. 1982.

[98] A. J. van Marle, F. Casse, and A. Marcowith, "On magnetic field amplification and particle acceleration near non-relativistic astrophysical shocks: particles in MHD cells simulations," , vol. 473, no. 3, pp. 3394–3409, Jan. 2018.

[99] A. Bykov, F. Vazza, J. Kropotina, K. Levenfish, and F. Paerels, "Shocks and non-thermal particles in clusters of galaxies," *Space Science Reviews*, vol. 215, no. 1, pp. 1–35, 2019.

[100] A. J. Van Marle, D. Ryu, H. Kang, and J.-H. Ha, "Using combined pic and mhd to model particle acceleration in galaxy cluster shocks," *Plasma and Fusion Research*, vol. 14, pp. 4 406 119–4 406 119, 2019.

[101] A. J. van Marle, "Diffusive shock acceleration of cosmic rays in low-mach galaxy cluster shocks." in *Journal of Physics: Conference Series*, vol. 1468, no. 1.   IOP Publishing, 2020, p. 012093.

[102] G. G. Howes, "Inertial range turbulence in kinetic plasmas," *Physics of Plasmas*, vol. 15, no. 5, pp. 055 904–055 904, May 2008.

[103] A. A. Schekochihin, S. C. Cowley, W. Dorland, G. W. Hammett, G. G. Howes, E. Quataert, and T. Tatsuno, "Astrophysical Gyrokinetics: Kinetic and Fluid Turbulent Cascades in Magnetized Weakly Collisional Plasmas," , vol. 182, no. 1, pp. 310–377, May 2009.

[104] D. Ryu, H. Kang, and J.-H. Ha, "A Diffusive Shock Acceleration Model for Protons in Weak Quasi-parallel Intracluster Shocks," , vol. 883, no. 1, p. 60, Sep. 2019.

[105] J.-H. Ha, D. Ryu, and H. Kang, "Gamma-Ray and Neutrino Emissions due to Cosmic-Ray Protons Accelerated at Intracluster Shocks in Galaxy Clusters," , vol. 892, no. 2, p. 86, Apr. 2020.

[106] V. S. Berezinsky, P. Blasi, and V. S. Ptuskin, "Clusters of Galaxies as Storage Room for Cosmic Rays," , vol. 487, no. 2, pp. 529–535, Oct. 1997.

[107] C. Pfrommer and T. A. Enßlin, "Constraining the population of cosmic ray protons in cooling flow clusters with γ-ray and radio observations: Are radio mini-halos of hadronic origin?" , vol. 413, pp. 17–36, Jan. 2004.

[108] M. Ackermann, M. Ajello, A. Albert, A. Allafort, W. B. Atwood, L. Baldini, J. Ballet, G. Barbiellini, D. Bastieri, K. Bechtol, R. Bellazzini, E. D. Bloom, E. Bonamente, E. Bottacini, T. J. Brandt, J. Bregeon, M. Brigida, P. Bruel, R. Buehler, S. Buson, G. A. Caliandro, R. A. Cameron, P. A. Caraveo, E. Cavazzuti, R. C. G. Chaves, J. Chiang, G. Chiaro, S. Ciprini, R. Claus, J. Cohen-Tanugi, J. Conrad, F. D'Ammando, A. de Angelis, F. de Palma, C. D. Dermer, S. W. Digel, P. S. Drell, A. Drlica-Wagner, C. Favuzzi, A. Franckowiak, S. Funk, P. Fusco, F. Gargano, D. Gasparrini, S. Germani, N. Giglietto, F. Giordano, M. Giroletti, G. Godfrey, G. A. Gomez-Vargas, I. A. Grenier, S. Guiriec, M. Gustafsson, D. Hadasch, M. Hayashida, J. Hewitt, R. E. Hughes, T. E. Jeltema, G. Jóhannesson, A. S. Johnson, T. Kamae, J. Kataoka, J. Knödlseder, M. Kuss, J. Lande, S. Larsson, L. Latronico, M. Llena Garde, F. Longo, F. Loparco, M. N. Lovellette, P. Lubrano, M. Mayer, M. N. Mazziotta, J. E. McEnery, P. F. Michelson, W. Mitthumsiri, T. Mizuno, M. E. Monzani, A. Morselli, I. V. Moskalenko, S. Murgia, R. Nemmen, E. Nuss, T. Ohsugi, M. Orienti, E. Orlando, J. F. Ormes, J. S. Perkins, M. Pesce-Rollins, F. Piron, G. Pivato, S. Rainò, R. Rando, M. Razzano, S. Razzaque, A. Reimer, O. Reimer, J. Ruan, M. Sánchez-Conde, A. Schulz, C. Sgrò, E. J. Siskind, G. Spandre, P. Spinelli, E. Storm, A. W. Strong, D. J. Suson, H. Takahashi, J. G. Thayer, J. B. Thayer, D. J. Thompson, L. Tibaldo, M. Tinivella, D. F. Torres, E. Troja, Y. Uchiyama, T. L. Usher, J. Vandenbroucke, G. Vianello, V. Vitale, B. L. Winer, K. S. Wood, S. Zimmer, Fermi-LAT Collaboration, A. Pinzke, and C. Pfrommer, "Search for Cosmic-Ray-induced Gamma-Ray Emission in Galaxy Clusters," , vol. 787, no. 1, p. 18, May 2014.

[109] K. Murase, S. Inoue, and S. Nagataki, "Cosmic Rays above the Second Knee from Clusters of Galaxies and Associated High-Energy Neutrino Emission," , vol. 689, no. 2, p. L105, Dec. 2008.

[110] K. Murase, M. Ahlers, and B. C. Lacki, "Testing the hadronuclear origin of PeV neutrinos observed with IceCube," , vol. 88, no. 12, p. 121301, Dec. 2013.

[111] F. Zandanel, I. Tamborra, S. Gabici, and S. Ando, "High-energy gamma-ray and neutrino backgrounds from clusters of galaxies and radio constraints," , vol. 578, p. A32, Jun. 2015.

[112] K. Murase and E. Waxman, "Constraining high-energy cosmic neutrino sources: Implications and prospects," , vol. 94, no. 10, p. 103006, Nov. 2016.

[113] K. Hagiwara, K. Abe, C. Bronner, Y. Hayato, M. Ikeda, H. Ito, J. Kameda, Y. Kataoka, Y. Kato, Y. Kishimoto, L. Marti, M. Miura, S. Moriyama, T. Mochizuki, M. Nakahata, Y. Nakajima, S. Nakayama, T. Okada, K. Okamoto, A. Orii, G. Pronost, H. Sekiya, M. Shiozawa, Y. Sonoda, A. Takeda, A. Takenaka, H. Tanaka, T. Yano, R. Akutsu, T. Kajita, K. Okumura, R. Wang, J. Xia, D. Bravo-Berguño, L. Labarga, P. Fernandez, F. D. M. Blaszczyk, E. Kearns, J. L. Raaf, J. L. Stone, L. Wan, T. Wester, J. Bian, N. J. Griskevich, W. R. Kropp, S. Locke, S. Mine, M. B. Smy, H. W. Sobel, V. Takhistov, P. Weatherly, K. S. Ganezer, J. Hill, J. Y. Kim, I. T. Lim, R. G. Park, B. Bodur, K. Scholberg, C. W. Walter, A. Coffani, O. Drapier, M. Gonin, T. A. Mueller, P. Paganini, T. Ishizuka, T. Nakamura, J. S. Jang, J. G. Learned, S. Matsuno, R. P. Litchfield, A. A. Sztuc, Y. Uchida, V. Berardi, N. F. Calabria, M. G. Catanesi, E. Radicioni,

G. De Rosa, G. Collazuol, F. Iacob, L. Ludovici, Y. Nishimura, S. Cao, M. Friend, T. Hasegawa, T. Ishida, T. Kobayashi, T. Nakadaira, K. Nakamura, Y. Oyama, K. Sakashita, T. Sekiguchi, T. Tsukamoto, M. Hasegawa, Y. Isobe, H. Miyabe, Y. Nakano, T. Shiozawa, T. Sugimoto, A. T. Suzuki, Y. Takeuchi, A. Ali, Y. Ashida, S. Hirota, M. Jiang, T. Kikawa, M. Mori, K. Naka-mura, T. Nakaya, R. A. Wendell, L. H. V. Anthony, N. McCauley, A. Pritchard, K. M. Tsui, Y. Fukuda, Y. Itow, T. Niwa, M. Taani, M. Tsukada, P. Mijakowski, K. Frankiewicz, C. K. Jung, C. Vilela, M. J. Wilking, C. Yanagisawa, D. Fukuda, M. Harada, T. Horai, H. Ishino, S. Ito, Y. Koshio, M. Sakuda, Y. Takahira, C. Xu, Y. Kuno, L. Cook, C. Simpson, D. Wark, F. Di Lodovico, S. Molina Sedgwick, B. Richards, S. Zsoldos, S. B. Kim, M. Thiesse, L. Thomp-son, H. Okazawa, Y. Choi, K. Nishijima, M. Koshiba, M. Yokoyama, A. Goldsack, K. Martens, B. Quilain, Y. Suzuki, M. R. Vagins, M. Kuze, M. Tanaka, T. Yoshida, M. Ishitsuka, R. Mat-sumoto, K. Ohta, J. F. Martin, C. M. Nantais, H. A. Tanaka, T. Towstego, M. Hartz, A. Konaka, P. de Perio, S. Chen, B. Jamieson, J. Walker, A. Minamino, K. Okamoto, G. Pintaudi, and Super-Kamiokande Collaboration, "Search for Astronomical Neutrinos from Blazar TXS 0506+056 in Super-Kamiokande," , vol. 887, no. 1, p. L6, Dec. 2019.

[114] J.-H. Ha, D. Ryu, and H. Kang, "Modeling of Cosmic-Ray Production and Transport and Estima-tion of Gamma-Ray and Neutrino Emissions in Starburst Galaxies," , vol. 907, no. 1, p. 26, Jan. 2021.

[115] S. R. Kelner, F. A. Aharonian, and V. V. Bugayov, "Energy spectra of gamma rays, electrons, and neutrinos produced at proton-proton interactions in the very high energy regime," , vol. 74, no. 3, p. 034018, Aug. 2006.

[116] M. G. Aartsen, M. Ackermann, J. Adams, J. A. Aguilar, M. Ahlers, M. Ahrens, D. Altmann, T. Anderson, C. Arguelles, T. C. Arlen, J. Auffenberg, X. Bai, S. W. Barwick, V. Baum, J. J. Beatty, J. Becker Tjus, K. H. Becker, S. BenZvi, P. Berghaus, D. Berley, E. Bernardini, A. Bern-hard, D. Z. Besson, G. Binder, D. Bindig, M. Bissok, E. Blaufuss, J. Blumenthal, D. J. Boersma, C. Bohm, D. Bose, S. Böser, O. Botner, L. Brayeur, H. P. Bretz, A. M. Brown, J. Casey, M. Casier, D. Chirkin, A. Christov, B. Christy, K. Clark, L. Classen, F. Clevermann, S. Coenders, D. F. Cowen, A. H. Cruz Silva, M. Danninger, J. Daughhetee, J. C. Davis, M. Day, J. P. A. M. de An-dré, C. De Clercq, S. De Ridder, P. Desiati, K. D. de Vries, M. de With, T. DeYoung, J. C. Díaz-Vélez, M. Dunkman, R. Eagan, B. Eberhardt, B. Eichmann, J. Eisch, S. Euler, P. A. Evenson, O. Fadiran, A. R. Fazely, A. Fedynitch, J. Feintzeig, J. Felde, T. Feusels, K. Filimonov, C. Finley, T. Fischer-Wasels, S. Flis, A. Franckowiak, K. Frantzen, T. Fuchs, T. K. Gaisser, J. Gallagher, L. Gerhardt, D. Gier, L. Gladstone, T. Glüsenkamp, A. Goldschmidt, G. Golup, J. G. Gonzalez, J. A. Goodman, D. Góra, D. T. Grandmont, D. Grant, P. Gretskov, J. C. Groh, A. Groß, C. Ha, C. Haack, A. Haj Ismail, P. Hallen, A. Hallgren, F. Halzen, K. Hanson, D. Hebecker, D. Heere-man, D. Heinen, K. Helbing, R. Hellauer, D. Hellwig, S. Hickford, G. C. Hill, K. D. Hoffman, R. Hoffmann, A. Homeier, K. Hoshina, F. Huang, W. Huelsnitz, P. O. Hulth, K. Hultqvist, S. Hus-sain, A. Ishihara, E. Jacobi, J. Jacobsen, K. Jagielski, G. S. Japaridze, K. Jero, O. Jlelati, M. Ju-

rkovic, B. Kaminsky, A. Kappes, T. Karg, A. Karle, M. Kauer, J. L. Kelley, A. Kheirandish, J. Kiryluk, J. Kläs, S. R. Klein, J. H. Köhne, G. Kohnen, H. Kolanoski, A. Koob, L. Köpke, C. Kopper, S. Kopper, D. J. Koskinen, M. Kowalski, A. Kriesten, K. Krings, G. Kroll, J. Kunnen, N. Kurahashi, T. Kuwabara, M. Labare, D. T. Larsen, M. J. Larson, M. Lesiak-Bzdak, M. Leuermann, J. Leute, J. Lünemann, O. Macías, J. Madsen, G. Maggi, R. Maruyama, K. Mase, H. S. Matis, F. McNally, K. Meagher, A. Meli, T. Meures, S. Miarecki, E. Middell, E. Middlemas, N. Milke, J. Miller, L. Mohrmann, T. Montaruli, R. Morse, R. Nahnhauer, U. Naumann, H. Niederhausen, S. C. Nowicki, D. R. Nygren, A. Obertacke, S. Odrowski, A. Olivas, A. Omairat, A. O'Murchadha, T. Palczewski, L. Paul, Ö. Penek, J. A. Pepper, C. Pérez de los Heros, C. Pfendner, D. Pieloth, E. Pinat, J. Posselt, P. B. Price, G. T. Przybylski, J. Pütz, M. Quinnan, L. Rädel, M. Rameez, K. Rawlins, P. Redl, I. Rees, R. Reimann, E. Resconi, W. Rhode, M. Richman, B. Riedel, S. Robertson, J. P. Rodrigues, M. Rongen, C. Rott, T. Ruhe, B. Ruzybayev, D. Ryckbosch, S. M. Saba, H. G. Sander, M. Santander, S. Sarkar, K. Schatto, F. Scheriau, T. Schmidt, M. Schmitz, S. Schoenen, S. Schöneberg, A. Schönwald, A. Schukraft, L. Schulte, O. Schulz, D. Seckel, Y. Sestayo, S. Seunarine, R. Shanidze, C. Sheremata, M. W. E. Smith, D. Soldin, G. M. Spiczak, C. Spiering, M. Stamatikos, T. Stanev, N. A. Stanisha, A. Stasik, T. Stezelberger, R. G. Stokstad, A. Stößl, E. A. Strahler, R. Ström, N. L. Strotjohann, G. W. Sullivan, H. Taavola, I. Taboada, A. Tamburro, A. Tepe, S. Ter-Antonyan, A. Terliuk, G. Tešić, S. Tilav, P. A. Toale, M. N. Tobin, D. Tosi, M. Tselengidou, E. Unger, M. Usner, S. Vallecorsa, N. van Eijndhoven, J. Vandenbroucke, J. van Santen, M. Vehring, M. Voge, M. Vraeghe, C. Walck, M. Wallraff, C. Weaver, M. Wellons, C. Wendt, S. Westerhoff, B. J. Whelan, N. Whitehorn, C. Wichary, K. Wiebe, C. H. Wiebusch, D. R. Williams, H. Wissing, M. Wolf, T. R. Wood, K. Woschnagg, D. L. Xu, X. W. Xu, J. P. Yanez, G. Yodh, S. Yoshida, P. Zarzhitsky, J. Ziemann, S. Zierke, M. Zoll, and IceCube Collaboration, "Observation of High-Energy Astrophysical Neutrinos in Three Years of IceCube Data," , vol. 113, no. 10, p. 101101, Sep. 2014.

[117] E. Richard, K. Okumura, K. Abe, Y. Haga, Y. Hayato, M. Ikeda, K. Iyogi, J. Kameda, Y. Kishimoto, M. Miura, S. Moriyama, M. Nakahata, T. Nakajima, Y. Nakano, S. Nakayama, A. Orii, H. Sekiya, M. Shiozawa, A. Takeda, H. Tanaka, T. Tomura, R. A. Wendell, R. Akutsu, T. Irvine, T. Kajita, K. Kaneyuki, Y. Nishimura, L. Labarga, P. Fernandez, J. Gustafson, C. Kachulis, E. Kearns, J. L. Raaf, J. L. Stone, L. R. Sulak, S. Berkman, C. M. Nantais, H. A. Tanaka, S. Tobayama, M. Goldhaber, W. R. Kropp, S. Mine, P. Weatherly, M. B. Smy, H. W. Sobel, V. Takhistov, K. S. Ganezer, B. L. Hartfiel, J. Hill, N. Hong, J. Y. Kim, I. T. Lim, R. G. Park, A. Himmel, Z. Li, E. O'Sullivan, K. Scholberg, C. W. Walter, T. Wongjirad, T. Ishizuka, S. Tasaka, J. S. Jang, J. G. Learned, S. Matsuno, S. N. Smith, M. Friend, T. Hasegawa, T. Ishida, T. Ishii, T. Kobayashi, T. Nakadaira, K. Nakamura, Y. Oyama, K. Sakashita, T. Sekiguchi, T. Tsukamoto, A. T. Suzuki, Y. Takeuchi, T. Yano, S. V. Cao, T. Hiraki, S. Hirota, K. Huang, T. Kikawa, A. Minamino, T. Nakaya, K. Suzuki, Y. Fukuda, K. Choi, Y. Itow, T. Suzuki, P. Mijakowski, K. Frankiewicz, J. Hignight, J. Imber, C. K. Jung, X. Li, J. L. Palomino, M. J. Wilking, C. Yanagisawa, D. Fukuda,

H. Ishino, T. Kayano, A. Kibayashi, Y. Koshio, T. Mori, M. Sakuda, C. Xu, Y. Kuno, R. Tacik, S. B. Kim, H. Okazawa, Y. Choi, K. Nishijima, M. Koshiba, Y. Totsuka, Y. Suda, M. Yokoyama, C. Bronner, M. Hartz, K. Martens, L. Marti, Y. Suzuki, M. R. Vagins, J. F. Martin, A. Konaka, S. Chen, Y. Zhang, R. J. Wilkes, and Super-Kamiokande Collaboration, "Measurements of the atmospheric neutrino flux by Super-Kamiokande: Energy spectra, geomagnetic effects, and solar modulation," , vol. 94, no. 5, p. 052001, Sep. 2016.

[118] L. Biermann, "Über den Ursprung der Magnetfelder auf Sternen und im interstellaren Raum (miteinem Anhang von A. Schlüter)," *Zeitschrift Naturforschung Teil A*, vol. 5, p. 65, Jan. 1950.

[119] R. M. Kulsrud, R. Cen, J. P. Ostriker, and D. Ryu, "The Protogalactic Origin for Cosmic Magnetic Fields," , vol. 480, no. 2, pp. 481–491, May 1997.

[120] H. Kang, R. Cen, J. P. Ostriker, and D. Ryu, "Hot Gas in the Cold Dark Matter Scenario: X-Ray Clusters from a High-Resolution Numerical Simulation," , vol. 428, p. 1, Jun. 1994.

[121] S. Roh, D. Ryu, H. Kang, S. Ha, and H. Jang, "Turbulence Dynamo in the Stratified Medium of Galaxy Clusters," , vol. 883, no. 2, p. 138, Oct. 2019.

[122] H. Kang, T. W. Jones, and U. D. J. Gieseler, "Numerical Studies of Cosmic-Ray Injection and Acceleration," , vol. 579, no. 1, pp. 337–358, Nov. 2002.

[123] T. Enßlin, C. Pfrommer, F. Miniati, and K. Subramanian, "Cosmic ray transport in galaxy clusters: implications for radio halos, gamma-ray signatures, and cool core heating," , vol. 527, p. A99, Mar. 2011.

[124] J. Wiener, S. P. Oh, and F. Guo, "Cosmic ray streaming in clusters of galaxies," , vol. 434, no. 3, pp. 2209–2228, Sep. 2013.

[125] J. Wiener, E. G. Zweibel, and S. P. Oh, "High β effects on cosmic ray streaming in galaxy clusters," , vol. 473, no. 3, pp. 3095–3103, Jan. 2018.

[126] C. Pfrommer, T. A. Enßlin, V. Springel, M. Jubelgas, and K. Dolag, "Simulating cosmic rays in clusters of galaxies - I. Effects on the Sunyaev-Zel'dovich effect and the X-ray emission," , vol. 378, no. 2, pp. 385–408, Jun. 2007.

[127] F. Vazza, M. Brüggen, C. Gheller, and G. Brunetti, "Modelling injection and feedback of cosmic rays in grid-based cosmological simulations: effects on cluster outskirts," , vol. 421, no. 4, pp. 3375–3398, Apr. 2012.

[128] G. Brunetti, S. Zimmer, and F. Zandanel, "Relativistic protons in the Coma galaxy cluster: first gamma-ray constraints ever on turbulent reacceleration," , vol. 472, no. 2, pp. 1506–1525, Dec. 2017.

[129] H. Kang and D. Ryu, "Re-acceleration of Non-thermal Particles at Weak Cosmological Shock Waves," , vol. 734, no. 1, p. 18, Jun. 2011.

[130] D. Caprioli, P. Blasi, E. Amato, and M. Vietri, "Dynamical feedback of self-generated magnetic fields in cosmic ray modified shocks," , vol. 395, no. 2, pp. 895–906, May 2009.

[131] S. Mei, J. P. Blakeslee, P. Côté, J. L. Tonry, M. J. West, L. Ferrarese, A. Jordán, E. W. Peng, A. Anthony, and D. Merritt, "The ACS Virgo Cluster Survey. XIII. SBF Distance Catalog and the Three-dimensional Structure of the Virgo Cluster," , vol. 655, no. 1, pp. 144–162, Jan. 2007.

[132] S. Mieske and M. Hilker, "Distance to the Centaurus cluster and its subcomponents from surface brightness fluctuations," , vol. 410, pp. 445–459, Nov. 2003.

[133] J. Aleksić, E. A. Alvarez, L. A. Antonelli, P. Antoranz, M. Asensio, M. Backes, U. Barres de Almeida, J. A. Barrio, D. Bastieri, J. Becerra González, W. Bednarek, A. Berdyugin, K. Berger, E. Bernardini, A. Biland, O. Blanch, R. K. Bock, A. Boller, G. Bonnoli, D. Borla Tridon, I. Braun, T. Bretz, A. Cañellas, E. Carmona, A. Carosi, P. Colin, E. Colombo, J. L. Contreras, J. Cortina, L. Cossio, S. Covino, F. Dazzi, A. de Angelis, G. de Caneva, E. de Cea Del Pozo, B. de Lotto, C. Delgado Mendez, A. Diago Ortega, M. Doert, A. Domínguez, D. Dominis Prester, D. Dorner, M. Doro, D. Eisenacher, D. Elsaesser, D. Ferenc, M. V. Fonseca, L. Font, C. Fruck, R. J. García López, M. Garczarczyk, D. Garrido, G. Giavitto, N. Godinović, S. R. Gozzini, D. Hadasch, D. Häfner, A. Herrero, D. Hildebrand, D. Höhne-Mönch, J. Hose, D. Hrupec, T. Jogler, H. Kellermann, S. Klepser, T. Krähenbühl, J. Krause, J. Kushida, A. La Barbera, D. Lelas, E. Leonardo, N. Lewandowska, E. Lindfors, S. Lombardi, M. López, R. López, A. López-Oramas, E. Lorenz, M. Makariev, G. Maneva, N. Mankuzhiyil, K. Mannheim, L. Maraschi, M. Mariotti, M. Martínez, D. Mazin, M. Meucci, J. M. Miranda, R. Mirzoyan, J. Moldón, A. Moralejo, P. Munar-Adrover, A. Niedzwiecki, D. Nieto, K. Nilsson, N. Nowak, R. Orito, S. Paiano, D. Paneque, R. Paoletti, S. Pardo, J. M. Paredes, S. Partini, M. A. Perez-Torres, M. Persic, L. Peruzzo, M. Pilia, J. Pochon, F. Prada, P. G. Prada Moroni, E. Prandini, I. Puerto Gimenez, I. Puljak, I. Reichardt, R. Reinthal, W. Rhode, M. Ribó, J. Rico, S. Rügamer, A. Saggion, K. Saito, T. Y. Saito, M. Salvati, K. Satalecka, V. Scalzotto, V. Scapin, C. Schultz, T. Schweizer, M. Shayduk, S. N. Shore, A. Sillanpää, J. Sitarek, I. Snidaric, D. Sobczynska, F. Spanier, S. Spiro, V. Stamatescu, A. Stamerra, B. Steinke, J. Storz, N. Strah, S. Sun, T. Surić, L. Takalo, H. Takami, F. Tavecchio, P. Temnikov, T. Terzić, D. Tescaro, M. Teshima, O. Tibolla, D. F. Torres, A. Treves, M. Uellenbeck, H. Vankov, P. Vogler, R. M. Wagner, Q. Weitzel, V. Zabalza, F. Zandanel, R. Zanin, MAGIC Collaboration, C. Pfrommer, and A. Pinzke, "Constraining cosmic rays and magnetic fields in the Perseus galaxy cluster with TeV observations by the MAGIC telescopes," , vol. 541, p. A99, May 2012.

[134] B. Thomsen, W. A. Baum, M. Hammergren, and G. Worthey, "The Distance to the Coma Cluster from Surface Brightness Fluctuations," , vol. 483, no. 1, pp. L37–L40, Jul. 1997.

[135] F. Durret, K. Wakamatsu, T. Nagayama, C. Adami, and A. Biviano, "Ophiuchus: An optical view of a very massive cluster of galaxies hidden behind the Milky Way ⋆," , vol. 583, p. A124, Nov. 2015.

[136] O. Urban, N. Werner, A. Simionescu, S. W. Allen, and H. Böhringer, "X-ray spectroscopy of the Virgo Cluster out to the virial radius," , vol. 414, no. 3, pp. 2101–2111, Jul. 2011.

[137] Y. Chen, T. H. Reiprich, H. Böhringer, Y. Ikebe, and Y. Y. Zhang, "Statistics of X-ray observables for the cooling-core and non-cooling core galaxy clusters," , vol. 466, no. 3, pp. 805–812, May 2007.

[138] K. Abe, T. Abe, H. Aihara, Y. Fukuda, Y. Hayato, K. Huang, A. K. Ichikawa, M. Ikeda, K. Inoue, H. Ishino, Y. Itow, T. Kajita, J. Kameda, Y. Kishimoto, M. Koga, Y. Koshio, K. P. Lee, A. Minamino, M. Miura, S. Moriyama, M. Nakahata, K. Nakamura, T. Nakaya, S. Nakayama, K. Nishijima, Y. Nishimura, Y. Obayashi, K. Okumura, M. Sakuda, H. Sekiya, M. Shiozawa, A. T. Suzuki, Y. Suzuki, A. Takeda, Y. Takeuchi, H. K. M. Tanaka, S. Tasaka, T. Tomura, M. R. Vagins, J. Wang, and M. Yokoyama, "Letter of Intent: The Hyper-Kamiokande Experiment — Detector Design and Physics Potential —," *arXiv e-prints*, p. arXiv:1109.3262, Sep. 2011.

[139] M. A. Riquelme and A. Spitkovsky, "Electron Injection by Whistler Waves in Non-relativistic Shocks," , vol. 733, no. 1, p. 63, May 2011.

[140] H. Kang, D. Ryu, and J.-H. Ha, "Electron preacceleration in weak quasi-perpendicular shocks in high-beta intracluster medium," *The Astrophysical Journal*, vol. 876, no. 1, p. 79, may 2019. [Online]. Available: https://doi.org/10.3847\%2F1538-4357\%2Fab16d1

[141] J. Niemiec, O. Kobzar, T. Amano, M. Hoshino, S. Matsukiyo, Y. Matsumoto, and M. Pohl, "Electron Acceleration at Rippled Low Mach Number Shocks in Merging Galaxy Clusters," in *36th International Cosmic Ray Conference (ICRC2019)*, ser. International Cosmic Ray Conference, vol. 36, Jul. 2019, p. 368.

[142] R. J. van Weeren, F. de Gasperin, H. Akamatsu, M. Brüggen, L. Feretti, H. Kang, A. Stroe, and F. Zandanel, "Diffuse Radio Emission from Galaxy Clusters," , vol. 215, no. 1, p. 16, Feb. 2019.

[143] S. Kim, J.-H. Ha, D. Ryu, and H. Kang, "Electron Firehose Instabilities in High-β Intracluster Shocks," , vol. 892, no. 2, p. 85, Apr. 2020.

[144] J. T. Gosling, M. F. Thomsen, S. J. Bame, and C. T. Russell, "Suprathermal electrons at Earth's bow shock," , vol. 94, no. A8, pp. 10 011–10 025, Aug. 1989.

[145] D. Burgess and M. Scholer, "Shock front instability associated with reflected ions at the perpendicular shock," *Physics of Plasmas*, vol. 14, no. 1, pp. 012 108–012 108, Jan. 2007.

[146] T. Amano and M. Hoshino, "Electron Shock Surfing Acceleration in Multidimensions: Two-Dimensional Particle-in-Cell Simulation of Collisionless Perpendicular Shock," , vol. 690, no. 1, pp. 244–251, Jan. 2009.

[147] S. Matsukiyo, Y. Ohira, R. Yamazaki, and T. Umeda, "Relativistic Electron Shock Drift Acceleration in Low Mach Number Galaxy Cluster Shocks," , vol. 742, no. 1, p. 47, Nov. 2011.

[148] Y. Matsumoto, T. Amano, and M. Hoshino, "Electron Accelerations at High Mach Number Shocks: Two-dimensional Particle-in-cell Simulations in Various Parameter Regimes," , vol. 755, no. 2, p. 109, Aug. 2012.

[149] S. Matsukiyo and M. Scholer, "On reformation of quasi-perpendicular collisionless shocks," *Advances in Space Research*, vol. 38, no. 1, pp. 57–63, Jan. 2006.

[150] A. Balogh and R. A. Treumann, *Physics of Collisionless Shocks*, 2013, vol. 12.

[151] D. Trotta and D. Burgess, "Electron acceleration at quasi-perpendicular shocks in sub- and super-critical regimes: 2D and 3D simulations," , vol. 482, no. 1, pp. 1154–1162, Jan. 2019.

[152] S. P. Gary, *Theory of Space Plasma Microinstabilities*, 1993.

[153] S. P. Gary and K. Nishimura, "Resonant electron firehose instability: Particle-in-cell simulations," *Physics of Plasmas*, vol. 10, no. 9, pp. 3571–3576, Sep. 2003.

[154] E. Camporeale and D. Burgess, "Electron firehose instability: Kinetic linear theory and two-dimensional particle-in-cell simulations," *Journal of Geophysical Research (Space Physics)*, vol. 113, no. A7, p. A07107, Jul. 2008.

[155] P. Hellinger, P. M. Trávníček, V. K. Decyk, and D. Schriver, "Oblique electron fire hose instability: Particle-in-cell simulations," *Journal of Geophysical Research (Space Physics)*, vol. 119, no. 1, pp. 59–68, Jan. 2014.

[156] S. P. Gary, "Electromagnetic electron beam instabilities: Hot, isotropic beams," , vol. 90, no. A11, pp. 10 815–10 823, Nov. 1985.

[157] S. Saeed, M. Sarfraz, P. H. Yoon, M. Lazar, and M. N. S. Qureshi, "Electron heat flux instability," , vol. 465, no. 2, pp. 1672–1681, Feb. 2017.

[158] S. M. Shaaban, M. Lazar, P. H. Yoon, and S. Poedts, "Beaming electromagnetic (or heat-flux) instabilities from the interplay with the electron temperature anisotropies," *Physics of Plasmas*, vol. 25, no. 8, p. 082105, Aug. 2018.

[159] T. H. Stix, *Waves in plasmas*, 1992.

[160] *Kinetic theory of plasma waves : homogeneous plasmas*, vol. 96, Jan. 1998.

[161] T. Katou and T. Amano, "Theory of Stochastic Shock Drift Acceleration for Electrons in the Shock Transition Region," , vol. 874, no. 2, p. 119, Apr. 2019.

[162] O. Kobzar, J. Niemiec, T. Amano, M. Hoshino, S. Matsukiyo, Y. Matsumoto, and M. Pohl, "Electron Acceleration at Rippled Low-mach-number Shocks in High-beta Collisionless Cosmic Plasmas," , vol. 919, no. 2, p. 97, Oct. 2021.

[163] J.-H. Ha, S. Kim, D. Ryu, and H. Kang, "Effects of multiscale plasma waves on electron preacceleration at weak quasi-perpendicular intracluster shocks," , vol. 915, no. 1, p. 18, jun 2021. [Online]. Available: https://doi.org/10.3847/1538-4357/abfb68

[164] S. Kim, J.-H. Ha, D. Ryu, and H. Kang, "Microinstabilities in the Transition Region of Weak Quasi-perpendicular Intracluster Shocks," , vol. 913, no. 1, p. 35, May 2021.

[165] J. E. Scharer and A. W. Trivelpiece, "Cyclotron wave instabilities in a plasma," *The Physics of Fluids*, vol. 10, no. 3, pp. 591–595, 1967. [Online]. Available: https://aip.scitation.org/doi/abs/10.1063/1.1762153

[166] S. P. Gary, "The mirror and ion cyclotron anisotropy instabilities," *Journal of Geophysical Research: Space Physics*, vol. 97, no. A6, pp. 8519–8529, 1992. [Online]. Available: https://agupubs.onlinelibrary.wiley.com/doi/abs/10.1029/92JA00299

[167] P. Hellinger and Š. Štverák, "Electron mirror instability: particle-in-cell simulations," *Journal of Plasma Physics*, vol. 84, no. 4, p. 905840402, Aug. 2018.

[168] D. Winske and K. B. Quest, "Magnetic field and density fluctuations at perpendicular supercritical collisionless shocks," , vol. 93, no. A9, pp. 9681–9693, Sep. 1988.

[169] S. P. Gary, J. Wang, D. Winske, and S. A. Fuselier, "Proton temperature anisotropy upper bound," , vol. 102, no. A12, pp. 27 159–27 170, Dec. 1997.

[170] D. Burgess, "Simulations of Electron Acceleration at Collisionless Shocks: The Effects of Surface Fluctuations," , vol. 653, no. 1, pp. 316–324, Dec. 2006.

[171] D. Verscharen and B. D. G. Chandran, "THE DISPERSION RELATIONS AND INSTABILITY THRESHOLDS OF OBLIQUE PLASMA MODES IN THE PRESENCE OF AN ION BEAM," *The Astrophysical Journal*, vol. 764, no. 1, p. 88, jan 2013. [Online]. Available: https://doi.org/10.1088%2F0004-637x%2F764%2F1%2F88

[172] N. Ahmadi, K. Germaschewski, and J. Raeder, "Effects of electron temperature anisotropy on proton mirror instability evolution," *Journal of Geophysical Research: Space Physics*, vol. 121, no. 6, pp. 5350–5365, 2016. [Online]. Available: https://agupubs.onlinelibrary.wiley.com/doi/abs/10.1002/2016JA022429

[173] S. P. Gary and H. Karimabadi, "Linear theory of electron temperature anisotropy instabilities: Whistler, mirror, and weibel," *Journal of Geophysical Research: Space Physics*, vol. 111, no. A11, 2006. [Online]. Available: https://agupubs.onlinelibrary.wiley.com/doi/abs/10.1029/2006JA011764

[174] R. E. Lowe and D. Burgess, "The properties and causes of rippling in quasi-perpendicular collisionless shock fronts," *Annales Geophysicae*, vol. 21, no. 3, pp. 671–679, Mar. 2003.

[175] S. Matsukiyo and Y. Matsumoto, "Electron Acceleration at a High Beta and Low Mach Number Rippled Shock," in *Journal of Physics Conference Series*, ser. Journal of Physics Conference Series, vol. 642, Sep. 2015, p. 012017.

[176] H. Hojo, A. Mase, R. Katsumata, M. Inutake, A. Itakura, and M. Ichimura, "Density fluctuations associated with electromagnetic waves in ion cyclotron range of frequencies," *Japanese Journal of Applied Physics*, vol. 32, no. Part 1, No. 7, pp. 3287–3288, jul 1993. [Online]. Available: https://doi.org/10.1143%2Fjjap.32.3287

[177] P. K. Shukla and L. Stenflo, "Nonlinear propagation of electromagnetic ion-cyclotron alfvén waves," *The Physics of Fluids*, vol. 28, no. 5, pp. 1576–1578, 1985. [Online]. Available: https://aip.scitation.org/doi/abs/10.1063/1.864946

[178] D. Verscharen and E. Marsch, "Compressive high-frequency waves riding on an alfvén/ion-cyclotron wave in a multi-fluid plasma," *Journal of Plasma Physics*, vol. 77, no. 5, p. 693–707, 2011.

[179] E. Marsch and D. Verscharen, "On nonlinear alfvén-cyclotron waves in multi-species plasma," *Journal of Plasma Physics*, vol. 77, no. 3, p. 385–403, 2011.

[180] P. Hellinger and A. Mangeney, "Upstream whistlers generated by protons reflected from a quasi-perpendicular shock," *Journal of Geophysical Research: Space Physics*, vol. 102, no. A5, pp. 9809–9819, 1997. [Online]. Available: https://agupubs.onlinelibrary.wiley.com/doi/abs/10.1029/96JA03826

[181] X. Guo, L. Sironi, and R. Narayan, "Electron Heating in Low-Mach-number Perpendicular Shocks. I. Heating Mechanism," , vol. 851, no. 2, p. 134, Dec. 2017.

[182] V. Krasnoselskikh, M. Balikhin, S. N. Walker, S. Schwartz, D. Sundkvist, V. Lobzin, M. Gedalin, S. D. Bale, F. Mozer, J. Soucek, Y. Hobara, and H. Comisel, "The Dynamic Quasiperpendicular Shock: Cluster Discoveries," , vol. 178, no. 2-4, pp. 535–598, Oct. 2013.

[183] F. de Hoffmann and E. Teller, "Magneto-Hydrodynamic Shocks," *Physical Review*, vol. 80, no. 4, pp. 692–703, Nov. 1950.

[184] V. V. Krasnoselskikh, B. Lembège, P. Savoini, and V. V. Lobzin, "Nonstationarity of strong collisionless quasiperpendicular shocks: Theory and full particle numerical simulations," *Physics of Plasmas*, vol. 9, no. 4, pp. 1192–1209, Apr. 2002.

[185] M. Oka, T. Terasawa, Y. Seki, M. Fujimoto, Y. Kasaba, H. Kojima, I. Shinohara, H. Matsui, H. Matsumoto, Y. Saito, and T. Mukai, "Whistler critical Mach number and electron acceleration at the bow shock: Geotail observation," , vol. 33, no. 24, p. L24104, Dec. 2006.

[186] X. Guo, L. Sironi, and R. Narayan, "Electron Heating in Low Mach Number Perpendicular Shocks. II. Dependence on the Pre-shock Conditions," , vol. 858, no. 2, p. 95, May 2018.

[187] H. Kang, D. Ryu, and T. W. Jones, "Diffusive Shock Acceleration Simulations of Radio Relics," , vol. 756, no. 1, p. 97, Sep. 2012.

[188] A. Pinzke, S. P. Oh, and C. Pfrommer, "Giant radio relics in galaxy clusters: reacceleration of fossil relativistic electrons?" , vol. 435, no. 2, pp. 1061–1082, Oct. 2013.

[189] H. Kang, "Re-Acceleration Model for the "Toothbrush" Radio Relic," *Journal of Korean Astronomical Society*, vol. 49, no. 3, pp. 83–92, Jun. 2016.

[190] ——, "Re-Acceleration Model for the "Sausage" Radio Relic," *Journal of Korean Astronomical Society*, vol. 49, no. 4, pp. 145–155, Aug. 2016.

[191] H. Kang and D. Ryu, "Re-acceleration Model for Radio Relics with Spectral Curvature," , vol. 823, no. 1, p. 13, May 2016.

[192] R. J. van Weeren, F. Andrade-Santos, W. A. Dawson, N. Golovich, D. V. Lal, H. Kang, D. Ryu, M. Brìggen, G. A. Ogrean, W. R. Forman, C. Jones, V. M. Placco, R. M. Santucci, D. Wittman, M. J. Jee, R. P. Kraft, D. Sobral, A. Stroe, and K. Fogarty, "The case for electron re-acceleration at galaxy cluster shocks," *Nature Astronomy*, vol. 1, p. 0005, Jan. 2017.

[193] S. Mandal, H. T. Intema, R. J. van Weeren, T. W. Shimwell, A. Botteon, G. Brunetti, F. de Gasperin, M. Brüggen, G. Di Gennaro, R. Kraft, H. J. A. Röttgering, M. Hardcastle, and C. Tasse, "Revived fossil plasma sources in galaxy clusters," , vol. 634, p. A4, Feb. 2020.

[194] J.-H. Ha, D. Ryu, H. Kang, and S. Kim, "Electron Preacceleration at Weak Quasi-perpendicular Intracluster Shocks: Effects of Preexisting Nonthermal Electrons," , vol. 925, no. 1, p. 88, Jan. 2022.

[195] J. G. Kirk, A. W. Guthmann, Y. A. Gallant, and A. Achterberg, "Particle Acceleration at Ultrarelativistic Shocks: An Eigenfunction Method," , vol. 542, no. 1, pp. 235–242, Oct. 2000.

[196] A. Achterberg, Y. A. Gallant, J. G. Kirk, and A. W. Guthmann, "Particle acceleration by ultrarelativistic shocks: theory and simulations," , vol. 328, no. 2, pp. 393–408, Dec. 2001.

[197] M. Melzani, C. Winisdoerffer, R. Walder, D. Folini, J. M. Favre, S. Krastanov, and P. Messmer, "Apar-T: code, validation, and physical interpretation of particle-in-cell results," , vol. 558, p. A133, Oct. 2013.

[198] D. Wittor, F. Vazza, D. Ryu, and H. Kang, "Limiting the shock acceleration of cosmic ray protons in the ICM," , vol. 495, no. 1, pp. L112–L117, Jun. 2020.

[199] G. Macario, T. Venturi, H. T. Intema, D. Dallacasa, G. Brunetti, R. Cassano, S. Giacintucci, C. Ferrari, C. H. Ishwara-Chandra, and R. Athreya, "153 MHz GMRT follow-up of steep-spectrum diffuse emission in galaxy clusters," , vol. 551, p. A141, Mar. 2013.

[200] M. Kierdorf, R. Beck, M. Hoeft, U. Klein, R. J. van Weeren, W. R. Forman, and C. Jones, "Relics in galaxy clusters at high radio frequencies," , vol. 600, p. A18, Apr. 2017.

[201] C. L. Sarazin, "Models for the Relativistic Electron Population and Nonthermal Emission in Clusters of Galaxies," in *Diffuse Thermal and Relativistic Plasma in Galaxy Clusters*, H. Boehringer, L. Feretti, and P. Schuecker, Eds., Jan. 1999, p. 185.

[202] J. Giacalone, "Particle Acceleration at Shocks Moving through an Irregular Magnetic Field," , vol. 624, no. 2, pp. 765–772, May 2005.

[203] F. Guo and J. Giacalone, "The Acceleration of Electrons at Collisionless Shocks Moving Through a Turbulent Magnetic Field," , vol. 802, no. 2, p. 97, Apr. 2015.

[204] P. Kajdič, L. Preisser, X. Blanco-Cano, D. Burgess, and D. Trotta, "First Observations of Irregular Surface of Interplanetary Shocks at Ion Scales by Cluster," , vol. 874, no. 2, p. L13, Apr. 2019.

[205] H. Kang, J. P. Rachen, and P. L. Biermann, "Contributions to the Cosmic Ray Flux above the Ankle: Clusters of Galaxies," , vol. 286, no. 2, pp. 257–267, Apr. 1997.

[206] A. Loeb and E. Waxman, "Cosmic γ-ray background from structure formation in the intergalactic medium," , vol. 405, no. 6783, pp. 156–158, May 2000.

[207] U. Keshet, E. Waxman, A. Loeb, V. Springel, and L. Hernquist, "Gamma Rays from Intergalactic Shocks," , vol. 585, no. 1, pp. 128–150, Mar. 2003.

[208] U. Keshet, E. Waxman, and A. Loeb, "Imprint of Intergalactic Shocks on the Radio Sky," , vol. 617, no. 1, pp. 281–302, Dec. 2004.

[209] S. Inoue, F. A. Aharonian, and N. Sugiyama, "Hard X-ray and Gamma-ray Emission Induced by Ultra-High Energy Protons in Cluster Accretion Shocks and their Detectability," *arXiv e-prints*, pp. astro–ph/0 507 068, Jul. 2005.

[210] U. Keshet, D. Kushnir, A. Loeb, and E. Waxman, "Preliminary Evidence for a Virial Shock around the Coma Galaxy Cluster," , vol. 845, no. 1, p. 24, Aug. 2017.

[211] U. Keshet and I. Reiss, "Evidence for an X-Ray to Gamma-Ray Virial Shock Signal from the Coma Cluster," , vol. 869, no. 1, p. 53, Dec. 2018.

Acknowledgements